Institute of Chemistry

Describing the Statically Correlated Si-terminated 3C-SiC(001) Surface with Single- and Multiconfigurational Methods

The school of Mathematics and Science of the Carl von Ossietzky Universität Oldenburg has accepted as partial fulfillment of the requirements for the degree and title of

Doktor der Naturwissenschaften (Dr. rer. nat.)

the above-mentioned thesis

by

Mr. Niklas Thoben

born on 08.03.1995 in Löningen, Germany

Oldenburg, 16.10.2024

This thesis was prepared under the supervision of Prof. Dr. Thorsten Klüner at the Institute of Chemistry of the Carl von Ossietzky Universität Oldenburg from October 2019 to August 2024.

First Assessor:	Prof. Dr. Thorsten Klüner
Second Assessor:	Prof. Dr. Thomas Müller
Date of Disputation:	07.10.2024

Space has a beginning but it has no end – infinite.
Stars too have a beginning but are by their own power destroyed – finite.
History dictates that he who holds wisdom is the greatest fool.
The fish in the sea know not the land.
If they too hold wisdom, they too will be destroyed.
It is more ridiculous for man to exceed light speed than for fish to live ashore.
This could be called God's final warning to those that still rebel.

— Hououin Kyouma

Abstract

In this thesis, the spatial and electronic structure of the Si-terminated (001) surface of cubic silicon carbide (3C-SiC) and its reconstructions was investigated theoretically by employing restricted and unrestricted single-configurational periodic slab model calculations as well as multiconfigurational cluster model calculations.

The single-configurational methods identified the well-known p(2×1) reconstruction with symmetric Si dimers and a p(4×1) reconstruction, in which two such dimers further dimerize, to be the most stable structures. Here, the reconstruction strength, characterized by the dimer bond length and the energy gain, significantly depends on the restricted or unrestricted approach applied, with the former generally showing lower and the latter stronger reconstruction. This can be explained by the energetically close and thus statically correlated bonding and antibonding interdimer (ID) surface state bands being poorly described by single-configurational methods in general but slightly better by the unrestricted approach due to its ability of partially including static correlation effects. The spin-symmetry breaking of the unrestricted methods results in a singlet diradicalic electronic structure of each dimer by basically bisecting the ID bonds at the expense of severe spin contamination. The restricted methods, on the other hand, enforce a double occupation of the ID bonds, inhibiting the formation of the actual dimer bonds and thus lowering the reconstruction strength. In contrast to the spin-symmetry breaking of the unrestricted methods, the restricted structures were further able to slightly stabilize by spatial symmetry breaking, leading to possibly artificial p(2×1) and p(4×2) reconstructions with buckled dimers.

Multiconfigurational methods do not suffer from spin contamination and the corresponding cluster model calculations of the p(2×1) reconstruction with symmetric dimers confirmed the anticipated static correlation of the ID and ID^* bands. Here, the composition of the wave function reveals an approximately equal mixture of the closed-shell and radicalic configurations, which is further supported by the reconstruction strength being located in between the values obtained for the restricted and unrestricted methods. Therefore, it can be concluded that single-configurational approaches are insufficient for a faithful description of this system. Furthermore, the multiconfigurational character of the ideal p(1×1) surface could be confirmed and excited state calculations suggest both p(2×1) and p(1×1) surfaces to be semiconducting.

Kurzfassung

In dieser Arbeit wurde die räumliche und elektronische Struktur der Si-terminierten (001) Oberfläche von kubischem Siliciumcarbid (3C-SiC) und deren Rekonstruktionen unter Durchführung von *restricted* und *unrestricted* Ein-Determinanten-Rechnungen an periodischen Schichtmodellen sowie durch Multikonfigurationsrechnungen an Clustermodellen theoretisch untersucht.

Die Ein-Determinanten-Methoden lieferten die wohlbekannte p(2×1)-Rekonstruktion mit symmetrischen Si-Dimeren und eine p(4×1)-Rekonstruktion, in welcher zwei dieser Dimere weiter dimerisieren, als stabilste Strukturen. Die Stärke der Rekonstruktion, welche durch die Länge der Dimerbindung und den Energiegewinn charakterisiert wird, hängt hierbei deutlich davon ab, ob ein *restricted* oder *unrestricted* Ansatz angewandt wurde, wobei ersterer generell schwächere und zweiterer stärkere Rekonstruktionen hervorbrachte. Dies ist begründet in den energetisch ähnlichen und damit statisch korrelierten bindenden und antibindenden inter-Dimer (ID) Oberflächenzustandsbändern, welche im Allgemeinen ungenügend durch Ein-Determinanten-Methoden beschrieben werden, jedoch etwas besser durch den *unrestricted* Ansatz, da dieser einen Teil der statischen Korrelation berücksichtigen kann. Der Spin-Symmetriebruch der *unrestricted* Methoden führt zu einer diradikalischen elektronischen Struktur jedes Dimers durch das Zerschneiden der ID-Bindungen, jedoch auf Kosten von starker Spinkontamination. Die *restricted* Methoden erzwingen dagegen eine doppelte Besetzung der ID-Bindungen, wodurch die Ausbildung der eigentlichen Dimerbindung gehemmt und damit die Stärke der Rekonstruktion verringert wird. Im Gegensatz zu dem Spin-Symmetriebruch der *unrestricted* Methoden konnten sich die *restricted* Strukturen durch weiteres Brechen der räumlichen Symmetrie stabilisieren, wodurch vermutlich artifizielle p(2×1)- und p(4×2)-Rekonstruktionen mit geknickten Dimeren erhalten wurden.

Multikonfigurationsmethoden sind frei von Spinkontamination und die entsprechenden Clustermodellrechnungen der p(2×1)-Rekonstruktion mit symmetrischen Dimeren konnten die vermutete statische Korrelation der ID- und ID^*-Bänder bestätigen. Die Zusammensetzung der Wellenfunktion offenbart etwa gleiche Anteile der geschlossenschaligen und der radikalischen Konfigurationen, was zusätzlich dadurch bestätigt wird, dass sich die Rekonstruktionsstärke zwischen den *restricted* und *unrestricted* Methoden einordnet. Daraus kann geschlussfolgert werden, dass der Ein-Determinanten-Ansatz unzureichend für eine genaue Beschreibung dieses Systems ist. Weiterhin konnte der Multikonfigurationscharakter der idealen p(1×1)-Oberfläche bestätigt werden und Berechnungen der angeregten Zustände suggerieren halbleitende Eigenschaften für beide p(2×1)- und p(1×1)-Oberflächen.

Contents

List of Figures

List of Tables

1 Introduction

Silicon carbide (SiC) is a group 14 wide band gap semiconductor, i.e., its band gap is larger than 2 eV,[1] and it exhibits favorable material properties for everyday applications like ecological friendliness, chemical and mechanical stability, and a high abundance of the involved elements Si and C.[2] It shows polytypism, which is a one-dimensional (1D) subtype of polymorphism. Here, each polytype consists of identical atomic planes with equal amounts of Si and C stacked on top of each other in one direction, but these atomic planes can take three different lateral positions along the remaining two directions, overall resulting in a multitude of possible stacking sequences.[3,4] The two simplest of these for SiC are the two-layer AB type with a hexagonal crystal structure and the three-layer ABC type corresponding to a cubic crystal system, accordingly denoted as 2H-SiC and 3C-SiC, respectively.[3,4] Other polytypes are obtained by mixing these two structural extremes, of which especially the 4H- and 6H-analogues are of further scientific and technical relevance.[2,5,6] The different stacking sequences of the discussed polytypes are schematically depicted in Fig. 1.1. Also, with respect to the electronic structure, 2H- and 3C-SiC correspond to limiting cases showing the largest and smallest band gaps E_g of all polytypes amounting to 3.33 eV and 2.36 eV, respectively.[5,7]

The mechanical properties of SiC are, however, mostly independent of the polytype.[4,6] Traditionally, this material is used, for example, as an abrasive for cutting, grinding, and polishing[6,8] due to its very high Mohs hardness of 9.[4] Furthermore, it decomposes around 2000 °C and is generally not attacked by acids,[4,8] making it suitable for application as a fireproof material.[8] Even though the semiconducting properties had already been observed in 1907

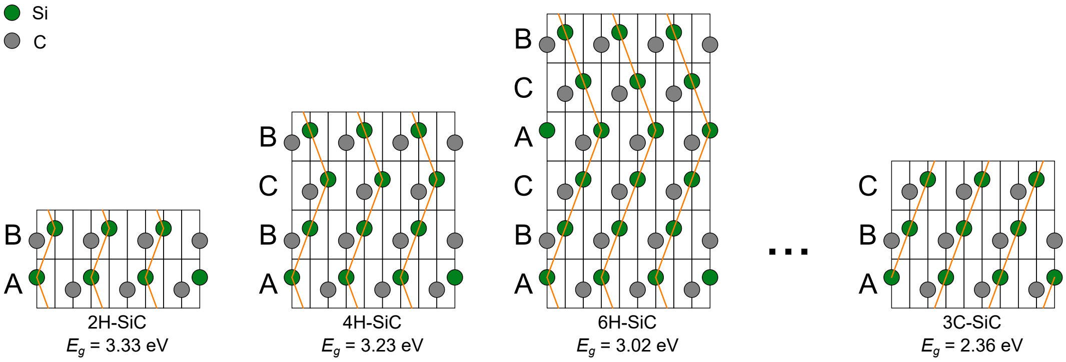

Figure 1.1: Stacking sequences of a small selection of different polytypes of SiC. The experimental values for the bulk band gaps E_g are taken from the following references: 2H-SiC[7], 4H-SiC[5], 6H-SiC[6], 3C-SiC[5,6]. Created based on Ref. [2].

through the discovery of electroluminescence to lay the foundation for the development of light-emitting diodes (LEDs), the challenging production of high-quality 6H- and 4H-SiC wafers was only commercialized in the 1990s. This can be attributed to the sensitive polytype control, the complex high-temperature sublimation or vapor deposition methods, as well as difficult subsequent slicing and polishing due to the extreme material properties.[6]

While SiC will most likely not dethrone Si as most commonly used semiconductor in the near future, it still generally exhibits more favorable properties like higher breakdown electric field strength, higher thermal conductivity and lower on-state resistance, resulting in much higher efficiency in electric power conversion compared to Si.[6,9,10] These properties are especially useful for high-power applications like electric vehicles, where SiC devices were introduced for the first time in 2014,[10] enabling a greater range and more efficient charging of these vehicles.[11] Since electrification is one of the key measures to mitigate the climate crisis according to the Intergovernmental Panel on Climate Change (IPCC),[12] in the last few years several companies have already and are further aiming to increase their SiC manufacturing capacity worldwide.[13] Generally, almost exclusively 4H-SiC is produced due to slightly superior electronic properties and a more refined commercial production of corresponding single-crystalline wafers compared to other polytypes.[6]

Besides these already existing applications, SiC is a promising material in the field of quantum computing as it is able to host quantum bits by the introduction of vacancies.[14] Quantum computing itself might become important with respect to the mitigation of climate change since smart grids for an efficient management of the available electric energy will be essential in this regard.[12] As the electricity grids grow, traditional computers might at some point not be powerful enough to fulfill this task effectively and quantum computers could be needed instead.[15]

As already indicated, the manufacturing of 3C-SiC wafers is not yet commercialized and still in development.[2,6,16] Since 3C-SiC is the thermodynamically most favored polytype, the lower temperature required to obtain it selectively actually limits the development of sublimation growth technology, in which high temperatures are necessary for high-quality results.[16] Accordingly, 3C-SiC can only be obtained by chemical vapor deposition (CVD) in the form of thin films on cubic Si or hexagonal SiC substrates,[2,6] though the deposition on the latter is generally not economic.[16] While the Si substrates are of low cost due to their high availability, the mismatch in lattice constant and thermal expansion coefficient for both materials of 20 % and 8 %, respectively, complicates obtaining low defect density thin films.[2,16] Nevertheless, the smaller band gap of 3C-SiC shows advantageous properties for certain high-power applications compared to its 4H- and 6H-counterparts, making the improvement of 3C-SiC growth methods desirable.[16]

Since 3C-SiC exhibits the smallest band gap of all polytypes with 2.36 eV, it is able to absorb the largest fraction of the solar spectrum and thus bears

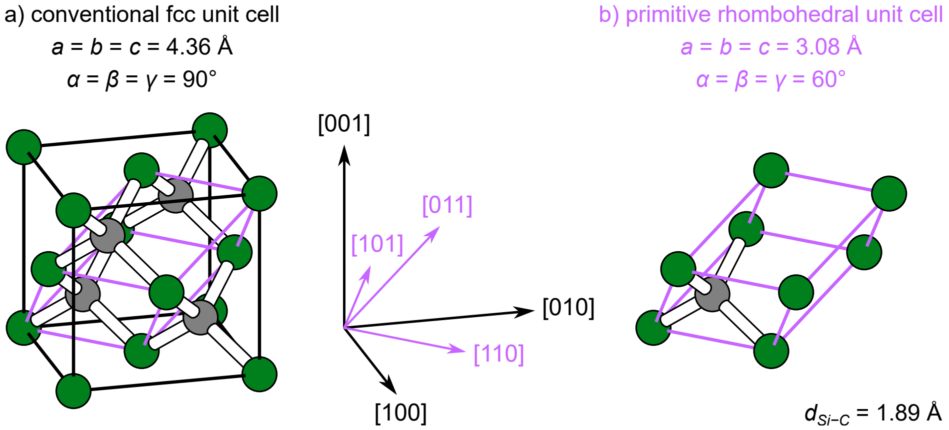

Figure 1.2: a) Conventional fcc and b) primitive rhombohedral bulk unit cells of 3C-SiC. The experimental values for the lattice parameters and the Si–C bond length d_{Si-C} are taken from Ref. [5].

the highest potential as a photoactive material. Furthermore, the band gap conveniently straddles the redox potentials of the hydrogen and oxygen evolution reactions, characterizing it as a promising material for photocatalytic or photoelectrochemical water splitting.[2] Traditionally investigated photocatalysts often show large band gaps greater than 3 eV like TiO_2 or ZnO, do not fully straddle the water splitting redox potentials like WO_3 or Fe_2O_3, or are not stable under reaction conditions like Cu_2O or CdS.[2,17] Accordingly, besides promoting the electric energy transformation by offering more efficient high-power devices, 3C-SiC could also potentially enable the chemical energy transformation through the renewable production of hydrogen. That is why increasing research effort has been devoted to 3C-SiC in this regard, especially in the last few years as the quality of corresponding samples improved.[2,18–25]

Obviously, any photocatalytic reaction has to take place at the surface of 3C-SiC. Since a large fraction of the corresponding thin films are grown on Si(001) substrates, 3C-SiC(001) is accordingly the most commonly investigated surface of this material[16,26–28] and derived in more detail in the following. The starting point is the bulk unit cell of 3C-SiC, which, according to its space group number 216, is generally described by its conventional face-centered cubic (fcc) unit cell exhibiting the zincblende structure[28] with a cell parameter a of 4.36 Å as depicted in Fig. 1.2a). Since the crystal system is cubic, the unit cell edges and thus the directions [100], [010], and [001] are conveniently parallel to the cartesian axes. Alternatively, the 3C-SiC bulk can also be described by the smaller primitive rhombohedral unit cell given in Fig. 1.2b) with lattice parameters of 3.08 Å in the [110], [101], and [011] directions and with angles of 60°. Here, the fundamental building block of CSi_4 or conversely SiC_4 tetrahedrons in 3C-SiC is directly apparent. If now the (001) surface has to be constructed, the corresponding plane is perpendicular to the [001] direction, which is simply represented by the top face of the fcc unit cell in Fig. 1.2a). It should be noted that the (100) and (010) surfaces are identical to their (001) counterpart due to the cubic symmetry. However, instead of using the whole conventional bulk unit cell to construct the (001) surface, its size can be halved by transformation into a tetragonal unit cell as depicted in Fig. 1.3b). Here, the lattice parameters a and b are shortened to the same value of 3.08 Å as in the primitive bulk unit cell and are aligned with the [110] and $[\bar{1}10]$ directions, generally denoted as x- and y-directions for the rest of this work. When ignoring the translational repetition of atoms on the corners, edges, and faces as depicted in c), this unit cell contains four atoms along [001] or the z-direction, each corresponding to one atomic layer of the (001) surface. As illustrated in d), stacking multiples of this unit cell on top of each other and adding vacuum regions above and below to obtain a proper surface unit cell, the helical building block becomes apparent, which essentially constructs

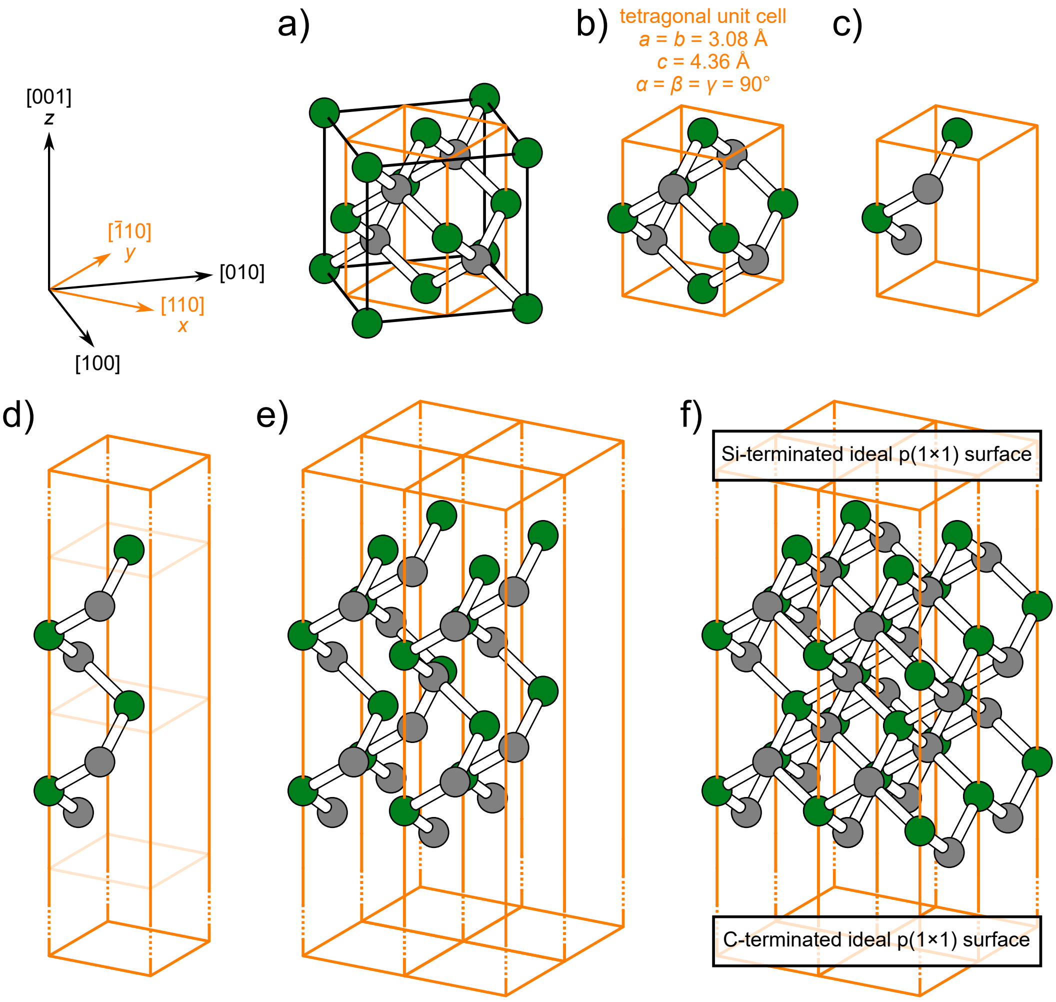

Figure 1.3: a) Conventional fcc 3C-SiC bulk unit cell with the tetragonal bulk unit cell used for the construction of the ideal 3C-SiC(001)-p(1×1) surface, b+c) the isolated tetragonal bulk unit cell b) with and c) without the repetition of atoms placed on the corners, edges, and faces of the unit cell due to translational symmetry, d) singular and e+f) multiples of an 8-layer surface unit cell of the ideal 3C-SiC(001)-p(1×1) surface f) with and d+e) without the repetition of atoms placed on the corners, edges, and faces of the unit cell due to translational symmetry. For the sake of clarity, no bonds between atoms of neighboring unit cells are depicted in e).

the 3C-SiC(001) surface as shown in e) and f). Due to the alternating Si and C layers in the z-direction, either a Si- or a C-terminated 3C-SiC(001) surface is possible. Since so far these surface unit cells are simply constructed from the bulk structure without any reconstruction or relaxation and since its size cannot be further reduced in x- and y-direction, they are denoted as ideal p(1×1) unit cells.

It was shown theoretically that the Si-terminated surface is hydrophilic, while its C-terminated counterpart is hydrophobic,[29–33] making the former potentially more suitable for the water splitting reactions and accordingly the focus of this work. However, even though a considerable amount of research was devoted to this system both experimentally and theoretically in the 1990s and early 2000s, the nature of the Si-terminated 3C-SiC(001) surface is not resolved in a fully consistent manner, as summarized and debated intensively in the two reviews by Soukiassian and Enriquez[27] and Pollmann and Krüger.[28] Generally, there is an experimental consensus that a c(4×2) reconstruction is the most stable phase at room temperature (RT). Furthermore, a p(2×1) reconstruction was also observed at the same conditions, which could be shown to occur especially for higher densities of defects or contaminations, interpreting it as a failed formation of the supposedly favored c(4×2) reconstruction.[27,34] Moreover, a reversible transition between the c(4×2) reconstruction and a p(2×1) phase was reported when increasing the temperature from RT to 400 °C.[27,35] Based on this, Soukiassian and Enriquez suggested two closely related structural models that could explain this behavior, namely the alternating up- and down-dimer (AUDD) model for the c(4×2) reconstruction and a failed AUDD[27,36] or symmetric dimer (SD) model[37] for the p(2×1) reconstruction depicted in Fig. 1.4c) and b), respectively. As apparent, both models consist of parallel rows of symmetric or unbuckled Si dimers aligned in x-direction, but in case of the AUDD model, these dimers alternate in height and bond length in x- and y-direction, i.e., every down-dimer is surrounded by four up-dimers and vice versa. Here, the down-dimers show a shorter and the up-dimers a longer dimer bond. However, the temperature-induced p(2×1) surface exhibits metallic character,[35] while the p(2×1) and c(4×2) reconstructions are both semiconducting at RT,[35,38] which questions the relation of these three phases.[28] To resolve this issue, it was argued that the high-temperature phase actually originates from the AUDD model and that the temperature-induced vibrations simply distort the originally covalent surface states to exhibit metallic character. This could also explain the apparent p(2×1) symmetry as result of the time-averaging in the experimental methods.[27,35,38]

Coming from a more theoretical background, Pollmann and Krüger reasoned the existence of the AUDD and SD models to be improbable due to the very low energy gain per dimer for the latter model of about −0.01 eV with respect to the ideal p(1×1) surface (Fig. 1.4a) obtained in various periodic slab model calculations employing density functional theory (DFT).[28,39–45] While it was never actually calculated in any of the studies finding the AUDD model,[42,46] it

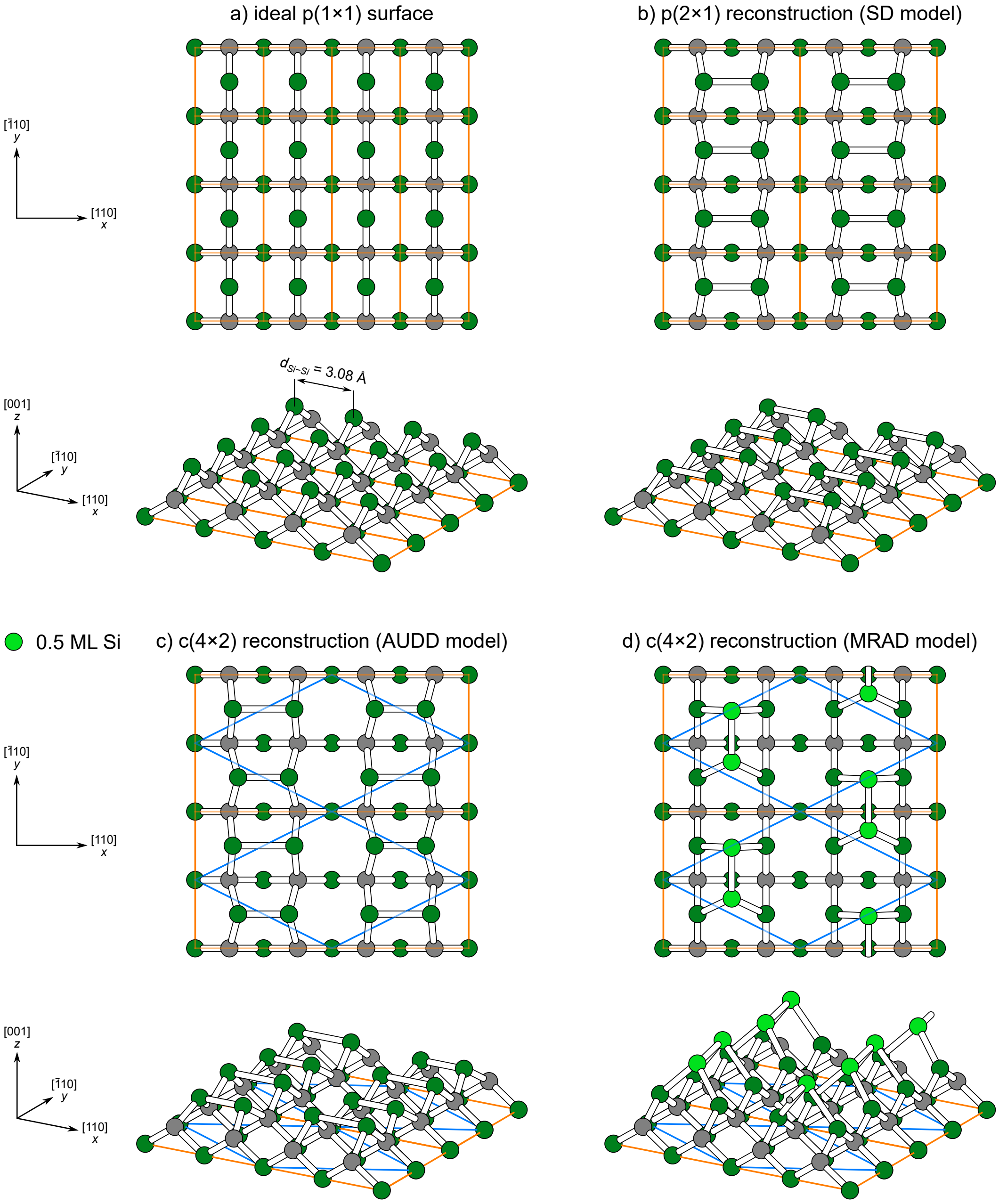

Figure 1.4: Top and lateral view of the topmost atomic layers of the a) ideal p(1×1), b) p(2×1) reconstructed symmetric dimer (SD) model, c) c(4×2) reconstructed alternating up-and-down dimer (AUDD) model, and d) c(4×2) reconstructed missing-row asymmetric-dimer (MRAD) model for the Si-terminated 3C-SiC(001) surface. In case of the c(4×2) reconstructions, the actual centered rectangular c(4×2) unit cell is depicted in orange and the primitive rhombic $(\sqrt{5}\times\sqrt{5})R(2\cdot\tan^{-1}(0.5))$ unit cell is colored blue. Reprinted with permission from *J. Phys. Chem. C* 2023, 127, 48, 23475–23488. Copyright 2023 American Chemical Society. Slightly modified and extended by c) and d).

is reasonable to expect comparably low stabilization energies due to their close structural relation. Accordingly, it is questionable whether these two weakly stabilized models can actually exist at RT, where the p(2×1) and c(4×2) reconstructions have been observed in the experiments. Besides, the theoretical studies generally favor the SD model over the AUDD model for unstrained surface unit cells[28,42,46–48] and only application of tensile stress by increasing the lateral lattice parameters in x- and y-direction yields the AUDD model.[28,42,46] Keeping in mind that the experimentally investigated 3C-SiC samples are thin films grown on a Si substrate exhibiting a larger lattice parameter compared to 3C-SiC, this mismatch might justify the consideration of tensile strain in the calculations. However, Pollmann and Krüger remark it is unresolved if the surface stress at the interface of the two materials can carry through several thousand atomic layers of the thin film of a few micrometers to the actual 3C-SiC surface.[28] Consequently, an alternative model for the c(4×2) reconstruction featuring an additional half monolayer of Si atoms was suggested by these authors, namely the missing-row asymmetric dimer (MRAD) model, in which the additional Si atoms form dimers as depicted in Fig. 1.4d).[28,47] However, as pointed out by Soukiassian and Enriquez, this model is not suitable to explain the reversible temperature-induced transition between the c(4×2) and p(2×1) reconstructions since the latter phase is not achievable without adding or removing Si atoms.[27] In conclusion, the discussion regarding the structure of the Si-terminated 3C-SiC(001) surface is not fully resolved until today, with only sparse additional research devoted to this topic in the last two decades.

Taking a closer look at the electronic structure of the AUDD and SD model, the unbuckled Si dimers of both models form to reduce the number of energetically unfavorable singly occupied dangling bonds present at the ideal p(1×1) surface from two to one per surface Si atom, which is comparable to the dimer formation of the closely related and extensively investigated Si(001) surface. This also explains why the ideal p(1×1) surface is not observed experimentally[28] as it reconstructs immediately. For Si(001), however, these dimers buckle as a result of the Jahn-Teller (JT) effect, which further stabilizes the surface by splitting the remaining degenerate singly occupied dangling bonds into a doubly occupied sp^3-like orbital at the upper and an empty p_z-like orbital at the lower Si atom.[49–52] Such JT splitting is not observed in the large majority of theoretical studies regarding the Si-terminated 3C-SiC(001) surface and thus the dimers remain unbuckled.[39–46,48,53,54] This difference between the two systems is supposedly caused by the smaller lattice parameter of 3C-SiC resulting in a stronger Coulomb repulsion between the Si–Si dimer bond and the Si–C back bonds to the surface,[28] or, put differently, by the higher ring strain of the involved five-membered rings in case of 3C-SiC (see Fig. 1.4b) compared to Si. Accordingly, two singly occupied dangling bonds remain at each dimer of the Si-terminated 3C-SiC(001)-p(2×1) reconstructed surface, which represents the typical example of a statically or strongly correlated singlet diradical. Such systems cannot be described faithfully by single-configurational methods like DFT and multiconfigurational wave function-based approaches are needed instead.[52,53,55,56] Alternatively, unrestricted single-configurational calculations might recover some of the static correlation compared to the usually applied restricted approach, but presumably at the expense of spin contamination. This negative effect is especially severe when the spin multiplicity is not maximal with respect to the number of singly occupied orbitals present, which is obviously the case for a singlet diradical. Besides the symmetric dimers of the p(2×1) reconstruction, it can be anticipated that the ideal p(1×1) surface supposedly shows even greater multiconfigurational character since there are basically two dangling bonds present per surface atom, which could already be confirmed for the Si(001) analogue.[56]

Despite this simple qualitative analysis of the electronic structure, to the best of this work's author's knowledge, the majority of theoretical studies regarding the Si-terminated 3C-SiC(001) surface employed restricted calculations,[39–46,48] while multiconfigurational[53] and unrestricted[54] approaches were only applied once, respectively. In 2003, Tamura and Gordon carried out the pioneering multiconfigurational calculations for a cluster model with a single Si dimer to observe a significant dimer bond shortening compared to previous restricted results and a supposedly fully diradicalic electronic structure.[53] Since no larger cluster models were investigated by the authors, most likely due to the limited computational power at that time, the question regarding the interaction of multiple dimers, which is the case on the real surface, is left unanswered. The first unrestricted periodic slab model calculation of this system by Xi et al. in 2019 gave a similar dimer bond shortening, though they did not further discuss this with respect to previous restricted results as they focused their work on the corrosion of this surface.[54]

Accordingly, the aim of this work is to gain a better understanding of the true nature of the spatial and electronic structure of the Si-terminated 3C-SiC(001) surface and its reconstructions. For this, single-configurational periodic slab model calculations are carried out to study the effect of the restricted and unrestricted approach as well as the influence of different DFT functionals to fill out the remaining gaps present in the literature. This is combined with a detailed analysis of the electronic structure to explain the difference in reconstruction of the several approaches. Afterwards, multiconfigurational calculations of cluster models containing multiple surface dimers are conducted to go beyond the single-dimer approach of Tamura and Gordon[53] and thus determine the interaction of multiple dimers at the supposedly highest theoretical level available to this date. Before presenting the actual results, however, a comprehensive introduction into the applied electronic structure theory methods is given for a better understanding. In particular, a large part is devoted to the electronic structure theory of solids to build a bridge between the band structure traditionally assigned to the field of physics and the orbital picture generally used by chemists.

2 Theoretical Foundations

2.1 General Electronic Structure Theory

2.1.1 Single-Configurational Methods

2.1.1.1 Hartree-Fock

In theoretical chemistry, the main goal is to solve the electronic, non-relativistic, time-independent Schrödinger equation (TISE) for an N-electron system like an atom or a molecule:[57–59]

$$\hat{H}\left|\Psi\right\rangle = E\left|\Psi\right\rangle \tag{2.1}$$

By solving this equation, the electronic wave function $\left|\Psi\right\rangle$ and its total energy E can be obtained. While the wave function of an arbitrary N-electron system with K nuclei is generally unknown, the corresponding electronic Hamiltonian $\hat{H}$ can be exactly written as the sum of the operators of the kinetic energy of electrons $\hat{T}_e$, the potential energy between nuclei and electrons $\hat{V}_{ne}$, between electrons $\hat{V}_{ee}$, and between nuclei $\hat{V}_{nn}$. The Hamiltonian can also be further reorganized to the one- and two-electron operators $\hat{h}_i$ and $\hat{g}_{ij}$:[57–59]

$$\begin{aligned}
\hat{H} &= \hat{T}_e + \hat{V}_{ne} + \hat{V}_{ee} + \hat{V}_{nn} && (2.2)\\
&= -\sum_{i=1}^{N}\frac{1}{2}\vec{\nabla}_i^2 - \sum_{\alpha=1}^{K}\sum_{i=1}^{N}\frac{Z_\alpha}{|\vec{r}_{\alpha i}|} + \sum_{i=1}^{N}\sum_{j>i}^{N}\frac{1}{|\vec{r}_{ij}|} + \sum_{\alpha=1}^{K}\sum_{\beta>\alpha}^{K}\frac{Z_\alpha Z_\beta}{|R_{\alpha\beta}|} && (2.3)\\
&= \sum_{i=1}^{N}\left(-\frac{1}{2}\vec{\nabla}_i^2 - \sum_{\alpha=1}^{K}\frac{Z_\alpha}{|\vec{r}_{\alpha i}|}\right) + \sum_{i=1}^{N}\sum_{j>i}^{N}\frac{1}{|\vec{r}_{ij}|} + \sum_{\alpha=1}^{K}\sum_{\beta>\alpha}^{K}\frac{Z_\alpha Z_\beta}{|R_{\alpha\beta}|} && (2.4)\\
&= \sum_{i=1}^{N}\hat{h}_i + \sum_{i=1}^{N}\sum_{j>i}^{N}\hat{g}_{ij} + \hat{V}_{nn} && (2.5)
\end{aligned}$$

In combination with the variational principle, the Hamiltonian can be used to find the ground state wave function of the investigated system by consecutively changing an arbitrary starting wave function until its energy is minimal. Afterwards, any observable/expectation value of interest is accessible by applying the corresponding operator. However, since the solution of the TISE for an N-electron system is very complex, the full N-electron wave function can be approximated by an antisymmetric product of N molecular spin orbitals

$\chi_a(\vec{x}_i)$ (one-electron wave functions) in the form of a single Slater determinant (SD), which fulfills the Pauli principle:[57–59]

$$|\Psi\rangle = \Psi(\vec{x}_1, \vec{x}_2, \ldots, \vec{x}_N) = \frac{1}{\sqrt{N!}} \begin{vmatrix} \chi_1(\vec{x}_1) & \chi_2(\vec{x}_1) & \ldots & \chi_N(\vec{x}_1) \\ \chi_1(\vec{x}_2) & \chi_2(\vec{x}_2) & \ldots & \chi_N(\vec{x}_2) \\ \vdots & \vdots & \ddots & \vdots \\ \chi_1(\vec{x}_N) & \chi_2(\vec{x}_N) & \ldots & \chi_N(\vec{x}_N) \end{vmatrix} \tag{2.6}$$

$$= |\chi_1 \chi_2 \cdots \chi_N\rangle \tag{2.7}$$

Here, the electronic coordinates $\vec{x}_i$ correspond to the space and spin coordinates $\vec{r}_i$ and ω_i of electron i. A molecular spin orbital $\chi_a(\vec{x}_i)$ is the product of a spatial molecular orbital $\psi_a(\vec{r}_i)$ (MO) and a spin function, either $\alpha(\omega_i)$ (spin up) or $\beta(\omega_i)$ (spin down):[57–59]

$$|\chi_a(\vec{x}_1)\rangle = \chi_a(\vec{x}_1) = \begin{cases} \psi_a(\vec{r}_1)\alpha(\omega_1) = |\psi_a(\vec{r}_1)\rangle\, |\alpha(\omega_1)\rangle \\ \text{or} \\ \psi_a(\vec{r}_1)\beta(\omega_1) = |\psi_a(\vec{r}_1)\rangle\, |\beta(\omega_1)\rangle \end{cases} \tag{2.8}$$

To now utilize the variational principle and find the best spin MOs, a way of obtaining the energy has to be derived. For this, the expectation value of the Hamiltonian is calculated using the SD, which results in the following energy expression including the sums over the one-electron integrals h_a and the two-electron integrals J_{ab} and K_{ab}, corresponding to the Coulomb and exchange interactions, respectively.[57–59] Note that the electronic coordinates are abbreviated by their indices in the following, e.g., $\vec{x}_1$ as 1.

$$E = \langle\Psi|\hat{H}|\Psi\rangle \tag{2.9}$$

$$= \sum_{a=1}^{N} \langle\chi_a(1)|\hat{h}(1)|\chi_a(1)\rangle + \sum_{a=1}^{N}\sum_{b>a}^{N}(\langle\chi_a(1)|\hat{J}_b(1)|\chi_a(1)\rangle - \langle\chi_a(1)|\hat{K}_b(1)|\chi_a(1)\rangle) + \hat{V}_{nn} \tag{2.10}$$

$$= \sum_{a=1}^{N} h_a + \sum_{a=1}^{N}\sum_{b>a}^{N}(J_{ab} - K_{ab}) + V_{nn} \tag{2.11}$$

While the Coulomb interaction is simply the classical electrostatic repulsion of two electrons, the non-classical exchange interaction only occurs for electrons of parallel spin, which have a reduced probability of coming close to one another due to the Pauli principle. That is why the exchange interaction reduces the magnitude of the Coulomb repulsion for electrons of parallel spin, indicated by its negative sign.[58] The operators $\hat{h}(1)$, $\hat{J}_b(1)$, and $\hat{K}_b(1)$ are defined as follows, with $\hat{P}_{12}$ being a permutation operator to change the positions of electrons 1 and 2 (change the orbital in which they are located in), which arises from the

Pauli principle/antisymmetry of the SD:[57–59]

$$\hat{h}(1) = -\frac{1}{2}\vec{\nabla}_1^2 - \sum_{\alpha=1}^{K} \frac{Z_\alpha}{|\vec{r}_{\alpha 1}|} \tag{2.12}$$

$$\hat{J}_b(1) = \langle \chi_b(2) | \hat{g}_{12} | \chi_b(2) \rangle \tag{2.13}$$

$$\hat{K}_b(1) = \langle \chi_b(2) | \hat{g}_{12} \hat{P}_{12} | \chi_b(2) \rangle \tag{2.14}$$

Note that the sums are running over all spin MOs (indices a and b) instead of over all electrons (indices i and j) and that the indices of the electrons are kept fixed at 1 and 2. However, since the numbers of occupied electrons and of spin MOs are identical up to this point and the values of the one- and two-electron integrals are independent of the actual index of the electron, the calculation of the energy is unchanged. If the energy expression is now combined with the Lagrange method to find its minimum value upon changing the spin MOs while maintaining their orthonormality, the N Hartree-Fock[60,61] (HF) equations with the one-electron Fock operators $\hat{f}_a(1)$ and the Lagrange coefficients λ_{ba} are obtained:[57–59]

$$\hat{f}_a(1) \, |\chi_a(1)\rangle = \sum_{b=1}^{N} \lambda_{ba} \, |\chi_b(1)\rangle \tag{2.15}$$

$$\hat{f}_a(1) = \hat{h}(1) + \sum_{b=1}^{N} \left(\hat{J}_b(1) - \hat{K}_b(1) \right) \tag{2.16}$$

By unitary transformation, the right hand side of equation Eq. 2.15, when thought of as a matrix, can be diagonalized to obtain the canonical HF equations with the canonical spin MOs. This results in the the Lagrange coefficients being transformed into the canonical spin MO energies ε_a as eigenvalues on the matrix diagonal:[57,59]

$$\hat{f}'_a(1) \, |\chi'_a(1)\rangle = \varepsilon_a \, |\chi'_a(1)\rangle \tag{2.17}$$

These canonical HF equations are a set of pseudo-eigenvalue equations since the Fock operators themselves depend on all the occupied spin MOs. Accordingly, to solve the eigenvalue equation of one spin MO, all other spin MOs need to be determined in advance, so an iterative treatment with a trial starting wave function is necessary until self-consistency is reached. Therefore, such approaches are often classified as SCF (self-consistent field) methods.[58,59] Furthermore, by inspection of the Fock operator in Eq. 2.16, it is apparent that the electron-electron repulsion is considered in an average manner since each electron only interacts with the charge clouds of the other electrons in the form of orbitals. Thus, this mean-field approach neglects the so-called dynamic electron correlation, which corresponds to a more realistic and advanced description of the electrons avoiding each other. These effects can be accounted for by using post-HF Methods like Møller-Plesset perturbation theory of second order (MP2),[62] configuration interaction (CI) or coupled cluster (CC),[63] which consider additional excited SDs constructed from the HF reference SD to obtain a more accurate wave function[59] (more details follow in Section 2.1.2).

The total energy of the whole N-electron wave function in form of the SD is not simply the sum of orbital energies since this would result in the electron-electron repulsions being counted twice. Accordingly, it is calculated as:[57,59]

$$E = \sum_{a=1}^{N} \varepsilon_a - \frac{1}{2}\sum_{a=1}^{N}\sum_{b=1}^{N}(J_{ab} - K_{ab}) + V_{nn} \tag{2.18}$$

$$\varepsilon_a = \langle \chi_a(1)|\hat{f}_a(1)|\chi_a(1)\rangle = h_a + \sum_{b=1}^{N}(J_{ab} - K_{ab}) \tag{2.19}$$

Note that the ' as indicator for the canonical MOs/Fock operators are disregarded in the following for convenience. Furthermore, the Coulomb and exchange integrals cancel each other for $i = j$.[57,59]

Up to this point, the spin MOs $|\chi_a\rangle$ were only discussed conceptually and their actual description in practice was omitted so far. As already mentioned, the shape of the spin MOs is given by the spatial MOs $|\psi_a\rangle$. These spatial MOs can take various shapes and are, just like the full N-electron wave function, generally unknown at the start. However, it is mathematically possible to exactly represent any unknown function by a linear combination of a complete set of known basis functions $\phi_\mu(\vec{r})$, the basis set $\{\phi_\mu(\vec{r})\}$. Since complete basis sets can consist of an infinite number of basis functions, in real calculations the basis set size has to be reduced to a finite value k:[57–59]

$$|\psi_a\rangle = \psi_a(\vec{r}) = \sum_{\mu=1}^{k} c_{\mu a}\ \phi_\mu(\vec{r}) = \sum_{\mu=1}^{k} c_{\mu a}\,|\phi_\mu\rangle \tag{2.20}$$

In principle, any kind of mathematical function can serve as a basis function as long as the basis set as a whole is able to recover the necessary properties of the wave function (e.g., for large $\vec{r}$, the wave function should approach zero). Accordingly, since the orbitals of an atom or a molecule are to be described, atomic orbitals (AOs) are a reasonable choice, hence the approach in Eq. 2.20 is called MO-LCAO (molecular orbitals from linear combination of atomic orbitals). Here, atom-centered Gaussian type orbitals (GTOs) are the computationally most efficient choice.[57–59] Due to the introduction of the MO-LCAO approach, the spin MOs and thus the N-electron wave function can now be changed through the expansion coefficients $c_{\mu a}$ in order to actually utilize the variational principle and minimize the total energy. By inserting the MO-LCAO approach into the restricted closed-shell variant of the canonical HF equations (not explicitly derived previously), multiplying with the AO basis functions on the left, and integrating, the Roothaan-Hall equations can be obtained, which correspond to the restricted closed-shell HF (RHF) method. These equations can be efficiently solved in the form of a matrix pseudo-eigenvalue problem by computers:[57,59]

$$\mathbf{FC} = \mathbf{SC}\boldsymbol{\varepsilon} \tag{2.21}$$

$$F_{\mu\nu} = \langle \phi_\mu | \hat{f} | \phi_\nu \rangle \tag{2.22}$$

$$S_{\mu\nu} = \langle \phi_\mu | \phi_\nu \rangle \tag{2.23}$$

Here, **F** corresponds to the Fock matrix, which contains integrals $F_{\mu\nu}$ of the Fock operator and the AO basis functions (Eq. 2.22), the **C** matrix contains the coefficients $c_{\mu a}$ for the MO-LCAO, the **S** matrix contains the overlap integrals $S_{\mu\nu}$ of the AO basis functions (Eq. 2.23), and $\boldsymbol{\varepsilon}$ corresponds to the eigenvalue matrix, which is diagonalized and thus contains the orbital energies ε_a.[57,59] Though not explicitly written in 2.21, due to the pseudo-eigenvalue character of HF theory, the **F** matrix is dependent on the occupied MOs and thus on the **C** matrix. While the details of the derivation of the Roothaan-Hall equations will not be discussed further, it should be noted that since the number of AOs and MOs is equal in MO-LCAO, k accordingly has to be equal (minimal basis set) or greater than $\frac{N}{2}$ so there is at least one spin MO for each electron (k spatial MOs generally lead to $2k$ spin MOs). In real calculations, k is actually about four to six times as large as $\frac{N}{2}$ because a larger number of basis functions allows for a more precise approximation of the exact MOs. Accordingly, the MOs can be split into occupied and unoccupied/virtual MOs, of which only the N occupied MOs are included in the SD. Thus, only these occupied MOs contribute to the total energy of the system and accordingly only these MOs are optimized during the SCF procedure.[58,59]

Overall, due to the neglect of the electron correlation beyond the mean-field approach, the HF method generally does not give good quantitative results.[58] Still, the appeal of the HF method is to use its wave function as a reference for the post-HF methods to systematically improve towards the exact wave function and energy. However, there are cases where the single-determinantial and -configurational approach of HF is already insufficient to serve as a reference for post-HF methods, which will be discussed in Sections 2.1.1.4 and 2.1.2.

2.1.1.2 Restricted and Unrestricted Slater Determinants

Since the HF method utilizes the variational principle, solving the Roothaan-Hall equations generally yields the ground state SD, corresponding to the restricted closed-shell singlet electron configuration with the energetically lowest spatial MOs being doubly occupied according to the Aufbau principle. To also make the calculation of open-shell systems possible, two additional flavors of the HF method have been developed besides RHF, which mainly differ in the way the α and β spin MOs of the SD are constrained: restricted open-shell HF (ROHF) and unrestricted HF (UHF). As already mentioned in Section 2.1.1.1, one set of k spatial MOs $|\psi_a\rangle$ will result in $2k$ spin MOs $|\chi_a\rangle$:[57]

$$\left.\begin{aligned} |\chi_{2a-1}\rangle &= |\psi_a\rangle\,|\alpha\rangle \\ |\chi_{2a}\rangle &= |\psi_a\rangle\,|\beta\rangle \end{aligned}\right\} a = 1, 2, \dots, k \tag{2.24}$$

In case of restricted SDs, for each α spin MO there exists one β spin MO with an identical spatial part, resulting in both spin MOs to also be energetically degenerate. This restriction is also kept during the whole SCF procedure. To make this pairing more clear when using the shorthand notation for a determinant as in Eq. 2.7, instead of simply numbering the spin MOs independently from $|\chi_1\rangle$ to $|\chi_{2k}\rangle$, one can use the k spatial MOs and add or omit a bar above the symbol ψ to identify them as β or α spin MOs, respectively:[57]

$$\left.\begin{aligned} |\psi_a\rangle &= |\psi_a\rangle\,|\alpha\rangle \\ |\bar{\psi}_a\rangle &= |\psi_a\rangle\,|\beta\rangle \end{aligned}\right\} a = 1, 2, \ldots, k \tag{2.25}$$

This notation also represents the SCF procedure more accurately since only the spatial part of the spin MOs is varied via the coefficients and not the spin function. This is why in the restricted closed-shell Roothaan-Hall equations of the RHF method (Eq. 2.21) actually only k spatial MOs and not $2k$ spin MOs are considered and accordingly the involved matrices are of the size $k \times k$. The correct interaction of electrons of different spin is then recovered by adjusted spatial Fock operators and an adjusted energy expression of an SD with spatial MOs.[57] If the number of electrons of the investigated system is now even, a restricted closed-shell SD with singlet configuration as used in RHF is obtained, exemplarily depicted in Fig. 2.1a). If, e.g., one additional electron is present as shown in Fig. 2.1b), a restricted open-shell SD with doublet spin configuration as utilized in ROHF is acquired. While the difference in occupation is subtle compared to the RHF formalism, the corresponding equations are a lot more complicated,[57] which is why they will not be presented in detail. The case of unrestricted spin MOs was basically assumed in most of Section 2.1.1.1 and before in Eq. 2.24, where they are denoted as $|\chi_a\rangle$. In unrestricted SDs, the spatial part of each spin MO pair can (but does not have to) differ, which can result in energetically non-degenerate spin MO pairs (see Fig. 2.1c). To express this independence in the notation of spatial MOs as in Eq. 2.25, one set of k α and one set of k β spatial MOs with their respective α and β expansion

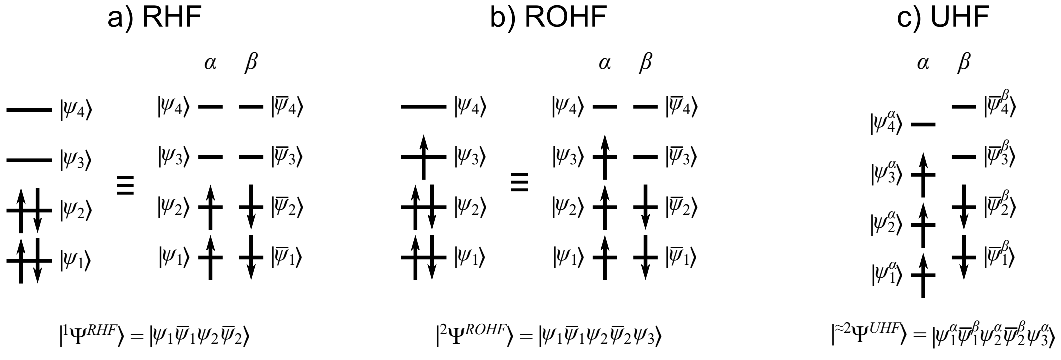

Figure 2.1: Example SDs according to a) RHF, b) ROHF, and c) UHF methods. In the equation at the bottom, the leading superscript of the wave function corresponds to the spin multiplicity M of the determinant, which in case of the UHF SD is not an exact doublet state due to spin contamination (see Section 2.1.1.4). Created based on Refs. [57, 59]

coefficients are needed:[57]

$$\left.\begin{array}{l} |\psi_a^\alpha\rangle = |\psi_a^\alpha\rangle\,|\alpha\rangle \\ |\overline{\psi}_a^\beta\rangle = |\psi_a^\beta\rangle\,|\beta\rangle \end{array} \text{ with } \begin{array}{l} |\psi_a^\alpha\rangle = \sum_{\mu=1}^{k} c_{\mu a}^\alpha\,|\phi_\mu\rangle \\ |\psi_a^\beta\rangle = \sum_{\mu=1}^{k} c_{\mu a}^\beta\,|\phi_\mu\rangle \end{array}\right\} a = 1, 2, \ldots, k \tag{2.26}$$

Inserting these two sets of unrestricted spin MOs into the HF equations yields the two so-called Pople-Nesbet equations, which are the unrestricted equivalent to the restricted Roothaan-Hall equations and are accordingly used in the UHF method:[57]

$$\mathbf{F}^\alpha\mathbf{C}^\alpha = \mathbf{S}\mathbf{C}^\alpha\boldsymbol{\varepsilon}^\alpha \tag{2.27}$$

$$\mathbf{F}^\beta\mathbf{C}^\beta = \mathbf{S}\mathbf{C}^\beta\boldsymbol{\varepsilon}^\beta \tag{2.28}$$

Even though there are two separate equations for each electron spin, obviously the two-electron parts in the Fock operators of one spin also depend on the electrons of opposite spin, which is why both equations have to be solved simultaneously in the self-consistent procedure.[57]

While the ROHF and UHF methods open up the possibility of calculating open-shell systems, there are certain systematic limitations and problems that are either tied to the respective method in particular or, as already indicated in Section 2.1.1.1, to the usage of single-determinantial and -configurational methods in general. These shortcomings will be further discussed in detail in Sections 2.1.1.4 and 2.1.2.

2.1.1.3 Density Functional Theory

The arguably most commonly used method for electronic structure calculations is the density functional theory (DFT). The foundation of this theory was laid out by Hohenberg and Kohn in 1964,[64] who showed that the energy of the ground state of a system can be exactly derived from its electron density $\rho(\vec{r})$. In comparison to wave function methods like HF, the appeal is the significantly reduced complexity. This is apparent in N-electron wave functions within the framework of the Born-Oppenheimer approximation (BOA) being dependent on N electronic coordinates $\vec{x}$, amounting to $4N$ variables in total, while the electron density is always dependent on only three spatial coordinates combined in $\vec{r}$ and thus independent of N. The correlation between the wave function and the electron density is clearly given by integrating out all but one spatial coordinate $\vec{r}$ of the absolute square of the wave function:[58,59,65]

$$\rho(\vec{r}_1) = N \int |\Psi(\vec{r}_1, \omega_1, \vec{x}_2, \ldots, \vec{x}_N)|^2 d\omega_1 d\vec{x}_2 \ldots d\vec{x}_N \tag{2.29}$$

While the calculation of the exact energy using a wave function is known in, e.g., full CI, the exact functional for obtaining the energy from only the electron density is unknown. This unknown exact DFT functional can, in analogy to the electronic Hamiltonian of Eq. 2.2, be written as the sum of the exact functional of the kinetic energy of electrons $T\left[\rho(\vec{r})\right]$, the exact functional of the potential energy between nuclei and electrons $V_{ne}\left[\rho(\vec{r})\right]$, and the exact functional of the potential energy between electrons $V_{ee}\left[\rho(\vec{r})\right]$:[58,59]

$$E_{DFT}\left[\rho(\vec{r})\right] = T\left[\rho(\vec{r})\right] + V_{ne}\left[\rho(\vec{r})\right] + V_{ee}\left[\rho(\vec{r})\right] \tag{2.30}$$

The attraction between the nuclei and the electrons, or, more specifically, the electron density, is given exactly by the following classical expression:[58,59]

$$V_{ne}\left[\rho(\vec{r})\right] = -\sum_{\alpha=1}^{K} \int \frac{Z_\alpha\ \rho(\vec{r})}{|\vec{r} - \vec{R}_\alpha|}\ d\vec{r} \tag{2.31}$$

However, the other two exact functionals are both unknown. In a first approximation, the exact functional of electron-electron repulsion can be split further:[59]

$$V_{ee}\left[\rho(\vec{r})\right] = J\left[\rho(\vec{r})\right] + E_{xc}\left[\rho(\vec{r})\right] \tag{2.32}$$

Here, in analogy to the nomenclature in the HF method, $J\left[\rho(\vec{r})\right]$ corresponds to the Coulomb repulsion of a classical charge distribution:[58,59]

$$J\left[\rho(\vec{r})\right] = \frac{1}{2} \iint \frac{\rho(\vec{r}_1)\rho(\vec{r}_2)}{|\vec{r}_1 - \vec{r}_2|}\ d\vec{r}_1 d\vec{r}_2 \tag{2.33}$$

However, in contrast to the HF method, the electrons are not treated separately in spin MOs but as one single electron density. From this, it follows that the unphysical interaction of “one electron” of this density with itself (self-interaction error) cannot be prevented and that the quantum mechanical exchange interaction K as well as further electron correlation are not considered. Accordingly, these missing effects and corrections are included in the exchange-correlation functional $E_{xc}\left[\rho(\vec{r})\right]$, which will be presented in detail further below. Prior to that, the exact functional of the kinetic energy $T\left[\rho(\vec{r})\right]$ is discussed. Describing this interaction mathematically by only relying on the electron density turned out to be challenging. By fermion statistical mechanics, Thomas[66] and Fermi[67] had already derived an expression in the 1920s to calculate the kinetic energy of the uniform electron gas, corresponding to an infinite number of electrons in an infinite volume with uniformly positively charged background. With the inclusion of exchange effects for the same model system derived by Bloch,[68] Dirac,[69] and Slater,[70] the resulting orbital-free Thomas-Fermi-Dirac DFT is only applicable to certain periodic metallic systems but not suitable for chemical problems due to the inability to describe bonds. Apparently, the lowest limit of complexity for solving the TISE for such systems seems to be MO theory,[58] which is why in 1965 Kohn and Sham[71] introduced orbitals into DFT, hence denoted as KS DFT and KS orbitals. While with this the advantage of DFT being dependent on only three spatial coordinates is lost, it is now possible to describe the functional of the kinetic energy of non-interacting electrons $T_S\left[\rho(\vec{r})\right]$ by summing over the kinetic energy of each single electron:[58,59]

$$T_S\left[\rho(\vec{r})\right] = \sum_{a=1}^{N} \langle \chi_a(\vec{r}_1)| - \frac{1}{2}\vec{\nabla}_1^2 |\chi_a(\vec{r}_1)\rangle \tag{2.34}$$

The term non-interacting might be a bit confusing at first since the expression in Eq. 2.34 contains the same one-electron operator of the kinetic energy as in Eq. 2.3 of the mean-field approach of HF, in which the electrons do interact and "only" the dynamic electron correlation is missing. However, the kinetic part of these correlation effects cannot be accounted for by such a simple sum of the kinetic energy of single particles, hence the respective expressions for T actually do resemble independent, non-interacting electrons both in HF and DFT. Still, most of the exact kinetic energy is covered in this way and thus this calculation is justified.[58,59] The subscript S in Eq. 2.34 highlights this single-particle nature[65] or, put differently, that it stems from an SD with single-particle wave functions.[59] Other than obtaining a reasonable expression for the kinetic energy, the main goal of Kohn and Sham was to create a Hamiltonian that can act on a system of non-interacting electrons, represented by a single SD of one-electron wave functions like in HF, but still give the electron density of the exact system of interacting electrons and thus the exact ground state energy. Within this MO approach, the total electron density of an N-electron system is given as:[58,59,65,72]

$$\rho(\vec{r}) = \sum_{a=1}^{N} |\chi_a(\vec{r})|^2 \tag{2.35}$$

It should be noted that the total electron density itself is a spinless quantity and hence only depends on $\vec{r}$, as do the functionals/potentials of DFT in its most general form.[72] That is why, for the sake of simplicity, the spin MOs $|\chi_a\rangle$ in Eqs. 2.34 and 2.35 and the following equations only depend on $\vec{r}$, i.e., only the spatial MOs are used. Utilizing the MO approach, the integral of the electron density over $\vec{r}$ can be expressed in Dirac notation:

$$\int \rho(\vec{r})\ d\vec{r} = \sum_{a=1}^{N} \langle \chi_a(\vec{r}) | \chi_a(\vec{r}) \rangle \tag{2.36}$$

Insertion into $V_{ne}\left[\rho(\vec{r})\right]$ (Eq. 2.31) and $J\left[\rho(\vec{r})\right]$ (Eq. 2.33) results in the following total KS DFT functional:[58,72]

$$\begin{aligned} E_{KS\ DFT}\left[\rho(\vec{r})\right] = & \sum_{a=1}^{N} \langle \chi_a(\vec{r}_1) | -\frac{1}{2}\vec{\nabla}_1^2 | \chi_a(\vec{r}_1) \rangle \\ & - \sum_{\alpha=1}^{K}\sum_{a=1}^{N} \langle \chi_a(\vec{r}_1) | \frac{Z_\alpha}{|\vec{r}_{\alpha 1}|} | \chi_a(\vec{r}_1) \rangle \\ & + \frac{1}{2}\sum_{a=1}^{N} \langle \chi_a(\vec{r}_1) | \int \frac{\rho(\vec{r}_2)}{|\vec{r}_{12}|}\ d\vec{r}_2 | \chi_a(\vec{r}_1) \rangle + E_{xc}\left[\rho(\vec{r})\right] \end{aligned} \tag{2.37}$$

In this equation, only the exchange-correlation functional $E_{xc}\left[\rho(\vec{r})\right]$ remains unknown. However, this is the crucial term since it contains, the missing parts of the exact electron-electron interaction functional $V_{ee}\left[\rho(\vec{r})\right]$, which are not covered by the classical mean-field functional $J\left[\rho(\vec{r})\right]$ (self-interaction error, missing exchange interaction, potential energy correlation effects), as well as the missing correlation effects of the exact kinetic energy of electrons $T\left[\rho(\vec{r})\right]$, which are not covered by the functional of the kinetic energy of non-interacting electrons $T_S\left[\rho(\vec{r})\right]$:[58,59,72]

$$E_{xc}\left[\rho(\vec{r})\right] = \left(T\left[\rho(\vec{r})\right] - T_S\left[\rho(\vec{r})\right]\right) + \left(V_{ee}\left[\rho(\vec{r})\right] - J\left[\rho(\vec{r})\right]\right) \tag{2.38}$$

Utilization of the variational principle for Eq. 2.37 and the Lagrange minimization method for the energy yields the KS equations and KS operators, which are the KS DFT analogues to the HF equations and Fock operators:[58,72]

$$\hat{f}_a^{KS}(\vec{r}_1)\left|\chi_a(\vec{r}_1)\right\rangle = \varepsilon_a\left|\chi_a(\vec{r}_1)\right\rangle \tag{2.39}$$

$$\hat{f}_a^{KS}(\vec{r}_1) = \hat{h}(\vec{r}_1) + \int \frac{\rho(\vec{r}_2)}{|\vec{r}_{12}|}\, d\vec{r}_2 + \hat{V}_{xc} \tag{2.40}$$

Here, $\hat{h}(\vec{r}_1)$ is identical to the one-electron operator of the Fock operator in HF (Eq. 2.12). Since the Lagrange method minimizes the total energy by changing the orbitals and thus the electron density, this is also applied to the exchange-correlation functional $E_{xc}\left[\rho(\vec{r})\right]$, hence the corresponding exchange-correlation potential $\hat{V}_{xc}$ is obtained:[58,72]

$$\hat{V}_{xc} = \frac{\delta E_{xc}\left[\rho(\vec{r})\right]}{\delta\rho(\vec{r})} \tag{2.41}$$

Mathematically, $\hat{V}_{xc}$ is a so-called functional derivative and represents the potential acting on the one-electron wave functions that arises from all effects combined in the exchange-correlation functional. Just like the corresponding functional, however, this potential remains unknown and has to be approximated.[58,72] Applying the MO-LCAO approach to the restricted closed-shell variant of the KS equations (not explicitly derived previously) yields the restricted closed-shell Kohn-Sham-Roothaan matrix eigenvalue equations, which are the restricted closed-shell KS DFT (RKS) analogues of the Roothaan-Hall equations (Eq. 2.21):[73]

$$\mathbf{F^{KS}C} = \mathbf{SC}\boldsymbol{\varepsilon} \tag{2.42}$$

While DFT, in principle, does not need any spin information in the electron density to give the exact ground state energy, in practice this is not the case since the exact exchange-correlation functional is not known. Accordingly, restricted and unrestricted open-shell variants of KS DFT, abbreviated as ROKS and UKS, are available to obtain improved results for open-shell systems.[72] Just like their HF counterparts, they utilize restricted and unrestricted SDs as presented in Section 2.1.1.2 and the corresponding functionals show dependencies on the α and β electron densities, the latter being calculated as follows from the spatial MOs:[65]

$$\rho^\alpha(\vec{r}) = \sum_{a=1}^{N_\alpha} |\psi_a^\alpha(\vec{r})|^2 \quad \text{and} \quad \rho^\beta(\vec{r}) = \sum_{a=1}^{N_\beta} |\psi_a^\beta(\vec{r})|^2 \tag{2.43}$$

While the total electron density $\rho(\vec{r})$ is just the sum of both partial densities, the so-called spin density $Q(\vec{r})$ is the difference of both, in which positive and negative values correspond to an excess of α or β electrons at a given point $\vec{r}$, respectively:[65]

$$\rho(\vec{r}) = \rho^{\alpha}(\vec{r}) + \rho^{\beta}(\vec{r}) \tag{2.44}$$

$$Q(\vec{r}) = \rho^{\alpha}(\vec{r}) - \rho^{\beta}(\vec{r}) \tag{2.45}$$

A comparison of KS DFT to HF is now helpful to understand their differences since they might appear to be quite similar up to this point. Both KS DFT and HF use one single SD with one-electron wave functions and corresponding effective one-electron operators, the Fock and KS operators. Accordingly, both methods can be classified as mean-field theories. The one-electron operators only differ in the fact that DFT includes all correlation effects and is thus, in principle, an exact theory, while the approximate HF theory does not include correlation effects beyond the mean-field approach. To account for the missing correlation interactions, post-HF methods would be needed to include additional excited SDs in the wave function. The problem of DFT, on the other hand, is that the exact exchange-correlation functional is unknown and thus, in reality, has to be approximated, resulting in the large variety of different available DFT functionals.[58,72] As concisely summarized by Cramer, HF is an approximate theory, which can be solved exactly, while KS DFT is an exact theory, which can only be solved approximately.[58] Put differently, while HF accepts the approximate nature of using a single SD as wave function, DFT tries to “bend” this single SD in a way that it still gives the correct density and energy, which, as the Hohenberg-Kohn theorem proofs, is, in principle, possible. It is important to stress, however, that the exact wave function is not available in DFT.[72] Coming back to the similarities, if one replaces the integral over $\rho(\vec{r}_2)$ in the total KS DFT functional (Eq. 2.37) with its MO representation and compares it to the energy of an SD (Eq. 2.10), HF and DFT share the same formulas to calculate the one-electron and Coulomb integrals h_a and J_{ab}, respectively. Furthermore, since the KS operators depend on the electron density and the density itself depends on the KS orbitals, the KS equations also have to be solved iteratively in a SCF procedure just like HF.[58,59]

There are several different ways to approximate the exact exchange-correlation functional $E_{xc}\left[\rho(\vec{r})\right]$, of which the most relevant in general and with respect to this work are presented in the following. Generally, all of these functionals contain parameters, resulting in KS DFT, strictly speaking, not being an *ab initio* method in practice. These parameters are, e.g., fitted to experimental data or to fulfill certain physically required properties. However, since these fits are done using a limited number of test systems, the performance of different functionals is accordingly also system- and property-dependent and thus there is no standard functional to use. The simplest functionals utilize the local density approximation (LDA), in which the electron density at each position in space $\vec{r}$ is treated as a uniform electron gas. Thus, the corresponding exchange-correlation functionals are only dependent on the value of the electron density at each local point $\vec{r}$ ($E_{xc}^{LDA}[\rho(\vec{r})]$).[58,59] Within this approach, different exchange and correlation functionals have emerged, of which the Dirac-Slater exchange[69] and the Perdew-Zunger correlation[74] functionals are used in this work when employing LDA calculations. Going a step further in accuracy beyond the uniform electron gas, the generalized gradient approximation (GGA) adds a dependency on the gradient of the electron density ($E_{xc}^{GGA}[\rho(\vec{r}), \vec{\nabla}\rho(\vec{r})]$). With this, the calculation of the energy in a sense also takes the surroundings of the electron density at a given point $\vec{r}$ into account, even though the derivative mathematically is also just a local property at $\vec{r}$.[58,59] The most commonly used GGA functional is the Perdew-Burke-Ernzerhof (PBE) exchange-correlation functional[75] also utilized in this work. Further improvements are possible in form of meta-GGA methods, where also the second derivative of the electron density $\vec{\nabla}^2\rho(\vec{r})$ is included. However, much more common are the so-called hybrid functionals, which are based on LDA or GGA functionals with a certain fraction a of the exchange-part of the DFT functional being replaced by HF exchange E_x^{HF} (computed with the KS orbitals):[58,59]

$$E_{xc}^{hDFT} = E_{xc}^{DFT} - a\ E_x^{DFT} + a\ E_x^{HF} \tag{2.46}$$

The idea behind this approach is that the exchange energy is the largest part of the exchange-correlation energy and this exchange energy is calculated exactly for one SD in the HF method. However, using 100 % HF exchange is not possible since its non-local nature combined with the local DFT correlation functionals leads to unphysical results for long-range electron interactions, which normally would cancel each other in wave function-based approaches due to the correlation also being non-local. Since the fraction a is determined by fitting, a similar system- and property-dependence as mentioned before is present. Still, generally the hybrid-DFT functionals perform better than pure GGA and meta-GGA functionals, being partly owed to the reduction of the self-interaction error, which in HF is nonexistent due to the previously mentioned cancellation of J and K for the interaction of one electron with itself.[58,59,73] The hybrid variant of the PBE functional, namely PBE0,[76,77] is used in this work, in which a amounts to 0.25. However, it was shown that exchange interactions in insulators/metals decay exponentially/algebraically with the distance between electrons due to shielding/screening effects.[78] But since the exact HF exchange is non-local, it considers both short- and long-range interactions at the same time. This leads to unnecessarily high computation times for hybrid functionals if the long-range exchange interactions can be neglected[78] and to calculated band gaps being too large compared to the experiment.[73] Thus, to further increase the accuracy and performance especially for extensive or periodic solid-state systems, so-called screened or range-separated hybrid DFT functionals were developed. For this, the two-electron operator is divided into a short- and long-range part by using error functions $erf(\omega)$, whose shapes are very similar to a natural growth function with function values in the range from 0 to 1 and thus serve as a smooth transition between both regions:[73,78]

$$\frac{1}{|\vec{r}_{12}|} = \frac{1 - erf(\omega \cdot |\vec{r}_{12}|)}{|\vec{r}_{12}|} + \frac{erf(\omega \cdot |\vec{r}_{12}|)}{|\vec{r}_{12}|} \tag{2.47}$$

Here, the parameter ω adjusts the slope of the error function and thus the position at which the short-range interactions end and the long-range interactions start.[78] Now, the HF exchange is only applied to the short-range region with a fraction a:[73,78]

$$E_{xc}^{shDFT} = E_{xc}^{DFT} - a\ E_{x}^{DFT,SR} + a\ E_{x}^{HF,SR} \tag{2.48}$$

In case of the popular HSE06 functional[78–80] also used in this work, ω amounts to $0.11\,a_0$ and a to 0.25, thus representing a screened variant of the PBE0 hybrid functional, significantly improving calculated properties for semiconductors like the band gap and lattice constants.[73]

To summarize, even with the exchange-correlation functionals being only approximated, DFT generally gives quantitatively better results than HF and often even of the same quality as MP2.[59] Especially for systems too large for post-HF methods, DFT most of the time is the only option to account for correlation effects in electronic structure calculations. However, the large variety of different DFT functionals and the strong system- and property dependence makes its usage less universal and requires careful validation of the obtained results. Even though it is debatable,[72] DFT can also be regarded as a single-determinantial and -configurational method and thus its limits in this regard are also included in the discussion of the following Section 2.1.1.4.

2.1.1.4 Limits of Single-Configurational Methods

As indicated multiple times in the previous sections, the presented methods HF and DFT are limited in the systems they are able to describe, which is owed the single-configurational and/or the single-determinantial approach they utilize. At first, the discussion is focused on the HF method since the problems are well defined for wave function-based method and less clear for DFT.

Since HF is derived from the non-relativistic TISE, the spin has to be introduced via the spin functions $|\alpha\rangle$ and $|\beta\rangle$, corresponding to the spin-up and spin-down states, respectively. These spin functions have to be eigenfunctions of the spin angular momentum operator for the z component $\hat{s}_z$ and the squared total spin angular momentum operator $\hat{s}^2$, giving the magnetic quantum number m_s and $s(s+1)$ as eigenvalues, respectively, with s being the total spin quantum number:[57,58]

$$\hat{s}^2 = \hat{s} \cdot \hat{s} = \hat{s}_x^2 + \hat{s}_y^2 + \hat{s}_z^2 \tag{2.49}$$

$$\hat{s}_z\,|\alpha\rangle = \frac{1}{2}\,|\alpha\rangle \qquad \hat{s}^2\,|\alpha\rangle = \frac{1}{2}\left(\frac{1}{2}+1\right)|\alpha\rangle = 0.75\,|\alpha\rangle \tag{2.50}$$

$$\hat{s}_z\,|\beta\rangle = -\frac{1}{2}\,|\beta\rangle \qquad \hat{s}^2\,|\beta\rangle = \frac{1}{2}\left(\frac{1}{2}+1\right)|\beta\rangle = 0.75\,|\beta\rangle \tag{2.51}$$

Here, the total spin s can generally take values of $0, \frac{1}{2}, 1, \frac{3}{2}, \ldots$ and the magnetic quantum number m_s values of $-s, -s+1, \ldots, s-1, s$, even though for a single fermion like an electron the total spin is always $\frac{1}{2}$ and thus m_s is either $\frac{1}{2}$ or $-\frac{1}{2}$. For an N-electron system, the total spin angular momentum operator $\hat{S}$ and the corresponding operator $\hat{S}_z$ for the z component are simply the sums of the operators for one electron:[57,58]

$$\hat{S} = \sum_{i=1}^{N} \hat{s}(i) \qquad \hat{S}_z = \sum_{i=1}^{N} \hat{s}_z(i) \tag{2.52}$$

Accordingly, the squared total spin angular momentum operator $\hat{S}^2$ is the product of two sums:[57,58]

$$\hat{S}^2 = \sum_{i=1}^{N} \sum_{j=1}^{N} \hat{s}(i) \cdot \hat{s}(j) \tag{2.53}$$

While not going into the mathematical details, it should be noted that, due to the independent indices, one-electron operators arise for $i = j$ and two-electron operators for $i \neq j$ within $\hat{S}^2$.[57,58] Since the non-relativistic Hamiltonian $\hat{H}$ itself does not contain spin coordinates, it commutes with both spin operators $\hat{S}_z$ and $\hat{S}^2$ and accordingly the N-electron wave function also has to be an eigenfunction of both operators:[57]

$$[\hat{H}, \hat{S}^2] = [\hat{H}, \hat{S}_z] = 0 \tag{2.54}$$

$$\hat{S}_z \left|\Psi\right\rangle = M_S \left|\Psi\right\rangle \qquad \hat{S}^2 \left|\Psi\right\rangle = S(S+1) \left|\Psi\right\rangle \tag{2.55}$$

The quantum numbers S and M_S correspond to the total spin and its z component of the N-electron system, respectively. With S available, the spin multiplicity of the system can be calculated via $M = 2S{+}1$, defining it as singlet, doublet, triplet, and so on. Due to the discrete nature of S, the eigenvalue $S(S{+}1)$ can accordingly also only take discrete values of $0, 0.75, 2, \ldots$. If the spin operators are now applied to a single SD as HF utilizes to approximate the N-electron wave function, it shows that the SD is always an eigenfunction of $\hat{S}_z$, with M_S simply being equal to the sum of all individual m_s, but not necessarily an eigenfunction of $\hat{S}^2$.[57] While a detailed mathematical application of the spin operators to SDs of a system with two electrons and two orbitals is given in the appendix of Ref. [58], the corresponding final results are presented in the following: The first case is a restricted closed-shell SD, which is always an eigenfunction of $\hat{S}^2$ with the eigenvalue $0(0{+}1) = 0$:[57,58]

$$\left|{}^1\Psi^{RHF}\right\rangle = \left|\psi_1\overline{\psi}_1\right\rangle = \frac{1}{\sqrt{2}}(\psi_1(1)\overline{\psi}_1(2) - \psi_1(2)\overline{\psi}_1(1)) \tag{2.56}$$

$$\left\langle {}^1\Psi^{RHF} \middle| \hat{S}^2 \middle| {}^1\Psi^{RHF} \right\rangle = 0 \tag{2.57}$$

Thus, a single SD is capable of describing a pure closed-shell singlet state with $S = 0$ as one would intuitively expect. Note that in the following the superscript in front of the wave function gives its spin multiplicity M. The next case is a restricted open-shell SD with both electrons exhibiting the same spin and thus occupying different orbitals. This also corresponds to an eigenfunction of $\hat{S}^2$ with the eigenvalue 1(1+1) = 2 and accordingly describing a pure diradicalic triplet state with $S = 1$:[57,58]

$$|^3\Psi^{ROHF}\rangle = |\psi_1\psi_2\rangle = \frac{1}{\sqrt{2}}(\psi_1(1)\psi_2(2) - \psi_1(2)\psi_2(1)) \tag{2.58}$$

$$\langle^3\Psi^{ROHF}|\hat{S}^2|^3\Psi^{ROHF}\rangle = 2 \tag{2.59}$$

By flipping the spin of one of the orbitals, a restricted open-shell SD with two electrons of opposite spin in different orbitals is obtained. Application of $\hat{S}^2$ and integration then gives an expectation value of $S(S{+}1) = 1$, which is not an allowed eigenvalue and thus the SD is not an eigenfunction of $\hat{S}^2$:[57,58]

$$|^{1?}\Psi^{ROHF}\rangle = |\psi_1\bar{\psi}_2\rangle = \frac{1}{\sqrt{2}}(\psi_1(1)\bar{\psi}_2(2) - \psi_1(2)\bar{\psi}_2(1) \tag{2.60}$$

$$\langle^{1?}\Psi^{ROHF}|\hat{S}^2|^{1?}\Psi^{ROHF}\rangle = 1 \tag{2.61}$$

The problem might get more intuitive by wondering why the spin-up is always located in orbital 1 and the spin-down in orbital 2 and not the other way around, indicating a broken spin-symmetry. Hence, both of these possible SDs show spin polarization, i.e., the spin density (Eq. 2.45) has positive and negative values in different regions of space, even though a pure singlet wave function should have zero spin density at every point in space.[81] However, by forming a linear combination of both possible restricted open-shell SDs, a two-determinantial wave function is obtained, which then is a pure diradicalic singlet state with correct spin-symmetry:[57,58]

$$|^1\Psi^{CSF}\rangle = \frac{1}{\sqrt{2}}(|\psi_1\bar{\psi}_2\rangle - |\bar{\psi}_1\psi_2\rangle) \tag{2.62}$$

$$\langle^1\Psi^{CSF}|\hat{S}^2|^1\Psi^{CSF}\rangle = 0 \tag{2.63}$$

Interestingly, by changing the sign of the linear combination, an additional pure triplet wave function is obtained, which has an eigenvalue of $M_S = 0$ in contrast to the single-determinantial triplet $|^3\Psi^{ROHF}\rangle$ with $M_S = 1$ (or -1 for two β electrons):

$$|^3\Psi^{CSF}\rangle = \frac{1}{\sqrt{2}}(|\psi_1\bar{\psi}_2\rangle + |\bar{\psi}_1\psi_2\rangle) \tag{2.64}$$

$$\langle^3\Psi^{CSF}|\hat{S}^2|^3\Psi^{CSF}\rangle = 2 \tag{2.65}$$

Wave functions that are proper eigenfunctions of $\hat{S}^2$ are called configuration state functions (CSF) or spin-adapted configurations. While more details regarding CSFs and their connection to configurations are discussed in Section 2.1.2.1, it is important to note that closed-shell or maximum-spin open-shell CSFs (e.g., a triplet diradical) can be described qualitatively correct by a single restricted SD in RHF and ROHF, a low-spin open-shell CSF (e.g., a singlet diradical) is only obtainable by a linear combination of two or more restricted SDs, which cannot be generated within the single-determinantial methods RHF and ROHF. Accordingly, multiconfigurational methods are needed,[57–59,81–83] which are further discussed in Section 2.1.2. An illustrative overview of the presented SDs/CSFs and further examples are given in Fig. 2.2.

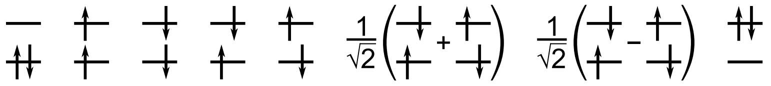

configuration	[20]	[11]	[11]	[11]	[11]	[11]	[11]	[02]
$\langle \hat{S}_z \rangle = M_S$	0	1	−1	0	0	0	0	0
$\langle \hat{S}^2 \rangle$	0	2	2	1	1	2	0	0
CSF?	✓	✓	✓	✗	✗	✓	✓	✓

Figure 2.2: Possible SDs, CSFs, and configurations for a two-electron two-orbital system. Created based on Refs. [57–59, 83]

Up to this point, the spin properties were only analyzed for the restricted SDs of RHF and ROHF. UHF is also able to describe open-shell systems by utilizing unrestricted SDs. Generally, the same problems for low-spin open-shell CSFs persist since UHF is also a single-determinantial method. Additionally, UHF SDs are generally impure spin states. This phenomenon is called spin contamination because the impure UHF spin state can be expanded in a basis of pure spin states (CSFs):[57–59]

$$|{}^{\approx 1}\Psi^{UHF}\rangle = C_1\,|{}^{1}\Psi^{CSF}\rangle + C_2\,|{}^{3}\Psi^{CSF}\rangle + C_3\,|{}^{5}\Psi^{CSF}\rangle + \ldots \tag{2.66}$$

Here, approximate UHF singlets are always contaminated by triplets, quintets, etc., approximated UHF doublets by quartets, sextets, etc., and so on. The amount of spin contamination $\Delta\langle\hat{S}^2\rangle$ is quantified by the difference between the calculated expectation value $\langle\hat{S}^2\rangle$ of the unrestricted SD and the ideal expectation value $\langle\hat{S}^2\rangle_{pure}$ for the corresponding pure spin state:[57–59,84]

$$\Delta\langle\hat{S}^2\rangle = \langle\hat{S}^2\rangle - \langle\hat{S}^2\rangle_{pure} \tag{2.67}$$

$$\langle\hat{S}^2\rangle_{pure} = M_S(M_S+1) \quad \text{with} \quad M_S = \frac{N_\alpha - N_\beta}{2} \tag{2.68}$$

Since the contaminating states of the UHF SD are always of higher multiplicity, they also have a larger total spin S and thus the spin contamination is always positive.[57] Generally, as soon as the spin contamination exceeds a few percent, the obtained UHF wave function should be treated with caution and multiconfigurational methods using CSFs should be considered.[59] The reason for the spin contamination is that the two sets of spatial orbitals $\{\psi_a^\alpha\}$ and $\{\psi_a^\beta\}$ can differ in their spatial part and are thus not necessarily orthogonal.[57] Using the example of a doublet state, this results in spin polarization, i.e., positive and negative values for the spin density, in the approximate doublet UHF SD, while the spin density is always zero or positive in the pure doublet ROHF

SD (if the unpaired electron is of α spin). Geometrically speaking, since in ROHF the spatial orbitals of α and β electrons are identical, the spin densities of the individual electrons cancel each other exactly except for the unpaired α electron. However, spin polarization is a real phenomenon, which can actually be observed in experiments, e.g., for the methyl radical, where the unpaired α electron is present in the p_z orbital orthogonal to the molecular plane. The other electrons in the molecular plane with the same spin are "pulled" towards the unpaired electron due to the exchange interaction reducing their Coulomb repulsion with the unpaired electron. This overall lowers the energy of the α orbitals compared to their β counterparts[57] (as already indicated in Fig. 2.1) and results in slightly negative spin density in the molecular plane. This spin polarization leads to hyperfine coupling between the magnetic moments of the nuclei and the unpaired electron,[58] observable in electron spin resonance (ESR) spectroscopy. From this, it can be concluded that ROHF sacrifices spin polarization for the sake of spin purity, while UHF sacrifices the spin purity to be able to describe spin polarization, so neither method can give a physically consistent description in this regard.

However, so called spin-projection or annihilation methods have been developed to reduce the spin contamination in UHF solutions. For this, the weights of the contaminating spin states in the UHF wave function, corresponding to the expansion coefficients C_r in Eq. 2.66, are determined by applying projection operators to the UHF wave function in order to subsequently subtract the contaminants so only the pure spin state remains. Since a UHF wave function can generally be contaminated by a lot of higher pure spin states but usually the next higher spin state than the desired one shows the highest contribution, approximate spin-projection methods like the AP (approximate projection) procedure[85] can be applied, in which only the next higher spin state is projected out. While AP methods generally improve energetics, the orbitals and geometries are not optimized for the corrected but only the contaminated wave function. Furthermore, if higher spin states are present to a larger degree, the spin contamination can even increase after the application of projection methods.[58,59]

With the definition of the spin contamination at hand, the wrong, broken spin-symmetry ROHF description of a singlet diradical $|^{1?}\Psi^{ROHF}\rangle$ (Eq. 2.60) can be revisited, for which $\Delta\langle\hat{S}^2\rangle$ shows a very high value of 1. This might be contradicting at first since it was just established that ROHF gives pure spin states due to restricted spatial orbitals. However, for this particular case, the reason for such high-spin contamination is the inability of single-determinantial methods to describe low-spin open-shell systems. Still, the obtained expectation value $\langle\hat{S}^2\rangle = 1$ is not arbitrary since it is the mean value of the expectation values for a pure singlet of 0 and a pure triplet of 2. These are exactly the two states that each can be described by a two-determinantial CSF, obtained from linearly combining the two spin arrangements of the erroneous $|^{1?}\Psi_{ROHF}\rangle$ SD (Eqs. 2.62 and 2.64). Conversely, $|^{1?}\Psi^{ROHF}\rangle$ can also be obtained by a 50:50 linear combination of these two CSFs when the spatial orbitals of both CSFs are identical:[58]

$$|^{1?}\Psi^{ROHF}\rangle = \frac{1}{\sqrt{2}}(|^{1}\Psi^{CSF}\rangle + |^{3}\Psi^{CSF}\rangle) \tag{2.69}$$

This perfectly fits the definition of spin contamination in Eq. 2.66, with the exception of only containing exactly two CSFs due to the restricted character of the SDs. If a UHF SD instead would be used, the higher contaminants would also be present even though it is easily imaginable that the main spin contamination still stems from the triplet state, making the previously discussed AP method very attractive and effective for such singlet diradical systems.[85]

Turning the attention to the ROHF method, one of the major drawbacks of this approach is that the ROHF equations cannot be diagonalized, resulting in no unique canonical MOs and thus no unique MO energies being available. Accordingly, interpretations of the orbital energies according to Koopmans' theorem are difficult as well as the additional implementation of electron correlation methods like perturbation theory. UHF, on the other hand, does not show these problems since the orbital energies are well-defined. Furthermore, due to the higher flexibility of the unrestricted SDs, UHF wave functions are generally of lower energy than their ROHF counterparts, resulting in UHF being the more popular method for the calculation of open-shell systems at HF level.[57–59]

As already mentioned, due to its mean-field approach, HF lacks dynamic electron correlation, which can be regarded as the temporary, instantaneous avoidance of electrons that are already in close spatial proximity, e.g., occupying the same orbital. However, for certain systems with (near-)degenerate orbitals and thus (near-)degenerate electron configurations, the so-called static electron correlation is also important, corresponding to the permanent avoidance of electrons by occupying different orbitals of similar energy. While dynamic correlation effects can be easily recovered in post-HF methods by including excited SDs built from the reference HF wave function, static correlation already has to be treated beforehand at HF level. But since HF itself is a single-determinantial and -configurational method, it is not able to describe the multiconfigurational character of these (near-)degenerate systems.[58,59] Accordingly, because in this work such systems are to be investigated, multiconfigurational methods are needed, which are presented in Section 2.1.2.

To finish this section, the classification of DFT within single- and multiconfigurational methods is attempted. Simply speaking, KS DFT is a single-determinantial method since it utilizes only one single SD of KS orbitals. Accordingly, it should suffer from the same problems as HF, namely missing spin polarization for ROKS, spin contamination for UKS, and the problems for describing multi-determinantial low-spin open-shell systems as well as (near-)degenerate multiconfigurational systems. However, it should be kept in mind that DFT in general is an exact theory and should thus be able to describe all of these systems. For this, "only" the exact electron density of the fully interacting N-electron system is needed, which KS DFT obtains by using a single SD of non-interacting electrons as foundation. Accordingly, if the exact exchange-correlation functional was known, KS DFT would give a, in the language of wave function theory, multiconfigurational electron density with a single SD, making the classification as a single-configurational method, as done in this work, ambiguous.[72] Along these lines, calculating the spin contamination for a KS SD is of limited value since it was not constructed to be a proper wave function in the first place.[58,59,65,72,86] It is even argued that non-spin-contaminated KS SDs for open-shell systems are wrong, implying that UKS should always be used instead of ROKS.[87] Regardless, for a correct evaluation of the spin contamination, a way to calculate $\langle \hat{S}^2 \rangle$ based on the KS density would be required, which is not known to date.[86] Still, UKS generally shows less spin contamination than UHF for the same systems, making it a suitable correlated alternative to post-HF methods not performing well with spin-contaminated references.[58,86] While, in principle, KS DFT would be able to recover all of the dynamic and static correlation, the approximate exchange-correlation functionals were mainly developed to cover the dynamic part, thus being deficient with respect to the static interactions.[86] Furthermore, in case of low-spin open-shell states like singlet diradicals, even the exact KS DFT would need a multi-determinantial treatment for meaningful results to avoid mixing of the singlet and triplet state and thus spin-symmetry breaking.[86,88] On the other hand, spin-symmetry breaking in UKS and UHF can be regarded as the partial inclusion of static correlation. But without a reliable method of calculating the spin contamination like in UHF, an evaluation of the quality of the UKS solution is complicated.[86] Overall, the performance of approximate KS DFT for the problematic low-spin open-shell systems of this work seems to be hard to predict, which is why a comparison to wave function-based multiconfigurational methods is necessary.

2.1.2 Multiconfigurational Methods

2.1.2.1 Configurations, Configuration State Functions and Slater Determinants

Before going into the details of the multiconfigurational wave function-based methods employed in this work, some definitions connected to these approaches should be specified since they can sometimes but not always be used synonymously. As already established in the previous Section 2.1.1, a Slater determinant (SD) is the antisymmetric product of N MOs, i.e., one-electron wave functions, serving as an approximate N-electron wave function. However, as further discussed in Section 2.1.1.4, not every single SD is an eigenfunction of the squared total spin operator $\hat{S}^2$, even though a proper wave function should fulfill this property. Using the example of the singlet diradical, it was shown that a fixed linear combination of two restricted SDs is needed to create a spin-adapted configuration or configuration state function (CSF), which then again is actually an eigenfunction of $\hat{S}^2$. A single restricted closed-shell

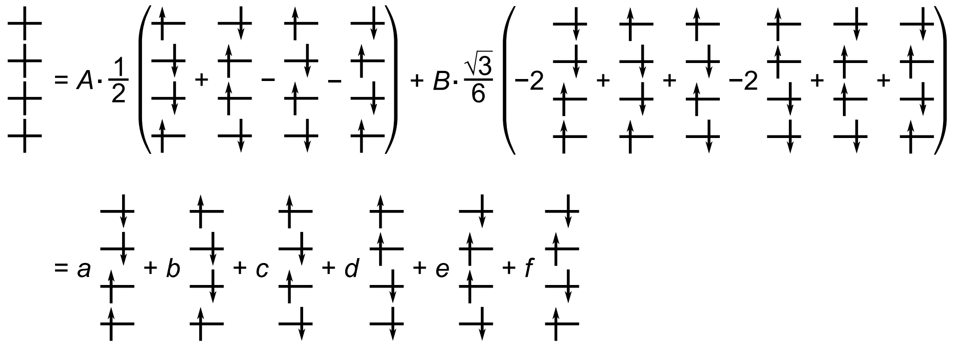

Figure 2.3: Description of the singlet tetraradical configuration [1111] of a four-electron four-orbital system by a linear combination of either the two possible CSFs or the six possible SDs. Created based on Ref. [82]

SD or single high-spin open-shell SD, on the other hand, does already fulfill this requirement and thus is SD and CSF at the same time. Accordingly, spin-pure CSFs can either be one or a fixed linear combination of multiple restricted SDs. Now, every SD and every CSF can be associated with one single electron/orbital configuration, which can be written as a vector of MO occupation numbers starting from the energetically lowest MO as previously depicted for the two-electron two-orbital case in Fig. 2.2. Since generally multiple CSFs can exist for a given configuration, one SD can be involved in multiple CSFs.[82] While in the example of Fig. 2.2 this was only true when considering singlet and triplet configurations, it can also be the case within one spin multiplicity as the example of a singlet tetraradicalic configuration in Fig. 2.3 illustrates. Here, two CSFs are possible, whose coefficients A and B are not fixed but depend on the actual system to be described. However, instead of first constructing the two CSFs, the configuration can also be described by a linear combination of the six possible SDs with the coefficients a to f, which still have to contain the fixed ratios between the SDs inside the two CSFs to ensure spin purity.[82] Using lines instead of arrows for the electrons in the illustration of the configuration emphasizes that up and down spins cannot be assigned to either of the orbitals, just as a spin-pure singlet with zero spin density at every point in space requires.[81] Because there are two CSFs for the one tetraradicalic configuration, the number of all possible CSFs for the four-electron four-orbital system of singlet multiplicity amounts to 20, while there are only 19 configurations in total.

With these definitions at hand, one can now classify HF more precisely. Generally, RHF, ROHF, and UHF are all single-determinantial. However, only RHF is always a true single-configurational method since restricted closed-shell SDs are always also a CSF and there exists only one configuration for one closed-shell CSF. ROHF, on the other hand, is, strictly speaking, not always single-configurational because, e.g., low-spin open-shell configurations need more than one SD for correct CSFs and sometimes even multiple CSFs for the description of the whole configuration. It should be noted, however, that ROHF in its most general formulation is able to handle multiple-determinants and thus multiple CSFs, accordingly considerable as single-configurational.[58] UHF is never single-configurational since it suffers from the same problems as ROHF and additionally always contains some level of spin contamination, thus never describing spin-pure configurations. Still, as also done regularly in the literature, in this work all of these methods will be referred to as single-configurational. The same will be done for the single-determinantial KS DFT even though it could, in principle, be considered as somewhat multi-configurational as already discussed at the end of the previous Section 2.1.1.4.

2.1.2.2 Exact Wave Function and Static Correlation

Since the single HF SD is by definition approximate due to the missing electron correlation caused by the mean-field approach, one could ask how to actually obtain the exact wave function. For this, the same approach as in MO-LCAO can be utilized: any unknown function can be exactly described by a linear combination using a complete basis set of known functions. While in MO-LCAO these basis functions are single-particle basis functions, namely the AOs for electrons, in case of the exact wave function, N-particle basis functions, namely SDs for the whole system, are used instead.[59] The idea of the configuration interaction (CI) method is now to construct this N-particle basis set from the single HF reference SD, hence classified as single-reference method, by creating excited SDs without further optimization of the HF MOs. As already mentioned, since the size k of the AO basis set is generally four to six times as large as $\frac{N}{2}$, a large number of unoccupied orbitals is available for the construction of excited SDs. If all possible excitations (single, double, …, N-times) within the k MOs are considered, the method is called full CI, the best solution possible within the incomplete AO basis set:[58,59]

$$|\Psi^{CI}\rangle = C_0\,|\Psi_0^{HF}\rangle + \sum_{r=1}^{exc.\ SDs} C_r\,|\Psi_r^{exc.\ SD}\rangle \tag{2.70}$$

Accordingly, if all possible excited restricted SDs are available, also all possible CSFs and configurations are considered, hence the name of the method. From this, it can be concluded that any N-electron system is strictly speaking only correctly representable by a multiconfigurational wave function. Since the full CI wave function is exact within the incomplete basis set, all of dynamic and static correlation is included. This is even true for statically correlated systems, although it was mentioned in the previous Section 2.1.1.4 that static correlation has to be treated at the HF level prior to the application of a post-HF method like CI. However, the complete N-particle basis set of full CI can compensate the lack in quality of the HF reference.[58] But since the number of excited SDs scales factorially with the number of electrons and orbitals, full CI is only feasible for very small systems, which is why truncated variants of CI like CIS (CI singles) or CISD (CI singles doubles) have been developed, only considering the lower but most important excitations.[58,59] However, these methods can no longer make up for poor HF references if statically correlated systems are treated due to the incompleteness of the N-particle basis set. On top of that, even truncated CI methods are very demanding and only applicable to quite small systems. To be able to treat statically correlated systems somewhat efficiently, multi-configurational methods are needed. But prior to their definition, it should be clarified what static correlation, also called strong correlation in the physics community, is in more detail.

As mentioned in the previous Section 2.1.1.4, static correlation can be regarded as the permanent avoidance of electrons by the occupation of different orbitals of similar energy. For this, revisiting the four-electron four-orbital example system is helpful. In Fig. 2.3, the energetic separation between the four orbitals was never defined since it is not important for the construction of CSFs. However, intuitively one would assume that the most stable singlet configuration is [2200], which corresponds to the RHF solution. Accordingly, when constructing the corresponding full CI wave function, the coefficient C_0 for the HF reference is very large, i.e., close to one, compared to the remaining SDs/CSFs and thus is allegedly a good single-determinantial approximation of the exact wave function. But if now the two central orbitals approach each other energetically or are even degenerate as depicted in Fig. 2.4, the energetic difference between the configurations [2200], [2020], and [2110] becomes very small. Accordingly, their coefficients are of comparable magnitude and thus of similar importance for the CI wave function, which is an indication of static correlation.[58] Higher excited configurations like [2101] or [0022] can be assigned to dynamic correlation since they are of higher energy and thus exhibit smaller CI coefficients. However, it should be noted that the distinction between static and dynamic correlation is not clear but instead there is a rather smooth transition between them[59] as indicated by the color gradient in Fig. 2.4. The problem is now that RHF would never arrive at degenerate orbitals since it would by definition only doubly occupy and optimize one orbital, while the other stays empty and unoptimized. A broken-symmetry "singlet" ROHF reference could achieve the correct degeneracy, but only strongly spin-contaminated due to the mixture of singlet and triplet states discussed above. Furthermore, it would not be able to include the closed-shell [2200] and [2020] CSFs at the same time. Accordingly, a HF reference SD is not suitable for truncated CI in case of statically correlated systems.

To overcome this issue, the multiconfigurational self-consistent field (MCSCF)

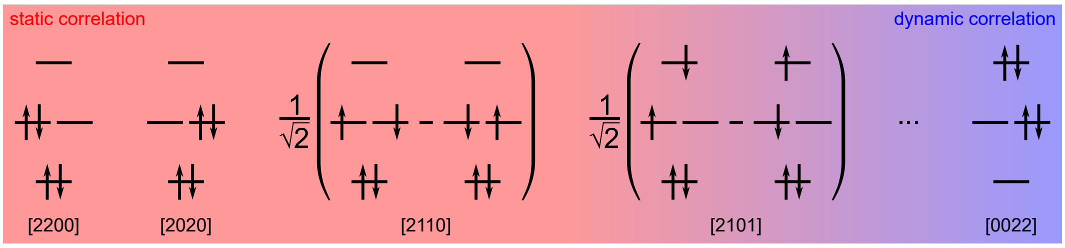

Figure 2.4: Excerpt of the possible configurations/CSFs for a four-electron four-orbital system with two degenerate central orbitals and assignment to static or dynamic correlation.

method can be employed. At maximum accuracy, the expansion of the MCSCF wave function is done in the same way as for full CI, namely by inclusion of all possible restricted SDs/CSFs. However, while CI uses a HF SD as reference to construct all excited SDs, meaning that the HF MOs are unchanged and only the expansion coefficients C_r of the SDs have to be optimized to minimize the energy utilizing the variational principle, MCSCF constructs the whole wave function from scratch, thus both the SD expansion coefficients C_r and the MO coefficients $c_{\mu a}$ have to be optimized. As pointed out previously, since full CI already gives the exact wave function within the incomplete AO basis set, the additional MO optimization of MCSCF will give no improvement.[58] But just like full CI is not feasible for bigger systems, the same is true for MCSCF at maximum accuracy, which is why it also has to be truncated as discussed in the following section.

2.1.2.3 Complete Active Space Self-Consistent Field

Instead of restricting MCSCF to certain types of excitations for all MOs and all electrons as in truncated CI, it still utilizes the full CI approach but only within a subset of electrons and orbitals of the whole system, the so-called active space. The corresponding method is called complete active space self-consistent field[89–93] (CASSCF) and an active space of m electrons and n orbitals is denoted as CAS(m,n). The orbitals below and above the active space are labeled as inactive and external space, respectively,[94] and remain doubly occupied and unoccupied for all SDs/CSFs as depicted in Fig. 2.5. From this figure, it is also apparent that CASSCF can recover the static correlation but generally just a small part of the dynamic correlation due to the missing excitations involving the inactive and external space.[59] The MCSCF or CASSCF wave function of the I-th electronic state (e.g., ground state (0), first excited state (1), ...), also often denoted as I-th root, for a given spin multiplicity M

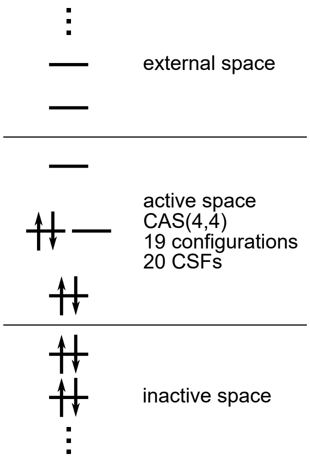

Figure 2.5: Example CAS(4,4) based on the four-electron four-orbital system of Fig. 2.4. Created based on Refs. [58, 59]

can be expanded in the basis set of CSFs of the same multiplicity M:[94]

$$|{}^{M}\Psi_{I}^{MCSCF}\rangle = \sum_{r=0}^{CSFs} C_{rI}\,|{}^{M}\Psi_{r}^{CSF}\rangle \tag{2.71}$$

Accordingly, the MCSCF energy can be calculated as:[58,59]

$$\begin{aligned} E_I &= \langle {}^{M}\Psi_{I}^{MCSCF}|\hat{H}|{}^{M}\Psi_{I}^{MCSCF}\rangle && (2.72)\\ &= \sum_{r=0}^{CSFs}\sum_{s=0}^{CSFs} C_{rI}C_{sI}\,\langle {}^{M}\Psi_{r}^{CSF}|\hat{H}|{}^{M}\Psi_{s}^{CSF}\rangle && (2.73)\end{aligned}$$

Just like in the CI method, the so-called CI matrix with the integrals involving the CSFs and the Hamiltonian (Eq. 2.73) arises. However, as already pointed out in the previous section, the energy is not only dependent on the CI coefficients C_{rI} of the respective state I but also on the MO coefficients $c_{\mu aI}$. Utilizing the variational principle through the Lagrange method, the energy of the MCSCF wave function can be minimized using the respective sets of coefficients, which also involves the diagonalization of the CI matrix. However, due to the factorial increase of the number of CSFs, the CI matrix, whose size is determined by the number of CSFs, grows even more rapidly. For example, a singlet CAS(14,14) gives rise to about $2.7 \cdot 10^6$ singlet CSFs[59] and thus about $7.3 \cdot 10^{12}$ CI matrix elements, making the method computationally very demanding and larger active spaces than this virtually impractical. Nevertheless, another great advantage of MCSCF methods is that, as indicated in Eq. 2.71, electronically excited states I are also accessible, which have their own CI and MO coefficients C_{rI} and $c_{\mu aI}$, respectively.[58] Since excited states are also often of multiconfigurational character, single-configurational methods accordingly give poor results for these and the usage of MCSCF methods is required.[58,59,95] Furthermore, compared to single-reference methods, the additional orbital optimization also of excited states in the MCSCF method resembles real orbital relaxation effects more accurately.[59]

The sum of the square of all CI coefficients has to be unity due to the orthogonality of the CSFs and accordingly the squared CI coefficient gives the percentage of the corresponding CSF in the full MCSCF wave function:[58]

$$\sum_{r=0}^{CSFs} |C_{rI}|^2 = 1 \tag{2.74}$$

However, as soon as not just one single CSF dominates the MCSCF wave function, its interpretation is generally less intuitive since the multiconfigurational nature is not easily transferable to the single-configurational picture chemistry is usually taught in. Still, this is not a problem of the method or the wave function but rather a human constraint.[58] A helpful tool to still interpret MCSCF wave functions conveniently are natural orbital occupation numbers (NOON). Since the active orbitals in the CSFs can either be occupied by two, one or zero electrons, no unique energy eigenvalues can be assigned to them, just like it is also the case for ROHF.[58] Accordingly, instead of the corresponding canonical orbitals, so-called natural orbitals (NOs) can be obtained by diagonalizing the first-order density matrix.[55] The associated NOONs can take any real value between 0.0 and 2.0, where orbitals with NOONs in the range of 1.98 – 0.02 should generally be included in the active space for a faithful description of multiconfigurational systems.[58] Active orbitals with NOONs of about 2.0, 1.0, and 0.0 can be interpreted as doubly, singly, and unoccupied, respectively.[55]

Since the MCSCF wave function is constructed from spin-pure CSFs, it does not suffer from spin contamination like UHF does in general and like ROHF does for multi-determinantial systems (e.g., singlet diradicals) and at the same time is able to correctly describe spin-polarization due to the inclusion of multiple CSFs (e.g., for the discussed methyl radical[96]) compared to ROHF as well as statically correlated systems in general. Even though these drawbacks of single-configurational methods can be overcome in this way, CASSCF calculations are generally missing a large part of dynamic correlation due to the limited size of the active space. To account for this, the CI method could be utilized in combination with the multiconfigurational CASSCF reference wave function, hence denoted as multireference CI (MRCI). However, as imaginable, applying the CI approach to every CSF of the CASSCF reference is very expensive and thus also only feasible for very small systems.[59] More economic alternatives are MR perturbation theory approaches, which will be presented in the following section.

2.1.2.4 Perturbation Theory

Since the mathematics behind perturbation theory in general and the MR analogues in particular are quite lengthy and advanced, it is only introduced for the single-reference case at the example of MP2. The basic idea behind perturbation theory is that the exact solution of a problem is unknown, while for a slightly less sophisticated model system the solution is known, so the difference is just a small perturbation. In case of electronic structure theory, such problems are the exact and the approximate (e.g., HF) solution to the N-electron TISE, in which the approximate method does not include all electron correlation effects. Perturbation theory now divides the exact Hamiltonian $\hat{H}$ into the less sophisticated unperturbed model Hamiltonian $\hat{H}^{(0)}$ and a perturbation operator $\hat{H}'$, where the parameter λ adjusts the strength of the perturbation:[57–59]

$$\hat{H} = \hat{H}^{(0)} + \lambda \hat{H}' \tag{2.75}$$

Since λ can be changed continuously from 0 to 1, the corresponding perturbed ground state wave function $|\Psi_0\rangle$ and energy E_0 have to do so analogously, which can be realized by a Taylor expansion of both as a function of λ using the unperturbed reference ground state wave function $|\Psi_0^{(0)}\rangle$ and energy $E_0^{(0)}$:[57–59]

$$|\Psi_0\rangle = \lambda^0 |\Psi_0^{(0)}\rangle + \lambda^1 |\Psi_0^{(1)}\rangle + \lambda^2 |\Psi_0^{(2)}\rangle + \lambda^3 |\Psi_0^{(3)}\rangle + \dots \tag{2.76}$$

$$E_0 = \lambda^0 E_0^{(0)} + \lambda^1 E_0^{(1)} + \lambda^2 E_0^{(2)} + \lambda^3 E_0^{(3)} + \dots \tag{2.77}$$

$$\text{with} \quad A^{(n)} = \frac{1}{n!}\frac{\partial^n A^{(0)}}{\partial \lambda^n} \tag{2.78}$$

Here, the superscript $^{(n)}$ denotes the n-th-order correction terms for the wave function and energy, i.e., the n-th differentiation with respect to λ as well as the factor $\frac{1}{n!}$, with the zeroth-order terms being simply the known reference wave function and energy of the unperturbed approximate Hamiltonian $\hat{H}^{(0)}$. Accordingly, if λ is set to 0, Eqs. 2.75 to 2.77 reduce to the first term and the unperturbed TISE is obtained:[57–59]

$$\hat{H}^{(0)} |\Psi_0^{(0)}\rangle = E_0^{(0)} |\Psi_0^{(0)}\rangle \tag{2.79}$$

For all other values of λ, the full expansions of Eqs. 2.75 to 2.77 have to be inserted into the TISE. The resulting equation with an infinite number of terms can then be split with respect to the different orders n, indicated by λ^n:[57–59]

$$\lambda^0: \quad \hat{H}^{(0)} |\Psi_0^{(0)}\rangle = E_0^{(0)} |\Psi_0^{(0)}\rangle \tag{2.80}$$

$$\lambda^1: \quad \hat{H}^{(0)} |\Psi_0^{(1)}\rangle + \hat{H}' |\Psi_0^{(0)}\rangle = E_0^{(0)} |\Psi_0^{(1)}\rangle + E_0^{(1)} |\Psi_0^{(0)}\rangle \tag{2.81}$$

$$\lambda^2: \quad \hat{H}^{(0)} |\Psi_0^{(2)}\rangle + \hat{H}' |\Psi_0^{(1)}\rangle = E_0^{(0)} |\Psi_0^{(2)}\rangle + E_0^{(1)} |\Psi_0^{(1)}\rangle + E_0^{(2)} |\Psi_0^{(0)}\rangle \tag{2.82}$$

$$\lambda^n: \quad \hat{H}^{(0)} |\Psi_0^{(n)}\rangle + \hat{H}' |\Psi_0^{(n-1)}\rangle = \sum_{i=0}^{n} E_0^{(i)} |\Psi_0^{(n-i)}\rangle \tag{2.83}$$

Since the infinite expansions can obviously not be realized in real calculations, the perturbed TISE can be approximated by only including the terms to a certain order n. Accordingly, the accuracy increases with the order of the perturbation theory. Now, all first- and higher-order correcting wave functions and energies are unknown. The former, however, can be expressed as a linear combination of all eigenfunctions $|\Psi_r^{(0)}\rangle$ of the unperturbed model Hamiltonian $\hat{H}^{(0)}$ with eigenvalues $E_r^{(0)}$, which is the approach of the Rayleigh-Schrödinger perturbation theory.[97] Consequently, the first- and second-order wave functions are written as:[57–59]

$$|\Psi_0^{(1)}\rangle = \sum_{r>0} C_r |\Psi_r^{(0)}\rangle \tag{2.84}$$

$$|\Psi_0^{(2)}\rangle = \sum_{r>0} D_r |\Psi_r^{(0)}\rangle \tag{2.85}$$

Without going into the details, inserting these expansions into the first- and second-order parts of the perturbed TISE (Eqs. 2.81 and 2.82) then allows to derive the corresponding coefficients C_r and D_r by multiplying from the left with $|\Psi_0^{(0)}\rangle$ and $|\Psi_{s\neq 0}^{(0)}\rangle$, respectively, and integrating. Furthermore, the first-and second-order energy corrections are obtained:[57–59]

$$E_0^{(1)} = \langle \Psi_0^{(0)} | \hat{H}' | \Psi_0^{(0)} \rangle \tag{2.86}$$

$$E_0^{(2)} = \sum_{s>0} \frac{\langle \Psi_0^{(0)} | \hat{H}' | \Psi_s^{(0)} \rangle \, \langle \Psi_s^{(0)} | \hat{H}' | \Psi_0^{(0)} \rangle}{E_0^{(0)} - E_s^{(0)}} \tag{2.87}$$

Møller and Plesset[62] applied this Rayleigh-Schrödinger perturbation theory to the HF formalism. Here, the HF wave function is used as unperturbed zeroth-order reference $|\Psi_0^{(0)}\rangle$ and the approximate unperturbed model Hamiltonian $\hat{H}^{(0)}$ is simply the sum of Fock operators (Eq. 2.16) of all k MOs:[58,59]

$$\hat{H}^{(0)} = \sum_{a=1}^{k} \hat{f}_a(1) = \sum_{a=1}^{k} \left(\hat{h}(1) + \sum_{b=1}^{k} \left(\hat{J}_b(1) - \hat{K}_b(1) \right) \right) \tag{2.88}$$

Applying this to the HF reference SD, which only consists of the N occupied MOs, gives the sum of the respective orbital energies as the zeroth-order energy:[58,59]

$$E_0^{MP0} = E_0^{(0)} = \langle \Psi_0^{(0)} | \hat{H}^{(0)} | \Psi_0^{(0)} \rangle = \sum_{i=1}^{N_{occ}} \varepsilon_i = \sum_{i=1}^{N_{occ}} \left(h_i + \sum_{j=1}^{N_{occ}} (J_{ij} - K_{ij}) \right) \tag{2.89}$$

As already pointed out in Section 2.1.1.1, this is not the correct HF energy due to the double counting of the electron-electron interactions. Accordingly, the Møller-Plesset perturbation theory of zeroth order, hence denoted as MP0, performs worse than the HF method. However, the perturbation operator $\hat{H}'$ can now be constructed to correct this error to give the result of the exact Hamiltonian $\hat{H}$ by subtracting half of the two-electron operators:[58,59]

$$\hat{H}' = -\frac{1}{2} \sum_{a=1}^{k} \sum_{b=1}^{k} \left(\hat{J}_b(1) - \hat{K}_b(1) \right) \tag{2.90}$$

With this, the first-order correction energy modifies the zeroth-order correction energy to yield the MP1 energy, which is equal to the HF energy (Eq. 2.18, without V_{nn}):[58,59]

$$E_0^{(1)} = \langle \Psi_0^{(0)} | \hat{H}' | \Psi_0^{(0)} \rangle = -\frac{1}{2} \sum_{i=1}^{N_{occ}} \sum_{j=1}^{N_{occ}} (J_{ij} - K_{ij}) \tag{2.91}$$

$$E_0^{MP1} = E_0^{(0)} + E_0^{(1)} = E_0^{HF} \tag{2.92}$$

Accordingly, the first estimation of post-HF electron correlation is included in MP2, which is the most widely used variant of the MPn method. For this, the second-order correction energy $E_0^{(2)}$ (Eq. 2.87) has to be evaluated, where all possible excited SDs/CSFs constructed from the HF reference are used as basis functions $|\Psi_r^{(0)}\rangle$ for the expansion of the higher-order correcting wave functions. Thus, the numerator of Eq. 2.87 contains integrals of the perturbation operator with the HF reference SD $|\Psi_0^{(0)}\rangle$ and the excited SDs, which vanish for all but the doubly excited SDs $|\Psi_{ij}^{ab}\rangle$ according to the Slater-Condon rules and Brillouins theorem. Furthermore, since $\hat{H}'$ is only a two-electron operator and the corresponding integrals in the numerator contain SDs differing by two orbitals, only one Coulomb and one exchange integral with the orbitals involved in the excitation, i.e., $|\chi_i\rangle$, $|\chi_j\rangle$, $|\chi_a\rangle$, and $|\chi_b\rangle$, remains according to the Slater-Condon rules. In the denominator, the difference between the zeroth-order energies reduces to the difference of the corresponding orbital energies. Thus, the second-order energy correction is written as:[58,59]

$$E_0^{(2)} = \sum_{j>i}^{N_{occ}} \sum_{b>a}^{N_{virt}} \frac{\langle \Psi_0^{(0)} | \hat{H}' | \Psi_{ij}^{ab} \rangle \, \langle \Psi_{ij}^{ab} | \hat{H}' | \Psi_0^{(0)} \rangle}{E_0^{(0)} - E_{ij}^{ab}} \tag{2.93}$$

$$= \sum_{j>i}^{N_{occ}} \sum_{b>a}^{N_{virt}} \frac{\left(\langle \chi_i(1)\chi_j(2) | \hat{g}_{12} | \chi_a(1)\chi_b(2) \rangle - \langle \chi_i(1)\chi_j(2) | \hat{g}_{12} | \chi_b(1)\chi_a(2) \rangle \right)^2}{\varepsilon_i + \varepsilon_j - \varepsilon_a - \varepsilon_b} \tag{2.94}$$

Accordingly, the MP2 energy can be calculated as:[58,59]

$$E_0^{MP2} = E_0^{HF} + E_0^{(2)} \tag{2.95}$$

Generally, it is possible to include higher orders of correction (MP3, MP4, . . .), but MP2 is the most economical choice to include dynamic correlation. It should be noted that the expansion coefficients of the reference HF MOs $c_{\mu a}$ and of the correcting wave functions C_r and thus the correction energies are not optimized further. Moreover, while perturbation theory in general performs best when the perturbation is small, the electron-electron repulsion energy defined as such in the MP formalism is a rather large part of the total energy, which is why it is not guaranteed to give reliable results.[58,59]

With this overview of the MP2 method using a single-determinantial HF SD as reference at hand, a qualitative look at perturbation theory with multi-determinantial CASSCF references is taken. The main problem is that, as already mentioned, the active orbitals of a CASSCF wave function cannot be canonicalized and thus have no unique set of orbital energies and one-electron operators, which are needed in the correction energies and the definition of the unperturbed model Hamiltonian $\hat{H}^{(0)}$, respectively. Accordingly, different flavors of MR perturbation theory have been proposed, generally of only second order,[58,59,98] with one of the most popular methods being the CAS perturbation theory of second order (CASPT2),[99,100] which, just like MP2, is based on one electron operators for $\hat{H}^{(0)}$. However, it was shown that this results in only the zeroth-order reference CASSCF wave function already considering the dielectronic interactions of the active electrons but not the correcting wave functions. Thus, a partly dielectronic model Hamiltonian $\hat{H}^{(0)}$ was proposed,[101] leading to the n-electron valence state perturbation theory of second order (NEVPT2).[102–104] The main advantage of this approach compared to MR perturbation theory methods using one-electron model Hamiltonians is the absence of so-called intruder states. These show zeroth-order energies $E_s^{(0)}$ close to the zeroth-order reference energy $E_0^{(0)}$, which leads to very small energy differences in the denominator of Eq. 2.87 and hence erroneously large contributions to the second-order correction energy.[94,98] Overall, MR perturbation theory methods are still very demanding and are thus only applicable to systems smaller than what is feasible for CASSCF regarding the number of AO basis functions and the active space size.

2.2 Electronic Structure Theory of Solids

2.2.1 Periodic Boundary Conditions

2.2.1.1 Reciprocal Space and Bloch Functions

Solid-state systems are macroscopic objects and, in comparison to molecules, contain an extremely large number of atoms in the magnitude of a mole, i.e., about 10^{23} atoms, and accordingly an even greater number of electrons. Obviously, solving the TISE for such systems as a whole is impossible.[105,106] Thankfully, many solids are crystalline and thus exhibit a unit cell as smallest building block, only amounting to a fraction of the whole system. Each three-dimensional (3D) unit cell is a parallelepiped defined by three non-coplanar 3D basis vectors $\vec{a}_1$, $\vec{a}_2$, and $\vec{a}_3$ or alternatively by six lattice parameters, namely the length of the basis vectors a, b, and c and the angles α, β, and γ between them. If a unit cell contains only one lattice point, it is called a primitive unit cell and the infinite translational repetition of a unit cell in the three directions of its basis vectors builds the so-called real or direct lattice. Note that a lattice point is only a mathematical object, which, in the end, can represent one or multiple atoms. In three dimensions, there exist seven primitive lattices and corresponding crystal systems, namely triclinic, monoclinic, orthorhombic, tetragonal, cubic, trigonal, and hexagonal, differing in the relationship between the lattice parameters, e.g., $a = b = c$ and $\alpha = \beta = \gamma = 90°$ in case of the cubic system. Even though the primitive (p) lattices are sufficient to describe any possible crystal, there are seven additional non-primitive lattices derived from the primitive ones. Assuming the primitive lattice points are located on the corners, non-primitive lattices contain additional lattice points centered (c) either on the unit cell faces or in the unit cell itself, hence denoted as face-centered (fc) or body-centered (bc), respectively. These non-primitive or conventional unit cells generally better reflect the point symmetry of the whole lattice compared to their primitive analogues as, e.g., apparent in Fig. 1.2 for the case of 3C-SiC. Overall, this gives 14 so-called Bravais lattices, whose translational symmetries combined with point group symmetries result in the 230 different space groups,[106,107] with 3C-SiC belonging to the cubic space group 216. Each of these space groups has specific symmetry elements, which can be exploited to only give the coordinates for a minimum number of atoms, the so-called asymmetric unit, and then let the symmetry operations fill the rest of the conventional unit cell.[106] Generally, the coordinates of an atom i in a unit cell is given in fractional units x_i, y_i, and z_i ranging from 0 to 1, which then can be multiplied with the basis vectors of the unit cell to give the actual coordinates:[106–108]

$$\vec{r_i} = x_i\vec{a}_1 + y_i\vec{a}_2 + z_i\vec{a}_3 \tag{2.96}$$

In case of 3C-SiC, the asymmetric unit only contains one Si and one C atom with fractional coordinates of $(0, 0, 0)$ and $(\frac{1}{4}, \frac{1}{4}, \frac{1}{4})$, respectively. As apparent in Fig. 1.2a), this corresponds to one of the C atoms in the volume of the conventional unit cell and one of the Si atoms at its corners. While there are a total of eight identical Si atoms present at the eight corners, only one eighth of their volume is actually located in the unit cell due to the translational symmetry, thus in total still representing only one single Si atom. The symmetry operations of space group 216 then yield three additional C and Si atoms each, the latter being located at the center of the six unit cell faces, hence only counting one half each to give the correct total amount of three Si.

Now, an infinite crystal lattice is translationally invariant with respect to all lattice vectors $\vec{G}$ being linear combinations of the basis vectors of the primitive unit cell with integer-valued coefficients n_1, n_2, and n_3 because such translations map identical points of two different unit cells of the crystal onto each other:[105–107]

$$\vec{G} = n_1\vec{a}_1 + n_2\vec{a}_2 + n_3\vec{a}_3 \tag{2.97}$$

Accordingly, the TISE also has to be invariant to the translations along all lattice vectors $\vec{G}$:[105,106]

$$\hat{H}(\vec{r} + \vec{G})\Psi(\vec{r} + \vec{G}) = E\Psi(\vec{r} + \vec{G}) \tag{2.98}$$

Bloch[109] could show that eigenfunctions for the solution of such translational invariant TISEs have to be of the form of a so-called Bloch function:[105,106]

$$\psi(\vec{r} + \vec{G}; \vec{k}) = e^{i\vec{k}\vec{G}}\psi(\vec{r}; \vec{k}) \tag{2.99}$$

Here, the 3D wave vector $\vec{k}$ is a parameter determining the periodicity of the eigenfunction, which does not have to show the exact same periodicity as the crystal lattice,[106] as will be clarified in the example following in Section 2.2.1.2. Basically, this Bloch theorem states that translating the eigenfunction along a lattice vector $\vec{G}$ is the same as multiplying the untranslated eigenfunction with the complex phase factor $e^{i\vec{k}\vec{G}}$, which mathematically is a complex number of absolute value 1, thus not changing the eigenfunction in a physical sense. Furthermore, it is evident from this equation that by knowledge of the eigenfunction at a point $\vec{r}$ in the reference unit cell, the eigenfunction at the points $\vec{r}+\vec{G}$ of all other unit cells is known, only differing by the complex phase factor dependent on $\vec{G}$.[105] This drastically reduces the infinitely sized problem of the whole crystal to a finitely sized problem of one unit cell. However, in return the TISE has to be solved for different values of $\vec{k}$:[105,106]

$$\hat{H}(\vec{r})\psi(\vec{r}; \vec{k}) = E(\vec{k})\psi(\vec{r}; \vec{k}) \tag{2.100}$$

Different wave vectors or quantum numbers $\vec{k}$ can also be interpreted as a label for different irreducible representations of the translational group of the crystal. Similar to the point groups in MO theory, this results in the Bloch functions of different irreducible representations being orthogonal to each other, making the solution of the TISE for different $\vec{k}$ independent of each other.[105,106]

Furthermore, $\vec{k}$ is not only a wave vector/quantum number and an irreducible representation for translational symmetry but also a point in reciprocal space. The concept of reciprocal space seems to be intuitive for most physicists[108] but this is generally not the case for chemists (including this work's author), which is why here it is attempted to shed some light on this topic to be able to interpret results of electronic structure calculations on solids in more detail. Due to its infinity and periodicity, the real/direct lattice is perfectly suited for the Fourier transform using plane waves $e^{i\vec{k}\vec{r}}$ as basis functions, which can, according to Euler's formula, be split into a real and an imaginary part containing sine and cosine and thus infinite, periodic functions:[107]

$$e^{i\vec{k}\vec{r}} = \cos(\vec{k}\vec{r}) + i \cdot \sin(\vec{k}\vec{r}) \tag{2.101}$$

The corresponding reciprocal lattice itself is infinite and periodic with basis vectors $\vec{b}_1$, $\vec{b}_2$, and $\vec{b}_3$ that can be derived from the real lattice basis vectors $\vec{a}_1$, $\vec{a}_2$, and $\vec{a}_3$ as follows:[105,107,108]

$$\vec{b}_1 = 2\pi \frac{\vec{a}_2 \times \vec{a}_3}{\vec{a}_1 \cdot \vec{a}_2 \times \vec{a}_3} \qquad \vec{b}_2 = 2\pi \frac{\vec{a}_3 \times \vec{a}_1}{\vec{a}_1 \cdot \vec{a}_2 \times \vec{a}_3} \qquad \vec{b}_3 = 2\pi \frac{\vec{a}_1 \times \vec{a}_2}{\vec{a}_1 \cdot \vec{a}_2 \times \vec{a}_3} \tag{2.102}$$

Here, $\cdot$ corresponds to the scalar product and $\times$ to the cross product (the latter is defined in Eq. A.2), thus the denominators overall giving the volume of the primitive unit cell in real space. Accordingly, each of the fractions in Eq. 2.102 is the division of an area by a volume, resulting in the reciprocal basis vectors having the unit of inverse length, hence the name.[107] Especially in the context of quantum dynamics, the reciprocal space is also called momentum space since the wave vector $\vec{k}$ is proportional to the momentum via the reduced Planck constant $\vec{p} = \hbar\vec{k}$.[110,111] While the reciprocal space at first glance is mainly a mathematical concept, it is actually observed in the patterns of crystal diffraction measurements.[107] From this, it might also be clear that one point $\vec{r}$ in real space is not mappable to only one point $\vec{k}$ in reciprocal space and vice versa since one point in the diffraction pattern of the reciprocal lattice is the result of constructive interference of electromagnetic waves scattered from multiple different atoms in the real lattice. Or in the case of quantum dynamics, a wave packet can exhibit one specific value for the momentum $\vec{k}$ (one point in momentum space), in principle, at every position $\vec{r}$ in real space.

Just like its real counterpart, the reciprocal lattice is invariant to translations along the reciprocal lattice vectors $\vec{K}$:[106,107]

$$\vec{K} = m_1\vec{b}_1 + m_2\vec{b}_2 + m_3\vec{b}_3 \tag{2.103}$$

Furthermore, the Bloch functions show an even more general translational behavior in reciprocal space compared to real space (Eq. 2.99), namely translation along a reciprocal lattice vector $\vec{K}$ does not change the Bloch function, not even the phase factor.[106] From this, it can be concluded that, just as in real space, only the Bloch function at $\vec{k}$ in one reciprocal reference unit cell has to be known to know all Bloch functions at $\vec{k} + \vec{K}$ in the entire reciprocal lattice.

As already mentioned at the start of the section, a primitive unit cell contains all information necessary to built the real lattice and the same is true for the reciprocal lattice. However, an alternative primitive unit cell to the parallelepiped defined by the reciprocal basis vectors $\vec{b}_1$, $\vec{b}_2$, and $\vec{b}_3$ is the so-called first Brillouin zone (BZ), which corresponds to a Wigner-Seitz cell in reciprocal space. For this, one central lattice point is connected to all other lattice points and then a plane is placed in the middle of and orthogonal to each connecting line. The volume enclosed inside corresponds to the first BZ.[105–107] In Fig. 2.6, this is shown exemplarily for the two-dimensional (2D) case, namely the first surface Brillouin zones (SBZ) of the p(1×1), p(2×1), and c(4×2) surfaces of Si-terminated 3C-SiC(001) investigated in this work. As apparent, the first BZ can but does not have to coincide with the primitive reciprocal unit cell. Another example where this is not the case is the first BZ of fcc lattices like bulk 3C-SiC, which unintuitively is a truncated octahedron despite the conventional unit cell being a cube.[107,112] Even though all possible primitive reciprocal unit cells of a specific crystal lattice contain the same information, i.e., all relevant, non-duplicate Bloch functions with respect to $\vec{k}$, the first BZ is somewhat more intuitive. It is easily imaginable that after going halfway to the next reciprocal lattice point, namely after the edge of the first BZ, the information in $\vec{k}$ starts to repeat itself. Additionally, depending on the space group of the real lattice, the reciprocal lattice also exhibits symmetry elements, which reduce the area in the first BZ with unique wave vectors $\vec{k}$, the so-called irreducible BZ (IBZ). But even if the real lattice has no symmetry elements besides the identity, the Bloch functions are always complex conjugate for positive and negative $\vec{k}$:[105,107,111,113]

$$\psi(\vec{r};\vec{k}) = \Big(\psi(\vec{r};-\vec{k})\Big)^* \tag{2.104}$$

Mathematically speaking, this is simply a property of every Fourier transform of real functions. From a physical perspective, this behavior of the Bloch functions can be attributed to time-reversal symmetry.[113] In crystallography, this effect is known as Friedel's law, resulting in all diffraction patterns being centrosymmetric even if the crystal in real space does not show this point symmetry.[114] From whatever perspective one might come, this property of reciprocal space ultimately results in the IBZ generally being at least only half the size of the BZ. However, there are cases where time-reversal symmetry is broken and this symmetry cannot be exploited, e.g., when applying external magnetic fields.[113]

It should be noted that, even if the direct lattice is not infinite, application of the Fourier transform automatically enforces Born-von Karman or periodic boundary conditions (PBCs), which ensures each Bloch function to show identical function values at the edges of the finite lattice for each dimension. This allows to seamlessly connect an infinite amount of the finite crystals to still obtain an infinite lattice, or, put differently but mathematically identical, to connect the ends of each dimension of one singular finite crystal, yielding a circular structure.[105,107,111,115]

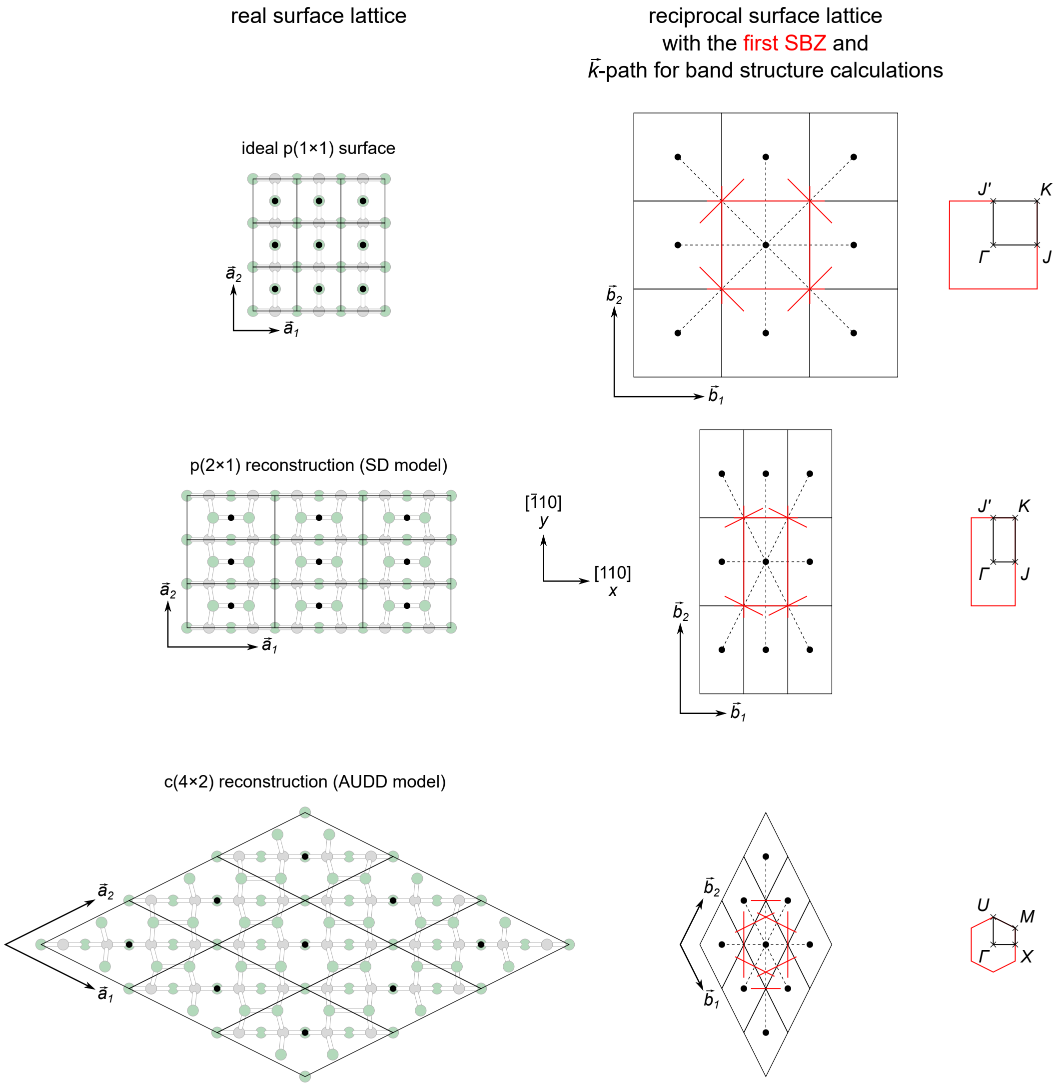

Figure 2.6: Real and reciprocal lattices of the ideal p(1×1), p(2×1) reconstructed (SD model), and c(4×2) reconstructed (AUDD model) Si-terminated 3C-SiC(001) surface. Dots represent equal lattice points in different unit cells and the first SBZ is indicated by red lines. Additionally, the $\vec{k}$-paths for each SBZ are given according to the following references: p(1×1),[116] p(2×1),[38] c(4×2).[47,117] The detailed calculation of the reciprocal lattice basis vectors is presented in Appendix A.1.1.

2.2.1.2 Interpretation of $\vec{k}$: Band Structures

Up to this point, the wave vector $\vec{k}$ was denoted as a parameter. However, with the knowledge of the reciprocal space at hand, one would assume it to be a continuous variable just like $\vec{r}$ is in real space. This is in fact the case for infinitely sized crystals as was assumed for the majority of this section. However, the number of unique $\vec{k}$ is actually equal to the number of unit cells contained in the crystal.[106,111] To show the reasoning for this and to make other points stated in the previous section more comprehensible as well as understand the significance of $\vec{k}$ in a general physical/chemical context, some simple example systems will be discussed in the following in close relation to a great publication of Hoffmann.[111]

Assuming an infinite 1D chain of unit cells with lattice parameter a and one s orbital at each lattice point, one could ask what the Bloch functions, up to this point just some abstract mathematical object suitable to describe eigenfunctions of the TISE in periodic systems, actually look like. Since a crystal in its essence is just a giant molecule, there should also be MOs present, i.e., one-electron eigenfunctions of the TISE, which are now called crystalline orbitals (COs) instead. Just like in MO theory, one could start to create all possible linear combinations of the s orbitals, of which there are an infinite number since the 1D chain is also infinite. It is easily imaginable that, as depicted in Fig. 2.7, the limiting cases are the fully bonding and fully antibonding linear combinations between the s orbitals and thus between the unit cells. Now, the wave vector, which in the 1D case is just a scalar value k like the real space coordinate x, serves as an irreducible representation labeling the different linear

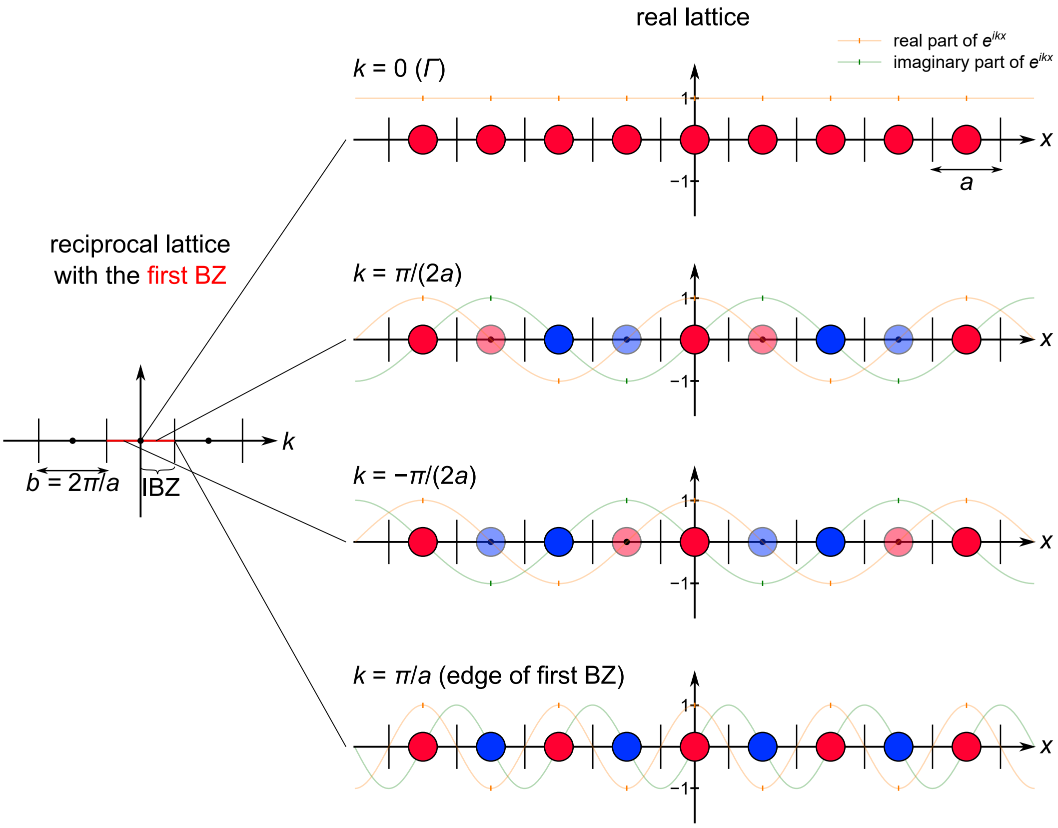

Figure 2.7: Correlation between the plane wave/phase factor e^{ikx} of Bloch functions and the phases of the corresponding linear combinations between orbitals of neighboring unit cells for certain wave vectors k (at certain k-points) of a periodic 1D chain of s orbitals. Purely imaginary orbitals are displayed in a faded manner.

combinations. The reciprocal lattice parameter b is simply $\frac{2\pi}{a}$ and accordingly the IBZ ranges from $k = 0$ to $k = \frac{\pi}{a}$, corresponding to the fully bonding and fully antibonding linear combinations, respectively. This assignment is mathematically consistent since a Bloch function $\psi(\vec{r};\vec{k})$ is a product of a plane wave $e^{i\vec{k}\vec{r}}$ and a periodic function $u(\vec{r};\vec{k})$, the latter corresponding to the sum of the s orbitals repeated periodically throughout the crystal:[106,108,113]

$$\psi(\vec{r};\vec{k}) = e^{i\vec{k}\vec{r}}u(\vec{r};\vec{k}) \tag{2.105}$$

Accordingly, the plane wave part of the Bloch function determines the complex phase factor of each orbital. Since the period length of the plane wave depends on $\vec{k}$, different $\vec{k}$ yield different linear combinations of orbitals. In the example in Fig. 2.7, the real and imaginary parts of the 1D plane wave e^{ikx} are shown, from which the connection between the plane wave and the phase factor of each s orbital is apparent. While not explicitly mentioned in the literature, it appears from the given equations[105,106,111] that the complex phase factor is only evaluated at the lattice points and then its value is transferred to all AOs inside the respective unit cell. This is indicated in Fig. 2.7 by the additional marks on the plane waves at each lattice point position and apparent from the following equation describing the μ-th AO-Bloch function $\psi_\mu(\vec{r};\vec{k})$ as the sum of all the μ-th AO basis functions $\phi_\mu(\vec{r} - \vec{r}_\mu - \vec{G}_j)$, located at the atomic position $\vec{r}_\mu$ with respect to the origin/lattice point of each unit cell, while each of the M unit cells is accessible through the lattice vectors $\vec{G}_j$ from the absolute origin/central lattice point of the system:[106]

$$\psi_\mu(\vec{r};\vec{k}) = \frac{1}{\sqrt{M}} \sum_{j=1}^{M} e^{i\vec{k}\vec{G}_j} \phi_\mu(\vec{r} - \vec{r}_\mu - \vec{G}_j) \tag{2.106}$$

Accordingly, instead of the continuous plane wave $e^{i\vec{k}\vec{r}}$, only the values at the lattice points $e^{i\vec{k}\vec{G}}$ are used. Of course, one CO-Bloch function $\psi_a(\vec{r};\vec{k})$, being the MO equivalent of crystals, can then be a linear combination of all available AO-Bloch functions $\psi_\mu(\vec{r};\vec{k})$ in the fashion of MO-LCAO.

From Fig. 2.7, it is also apparent that the Bloch functions halfway through the first BZ in both directions, namely at $k = \frac{\pi}{2a}$ and $k = -\frac{\pi}{2a}$, are complex conjugates of each other (Eq. 2.104), i.e., the real part of both linear combinations is identical and only the imaginary part is inverted. It should be noted that the imaginary part of the Bloch functions is important, only the illustration and comprehension of complex functions is less intuitive. However, just like the purely real p_x and p_y orbitals are “only” convenient linear combinations of the true degenerate complex conjugate p_+ and p_- eigenfunctions with magnetic quantum numbers m_l of $+1$ and -1, respectively,[118] the same can be done for the degenerate complex conjugate Bloch functions with quantum numbers $\vec{k}$ and $-\vec{k}$. Application to the example in Fig. 2.7 results in purely real linear combinations, which are easier to grasp:[105]

$$\psi(x;\frac{\pi}{2a}) = \cdots - \phi_{-2} - i\cdot\phi_{-1} + \phi_0 + i\cdot\phi_1 - \phi_2 \ldots \tag{2.107}$$

$$\psi(x;-\frac{\pi}{2a}) = \cdots - \phi_{-2} + i\cdot\phi_{-1} + \phi_0 - i\cdot\phi_1 - \phi_2 \ldots \tag{2.108}$$

$$\frac{1}{\sqrt{2}}\left(\psi(x;\frac{\pi}{2a}) + \psi(x;-\frac{\pi}{2a})\right) = \frac{1}{\sqrt{2}}(\cdots - 2\phi_{-2} + 2\phi_0 - 2\phi_2) \tag{2.109}$$

$$\frac{i}{\sqrt{2}}\left(\psi(x;\frac{\pi}{2a}) - \psi(x;-\frac{\pi}{2a})\right) = \frac{1}{\sqrt{2}}(\cdots + 2\phi_{-1} - 2\phi_1 \ldots) \tag{2.110}$$

Here, the indices of the AOs corresponds to the number of the respective lattice point. The corresponding linear combinations are depicted in Fig. 2.8 and are easily characterized as fully nonbonding, thus in accordance with being located halfway through the first BZ from the fully bonding to the fully antibonding Bloch function.[115]

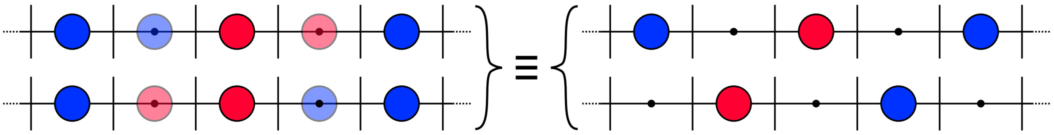

Figure 2.8: Linear combinations of the degenerate complex Bloch functions (left side) of a periodic 1D chain of s orbitals for $k = \frac{\pi}{2a}$ and $k = -\frac{\pi}{2a}$ as depicted in Fig. 2.7 and given in Eqs. 2.107 and 2.108 to obtain purely real Bloch functions (right side) as given in Eqs. 2.109 and 2.110. Purely imaginary orbitals are displayed in a faded manner. Created based on Refs. [105, 111, 115].

Two points mentioned in the previous section are also apparent in Fig. 2.7: firstly, one point $\vec{k}$ in reciprocal space corresponds to a Bloch function spanning the whole real space and thus all $\vec{r}$ or, vice versa, one point in real space $\vec{r}$ "contains" a part of all Bloch functions and thus of all $\vec{k}$. Secondly, the plane waves of the Bloch functions can have different periodicity than the lattice, which can lead to a change in the phase upon translation along an arbitrary lattice vector $\vec{G}$, as expressed in the Bloch theorem in Eq. 2.99. Furthermore, it is easily imaginable from Fig. 2.7 that, as mentioned at the start of this section, the number of wave vectors $\vec{k}$ inside the first BZ is equal to the number of unit cells M of a finite crystal since this is also the maximum amount of different possible linear combinations between them.[106,111]

Just like in MO theory, the different COs can be listed according to their energy in an MO diagram. While the number of COs is only dependent on the number of AO basis functions k, the TISE, on the other hand, as already indicated in the previous section, has to be solved for every of the M wave vectors $\vec{k}$, resulting in a very large number of linear combinations and energies for each CO. Instead of now vertically displaying the energy levels of all these linear combinations in an MO diagram, an additional horizontal dimension is added, which gives the dependence of the COs on the wave vector $\vec{k}$ and thus results in a band structure plot.[105,111,115] Put simply, a band structure is just all the M MO diagrams put next to each other with the COs forming the bands, of which there are as many as AO basis functions.

Fig. 2.9 shows the qualitative band structure of the discussed periodic 1D chain of s orbitals as well as the same system with p orbitals, which will be used in the following to better understand the information given in band structures in general. It is apparent that the bands of the s and p orbitals show a different trend, namely the s band increasing and the p band decreasing in energy when going from the center of the first BZ at $k = 0$ to its edge at $k = \frac{\pi}{a}$. This can simply be explained by the different symmetry of the s and p orbitals. At the BZ center, the phase between neighboring unit cells is the same, resulting in the fully bonding linear combination of s orbitals and a fully antibonding linear combination of p orbitals. At the edge of the first BZ, the phase alternates from unit cell to unit cell, inverting the situation and accordingly the s orbitals are fully antibonding, while the p orbitals are fully bonding.[105,111,115] It should be noted that, for the sake of simplicity, the bands in these examples are centrosymmetric even though the antibonding linear combinations should actually be destabilized more strongly than the bonding linear combinations are stabilized.[111] Another interesting feature of

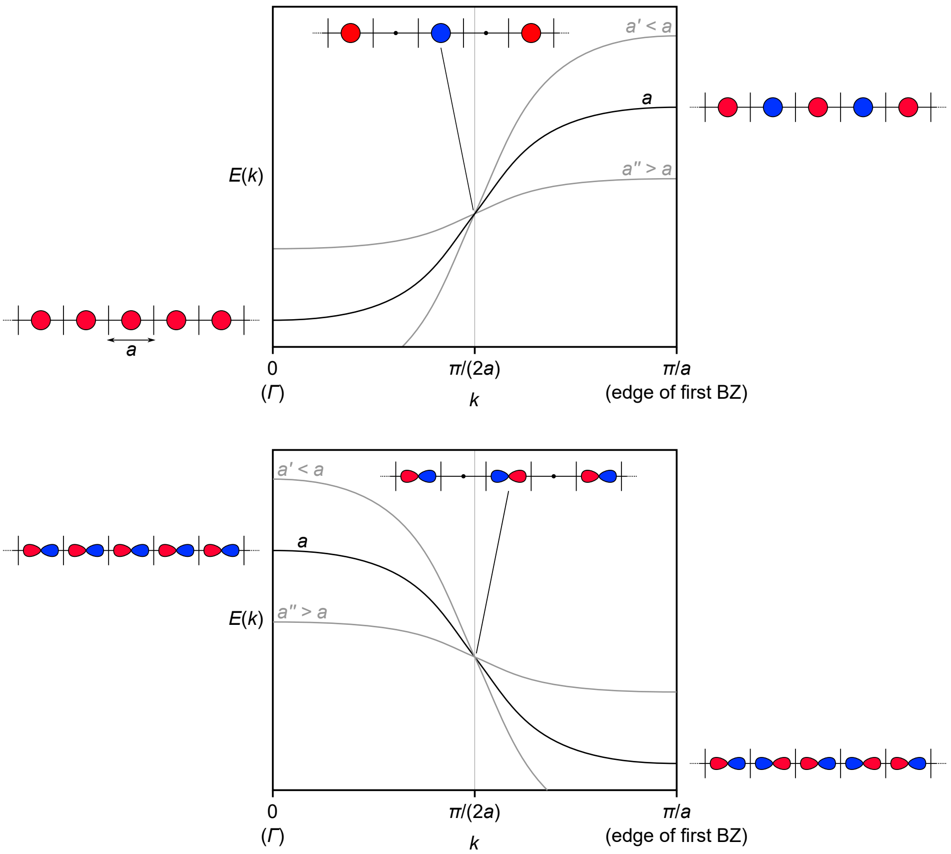

Figure 2.9: Correlation between the qualitative band structure of a periodic 1D chain of s (top) and p orbitals (bottom) and the corresponding linear combinations between the respective orbitals of neighboring unit cells for certain wave vectors k (at certain k-points). Created based on Ref. [111].

band structures is the band width with respect to the energy range they cover, also called dispersion. The magnitude of dispersion is directly connected to the strength of overlap between neighboring unit cells. In Fig. 2.9, this is indicated by additional bands shown in gray, which represent the same systems but with smaller or larger lattice parameters a' and a'', respectively, compared to the reference band structure with lattice parameter a. Here, for the smaller a' the dispersion increases due to stronger overlap between unit cells and thus stronger energy level splitting, while it decreases for the larger a'' for opposite reasons.[105,111]

Increasing the dimensionality of the 1D example, a 2D square lattice of s orbitals is obtained. Accordingly, the reciprocal space, the first BZ, and the wave vectors $\vec{k}$ are also 2D as depicted in Fig. 2.10. While in the 1D case it was quite obvious that the band structure has to be analyzed along the only existing direction, it is less clear in this higher-dimensional case. Generally, to not lose any information on the energy levels, every $\vec{k}$ of the IBZ would have to be plotted, which would result in a very large graph. Instead, the properties of the first BZ can be exploited. In the 1D example, it was shown that the fully bonding and fully antibonding linear combinations are located at the center and the edges of the first BZ. This concept can be transferred to the 2D case, i.e., the extremes of the band structure are located at the center, corners, and edges of the BZ/IBZ, as the corresponding linear combinations in Fig. 2.10 show. These positions in the first BZ are called special or high-symmetry $\vec{k}$-points, which are generally abbreviated by single letters. For example, Γ is

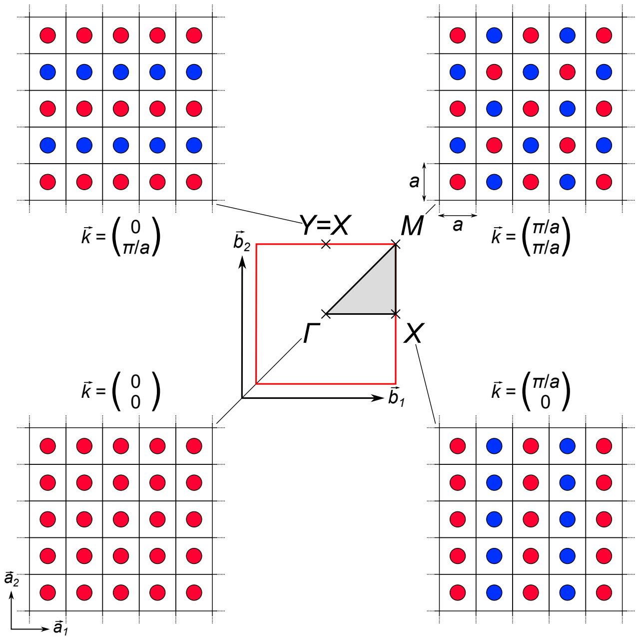

Figure 2.10: Assignment of linear combinations between orbitals of neighboring unit cells to high symmetry $\vec{k}$-points of the first BZ (red) for a 2D square lattice of s orbitals. The IBZ is shaded in gray and the $\vec{k}$-path for the calculation of band structures is indicated by black lines. Created based on Refs. [105, 111].

the center of the first BZ (already indicated in Figs. 2.6, 2.7 and 2.9).[105,111] The classification as high-symmetry $\vec{k}$-points stems from the fact that they are located on point symmetry elements of the first BZ, whose corresponding symmetry operations map these points onto themselves.[113] Since these high-symmetry $\vec{k}$-points generally also represent the extremes of the band structure, it is reasonable to only plot the bands along a $\vec{k}$-path connecting these points in the IBZ. In this way, the most important energy values of the system are considered while minimizing the overall size of the band structure plot. In the example of Fig. 2.10, a reasonable $\vec{k}$-path would be $\Gamma \rightarrow X \rightarrow M \rightarrow \Gamma$. The point Y can be discarded since it is degenerate to X due to the high symmetry of the square lattice.[105,111] The $\vec{k}$-paths of the first SBZs of the investigated Si-terminated 3C-SiC(001) surfaces were already given in Fig. 2.6.

While band structures can always be interpreted from a chemical perspective as shown for the discussed examples,[111] their complexity further increases for 3D systems and thus a detailed analysis is rarely attempted.[105] A more popular alternative are density of states (DOS) plots, in which the energy axis of the band structure is divided into small intervals of equal size. Now, the number of energy eigenvalues falling into each interval are counted for all $\vec{k}$ in the IBZ and the respective numbers are plotted and connected to each other to obtain a curve,[111] generally in a smoothed manner by representing every point by, e.g., a Gaussian function.[105] In a DOS plot, the dependence on $\vec{k}$ and thus on the reciprocal space is lost, allowing for a simplified overview of the electronic structure of the investigated material. The generation of the DOS plot from one band is shown exemplarily in Fig. 2.11. The small slopes at both ends of the depicted band correspond to a high number of energy eigenvalues per interval and thus two peaks arise at these positions in the DOS plot. Accordingly, the steep slope at the center of the band results in smaller DOS values. From this, it follows that bands with strong dispersion correspond to broad peaks and bands with low dispersion to narrow peaks in the DOS.[105,111]

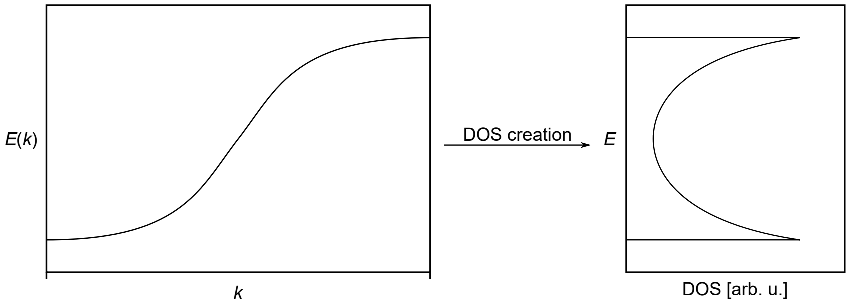

Figure 2.11: Creation of the DOS plot for a single band. Created based on Ref. [111].

2.2.1.3 Band Folding and Peierls Distortion

Going back to the 1D example of s orbitals, if the structure is unchanged but the unit cell size is now doubled to $2a$ and thus contains 2 s orbitals, i.e., a supercell is created, an effect called band folding occurs in the band structure as depicted in Fig. 2.12. Doubling the lattice parameter a in real space results in the lattice parameter b of the reciprocal space, which is also the length of the first BZ, being halved from $\frac{2\pi}{a}$ to $\frac{2\pi}{2a} = \frac{\pi}{a}$. Accordingly, the length of the IBZ is also halved from $\frac{\pi}{a}$ to $\frac{\pi}{2a}$, resulting in the k-axis of the band structure for the supercell being only half the length of the original band structure. Doubling of the real space unit cell allows two possibilities of linearly combining the two s orbitals inside the supercell itself, namely a bonding σ and an antibonding σ^* combination. Each of these give rise to one band as shown on the right side of Fig. 2.12. However, since the overall system is unchanged, the two bands combined give exactly the same energies and contain the same linear combinations of s orbitals as the band of the system with the original unit cell size. This is easily understandable by the folding process depicted in the center of Fig. 2.12 and is transferable to further multiplications of the real space unit cell size.[105,111,115] The limiting case would be the whole crystal fitting inside one unit cell, resulting in the band structure collapsing to an MO diagram without dependence on k since there are no neighboring unit cells available to form different linear combinations between their orbitals. Understanding the process of band folding allows for a better interpretation of band structures since it corresponds to one electronic unit being present more than once inside a unit cell.[111]

Up to this this point, the creation of the supercell and folding of the bands seems to be redundant. However, it allows the orbitals or atoms inside to be less constrained by translational symmetry. In the case of the minimal unit cell, movement of the s orbital inside a reference unit cell does not affect the electronic structure since the positions of all other s orbitals are changed accordingly. If instead two s orbitals are present inside one supercell, they can,

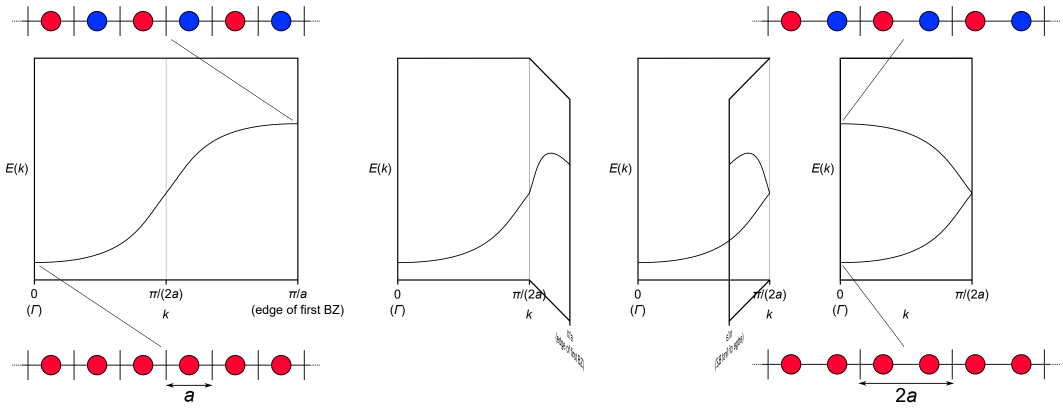

Figure 2.12: Band folding upon duplication of the unit cell for a periodic 1D chain of s orbitals. Created based on Ref. [111].

e.g., move towards each other, resulting in a different band structure. As the chemist can easily imagine, this is exactly what happens when the s orbitals receive a proton and an electron each: at ambient pressure, rather than an infinite chain of H atoms, H_2 molecules are formed. As Fig. 2.13 illustrates, this can also be explained by the corresponding band structures. For the case of equally spaced H atoms, there are two electrons per supercell but each of the two s/σ orbitals can be occupied by two electrons each. Accordingly, the energetically lower σ band will be almost fully occupied, while the energetically higher σ^* band is almost fully unoccupied, indicated by the Fermi level E_F located exactly at the contact point of both bands. As apparent from Fig. 2.13, two degenerate linear combinations are present at $k = \frac{\pi}{2a}$, only differing by a translation in their phase, which have to share the last two electrons available, thus being singly occupied each (in a single-configurational picture). From the perspective of the minimal unit cell, the non-folded band would be cut in half by the Fermi energy level, corresponding to a metallic system with a partly filled band. To overcome this energetically unfavorable situation, the two H atoms inside each unit cell move towards each other to form H_2, resulting in the opening of a band gap E_g by stabilizing the σ and destabilizing the σ^* band, removing the singly occupation and overall lowering the energy of the system. This sacrifice of translational symmetry for energetic stabilization is called Peierls distortion, which is the solid-state analogue of the JT effect and very important for understanding the structure of solids. Since the synchronized movement of all atoms is basically a lattice vibration, namely a phonon, this process can be characterized as an electron-phonon coupling. The (de)stabilization is most pronounced for the region of the band structure around the originally degenerate linear combinations and less important for the bottom of the valence and the top of the conduction band.[105,111,115]

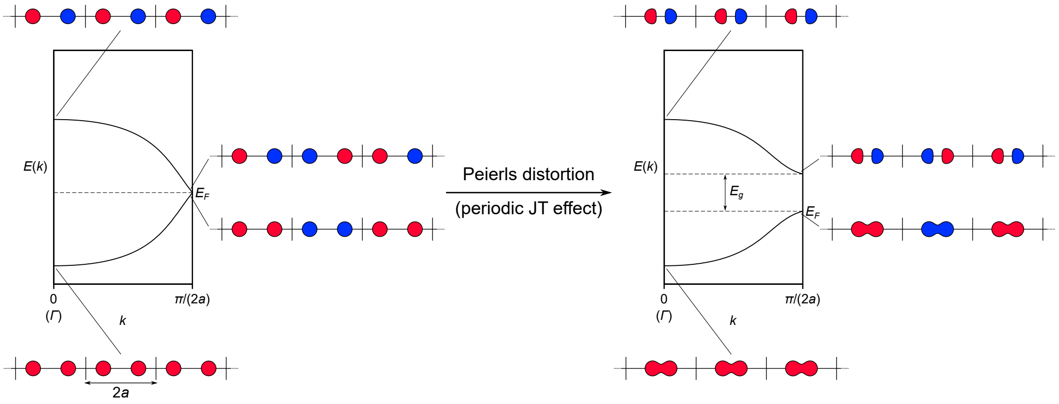

Figure 2.13: Influence of the Peierls distortion (periodic JT effect) on the band structure of a periodic 1D chain of H atoms. Created based on Ref. [111].

2.2.1.4 Hybridization of Bands

Besides the Peierls distortion, band gaps can also open up through hybridization of bands compatible in energy and symmetry. If the 1D chain of s orbitals is extended by p_x, p_y, and p_z orbitals located at the lattice points, this effect is observable as depicted in Fig. 2.14. Just like before, the s orbitals form a band of σ symmetry, being bonding at Γ ($k = 0$), nonbonding halfway through the IBZ ($k = \frac{\pi}{2a}$) and antibonding at the edge of the first BZ/IBZ ($k = \frac{\pi}{a}$). Assuming that the z-axis is parallel to the direction of the chain, the p_z orbitals also form a band of σ symmetry but with inverse trend compared to the s band. These pure pre-hybridization bands, indicated by gray dotted lines, cross near $k = \frac{\pi}{2a}$ and due to similar symmetry and energy are able to hybridize. The degenerate p_x and p_y bands, on the other hand, are of π symmetry and can accordingly not hybridize with the s and p_z bands and also not with each other due to their orthogonality. The hybridization of the s and p_z bands leads to one σ and one σ^* band, the former starting with the fully bonding linear combination of only s orbitals at $k = 0$ and ending with the fully bonding linear combination of only p_z orbitals at $k = \frac{\pi}{a}$, the latter starting with fully antibonding p_z and ending with fully antibonding s orbital linear combinations.[105,115,119] It should be noted that this swapping of orbitals within the hybrid bands is caused by the crossing of the pure bands but is not mandatory for hybridization itself, which only requires sufficient energetic proximity and matching symmetry.[105,115] Furthermore, it can be shown that the bands

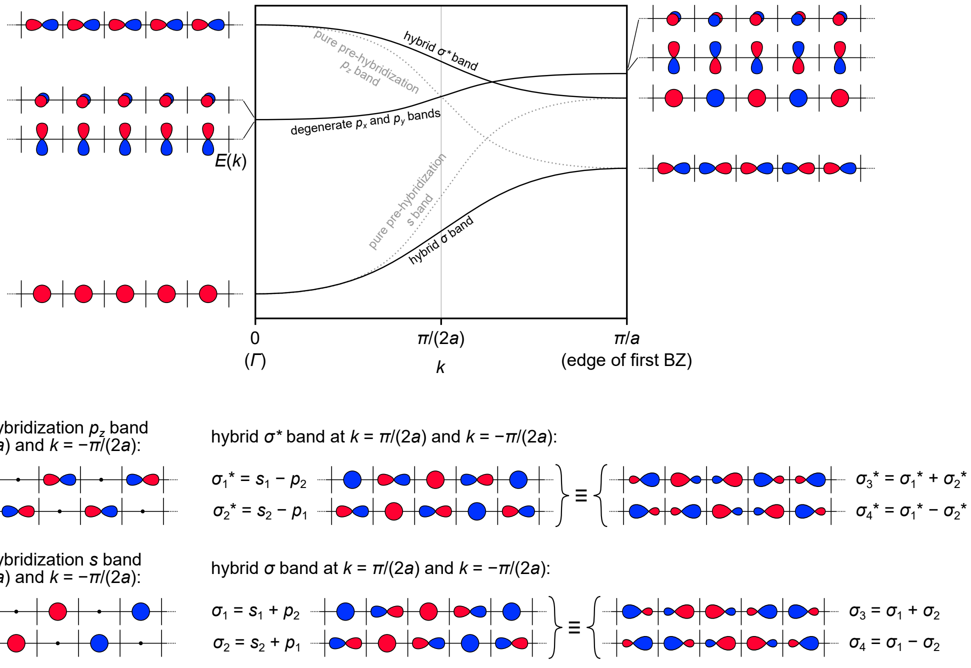

Figure 2.14: Hybridization of bands for a periodic 1D chain of s and p orbitals. The linear combinations s_1, s_2, p_1, and p_2 at the bottom left are created in the same fashion as depicted in Fig. 2.8. The normalization constants of the σ and σ^* linear combinations are ignored for the sake of clarity. Created based on Refs. [105, 115, 119].

hybridize through the whole first BZ except at the center and at the edges, where they remain pure.[105,115] Here, the term pure does not mean that the bands at these $\vec{k}$-points are exclusively constructed from one kind of AOs since they can also be constructed from MOs,[105] as will be observable in the results of Chapter 3.

What the hybridization halfway through the IBZ at $k = \frac{\pi}{2a}$ actually looks like in detail is depicted at the bottom of Fig. 2.14. As was shown before in Figs. 2.8 and 2.9, by linearly combining the complex Bloch functions at k and $-k$, the purely real and fully nonbonding linear combinations for the pure pre-hybridization s and p_z bands can be obtained, labeled as s_1, s_2, p_1, and p_2. As apparent, s_1 and p_2 as well as s_2 and p_1 perfectly complement each other since they fill each others orbital gaps responsible for their nonbonding character. Accordingly, the respective linear combinations result in the bonding hybrid σ_1 and σ_2 as well as antibonding hybrid σ_1^* and σ_2^* linear combinations, which cause the energy splitting at $k = \frac{\pi}{2a}$ in the band structure. Further linear combinations among σ_1 and σ_2 as well as σ_1^* and σ_2^* allow a representation with only sp hybrid orbitals (σ_3, σ_4, σ_3^*, and σ_4^*), also fitting the common picture of hybridization in MO theory.[119]

2.2.1.5 Periodic Slab Models and Projected Bulk Band Structure

While an infinite bulk crystal is periodic in all three dimensions, a surface corresponds to losing the periodicity in the direction of the surface normal,[108,120] resulting in an infinite vacuum on one side and an infinite crystal on the other side of the surface. Accordingly, the unit cell also would need to be of infinite size in this direction, thus containing an infinite number of atoms and breaking the PBCs. Since such systems are obviously not feasible for electronic structure calculations, an alternative approach is to still employ PBCs along all basis vectors of a 3D unit cell and place a finite number of atomic layers of the surface to be investigated inside, the so-called periodic slab model, as depicted exemplary for the Si-terminated 3C-SiC(001)-p(2×1) reconstruction in Fig. 2.15a). Generally, there are two possibilities for slab models available, namely a symmetric or an asymmetric slab model. In case of a symmetric slab model, the middle layers are kept fixed during geometry optimization, resulting in the description of one surface on each side of the slab. To reduce the computational effort, mirror symmetry can be exploited in symmetric slab models if the crystal structure allows this. For example, the 3C-SiC(001) surface to be investigated in this work consists of helical building blocks (see Fig. 1.3) and is thus not suitable for mirror symmetry. Alternatively, a smaller asymmetric slab model can be utilized, in which only a few bottom layers are kept fixed.[108] It is often reasonable to saturate such asymmetric slabs with H atoms, as depicted in Fig. 2.15a), to avoid the presence of spurious unsaturated dangling bonds.[45,121] To now prevent the surfaces of neighboring unit cells from interacting with each other while applying PBCs, a sufficiently sized vacuum region has to be added above/below the layers.[105,108,120] While in elec-

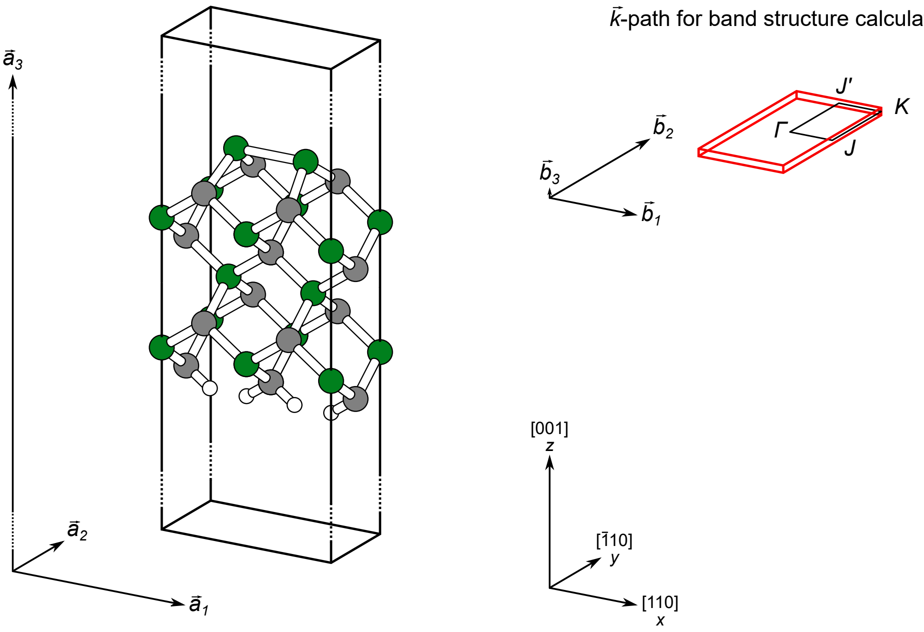

a) real space p(2×1) surface unit cell

b) corresponding reciprocal space surface unit cell/first SBZ and $\vec{k}$-path for band structure calculations

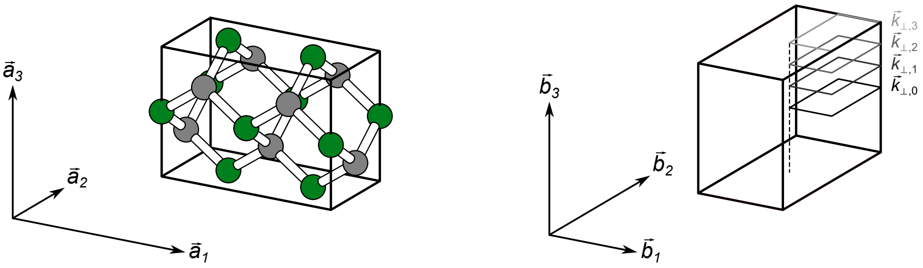

c) underlying orthorhombic real space bulk unit cell

d) corresponding underlying reciprocal space bulk unit cell with surface $\vec{k}$-paths at different $\vec{k}_\perp$-values for the calculation of the PBBS

e) generation of an arbitrary PBBS

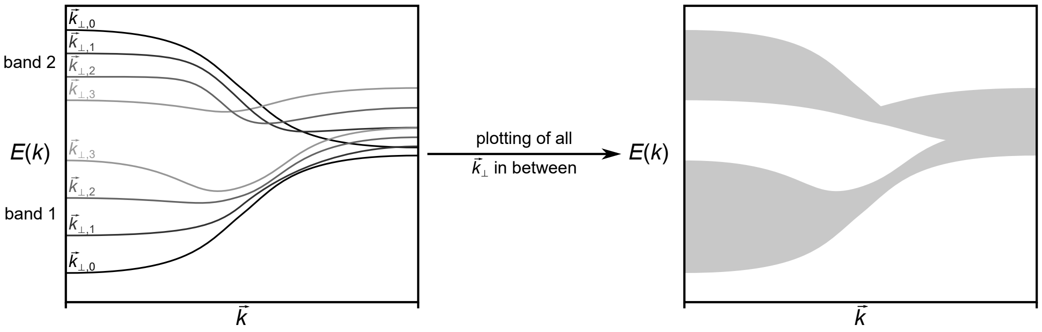

Figure 2.15: a–d) Real and reciprocal space surface and bulk unit cells of the Si-terminated 3C-SiC(001)-p(2×1) reconstruction (SD model) to illustrate the generation of the e) PBBS. The generation of the actual PBBS for this system is additionally depicted in Fig. A.8.

tronic structure codes employing plane wave basis functions like VASP[122,123] this vacuum region also adds to the computational cost, this is not the case for programs utilizing atom-centered basis functions like the CRYSTAL17[84] program used in this work. Accordingly, the lattice parameter parallel to the surface normal is generously set to 500 Å by default for surface unit cells in the latter program.[124] As was already indicated in Section 2.2.1.3, lengthening of a real space basis vector results in the shortening of the corresponding reciprocal space basis vector,[108] hence $\vec{b}_3$ of the reciprocal space surface unit cell associated with the real space basis vector $\vec{a}_3$ is very short (Fig. 2.15a) and b). Now, the depicted $\vec{k}$-path for the band structure of the surface slab is restricted to the directions of $\vec{b}_1$ and $\vec{b}_2$ and does not contain portions of this very short $\vec{b}_3$. This is consistent with the model surface with an infinitely large $\vec{a}_3$ and thus $\vec{b}_3$ being zero, corresponding to no dependence on $\vec{k}$ in this direction because there are simply no neighboring unit cells available to form different linear combinations. But also for the slab model with PBCs and hence neighboring unit cells being present, this 2D $\vec{k}$-path is appropriate since the vacuum layer prevents overlap between orbitals of neighboring unit cells along $\vec{a}_3$, resulting in a dispersionless band along $\vec{b}_3$ and thus making its analysis redundant in the third dimension.[108]

While the electronic structure of the surface is generally different from the bulk due to the missing periodicity and unsaturated surface atoms and is consequently of high interest, it still represents just a very small fraction of the whole crystal. This is also the reason why the application of PBCs simulating an infinite crystal is reasonable in the first place because the perturbation of the surface of a real finite crystal on the bulk properties is usually very small.[105,106] Accordingly, the main contribution to the electronic and thus band structure is coming from the bulk. This would be included in the band structure of the model surface with an infinite number of atoms but not by the finite slab models only containing a small number of surface layers and no bulk atoms. To account for this shortcoming of the slab models, the so-called projected bulk band structure (PBBS) can be calculated and plotted in addition to the band structure of the surface slab.[120,125] Basically, the PBBS is just the band structure of the bulk material but not evaluated for the $\vec{k}$-path in the first BZ/IBZ of the conventional unit cell. Instead, a bulk unit cell is created matching the size and alignment of the investigated surface unit cell so that it could, in principle, be placed seamlessly underneath. For the example of the p(2×1) reconstruction in Fig. 2.15, the corresponding orthorhombic real space bulk unit cell is shown in c), with the basis vectors $\vec{a}_1$ and $\vec{a}_2$ being identical to the surface unit cell. $\vec{a}_3$ is still parallel to the corresponding vector in the surface unit cell but significantly shorter, namely 4.36 Å, which is the lattice parameter of the conventional bulk unit cell (see Figs. 1.2 and 1.3). Accordingly, the basis vector $\vec{b}_3$ in the corresponding reciprocal space bulk unit cell in d) is longer than in the reciprocal surface unit cell in b). Furthermore, in contrast to the surface unit cell, the orbitals of the bulk unit cell are obviously able to form linear combinations with neighboring unit cells also in the direction of $\vec{a}_3$, which is why the band structure has to be evaluated along $\vec{b}_3$. To be able to simultaneously plot the band structure of this reciprocal bulk unit cell d) and the reciprocal surface unit cell b), the same $\vec{k}$-path of the latter has to be calculated in the former. But due to the additional dependence along $\vec{b}_3$, the $\vec{k}$-path has to be calculated at different $\vec{k}$-values along this vector as indicated in d), denoted as $\vec{k}_\perp$ because of their orthogonal alignment with respect to the surface. One can interpret each point in the $\vec{k}$-path of the reciprocal surface unit cell as a rod reaching into the "underlying" reciprocal bulk unit cell.[120,125] In this particular case of the 3C-SiC(001) surface, it is sufficient to only calculate the $\vec{k}$-paths halfway along $\vec{b}_3$ as a result of the symmetry of the bulk. For an arbitrary example, the two bands for the same $\vec{k}$ path at four different $\vec{k}_\perp$-values are plotted, all showing different curvature. If now all possible $\vec{k}_\perp$-values are evaluated and plotted at the same time, the PBBS is obtained, in which the individual bands are not distinguishable anymore. If now the band structure of the surface slab is plotted additionally, it is easily discernible if there are bands located within the band gaps of the PBBS, hence corresponding to surface states deviating from the bulk states. Often, these surface states also reach into the PBBS and thus hybridize with the bulk states, resulting in so-called surface resonances.[120,125] For the creation of the actual PBBS of 3C-SiC, see Fig. A.8.

When plotting the surface band structure and the PBBS simultaneously, a reasonable energetic alignment has to be considered.[126] It is easily imaginable that the atoms of the slab models feel a substantially different chemical environment than the bulk atoms due to the small number of layers. This can result in different total energies of supposedly equal states of both system and a large offset between both band structures. To try to account for this problem in this work, the lowest energy eigenvalues, i.e., the Si 1s core levels, are averaged for the most inner and thus most bulk-like Si atoms. Then, the whole surface band structure, including the Fermi energy, is shifted in a way that these averaged Si core levels match the Si core levels of the bulk atoms in the PBBS (more details are given in Section 3.2.1). This strategy was inspired by the work of Sagisaka et al. covering a similar problem, namely the comparison of the energy levels of differently sized slab models.[127] However, it should be noted that, as indicated in the work of Bechstedt and Furthmüller,[126] there seem to be different possible strategies for the alignment of surface slab band structures and the PBBS, albeit unfortunately not described in the textbooks[120,125] or publications[35,39,43–45,47,126] considered in this work, in which the topic of the PBBS is treated.

2.2.1.6 $\vec{k}$-Point Sampling

As was pointed out in the previous sections, for an infinite lattice there are an infinite number of possible $\vec{k}$-values inside the first BZ/IBZ. At each of these, there are a finite number of COs, depending on the number of AO basis functions. The shape of the COs has to only be determined inside one unit cell instead of the whole crystal. Accordingly, the usage of Bloch functions transforms the infinitely sized problem of the whole infinite crystal into an infinite number, namely at each $\vec{k}$, of finitely sized problems. While this might not seem like a big advantage in the first place, the energy eigenvalues of the COs/bands generally show a smooth dependence on $\vec{k}$. Thus, it is sufficient to only solve the TISE for a small selection of wave vectors $\vec{k}$, which can geometrically be interpreted as a $\vec{k}$-point grid in the first BZ/IBZ.[106,113] Recalling that Bloch functions of different wave vectors $\vec{k}$ are orthogonal to each other, the Roothaan-Hall equations (for the closed-shell case) can be solved independently for each $\vec{k}$-point:[106]

$$\mathbf{F}(\vec{k})\mathbf{C}(\vec{k}) = \mathbf{S}(\vec{k})\mathbf{C}(\vec{k})\boldsymbol{\varepsilon}(\vec{k}) \tag{2.111}$$

The most common method of constructing the $\vec{k}$-point grid is the scheme proposed by Monkhorst and Pack.[128] Here, a $q_1 \times q_2 \times q_3$ Monkhorst-Pack grid corresponds to the reciprocal space basis vectors $\vec{b}_1$, $\vec{b}_2$, and $\vec{b}_3$ being divided into q_1, q_2, and q_3 equally spaced segments, respectively, overall resulting in a division of the reciprocal space unit cell into multiple identical subcells with one $\vec{k}$-point in each center.[128] Depending on the integers q_1 to q_3 being odd or even, the Γ-point is excluded from a fully even $\vec{k}$-point grid and included in a $\vec{k}$-point grid being sampled by an odd number of $\vec{k}$-points for at least one reciprocal basis vector, as depicted in Fig. 2.16a) and b) for the example of the 2D square lattice discussed before, respectively. After acknowledging the physical meaning of the Γ-point in the previous sections, one might think that considering this high-symmetry $\vec{k}$-point is important because it resembles linear combinations of orbitals with the same phase between neighboring unit cells, often corresponding to band maxima or minima,[113] as apparent in the examples shown before in Fig. 2.9. This physical importance does not only concern the Γ-point but all high-symmetry $\vec{k}$-points in general, which are also not included in the Monkhorst-Pack scheme since they are located on the BZ

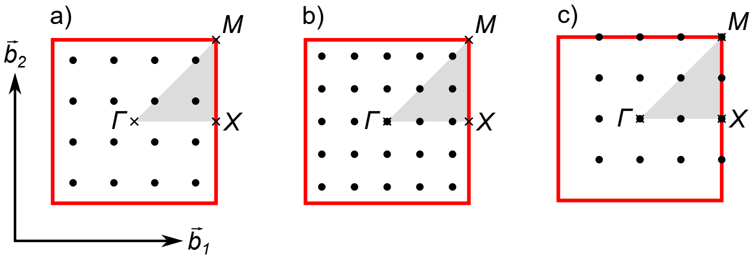

Figure 2.16: a) 4×4, b) 5×5, and c) Γ-centered 4×4 Monkhorst-Pack $\vec{k}$-point grids (black dots) in the first BZ (red) of a 2D square lattice. The IBZ is shaded in gray.

edges. A solution to this are the so-called Γ-centered Monkhorst-Pack $\vec{k}$-point grids as depicted in Fig. 2.16c), which include these high-symmetry $\vec{k}$-points. However, it has to be noted that Γ-centering is only possible for fully even $\vec{k}$-point grids because grids with already only one oddly sampled basis vector are always centered at Γ.

Still, from a computational efficiency perspective, generally even $\vec{k}$-point grids are preferred since less $\vec{k}$-points are located on symmetry planes or axes. If a $\vec{k}$-point is located on these symmetry elements, it gets mapped onto itself for the respective symmetry operation. Accordingly, symmetry cannot be exploited for these high-symmetry $\vec{k}$-points, resulting in an overall higher number of $\vec{k}$-points being needed to sample the IBZ.[108,113] The different efficiency of the introduced $\vec{k}$-point grid types is exemplarily indicated in Fig. 2.16, where 18.75 % of the $\vec{k}$-points are located in the IBZ (gray area) for the even $\vec{k}$-point grid, 24 % for the odd and 37.5 % for the Γ-centered grid. Accordingly, the general suggestion for electronic structure calculations is to use an even $\vec{k}$-point grid for self-consistent calculations and only contain the high-symmetry $\vec{k}$-points in consecutive non-self-consistent calculations for, e.g., DOS or band structure analysis.[113] However, the program package CRYSTAL17[84] used in this work always employs Γ-centered $\vec{k}$-point grids, which is why this suggestion was ignored.

As one would expect, the higher the number of $\vec{k}$-points, i.e., the denser the $\vec{k}$-point grid, the more accurate the solution of the TISE gets.[108,113] How high this density has to be can change with the system or the accuracy to be achieved. For example, metals generally require a more dense $\vec{k}$-point grid than semiconductors or insulators. But also surface states of the latter can exhibit metallic character, requiring denser $\vec{k}$-point sampling.[113] Nevertheless, the $\vec{k}$-point density is obviously dependent on the (inverse) volume of the reciprocal unit cell. Accordingly, if one has decided on a sufficient $\vec{k}$-point density for a certain system and unit cell volume, for consistency it is reasonable to use the same density for all supercells.[108] Since enlarging the unit cell in real space results in a reduction of the reciprocal unit cell size, a smaller $\vec{k}$-point grid can be employed in this case. This is apparent in Fig. 2.17, where the different Γ-centered Monkhorst-Pack grids employed for the surface supercells of this work are depicted, ensuring a constant $\vec{k}$-point density. For example, when going from a 1×1 to a 2×1 supercell, the $\vec{k}$-point grid has to be halved just like the corresponding reciprocal space vector, i.e., from 12×12×1 to 6×12×1. Also from a physical perspective, this $\vec{k}$-point grid reduction is reasonable since, as apparent from the example of band folding in Section 2.2.1.3, enlarging the unit cell results in multiple electronic units being present. These form different linear combinations inside the supercell, thus in a sense already doing a part of the work that the different wave vectors $\vec{k}$ are supposed to do, justifying the inclusion of less $\vec{k}$-points. Besides consistency reasons, computational cost can also be reduced in this way without generally changing the accuracy of the calculations.[108] Further details and examples regarding the reciprocal space surface supercells and the $\vec{k}$-point grids employed in this work are given in Appendices A.1.1 and A.1.2.

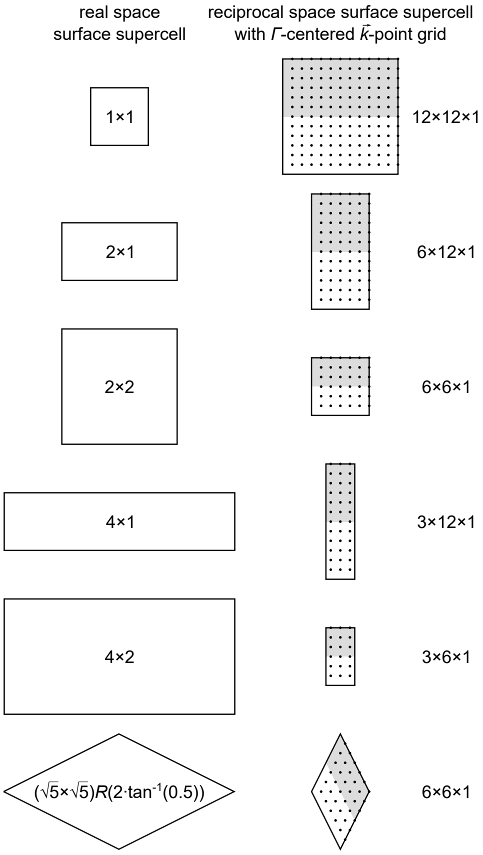

Figure 2.17: Geometric relation of the real and reciprocal space surface supercells with constant $\vec{k}$-point density for the Γ-centered Monkhorst-Pack grids used in this work. The irreducible part of the reciprocal space surface unit cell in case of the imposed $P1$-symmetry is shaded in gray.

2.2.2 Cluster Models

Unfortunately, most post-HF and especially the multiconfigurational methods to be used in this work and presented in Section 2.1.2 are not available in combination with PBCs. Though there have been recent developments for, e.g., periodic CC[129] or CASSCF,[130] the most common and efficient approach is to represent the bulk or surface of interest by a small cutout of atoms, the so-called cluster model, which can then be described with the discussed methods implemented in standard molecular electronic structure codes.

The most simplistic cluster model is a free cluster, which directly uses the aforementioned cutout for the respective calculations. While such cluster models can be created easily and their convergence can, in principle, be checked systematically by increasing the size, the high percentage of surface atoms generally causes slow convergence with cluster size, especially of bulk properties. Local properties like adsorption energies/geometries or defect energies, on the other hand, converge faster, particularly properties that are free of charge generation/transfer. Still, since multipoles are additive, they increase with the size of the cluster model and thus possibly prevent the convergence of certain properties.[131] Furthermore, free clusters are lacking the influence of the remaining virtually infinite crystal surrounding them. To account for this, so-called embedded cluster models can be constructed. In case of covalent crystals, a molecular mechanics (MM) environment can be applied to the free cluster, corresponding to moveable host atoms being placed at the positions of the surrounding crystal. These host atoms are connected to each other and the quantum cluster by force constants adjusted to reproduce the mechanical conditions in the investigated system calculated with PBCs.[132] For ionic crystals, it is more common to replace the host atoms by static point charges to account for the long-range Coulomb interactions.[131,132] While simply using the formal charges has proven to be reasonable for strongly ionic systems, for partly covalent crystals this choice is less obvious since theoretical and experimental methods for determining the effective charges can deviate quite strongly.[131] To prevent electron density from flowing towards the positive charges of the point charge field, an additional embedding layer consisting of effective core potentials can be inserted in between.[131,132]

However, these embedding approaches are not feasible for metals since the corresponding quantum clusters suffer from quantum size effects due to the inability of describing the usual strong delocalization of the electrons in metals, thus severely altering the properties compared to the calculations with PBCs. Accordingly, more advanced periodic embedding potentials derived from, e.g., DFT calculations are required.[131,133–136] But also the embedded quantum clusters of covalent systems suffer from dangling bonds arising at the cluster edges as a result of cutting it out of the periodic system. These unsaturated and, in principle, singly occupied dangling bonds often manifest as spurious states within the band gap, causing problems especially for multiconfigurational calculations. To account for this within the embedded cluster approach, Gerhards and Klüner recently developed an anionic quantum cluster for TiO_2, in which the additional electrons fill the singly occupied dangling bonds.[137] For covalent and weakly ionic systems, an alternative to the embedding scheme are saturated cluster models. Here, the dangling bonds are saturated by monovalent pseudo atoms, whose parameters are fitted to obtain a saturated bond with properties as close as possible to the bond originally present in the periodic crystal. An even simpler and often sufficient approach is the saturation with H atoms, similar to the periodic slab models presented in Fig. 2.15. Even though the electronegativity of H most of the time is different from the atom it represents, thus resulting in an artificial dipole layer at the cluster edges, H-saturated cluster models generally perform well for adsorption phenomena.[131,132] However, with the knowledge about the electronic structure of solids of Section 2.2.1 in mind, it is easily imaginable that cluster models, embedded or saturated, are generally not able to recover the band structure due to the limited number of unit cells and thus linear combinations between the orbitals of these, which is why, e.g., the band gap converges very slowly with cluster size.[132] Accordingly, all of the presented cluster models need careful investigation regarding convergence with respect to their size, shape, and properties of interest.[131]

3 Results and Discussion

In this chapter, the theoretical results of this work are presented, starting with a qualitative in-depth analysis of the surface state band structure of the investigated Si-terminated 3C-SiC(001) surface. Afterwards, the single-configurational results utilizing PBCs are presented, shortly discussing the calculations regarding the bulk structure of 3C-SiC, then focusing on the aforementioned surface and bringing the results into the context of published experimental and theoretical studies. In the last section, the high-level multiconfigurational cluster model calculations of the Si-terminated 3C-SiC(001) surface are presented and compared to the preceding single-configurational findings.

The most relevant results of this work can also be found in the following publication:

N. Thoben, T. Klüner, *J. Phys. Chem. C* **2023**, *127*, 23475–23488.
DOI: 10.1021/acs.jpcc.3c06305

3.1 Surface States of the Si-terminated 3C-SiC(001) Surface

Before presenting the computational results of this work, a closer qualitative look at the surface states of the Si-terminated 3C-SiC(001) surface is taken to better understand the calculations following afterwards. When the (001) surface is cut from the 3C-SiC bulk, in an intuitive picture this also results in bisecting the bonds of the SiC tetrahedra at the position of the surface plane. Accordingly, two singly occupied sp^3 dangling bond surface states are present at each Si surface atom and thus in each unit cell of the ideal p(1×1) surface as depicted on the left side of Fig. 3.1. As further apparent, this situation violates the C_{2v}-symmetry of the system, which is why these sp^3 dangling bonds dehybridize to the actual eigenfunctions being one sp^2 dangling bond (D) perpendicular and one bridging (Br) p_x orbital parallel to the surface plane. The same situation occurs at the closely related Si(001) surface, where the D state is stabilized relative to the Br state due to its s character.[28,45,138] From a chemists perspective, this electronic structure is equivalent to the frontier orbitals of silylenes, whose ground state generally is a singlet with a doubly occupied sp^2 and an empty p orbital.[139,140] At the surface, however, the orbitals of neighboring unit cells can overlap to form bands, resulting in a more complex electronic structure. LDA calculations of the ideal Si(001)-p(1×1) surface pre-

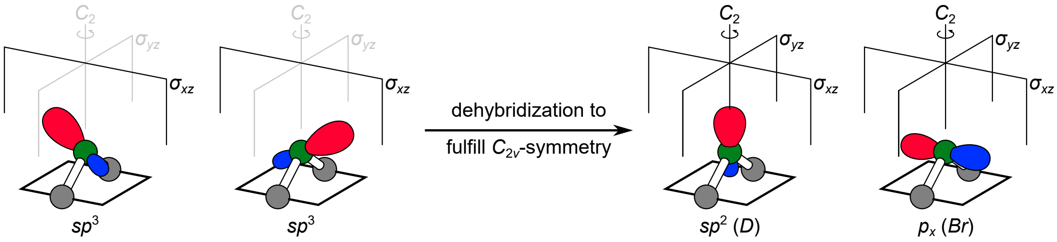

Figure 3.1: Dehybridization of the two sp^3 surface state orbitals to one dangling bond (D) sp^2 and one bridging (Br) p_x orbital at the ideal Si-terminated 3C-SiC(001)-p(1×1) surface to fulfill the C_{2v}-symmetry of the system.

dict a metallic character, while the 3C-SiC(001) counterpart is supposed to be semiconducting,[45,138] presumably caused by the differing lattice constants and thus stronger overlap between neighboring unit cells in case of 3C-SiC(001). However, as indicated in Chapter 1, single-configurational calculations might not be able to correctly describe the predicted multiconfigurational character of these surfaces. This could already be confirmed by Paulus for the Si(001) case by MCSCF calculations on a cluster model containing four surface Si atoms arranged in a square giving averaged NOONs in the range of 1.5 to 0.5 and multiple configurations in the wave function exhibiting coefficients greater than 0.1, hence questioning the LDA results.[56] Furthermore, the conductivity cannot be verified experimentally because the ideal p(1×1) surface of both systems is not observable due to reconstruction taking place immediately. Still, a correct description of this surface is important for the calculation of reasonable reconstruction energies, for which its energy is needed as reference.

Since in the multiconfigurational cluster model calculations to be employed in Section 3.3 an active space has to be selected manually, a detailed understanding of the surface state band structure is necessary, which is proposed qualitatively in Fig. 3.2. Because the p_x orbitals of the Br state are aligned in x-direction, the strongest interaction between these orbitals of neighboring unit cells and thus the strongest dispersion of the associated bands is expected in the corresponding $\mathit{\Gamma}-J$-section of the $\vec{k}$-path as apparent from the depicted first SBZ. Overlap in y-direction is presumably negligible for the Br state and in all directions for the sp^2 orbitals of the D state due to the small spatial extension in both directions of the latter, which is why other sections of the $\vec{k}$-path are ignored here. The pure pre-hybridization band (dotted gray line) of the D state accordingly shows presumably small dispersion with slightly lower energy at $\mathit{\Gamma}$ with the same phase in all unit cells than at J with alternating phases. The pure pre-hybridization Br band, on the other hand, exhibits strong dispersion with high energy at the $\mathit{\Gamma}$-point due to a fully antibonding linear combination and low energy for the fully bonding linear combination at J. It is reasonable to expect the latter to be energetically close to, and in this case slightly lower than, the fully "bonding" situation of the D state, resulting in a crossing of both pure pre-hybridization bands. Since both bands have a σ-like electronic structure connecting the surface Si atoms, they are of matching symmetry and can hybridize to open up a band gap just like in the

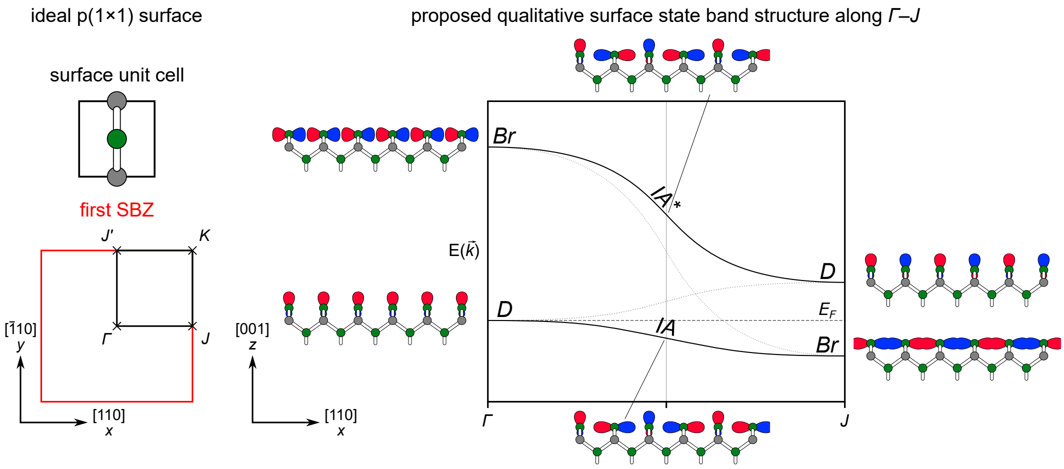

Figure 3.2: Surface unit cell, first SBZ, and proposed qualitative surface state band structure along the $\Gamma - J$-path with corresponding linear combinations of the surface states between neighboring unit cells of the ideal Si-terminated 3C-SiC(001)-p(1×1) surface. The pure pre-hybridization bands are implied by gray dotted lines. The linear combinations of the hybrid bands in the middle of the band structure plot are created according to the example in Fig. 2.14.

previous example of Fig. 2.14. The corresponding hybrid linear combinations consisting of alternating sp^2 and p_x orbitals halfway through the $\Gamma - J$-section show the nature of this hybridization with the lower band being of bonding and the upper band of antibonding character. Accordingly, the crossing and hybridization of the bands makes labeling them as D and Br bands, as is done in the literature,[45] imprecise, which is why in this work they are denoted as bonding interatomic (IA) and antibonding interatomic (IA^*) bands. Since there are two electrons per unit cell available for the two surface states, the IA band is fully occupied and the IA^* band is empty as indicated by the Fermi energy level E_F. The actual calculated band structure with the depiction of the COs of both bands to illustrate the energetic swapping of the orbitals with $\vec{k}$ is shown in Fig. A.9.

Decreasing the translational symmetry of the system by enlarging the unit cell from 1×1 to 2×1 allows the formation of Si dimers and thus leads to the Si-terminated 3C-SiC(001)-p(2×1) reconstructed surface, for which the two Si atoms of each unit cell have to move towards each other. Restricting the attention to the isolated Si dimers at first as depicted in the qualitative MO diagram of Fig. 3.3, a rehybridization of the D and Br surface states to two degenerate sp^3 orbitals is reasonable to enhance the overlap for the formation of a σ bond between the two Si atoms. The driving force for the dimerization thus is to reduce the number of energetically unfavorable singly occupied dangling bonds. Accordingly, the strongly split σ- and σ^*-like surface states arise. The remaining two possible linear combinations of the two sp^3 orbitals facing away from each other result in the almost degenerate π- and π^*-like surface states still exhibiting dangling bond character at each dimer atom. With a total of four electrons for one dimer, assigning the occupation numbers two and zero to the σ and σ^* orbitals, respectively, is straight forward. However,

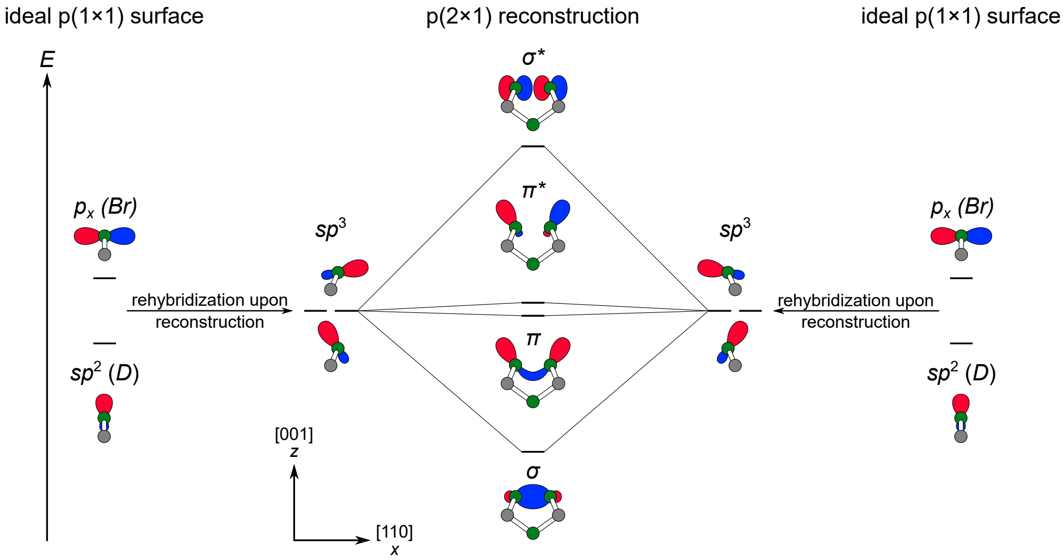

Figure 3.3: Qualitative MO scheme of the surface states of one Si dimer of the Si-terminated 3C-SiC(001)-p(2×1) reconstructed surface (SD model). A total of four electrons are present, which are not shown due to the multiconfigurational character of the system. Reprinted with permission from *J. Phys. Chem. C* 2023, 127, 48, 23475–23488. Copyright 2023 American Chemical Society. Modified and extended. Created based on CAS(4,4) NOs from Ref. [53].

the two remaining electrons now have to be split among the almost degenerate π states, which is a similar situation as the statically correlated four-electron four-orbital example system discussed before in Fig. 2.4. Accordingly, it is easily imaginable for the configurations [2200], [2020], and [2110] to be of similar energy (occupation numbers in the order $[\sigma\pi\pi^*\sigma^*]$), indicating the necessity of a multiconfigurational approach for a correct description of the singlet ground state. In fact, Tamura and Gordon could confirm this with a CAS(4,4) calculation for a 1-dimer cluster model of the Si-terminated 3C-SiC(001)-p(2×1) reconstructed surface yielding NOONs of 1.98, 1.08, 0.92, and 0.02, concluding a fully diradical character of the dimer.[53] Single-configurational methods would by definition only consider the [2200] configuration in the restricted case or a strongly spin-contaminated singlet diradicalic [1100] + [1100] configuration (brackets representing α- and β-electron configurations) in the unrestricted case.

Since the ideal p(1×1) surface can be interpreted as a 2D array of silylenes, the p(2×1) reconstruction accordingly is the dimerization of these to yield disilenes.[141] The dimerization of such group 14 carbene analogues is well investigated. As depicted in Fig. 3.4a), singlet carbenoids are not able to dimerize when approaching each other with all substituents being in the same molecular plane due to the repulsion of the two doubly occupied sp^2 orbitals. In case of actual carbenes, which generally have a triplet ground state, this reaction is possible by recombination of the radicalic electrons to form one σ and one π bond and thus a planar alkene. Heavier group 14 carbene analogues with a singlet ground state have to tilt out of the molecular plane instead for

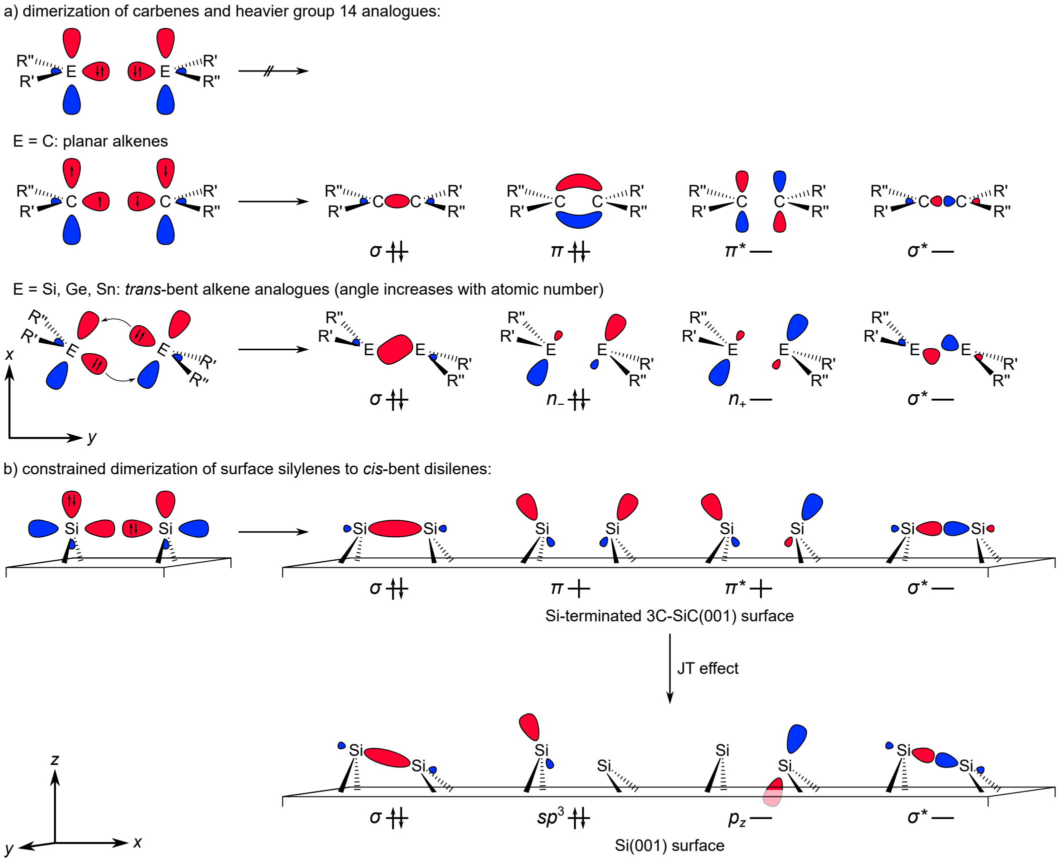

Figure 3.4: Comparison of a) the dimerization of molecular carbenes and heavier group 14 analogues to b) the constrained dimerization of surface silylenes. Created a) based on Refs. [139, 142–144] and b) based on Refs. [52, 53, 145].

the doubly occupied sp^2 orbitals to attack the empty p_x orbitals of the other molecule, resulting in the formation of *trans*-bent alkene analogues.[139,144,146] Consequently, the singlet-triplet energy gap of the carbenoids has proven to be a useful metric to predict the structure of the corresponding dimers, which are planar if the energy gain of the σ and π bonds is greater than twice the excitation energy and vice versa.[142,147] From an MO theory perspective, the bending flexibility can be attributed to the decreasing p_x orbital overlap and thus π bond strength in the planar structure when increasing the σ bond length upon going down group 14 in the periodic table.[146] In the literature,[143,144] the *trans*-bending is then rationalized by a second-order JT effect with respect to the planar situation, splitting the occupied and unoccupied MOs by σ+π^* and $\pi + \sigma^*$ mixing and resulting in an overall energetic stabilization of the whole molecule. While this is consistent from a symmetry perspective, the shape of the MOs does not quite clarify why the resulting nonbonding n_- and n_+ orbitals should split up since the reduced overlap should make them more degenerate and the additional s character should stabilize both of them. However, it is indicated that the mixing is somewhat more involved than described above[146] and hard to generalize for the whole group 14 due to the strong shifts in MO energies when exchanging the elements.[144] Nevertheless, disilenes often exhibit this *trans*-bent structure but, as the first of the heavier alkene analogues, only with small angles in the magnitude of about 10°.[139,143] Accordingly, the n_- and n_+ orbitals are not as nonbonding and degenerate as the exaggerated depiction in Fig. 3.4a) might indicate. This can be confirmed by a NEVPT2 optimization of Si_2H_4 with a CAS(4,4) and def2-TZVP[148] basis set yielding NOONs of about 1.84 and 0.16, respectively, in accordance with previous calculations by Windus and Gordon.[149] While this still corresponds to considerable multiconfigurational character with the [2200] and [2020] configurations amounting to about 91 % and 7 %, respectively, the responsible bending-angle of 34.6° for Si_2H_4 is comparatively large within the group of experimentally observed disilenes that are generally higher-substituted.[144] The latter are accordingly expected to show less multiconfigurational character.

Now, as apparent from Fig. 3.4b), the p(2×1) reconstruction at the ideal Si-terminated 3C-SiC(001)-p(1×1) and Si(001)-p(1×1) surfaces corresponds to a constrained dimerization of the surface silylenes. Here, instead of approaching each other with the sp^2 orbitals and within a shared molecular plane, each silylene is rotated by 90° so that the resulting dimer resembles a strongly *cis*-bent disilene with the same frontier orbitals already presented in the MO diagram of Fig. 3.3. Transferring the concept of reactivity of the molecular carbenoids with respect to the electronic ground state being either singlet or triplet to these surface silylenes is redundant since the constraint of being bound to the surface permits only one possible way for the dimerization to occur in the first place, namely the *cis*-bent route. Also, considering the band structure of the ideal p(1×1) surface discussed before, there is basically electron density present in the sp^2 and the p_x orbitals at the same time without excitation, as implied by the corresponding initial occupation of the silylenes in Fig. 3.4b). To the best of this work's author's knowledge, only one molecular *cis*-bent disilene with an angle of 3.6° has been found so far.[150] Just like on the 3C-SiC(001) and Si(001) surfaces, the *cis*-bending is imposed by two cyclic substituents each connecting both ends of the disilene, resulting in an overall bicyclo[3.3.0] structure of two five-membered Si rings. As apparent from Fig. 3.4b), the overlap within the π and π^* orbitals for *cis*-bent disilenes is supposedly even smaller than for the *trans*-bent counterparts since only the small orbital lobes of each sp^3-like orbital are facing each other. This increases the degeneracy and the partial multiconfigurational and thus diradicalic character already present in *trans*-disilenes. While the experimentally observed *cis*-bent disilene was unfortunately not further investigated theoretically to confirm this trend, a comparable but significantly more strongly *cis*-bent disilene, caused by exchanging three Si atoms with C atoms in each of the five-membered rings, exhibits NOONs of 1.32 and 0.68 in a CAS(4,4) calculation.[145] Since on the mentioned surfaces these five membered rings are further constrained by the incorporation into the crystal, the *cis*-angles are even more sharp as apparent from Fig. 1.4b), increasing the diradicality compared to the molecular case. This effect is more pronounced for 3C-SiC(001) due to its smaller surface lattice constant of 3.08 Å compared to the 3.84 Å of Si(001). Additional CAS(4,4) 1-dimer cluster calculations of the Si(001) surface of Tamura and Gordon confirm this with NOONs amounting to 1.71 and 0.29 for the π and π^* orbitals of symmetric dimers, contrasting the almost fully diradicalic NOONs of 3C-SiC acquired in the same study.[53] Paulus obtained similar results for MCSCF calculations on a Si(001) cluster model of two parallel symmetric Si dimers with averaged NOONs of 1.63 and 0.37.[56] Furthermore, due to the lower spatial constraints, Si(001) can undergo a JT splitting to asymmetric/buckled dimers and reduce the partial diradical character, resulting in a doubly occupied sp^3 orbital at the upper and an empty p_z orbital at the lower Si atom[50–52] in the limiting case of a single-configurational picture as shown at the bottom of Fig. 3.4b).

Nevertheless, since there are multiple dimers present at the Si-terminated 3C-SiC(001)-p(2×1) reconstructed surface, the MO-like surface states of neighboring unit cells can also overlap to form bands, possibly compensating the multiconfigurational character of the isolated disilene-like dimers. Just like in case of the ideal p(1×1) surface, the $\mathit{\Gamma}-J$-path of the corresponding first SBZ is supposedly showing the strongest dispersion, for which the proposed band structure is shown in Fig. 3.5. The σ and σ^* bands remain strongly split like the MOs of a single dimer and, if any, show small dispersion since there is negligible overlap between the orbitals of neighboring unit cells. The dangling bonds of the π and π^* orbitals, however, can reach neighboring unit cells, giving rise to a much more pronounced dispersion of the pure pre-hybridization bands depicted by gray dotted lines. At $\mathit{\Gamma}$, the π band is stabilized by the fully bonding interaction between neighboring dimers, while the π^* band shows fully antibonding character due to the opposite symmetry. This symmetry discrepancy causes an inverted situation at J, namely the π^* band being fully bonding

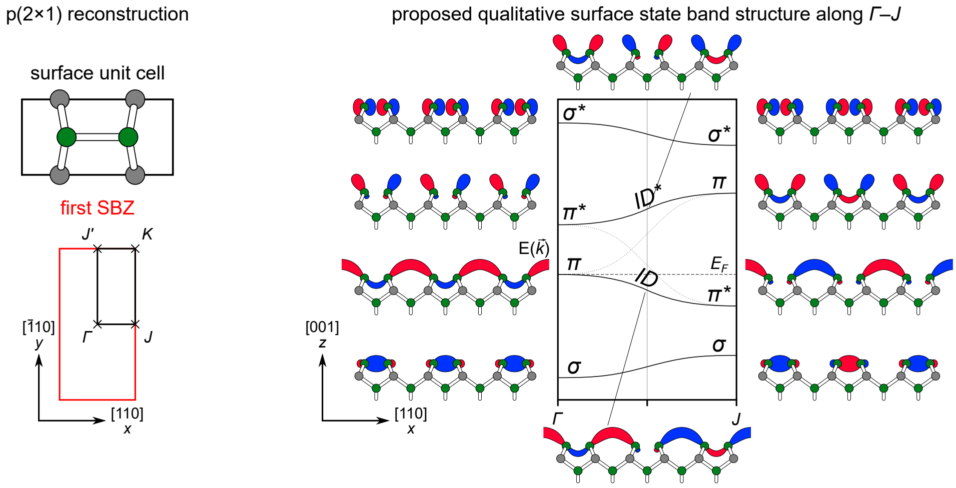

Figure 3.5: Surface unit cell, first SBZ, and proposed qualitative surface state band structure along the $\mathit{\Gamma}-J$-path with corresponding linear combinations of the surface states between neighboring unit cells of the Si-terminated 3C-SiC(001)-p(2×1) reconstructed surface. The pure pre-hybridization bands are implied by gray dotted lines. The linear combinations of the hybrid bands in the middle of the band structure plot are created according to the example in Fig. 2.14. Reprinted with permission from *J. Phys. Chem. C* 2023, 127, 48, 23475–23488. Copyright 2023 American Chemical Society. Modified and extended.

and the π band fully antibonding. Overall, this results in the crossing of these pure pre-hybridization bands and a potentially metallic situation with the Fermi level being located at the crossing point. However, just like at the ideal p(1×1) surface, due to compatible symmetry and energy, the π and π^* bands are able to hybridize to open up a band gap and give the actual bands represented by black lines. The corresponding hybrid linear combinations halfway through the $\mathit{\Gamma}-J$-path illustrate the π and π^* orbitals complementing each other to still consistently maintain a bonding or antibonding interaction between neighboring dimers in the respective bands. While in the literature these bands are often simply named like the involved π and π^* orbitals,[28,39,42,43,45] thus disregarding the hybridization taking place, in this work they will be denoted more precisely as bonding interdimer (ID) and antibonding interdimer (ID^*) bands. The actual calculated band structure with the depiction of the COs of both bands to illustrate the energetic swapping of the orbitals with $\vec{k}$ is shown in Fig. A.10.

Instead of starting from the MO-like surface states of one Si dimer, the band structure can also be derived from the band structure of the ideal p(1×1) surface as depicted in Fig. 3.6 by using the concepts of band folding and Peierls distortion introduced in Section 2.2.1.3. By doubling the unit cell in the x-direction, the corresponding first SBZ and thus the $\mathit{\Gamma}-J$-section as well as the band structure is halved in this direction. The resulting band folding flips the Bloch functions from J to $\mathit{\Gamma}$ and the $sp^2 + p_x$ hybrid bands are now located at the new J, i.e., the edge of the first SBZ of the p(2×1) reconstruction. Both the IA and the IA^* bands are each cut into two separate bands and exhibit degenerate linear combinations at their touching point at J, only differing by a translational shift of one ideal p(1×1) surface basis vector in x. Here, in analogy to Fig. 2.14, these $sp^2 + p_x$ states can alternatively be linearly combined to give Bloch functions of actual sp^3 character, which show bonding and antibonding interaction between pairs of neighboring surface Si atoms for the former IA and IA^* bands, respectively. Since they still exhibit the translational shift, the Peierls distortion forming dimers will split these bands at J, resulting in the former IA band to yield the σ and the ID bands and the former IA^* band to yield the antibonding counterparts. While it was established in Section 2.2.1.3 that the Peierls distortion only influences the band structure in the region of the touching point, namely J in this example, this does not prevent the bands at $\mathit{\Gamma}$ to hybridize as a result of the reconstruction. Accordingly, the former pure p_x band is stabilized by mixing with the former pure sp^2 band to give better σ bonds. Conversely, the former pure sp^2 band obtains more p_x character and is thus energetically elevated but also gains some energy from forming interdimer bonds. Since both of the corresponding σ and ID bands are fully occupied as indicated by the Fermi level, it is easily imaginable that not too much energy can be gained by this splitting. This explains the very low reconstruction energies found in theoretical studies, as was already argued more generally by Sabisch et al.[45] Put differently, when going from the ideal p(1×1) surface to the p(2×1) reconstruction, the IA band, which consists of p_x bonding between all surface

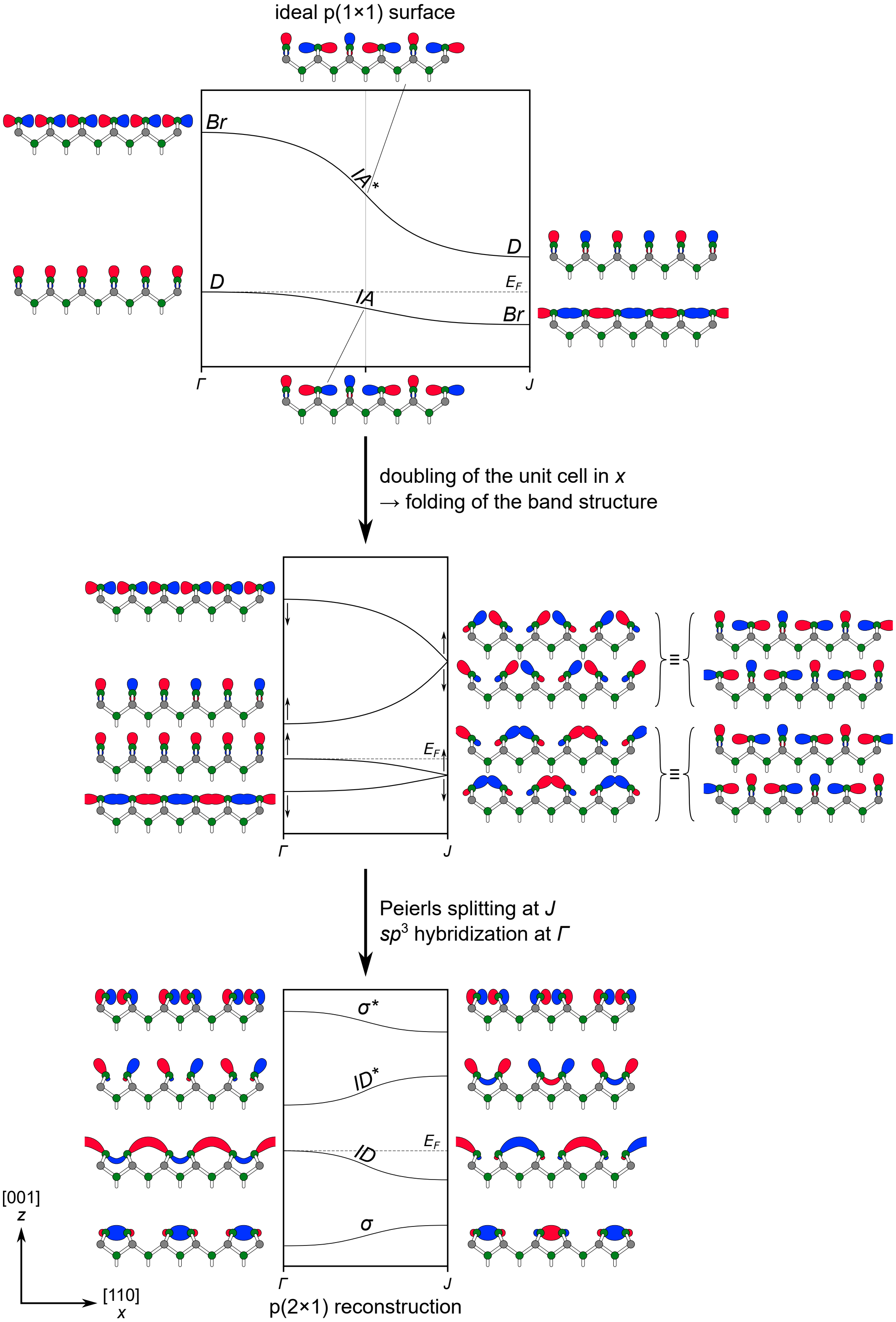

Figure 3.6: Derivation of the proposed qualitative band structure of the Si-terminated 3C-SiC(001)-p(2×1) reconstructed surface from the band structure of the ideal p(1×1) surface using the concept of band folding and Peierls distortion (see Section 2.2.1.3). The linear combinations of the sp^3 hybrid bands at J of the central band structure are created according to the example in Fig. 2.14.

atoms of each row and nonbonding but quite stable sp^2-orbitals, is replaced by the σ band containing strong σ bonds and the ID band showing weak interdimer bonds, both only between every other dimer. This low energy gain is not obvious when solely focusing on the reduction of the number of singly occupied dangling bonds for isolated dimers as the driving force for the dimerization and thus disregarding the interaction between neighboring dimers.

To conclude this section, it has to be emphasized that the presented analysis of the surface state band structure is purely qualitative and based on previous theoretical and experimental investigations finding both surfaces to be semiconducting.[28,38–40,42–45,151–154] Any quantitative statements require the inclusion of all other atoms and their orbitals, which is why the corresponding calculations are presented in the following sections.

3.2 Single-Configurational Calculations with PBCs

3.2.1 Computational Details

The CRYSTAL17[84] program package (version 1.0.1) was used to carry out single-configurational calculations utilizing PBCs. Restricted and unrestricted Hamiltonians according to HF[60,61] theory or KS DFT[71] were employed, with the LDA,[69,74] PBE,[75] PBE0,[76,77] and HSE06[78–80] functionals being used for the latter method. In CRYSTAL17, the electronic structure is described via MO-LCAO of atom-centered GTOs. Basis sets of triple-zeta-valence and double polarization (TZVPP) quality for Si[155] and of TZVP quality for C and H[156] were chosen, which have been derived from the molecular def2-TZVPP[148] and def-TZVP[157] basis sets and optimized for calculations using PBCs by the respective authors. As further recommended by the basis set authors,[155] the truncation thresholds for two-electron integrals in CRYSTAL17 were slightly tightened to TOLINTEG 8 8 8 8 16 for these basis sets compared to the default values. Furthermore, the pob-TZVP[158] basis set was used for Si, C, and H for comparison utilizing the same two-electron integral thresholds. The reciprocal space unit cell of the primitive bulk unit cell of 3C-SiC (see right side of Fig. 1.2) was sampled by a $\mathit{\Gamma}$-centered 12×12×12 Monkhorst-Pack[128] $\vec{k}$-point grid. For the different reciprocal space surface unit cells associated with the $M \times N$ supercells of the periodic slab models representing the Si-terminated 3C-SiC(001) surface, $\frac{12}{M} \times \frac{12}{N} \times 1$ $\mathit{\Gamma}$-centered Monkhorst-Pack $\vec{k}$-point grids were used to ensure a constant $\vec{k}$-point density (see Fig. 2.17). The periodic slab models were constructed from the converged bulk structures (see Table 3.1) and, in case of asymmetric H-saturated slab models, contained an in total even number of alternating Si and C atomic layers with the dangling bonds of the lowest C layer being saturated by H atoms (see Fig. 2.15). The symmetric slab models contained an odd number of atomic layers, meaning both surfaces were Si-terminated and the central layer was a C layer. For unrestricted calculations of the reconstructed Si-terminated 3C-SiC(001) surfaces, the spin density sum was fixed to a value of zero until total energy convergence of $10^{-6}\,E_\mathrm{h}$ was reached (SPINLOCK 0 −6) for strongly spin-contaminated singlets and to a value of two (SPINLOCK 2 −6) for slightly spin-contaminated triplets. For the unrestricted singlet solution to differ from the restricted results, the spins of the Si dimer atoms at the surface had to be set individually at the start of each calculation to match the intended spin arrangement (ATOMSPIN). During geometry optimizations, the unit cell parameters were kept fixed to simulate the constraint of the underlying bulk. The four lowest atomic layers with the saturating H layer were kept fixed in case of the asymmetric H-saturated slab models and the central five atomic layers (three C and two Si) in case of the symmetric slab models. P_1-symmetry was imposed to achieve the highest possible translational freedom for the atoms to move in the slab models. To plot the band structure of the periodic slab models and the PBBS at the same time, the average Si 1s core energy level of all Si layers except for the topmost two and the lowermost one Si layers is calculated as these inner layers generally exhibited Mulliken[159] charges virtually identical to the one of the bulk atoms. Subsequently, the energy eigenvalues of the slab models are shifted by this mean value to match the Si 1s core levels of the bulk Si atoms. Molecular structures and orbital or electron density isosurfaces were visualized with Jmol[160] and VESTA.[161]

3.2.2 Bulk 3C-SiC

Before treating the Si-terminated 3C-SiC(001) surface theoretically, a sophisticated bulk structure of 3C-SiC has to be determined by geometry optimization. Due to the high symmetry of the cubic space group 216 this material belongs to, only the lattice parameter a can be changed. Table 3.10 shows the obtained lattice parameters a and bulk band gaps E_g for the different functionals and basis sets applied as well as corresponding experimental values. Regarding the lattice parameter a, all functionals achieve very good agreement with the experiment for both basis sets, quantified by small deviations of less than 1 %. Especially the two hybrid functionals PBE0 and HSE06 in combination with the TZVPP/TZVP basis set as well as the HF method with the pob-TZVP basis set yield the best results with deviations smaller than 0.1 % and the closest agreement for the HSE06 functional. It should be noted that the HF method with the TZVPP/TZVP basis set was not able to converge in the SCF cycle as soon as the lattice constant fell below a certain value over the course of the geometry optimization. This might indicate the known possible problem of linear dependencies when using atom-centered GTO basis sets in solid-state calculations[106] since the basis functions of the TZVPP/TZVP basis are slightly more diffuse than the pob-TZVP basis. These linear dependencies get more relevant as the atoms move closer to another and their basis

Table 3.1: Optimized conventional fcc bulk unit cell parameters of 3C-SiC for different restricted methods and basis sets. Reprinted with permission from *J. Phys. Chem. C* 2023, 127, 48, 23475–23488. Copyright 2023 American Chemical Society. Extended by pob-TZVP and experimental values.

Method	Lattice Parameter a [Å]		Bulk Band Gap E_g [eV]	
	pob-TZVP	TZVPP/TZVP	pob-TZVP	TZVPP/TZVP
HF	4.3559	-	8.58	-
LDA	4.3303	4.3401	1.31	1.32
PBE	4.3742	4.3876	1.39	1.39
PBE0	4.3433	4.3575	2.91	2.88
HSE06	4.3449	4.3591	2.25	2.25
Exp.[5,162]	4.3596		2.36	

sets overlap more strongly. However, why this problem only occurred for the HF method and not also for the hybrid functionals utilizing the same basis set is not clear. It might be possible that the approximate local DFT correlation and exchange of the hybrid functionals is able to stabilize the convergence of the only partially included non-local exact HF exchange, which might be vulnerable to diffuse basis sets. This is supported by additional PBE0 bulk optimizations with the TZVPP/TZVP basis set also not converging for 50 % and higher percentages of HF exchange, while the amount of HF exchange can go up to 100 % when using the pob-TZVP basis set. Furthermore, in HSE06 calculations, the HF exchange can also be increased to 100 % for both basis sets without any issues. Since the HF exchange is restricted to a short range in HSE06 compared to PBE0, this hints towards the non-local HF exchange causing convergence problems for the more diffuse TZVPP/TZVP basis set. However, this is rather speculative and to the best of this work's author's knowledge has not been discussed in the literature yet.

While the basis set virtually does not influence the value of the bulk band gap E_g, the deviations from the experiment with respect to the functional used are far more severe compared to the lattice constant a. As is well known, the pure DFT functionals LDA and PBE generally underestimate[73,106,163] and the HF method strongly overestimates[106,164] band gaps. Still, it should be noted that energy gaps between the highest occupied MO (HOMO) and the lowest unoccupied MO (LUMO) are conceptionally not the same as excitation energies, which are obtained correctly from excited state calculations.[73] Nevertheless, it is accordingly easily imaginable that mixing a certain amount of HF exchange into DFT functionals increases the otherwise underestimated band gap values,[165] hence the hybrid PBE0 and the range-separated hybrid HSE06 functionals give the best agreement, the latter only deviating by about 0.1 eV.

Overall, the results regarding the lattice parameter a and the bulk band gap E_g are in accordance with the generally observed trend of DFT functionals containing some amount of HF exchange to perform better than pure DFT functionals.[73] Here, specifically the HSE06 functional with the TZVPP/TZVP basis set shows the most accurate results for 3C-SiC, as was already established for the band gap in a previous study using a different basis set.[166] Accordingly, this combination of functional and basis set will mainly be employed in the rest of this work. However, it should still be noted that hybrid functionals have shown to be less accurate for non-*sp* bonded semiconductors,[165] stressing the system-dependence of DFT functionals mentioned in Section 2.1.1.3.

While nothing more of the 3C-SiC bulk has to be analyzed in the context of this work, a noteworthy observation was made related to the convergence of the two parameters a and E_g with the $\vec{k}$-point grid applied. Using the results for the HSE06 functional with the TZVPP/TZVP basis set as an example, it is apparent from Fig. 3.7 that the lattice constant a shows regular convergence behavior when increasing the number of $\vec{k}$-points in the first BZ with a very tight convergence window of only a few 0.001 Å (violet curve). The black convergence curve of the bulk band gap E_g, on the other hand, is strongly diverging and thus can be divided into two significantly differing curves, one for an even and one for an odd number q of $\vec{k}$-points along each reciprocal basis vector. While E_g is basically converged from the start for an even 4×4×4 $\vec{k}$-point grid with a convergence window of less than 0.002 eV, this is not the case for odd values of q, resulting in a convergence window of about 1.4 eV and no full convergence even for a 11×11×11 $\vec{k}$-point grid. This unexpected convergence behavior of E_g can directly be connected to the details of $\vec{k}$-point sampling established in Section 2.2.1.6: without plotting the band structure, the CRYSTAL17 output reveals the indirect band gap to occur between the Γ- and the X-point, as is typically the case for zincblende materials.[167] Since X is a high-symmetry $\vec{k}$-point, it is located on the edge of the first BZ of the bulk. This edge, however, is not included in Γ-centered Monkhorst-Pack $\vec{k}$-point grids with an odd number q of $\vec{k}$-points along each reciprocal basis vector (see Fig. 2.16) and vice versa for even numbers q, resulting in the slow and

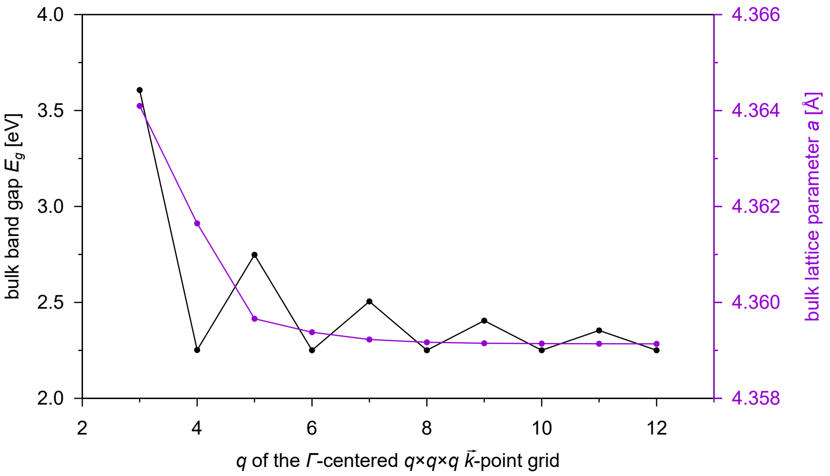

Figure 3.7: Convergence of the the bulk band gap E_g and the fcc lattice parameter a of 3C-SiC at RKS DFT HSE06 level with the TZVPP/TZVP basis set with respect to the density of the Γ-centered Monkhorst-Pack $\vec{k}$-point grid applied.

fast convergence of the bulk band gap E_g with respect to odd and even values q, respectively. This stresses the importance of checking the convergence of E_g with respect to the $\vec{k}$-point sampling.

3.2.3 Si-terminated 3C-SiC(001) Surface

3.2.3.1 Hydrogen Layer Optimization

With the optimized bulk structures at hand, the slab models for the Si-terminated 3C-SiC(001) surface could be constructed. In the following investigations, mainly the asymmetric H-saturated slab models will be used as the symmetric slab models only serve as a validation system later in Section 3.2.3.5. Accordingly, the H layer had to be optimized as a first step to obtain these slab models, which was done by saturating both the Si- and C-terminated sides of an asymmetric 12-layer 1×1 supercell periodic slab model of the ideal p(1×1) surface with two H per surface atom. Only the H atoms were then able to move during the optimization. Interestingly, when imposing no further optimization constraints, the C atoms give an expected, though tilted, tetrahedral structure, while on the Si-terminated side the Si atoms are bridged almost horizontally in x-direction (d_{Si-H} = 1.55 Å, $\angle(Si{-}H{-}Si)$ = 166.5°, RKS DFT HSE06 with TZVPP/TZVP basis set) by one H. The second H is located directly on top of each Si, forming a bond perpendicular to the surface and resulting in overall trigonal-bipyramidal coordinated Si atoms as depicted in Fig. 3.8a). This bonding situation structurally seems to maintain the electronic structure of the surface silylenes of the ideal p(1×1) surface with the perpendicular sp^2 and the horizontal p_x orbitals. Apparently, this structure is energetically more favorable than trying to achieve a tetrahedral sp^3 coordination of the Si atoms as depicted in Fig. 3.8b) due to the associated repulsion between neighboring H atoms in the latter case caused by the limited space. Acquiring the tetrahedral geometry was only possible by not allowing the H atoms to move along y and force their z-coordinates to be equal during optimization. These constraints were also applied to the C-terminated side for consistency reasons.

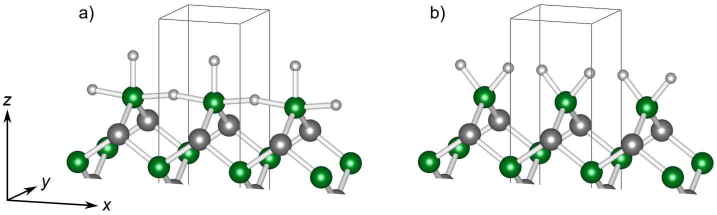

Figure 3.8: a) Unconstrained and b) constrained geometry optimization of the saturating H atom layer on the Si-terminated side of a 1×1 supercell 8-layer periodic slab model for the ideal 3C-SiC(001)-p(1×1) surface at RKS DFT HSE06 level with the TZVPP/TZVP basis set. In case of the constrained optimization in b), the H atoms were not allowed to relax in y and their z-coordinates had to be equal. The lattice parameter of the unit cells in z is depicted smaller than it is in the actual calculations.

Very similar Si–H–Si bridges ($d_{Si-H} = 1.62\,\text{Å}$, $\angle(Si-H-Si) = 166°$) have been found before by Gali et al.[168] and Aradi et al.[169] in LDA calculations for interstitial H atoms at single C vacancies in bulk 3C-SiC. In the charge-neutral doublet state, the electron introduced by the H occupies the antibonding linear combination of the sp^3 orbitals of the two triply substituted Si atoms, where the H atom is located on the corresponding nodal plane. Furthermore, the singly positively charged singlet state is also stable with the same bridged structure. Along these lines, Müller reported a singly charged silyl cation with two triply substituted Si atoms bridged by one H atom in a three-center two-electron bond, so an overall tetrahedral Si coordination.[170] According to the associated hybrid DFT calculations, the LUMO also corresponds to the antibonding combination of two sp^3-like orbitals of both Si atoms (the nonbonding combination in the language of three-center bonds) with the H atom on the nodal plane, thus in agreement with the cationic state of the aforementioned defect calculations of bulk 3C-SiC. Pavlova found a similar singly cationic Si–H–Si bridge when inserting H into the hydrogenated dimers of the Si(001) surface in PBE DFT calculations.[171] In case of the results of this work, cutting the ideal p(1×1) surface can also be regarded as introducing a periodic array of C vacancies into the bulk, explaining the same bridging geometry, which is periodic in x since there are basically two C vacancies for each Si atom. However, while the three-center two-electron bond in the silyl cation of Müller shows an expected negatively charged bridging H and positively charged Si atoms, at the surface of this work the situation is inverted with a Mulliken charge of $0.45\,e$ at the bridging H and of $-0.53\,e$ for the Si atom (RKS DFT HSE06 with TZVPP/TZVP basis set). This indicates a different bonding situation that cannot be explained easily. Nevertheless, since the ideal p(1×1) surface and thus such H-saturation is not observable experimentally and the H layer on the Si-terminated side of the asymmetric periodic slab models is discarded anyway to reveal the surface states, no further analysis of these scientifically still interesting periodic Si–H–Si bridge bonds was undertaken. Accordingly, the H layer coordinates of the C-terminated surface obtained from the constrained geometry optimization were used for all following calculations that utilize asymmetric H-saturated slab models.

3.2.3.2 Spatial Structure of p(2×1) Reconstructions

As presented in Chapter 1, the ideal Si-terminated 3C-SiC(001)-p(1×1) surface is not observable since it immediately reconstructs to lower its energy. While experimentally c(4×2) and p(2×1) reconstructions have been found at RT with the former supposedly being the more stable structure, periodic slab model DFT calculations prefer the p(2×1) reconstruction with the SD model over the AUDD model for the c(4×2) case.[28,42,46–48] The latter model is only observed for strained surfaces[28,42,46] or cluster model DFT calculations.[172] More recently, alternative p(4×1) and p(4×2) reconstructions have also been found, in which two neighboring dimers further dimerize, resulting in buckled structures.[173] However, most of the periodic slab model calculations in the literature only utilized restricted approaches, which, after discussing the delicate electronic structure in Section 3.1, might be insufficient as the only published unrestricted[54] and multiconfigurational[53] calculations indicate. Accordingly, a comprehensive theoretical study of the possible reconstructions of the Si-terminated 3C-SiC(001) surface is presented in the following using periodic slab model calculations in combination with restricted and unrestricted single-configurational HF and DFT.

At first, only the smallest possible supercell, namely a 2×1 supercell, was employed to restrict the additional translational freedom and thus the number of possible reconstructions to a minimum. Both buckled and unbuckled dimers have been used as starting structures for the geometry optimizations of the periodic slab models containing a generous number of 12 atomic layer as depicted in Fig. 3.9b). Besides the singlet state, also the high-spin configuration, which is a triplet in case of the 2×1 supercell, was investigated to check if it is energetically favored and to serve as a structure for comparison due to the generally negligible amount of spin contamination of unrestricted high-spin states. The most common parameters to discuss the strength of the recon-

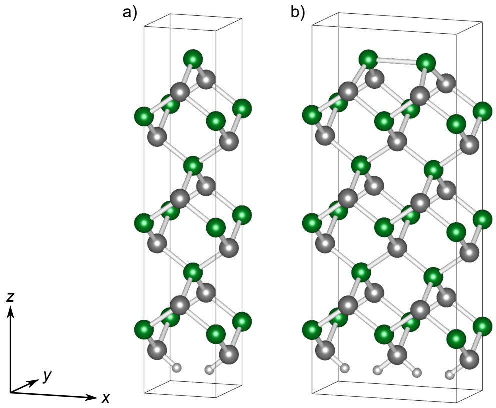

Figure 3.9: H-saturated 12-layer periodic slab models for the a) unoptimized ideal p(1×1) surface in a 1×1 supercell and b) optimized p(2×1) reconstructed surface (SD model) in a 2×1 supercell of the Si-terminated 3C-SiC(001) surface. b) was optimized at singlet UKS DFT HSE06 level with the TZVPP/TZVP basis set (see Table 3.2). The lattice parameter of the unit cells in z is depicted smaller than it is in the actual calculations.

struction are the Si dimer bond length d_{Si-Si} and the energy gain per dimer or reconstruction energy ΔE_{dimer}, the latter being calculated according to the following equation:

$$\Delta E_{dimer} = \frac{E_{recons,M\times N} - M \cdot N \cdot E_{ideal,1\times 1}}{\frac{M\cdot N}{2}} \tag{3.1}$$

Here, M and N give the size of the supercell in x and y, respectively, $E_{recons,M\times N}$ is the total energy of the optimized reconstructed $M\times N$ supercell, and $E_{ideal,1\times 1}$ is the total energy of the unoptimized 1×1 supercell of the ideal p(1×1) surface (Fig. 3.9a). It should be noted that the latter energy was calculated only using a restricted approach since unrestricted singlet calculations always collapsed to the restricted solution. This is generally a known occurrence for unrestricted methods[57] when the energy-raising effect of (often) energetically less stable higher-spin states (spin contamination) outweighs the energy gain by the inclusion of partial static correlation achieved by the spin-symmetry breaking.[59] Furthermore, in this particular case, an unrestricted solution for the the ideal p(1×1) should not be possible because the positive and negative parts of the spin density would be located at the same surface atom and thus cancel each other. Accordingly, the ATOMSPIN keyword of CRYSTAL17 does not even offer the possibility of assigning such starting spins.

Table 3.2 lists the results of the conducted calculations for the 2×1 supercell slab models. Here, values are only given if the converged geometry corresponds to the SD model. If the calculations instead gave buckled dimers, no reconstruction, or even no convergence at all, only a "-" is displayed. From the additional comments at the bottom, it is apparent that a significant part of the calculations virtually gave no reconstruction with the dimer atoms showing distances in the range of 3.04 Å – 3.09 Å, which are almost identical to the distances on the ideal p(1×1) surface ranging from 3.06 Å – 3.10 Å for the different DFT functional and basis set combinations. The corresponding reconstruction energies are also very low with values of only $-0.01\,\text{eV} - -0.02\,\text{eV}$. This phenomenon mainly occurred for the slightly less sophisticated and less diffuse pob-TZVP basis set, especially in case of the restricted calculations, where for none of the DFT functionals a reconstruction took place and only a buckled dimer emerged for the HF method. This indicates a high sensitivity of the reconstruction to the basis set accuracy, which is indirectly supported by the only other published GTO study for this system of Sabisch et al. employing more basis functions specifically for the surface atoms than for the bulk atoms.[45] Concerning the unrestricted results, the convergence towards the ideal p(1×1) surface resulted in a collapse to the the restricted solution, as was expected with the discussion at the end of the previous paragraph in mind. The LDA high-spin geometry optimizations were trapped in a trailing convergence without meeting the associated thresholds for both basis sets. In case of the PBE functional for both basis sets and in case of the the HSE06 functional for the pob-TZVP basis set, the high-spin calculations did converge but gave unreasonable spin density sums of less than the required value of

Table 3.2: Dimer bond lengths d_{Si-Si} and reconstruction energies ΔE_{dimer} of H-saturated 2×1 supercell 12-layer periodic slab models of the Si-terminated 3C-SiC(001) surface with respect to the DFT functional, spin state, and basis set applied. Geometry optimizations not converging, giving unreasonable results, or other reconstructions than the symmetric dimers of the p(2×1) reconstruction (SD model) are indicated by "-" and further characterized by the comments at the bottom. HF calculations with the TZVPP/TZVP basis set were not possible since the bulk structure did not converge.

Parameter	Functional	Singlet Restricted		Singlet Unrestricted		High-Spin Unrestricted	
		pob-TZVP	TZVPP/TZVP	pob-TZVP	TZVPP/TZVP	pob-TZVP	TZVPP/TZVP
d_{Si-Si} [Å]	HF	$-^{a}$		2.46		2.41	
	LDA	$-^{b}$	2.71	$-^{b,c}$	2.72^{c}	$-^{d}$	$-^{d}$
	PBE	$-^{b}$	2.72	$-^{b,c}$	2.56	$-^{e}$	$-^{e}$
	PBE0	$-^{b}$	2.80	2.54	2.45	2.42	2.38
	HSE06	$-^{b}$	2.80^{f}	2.56	2.46	$-^{e}$	2.39
ΔE_{dimer} [eV]	HF	$-^{a}$		−1.25		−1.22	
	LDA	$-^{b}$	−0.03	$-^{b,c}$	-0.03^{c}	$-^{d}$	$-^{d}$
	PBE	$-^{b}$	−0.03	$-^{b,c}$	−0.06	$-^{e}$	$-^{e}$
	PBE0	$-^{b}$	−0.02	−0.14	−0.28	+0.01	−0.21
	HSE06	$-^{b}$	-0.01^{f}	−0.10	−0.23	$-^{e}$	−0.14

[a] buckled dimer found instead ($d_{Si-Si} = 2.84$ Å, $\Delta z_{Si-Si} = 0.13$ Å, $\Delta E_{dimer} = -0.37$ eV)

[b] virtually no reconstruction ($d_{Si-Si} =$ 3.04 Å – 3.09 Å, $\Delta E_{dimer} = -0.01$ eV – −0.02 eV)

[c] unrestricted solution collapses to restricted solution

[d] no convergence in geometry optimization

[e] erroneous spin density sum of 1.57 (PBE + pob-TZVP), 1.61 (PBE + TZVPP/TZVP) and 1.95 (HSE06 + pob-TZVP)

[f] a more stable buckled dimer was found additionally ($d_{Si-Si} = 2.61$ Å, $\Delta z_{Si-Si} = 0.21$ Å, $\Delta E_{dimer} = -0.05$ eV, see Fig. 3.10)

two. Overall it can be concluded that the Si-terminated 3C-SiC(001) surface represents a challenging system for single-configurational periodic slab model calculations.

Going into the details of the converged restricted calculations yielding symmetric dimers, the DFT functionals with the TZVPP/TZVP basis set all yield very weak p(2×1) reconstructions with d_{Si-Si} ranging from about 2.7 Å – 2.8 Å and ΔE_{dimer} from −0.01 eV – −0.03 eV. Here, the pure DFT functionals LDA and PBE show slightly stronger reconstruction with dimer bond lengths closer to 2.7 Å and reconstruction energies of −0.03 eV, while the hybrid functionals PBE0 and HSE06 both give values of 2.80 Å and −0.02 eV and −0.01 eV, respectively. Accordingly, the additional exact HF exchange seems to slightly inhibit the reconstruction for the restricted calculations, which is in accordance with the RHF optimization not giving symmetric dimers at all.

Interestingly, the restricted HSE06 optimizations furthermore yielded a more stable buckled dimer as depicted in Fig. 3.10 with d_{Si-Si} of 2.61 Å, a height difference between the dimer atoms Δz_{Si-Si} of 0.21 Å and ΔE_{dimer} of −0.05 eV. For the HF Hamiltonian with the pob-TZVP basis set, a similar but less pronounced buckling with d_{Si-Si} of 2.84 Å and Δz_{Si-Si} of 0.13 Å was observed, yet

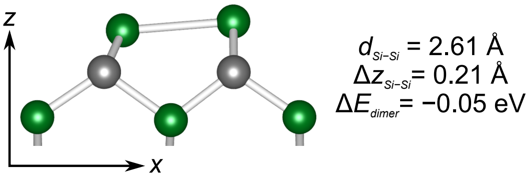

Figure 3.10: Buckled/asymmetric dimer of the Si-terminated 3C-SiC(001)-p(2×1) reconstructed surface found for a H-saturated 2×1 supercell 12-layer periodic slab model at RKS DFT HSE06 level with the TZVPP/TZVP basis set.

giving a rather high reconstruction energy of $-0.37\,\text{eV}$. Since HF is missing any post-HF electron correlation, this might indicate a distinct energetic balance between stabilizing exchange effects and destabilizing correlation effects, which are both considered in the DFT calculations, thus leading to lower reconstruction energies compared to HF. Buckled dimers for periodic slab model calculations of the Si-terminated 3C-SiC(001)-p(2×1) reconstruction have only been reported before twice, namely in the semi-empirical calculations of Craig and Smith[174] and the DFT calculations of Yan et al.[175] Sabisch et al.[45] explained these results, which contradict the large majority of other theoretical studies giving symmetric dimers, by the insufficient quality of semi-empirical methods for this delicate reconstruction as well as a poor $\vec{k}$-point sampling in case of the cited DFT study. In fact, when Sabisch et al. applied a similarly sparse $\vec{k}$-point grid, they also arrived at semiconducting buckled dimers, which are metallic when applying a more accurate $\vec{k}$-grid. In this work, however, this should not be an issue because more than twice as many $\vec{k}$-points are sampled compared to the study of Sabisch et al. Furthermore, the buckled structures of both HF and HSE06 are found to be semiconducting. Since in this work the HF method and hybrid functionals are applied for the first time, the buckling behavior might be a feature of the exact HF exchange since additional PBE and LDA calculations with the same buckled starting structure as the HSE06 result still converged to symmetric dimers. However, with regard to the supposedly multiconfigurational character of the surface and buckled dimers only occurring for restricted calculations, they still appear to be unreasonable and could be an artifact instead.

Turning the attention to the unrestricted singlet calculations in Table 3.2, a significantly stronger degree of reconstruction is observable compared to the restricted formalism with dimer bond lengths in the range of $2.46\,\text{Å} - 2.56\,\text{Å}$ and reconstruction energies of $-0.06\,\text{eV} - -1.25\,\text{eV}$. Here, the very high ΔE_{dimer} of $-1.25\,\text{eV}$ for the UHF method might again be attributed to the missing and supposedly compensating post-HF electron correlation. In case of the PBE0 and HSE06 functional, the basis set sensitivity is apparent once more as ΔE_{dimer} approximately doubles and d_{Si-Si} reduces by about $0.1\,\text{Å}$ when going from the pob-TZVP to the TZVPP/TZVP basis. Furthermore, while the exact HF exchange supposedly inhibits the reconstruction for the restricted calculations, it seems to amplify this effect in case of the unrestricted methods because the hybrid functionals give shorter dimer bonds and more negative reconstruction energies of about 2.45 Å compared to the PBE results of 2.56 Å. In case of the reconstruction energies, this dependence is even more clear as it increases with the amount of HF exchange included, i.e., from PBE with 0 % HF exchange and −0.06 eV, HSE06 with 25 % short-range HF exchange and −0.23 eV, PBE0 with 25 % full-range HF exchange and −0.28 eV, and pure HF without correlation effects giving −1.25 eV. A similar trend is observable in the corresponding Mulliken atomic spin densities and the spin contamination $\Delta \langle \hat{S}^2 \rangle$ listed in Table 3.3, also increasing with the amount of HF exchange. This is in accordance with the general observations that HF exchange favors spin localization[84] and that the degree of spin contamination increases with amount of HF exchange,[58,176] thus UKS generally showing less spin contamination than UHF.[58,86] Furthermore, the values of $\Delta \langle \hat{S}^2 \rangle$ approach one, which, as established in Section 2.1.1.4, corresponds to the expected value of an unrestricted singlet determinant being a 50:50 mixture of the spin-pure singlet and triplet states.

The unrestricted high-spin optimizations shown in Table 3.2 were only successful for the HF method and the hybrid functionals, also in accordance with the favored spin localization when including HF exchange, which is further apparent in the atomic spin densities in Table 3.3. Moreover, as expected for unrestricted high-spin determinants, the spin contamination amounts to negligible values of less than 0.01. The dimer bond lengths are in the range of 2.42 Å – 2.38 Å and thus shorter by about 0.05 Å – 0.12 Å than their singlet counterparts. This shortening is easily explainable by the missing *ID* bonding due to the parallel spins of all dangling bonds at the dimer atoms, which would otherwise counteract the dimer formation. Furthermore, the additional exchange interaction between these parallel spins within each dimer possibly also reduces the Coulomb repulsion. With respect to the reconstruction energy, the HF method again shows very strong and supposedly overestimated stabilization of −1.22 eV. For the pob-TZVP basis set, only the PBE0 functional

Table 3.3: Mulliken atomic spin densities of the two dimer atoms and spin contamination $\Delta \langle \hat{S}^2 \rangle$ for the H-saturated 2×1 supercell 12-layer periodic slab models of the Si-terminated 3C-SiC(001)-p(2×1) reconstructed surface (SD model). The given values belong to some of the optimizations already presented in Table 3.2. The TZVPP/TZVP basis set was used except for the HF results, in which the pob-TZVP basis was applied. The values for $\Delta \langle \hat{S}^2 \rangle$ slightly differ from the ones given in the author's publication (*J. Phys. Chem. C* 2023, 127, 48, 23475–23488.) as they accidentally were not fully converged with respect to the $\vec{k}$-point grid in the latter.

Functional	Singlet Unrestricted		High-Spin Unrestricted	
	Spin Density at Si Dimer Atoms	$\Delta \langle \hat{S}^2 \rangle$	Spin Density at Si Dimer Atoms	$\Delta \langle \hat{S}^2 \rangle$
HF[a]	+0.87, −0.87	0.96	+0.90, +0.90	< 0.01
PBE	+0.46, −0.46	0.48		
PBE0	+0.66, −0.66	0.83	+0.81, +0.81	< 0.01
HSE06	+0.64, −0.64	0.80	+0.81, +0.81	< 0.01

[a] obtained with the pob-TZVP basis set

gave physically reasonable results with ΔE_{dimer} being 0.01 eV, thus slightly destabilized compared to the unreconstructed ideal p(1×1) surface. However, just like for the singlet case, employing the TZVPP/TZVP basis set increases the reconstruction strength to −0.21 eV for PBE0 and yielding a value of −0.14 eV for HSE06, opening up the possibility for the surface to also exist in this high-spin state, though less stabilized than the singlet state due to the missing ID bonds. Such high-spin surfaces could show magnetic properties and similar theoretical and experimental investigations in this regard have been undertaken for the same or other covalent semiconductors exhibiting dangling bond surface states.[177–183]

However, it should be noted that single-configurational approaches are not able to correctly describe antiferromagnetic states, i.e., singlet polyradicals, because the spin density should be zero everywhere,[81] which is not the case and leads to spin contamination as apparent from Table 3.3. Since the ferromagnetic states, i.e., high-spin polyradicals, are correctly described, relative energies between such singlet and triplet states have to be taken with care. Unfortunately, correction methods for spin contamination like the AP scheme presented in Section 2.1.1.4 are object of current research for calculations employing PBCs[184] and could thus not be utilized in this work to obtain more reliable quantitative results. Furthermore, the influence of the spin contamination on the total energy cannot be generalized to allow for an estimation of its impact, e.g., always a decrease or an increase, but it is system dependent instead. While often the higher-spin contaminants are higher in energy and thus result in an increase in total energy through spin contamination,[59] the opposite is the case, e.g., for methylene, where mixing of the triplet state stabilizes the unrestricted singlet diradical.[185] Then again, because singlet methylene is not solely defined by the diradical configuration but is of multiconfigurational character,[55,83] the unrestricted single-configurational methods cannot be expected to always yield accurate results for such systems even with spin contamination correction. Nevertheless, since the unrestricted diradicalic singlet states of the Si-terminated 3C-SiC(001) surface in this work are supposedly contaminated by the pure diradicalic triplet states, the latter showing shorter dimer bonds and less negative reconstruction energies than the former, the uncontaminated diradicalic singlet configuration can roughly be estimated to exhibit longer dimer bonds and more negative reconstruction energies than the spin-contaminated singlets. However, the longer dimer bonds could obviously also make the reconstruction energies more positive, so this estimation has to be taken with care. Furthermore, the reconstruction energies are calculated with respect to the restricted single-configurational total energy $E_{ideal,1\times1}$ of the ideal p(1×1) surface, in which, contrary to the reconstructed surfaces, no spin polarization could be induced and which is most likely of multiconfigurational character as established in Section 3.1. Accordingly, if this energy is decreased through a more correct description, the relative energies ΔE_{dimer} could get more positive. Of course, this reduction in total energy could also occur for the multiconfigurational description of the reconstructed surfaces, possibly leading to an error compensation. From this lengthy discussion, it is obvious that quantitative results for the Si-terminated 3C-SiC(001) surface cannot be expected from single-configurational approaches, which is why the multiconfigurational calculations presented in Section 3.3 hopefully give further insight.

Table 3.4 lists the singlet results of this work as well as theoretical and experimental results from the literature regarding the Si-terminated 3C-SiC(001)-p(2×1) reconstructed surface, mostly concerning the SD model. In case of this work's results, except for the HF method, only the calculations utilizing the

Table 3.4: Methodological and reconstruction parameters for several theoretical and experimental studies of the Si-terminated 3C-SiC(001)-p(2×1) reconstructed surface (SD model). The TZVPP/TZVP basis set was used for the calculations of this work except for the HF result, where the pob-TZVP basis was applied. Energy values listed below "Method" represent the cutoff energy E_{cut} for calculations employing plane wave basis sets. If values are not given in the corresponding reference, they are denoted with "-". Reprinted with permission from *J. Phys. Chem. C* 2023, 127, 48, 23475–23488. Copyright 2023 American Chemical Society. Slightly modified.

Reference	Method	Unrestricted?	d_{Si-Si} [Å]	ΔE_{dimer} [eV]	$E_{g,surf}$ [eV]
[39, 40]	LDA/259 eV	no	2.75	−0.02	0.26
[41, 42]	LDA/544 eV	no	2.58, 2.63[a]	−few meV	0.3
[43]	LDA/- eV	no	2.72	-	0.25
[44, 45]	LDA/GTO	no	2.73	−0.02	-
this work	LDA/GTO	no	2.71	−0.03	0.24
[46]	PBE/400 eV	no	2.69	-	-
this work	PBE/GTO	no	2.72	−0.03	0.15
this work	PBE0/GTO	no	2.80	−0.02	1.01
this work	HSE06/GTO	no	2.80	−0.01	0.53
[54]	PBE/500 eV	yes	2.45	-	-
this work	LDA/GTO	yes	collapses to restricted solution		
this work	PBE/GTO	yes	2.56	−0.06	0.39
this work	PBE0/GTO	yes	2.45	−0.28	2.07
this work	HSE06/GTO	yes	2.46	−0.23	1.34
this work	HF/GTO[b]	yes	2.46	−1.25	7.86
[53]	CAS(4,4)/GTO		2.46	-	-
[186]	Fit to LEED		2.31[c]		
[46]	Fit to PED		2.2 –2.5[d]		
[35]	STS				1.7[d]

[a] dimer bond length dependent on size of supercell

[b] obtained with the pob-TZVP basis set

[c] obtained for the p(2×1) reconstruction with buckled dimers

[d] obtained for the c(4×2) reconstruction (AUDD model)

TZVPP/TZVP basis set are considered due to the higher basis set accuracy and generally higher reliability during the calculations. As apparent, the available restricted LDA and PBE data align well with the restricted results of this work showing long dimer bonds of about 2.7 Å – 2.8 Å and low reconstruction energies of only a few -0.01 eV. An exception are the studies of Catellani et al. with significantly shorter d_{Si-Si} of 2.58 Å and 2.63 Å.[41,42] Here, the two values were obtained for different supercell sizes, namely the one- and twofold of a $2\sqrt{2}\times2\sqrt{2}R(45°)$ supercell with respect to the 1×1 surface supercells defined in this work (this simply corresponds to a 2×2 supercell of the (001) face of the fcc bulk unit cell of 3C-SiC with $a = 4.36$ Å, see Fig. 1.3a). Since for both of these supercells only Γ was included in the $\vec{k}$-point grid, this insufficient $\vec{k}$-sampling resulted in two differently well converged geometries. This explains why the longer dimer bond closer to the other converged theoretical data is found for the larger supercell because the corresponding smaller reciprocal unit cell utilized an overall denser $\vec{k}$-point grid.

The unrestricted results of this work also agree with the only other published unrestricted calculation of the Si-terminated 3C-SiC(001)-p(2×1) reconstruction of Xi et al., who also obtained a significantly shorter dimer bond of 2.45 Å using the PBE functional.[54] While this is slightly shorter than the PBE result of this work, this deviation is most likely caused by the different plane wave basis set since changes of similar magnitude were also observed in this work for different basis sets as apparent from Table 3.2. Unfortunately, no information regarding the reconstruction energy is given in the cited publication as their work focused on the corrosion of this surface. Nevertheless, these unrestricted calculations are in very good agreement with the high-level CAS(4,4) results of Tamura and Gordon yielding a dimer bond length of 2.46 Å.[53] As the corresponding NOONs revealed an almost pure diradicalic dimer, this agreement might come to no surprise because the unrestricted single-configurational calculations approximately simulate the same electronic structure. However, the cluster model of Tamura and Gordon featured only one single dimer, thus neglecting the interaction between neighboring dimers to form the band structure, which is why this effect on the structure of this surface will be accounted for using multi-dimer cluster models in Section 3.3.

Regarding the dimer bond length, only two experimental studies are available to the knowledge of this works's author, in which structural models of the Si-terminated 3C-SiC(001) surface were fitted to low electron energy diffraction (LEED)[186] and photoelectron diffraction (PED)[46] data, resulting in values of 2.31 Å and 2.2 Å – 2.5 Å, respectively. However, the final model for the LEED measurements yielded buckled dimers for the observed p(2×1) reconstruction,[186] thus disagreeing with most of the theoretical studies. In case of the PED experiment, the structural model was actually fitted to a c(4×2) reconstructed surface, resulting in the AUDD model giving the best agreement. But since the AUDD model is related to the SD model in a symmetric manner, the actual bond length of the latter model should be in the range of 2.2 Å – 2.5 Å, thus in good agreement with the LEED study. Even though the experimental dimer bond lengths are accordingly of limited value, they seem to be in better accordance with the shorter dimer bonds of the unrestricted than the restricted calculations.

Another parameter to check is the surface band gap $E_{g,surf}$ determined by the surface states of the Si-terminated 3C-SiC(001) surface. Aristov et al. observed this to be 1.7 eV for the c(4×2) reconstruction using scanning tunneling spectroscopy (STS).[35] Again, due to the close structural relation of the AUDD model and the SD model of the p(2×1) reconstruction, a similar surface band gap can be expected for both reconstructions, as was shown before by DFT calculations.[28,42,47] Just like in case of the bulk band gaps, it is apparent from Table 3.4 that the surface band gaps also vary strongly with respect to the DFT functional used. Since the HSE06 calculations proved to give the best bulk band gaps, the same can be assumed for the surface analogue, which is why only the corresponding restricted and unrestricted results of 0.53 eV and 1.34 eV are considered, respectively. Hence, also in this regard, the unrestricted calculations show better agreement than the restricted methodology.

While the reconstruction energy is not accessible experimentally, the higher values of the hybrid UKS results of about −0.20 eV appear to be more reasonable than the RKS values of about −0.02 eV. In the context of the p(2×1) reconstruction being observable at RT, where k_BT, which was used as a metric by Dabrowski to characterize the temperature stability of the Si dimers at the Si(001) surface,[138] amounts to 0.025 eV, such low reconstruction energies might not be sufficient to form dimers under these conditions. On the other hand, since the dimers supposedly interact with each other in each dimer row through the ID bonds, the effective stability might be higher nonetheless.

3.2.3.3 Electronic Structure of p(2×1) Reconstructions

The most striking observation of the theoretical results presented so far is the large difference between the restricted and unrestricted calculations regarding the p(2×1) reconstruction strength of symmetric dimers on the Si-terminated 3C-SiC(001) surface. To explain this, a closer look at the electronic structure of both methodologies is taken as presented in Fig. 3.11. Since the HSE06 functional supposedly gives the best bulk and surface band gaps, the results of this functional will be discussed representatively but the conclusions can also be transferred to the other functionals. First off, the calculated electronic structure of the reference system, the ideal p(1×1) surface, is shown in a) but for a 2×1 supercell for a direct comparability to the p(2×1) reconstructions. As apparent from the band structure plot, most of the bands of the surface slab are located in the PBBS and can thus be regarded as bulk states. Furthermore, all bands are subject to band folding due to the doubled size of the supercell. The IA and IA^* bands extensively derived in Section 3.1 are partly located within the band gap of the PBBS, as is expected for surface states that are less stable/unstable than the occupied/unoccupied bulk states. Since these bands are not exclusively located within the bulk band gap but also

a) ideal p(1×1) surface (2×1 supercell) at singlet RKS DFT HSE06 level

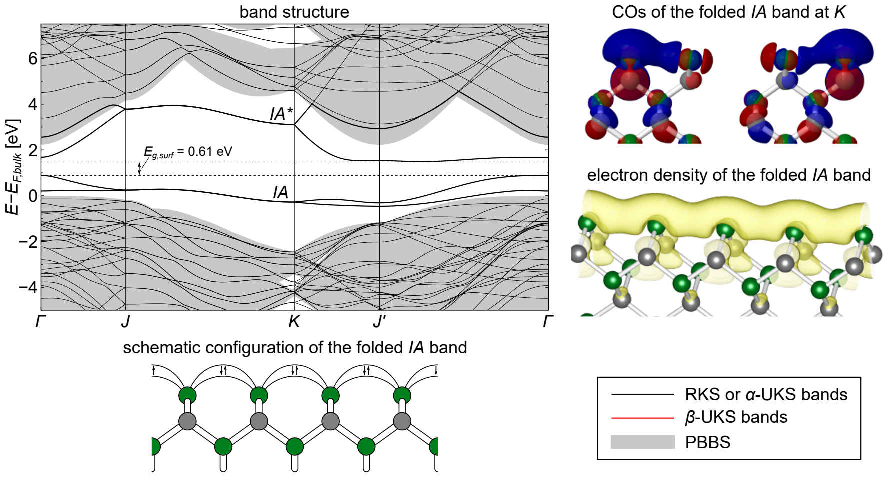

b) p(2×1) reconstruction at singlet RKS DFT HSE06 level

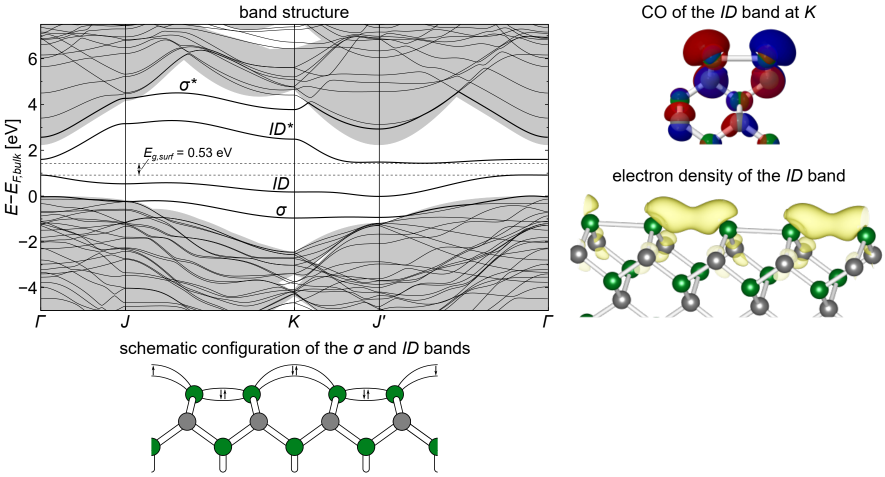

c) p(2×1) reconstruction at singlet UKS DFT HSE06 level

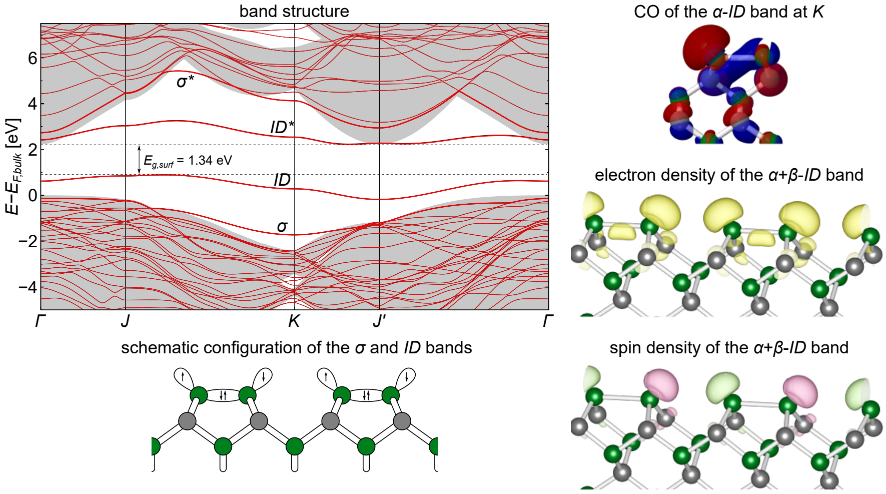

Figure 3.11: Electronic structure of the a) ideal p(1×1) and b+c) p(2×1) reconstructed (SD model) Si-terminated 3C-SiC(001) surface at singlet a+b) RKS and c) UKS DFT HSE06 level with the TZVPP/TZVP basis set for H-saturated 2×1 supercell 12-layer periodic slab models. The isosurface value of the calculated orbitals and densities amounts to $0.01\,{a_0}^{-3}$. In c), only the β-UKS bands are visible as they coincide with their degenerate α counterparts. Reprinted with permission from *J. Phys. Chem. C* 2023, 127, 48, 23475–23488. Copyright 2023 American Chemical Society. Slightly modified and extended by a).

overlap with the PBBS, they accordingly hybridize with the bulk-like states of the slab model to yield surface resonances or at least swap energetic positions with these bulk-like states. This results in the actual orbitals of the surface states, i.e., the p_x/Br and the sp^2/D orbitals of the surface Si atoms, to be located in other bands with respect to their numbering, as is depicted together with bulk-like state examples in Fig. A.9 (and analogously for π and the π^* orbitals of the p(2×1) reconstruction in Figs. A.10 to A.13). In Fig. 3.11a), the degenerate COs of the folded IA band at the K-point are also shown, illustrating the hybridization of the sp^2 and p_x orbitals within the bands as discussed before in Section 3.1. The depicted electron density of the IA band, which is integrated over all $\vec{k}$, accordingly also exhibits both the dangling bond (D) and bridging (Br) character of these orbitals. At the bottom of Fig. 3.11a), a simplified schematic configuration of the IA band of the ideal p(1×1) surface using localized banana-shaped bonds between the surface atoms is shown, which will be helpful to understand the p(2×1) reconstruction process.

Turning the attention to the band structures of the RKS and UKS DFT HSE06 calculations of the p(2×1) reconstruction in Fig. 3.11b) and c), respectively, it is apparent that the folded IA and IA^* bands of the ideal p(1×1) surface split into the depicted σ, ID, ID^* and σ^* bands as a result of the Peierls distortion responsible for the dimerization. Since the folded IA band is located below the Fermi level E_F and is thus fully occupied, the same is true for the σ and ID bands emerging from it. Consequently, as the IA^* band is unoccupied, so are the corresponding ID^* and σ^* bands. Accordingly, the occupation of the band structure for both RKS and UKS is identical. However, as apparent from Fig. 3.11b) and c), the COs at the K-point are different for both methods. In case of the RKS results, the established π^*-like orbital with C_{2v}-symmetry and dangling bond lobes of opposing phase at each dimer atom is depicted, which can form the ID bonds to neighboring dimers due to the alternating phase factor in x-direction at K. The corresponding UKS orbital for the α-ID band, on the other hand, shows a broken spin-symmetry shape with only one dangling bond lobe at one of the dimer atoms. Basically, this corresponds to a linear combination of the π and π^* frontier orbitals, in which only one dangling bond survives. On a side note, such HOMO-LUMO-mixing is actually a common approach to obtain broken spin-symmetry starting orbitals from a regular closed-shell or high-spin solution.[94,187] As the α- and β-ID bands are degenerate, the corresponding CO of the β-ID band is identical to its α counterpart but symmetric to the σ_{yz} mirror plane centered in the dimer bond. Unfortunately, plotting the β-COs seems to be corrupted in CRYSTAL17, which is why they are not displayed here explicitly. Due to the broken spin-symmetry of the α- and β-ID bands, opposing spin density arises at both dimer atoms as was shown in Table 3.3 and is also visible in the spin density plot of Fig. 3.11c), mimicking diradicalic behavior. However, it is important to stress that in this UKS solution, only the broken spin-symmetry ID bands are singly occupied each, which contrasts a high-spin or true diradicalic configuration with the ID and ID^* bands of correct spin-symmetry carrying one electron each. Still, this approximate spin-contaminated diradicalic UKS description greatly influences the reconstruction compared to the RKS case. Since the α- and β-ID COs can only overlap with themselves on neighboring dimers under PBCs and not with the orbital of opposite spin, the single dangling bond lobe is not able to form a significant ID bond. This contradicts the RKS solution and is easily understandable when comparing the two schematic configurations of Fig. 3.11b) and c): in the RKS calculation, the ID band has to be fully occupied, thus forming the ID bond counteracting the formation of the intradimer σ bond and inhibiting a stronger reconstruction. In the UKS solution, this ID bond is bisected, yielding two singly occupied dangling bonds and consequently resulting in stronger reconstruction with shorter d_{Si-Si} and more negative ΔE_{dimer}. The depicted calculated electron densities also support this since the dangling bond lobes of neighboring dimers overlap in the RKS case and do not in the UKS case.

The difference in reconstruction strength should also be the reason for the significantly different surface band gaps $E_{g,surf}$ of 0.53 eV for the RKS and 1.34 eV for the UKS HSE06 solution. As apparent from the band structures, the shorter dimer bonds of UKS obviously results in a stronger energetic splitting of the σ and σ^* bands compared to RKS. Consequently, it would be reasonable for the UKS ID and ID^* bands to become more degenerate since the shorter dimer bond is accompanied by larger ID distances and thus reduced overlap between neighboring dimers, which should decrease the bonding and antibonding character of both bands, respectively. This is, however, not the case as the surface band gap determined by these two bands increases significantly with respect to the RKS solution. A closer comparison of the ID band electron densities of both methodologies reveals the additional small electron cloud right below the σ bond of the dimer in the UKS case, which is quite similar to the small bonding orbital lobe at the same position of the π-like orbital in the MO diagram in Fig. 3.3. This intradimer bonding interaction might become more relevant in the UKS case due to the enhanced overlap as the dimer bond shortens and due to the supposed absence of the ID bonding. Accordingly, the corresponding antibonding interaction of the π^*-like orbital might also increase owed to the shorter dimer bond, explaining the observed increase in energy of the ID^* band parallel to the ID band. Since this increase of the surface band gap of UKS compared to RKS is most prominent at the J'-point, the corresponding ID and ID^* COs for both methodologies are additionally depicted in Fig. 3.12. While there is not any obvious antibonding intradimer interaction in the UKS α-ID^* CO, there certainly is intradimer bonding in the RKS ID^* CO, explaining the lower energy of the corresponding RKS ID^* band compared to its UKS counterpart. However, since only investigating a few $\vec{k}$-points might not be sufficient as it represents just a small part of the whole band structure, this interpretation has to be treated with caution.

Interestingly, as further apparent from Fig. 3.11a) and b), the RKS HSE06 surface band gap of the p(2×1) reconstruction with 0.53 eV is even smaller than for the ideal p(1×1) surface with 0.61 eV. Sabisch et al. observed a very similar behavior in their LDA calculations with virtually no change of the

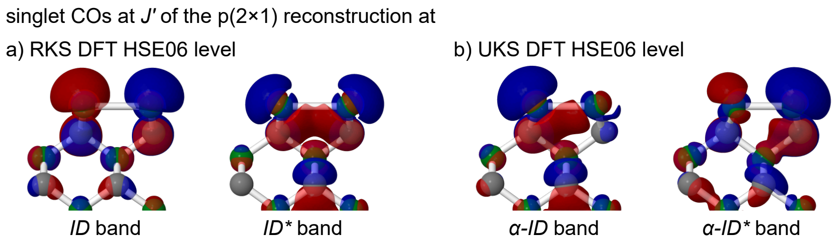

Figure 3.12: Singlet COs at J' of the ID and ID^* bands of the Si-terminated 3C-SiC(001)-p(2×1) reconstruction (SD model) at a) RKS and b) UKS DFT HSE06 level with the TZVPP/TZVP basis set for 2×1 supercell 12-layer periodic slab models. The isosurface value of the calculated orbitals and densities amounts to $0.01\,a_0{}^{-3}$.

band gap upon reconstruction.[45] This behavior is reasonable as the folded IA and IA^* bands split up, causing the emerging ID and ID^* bands to approach each other to overall reduce the band gap. The symmetry breaking of UKS, on the other hand, can counteract this effect, mainly by raising the energy and flattening the dispersion of the ID^* band, while the ID band is mostly unaffected in Fig. 3.11c).

As summarized in the review of Pollmann and Krüger,[28] various experimental studies confirm the presence of two occupied surface states for the p(2×1) reconstruction,[26,38,151–153,188,189] one emerging above the valence band maximum (VBM) of the bulk and the second about 1 eV below the first band,[28] which should correspond to the σ and ID bands in the calculated band structures of this work and previous theoretical studies.[39,43–45,151] However, as Pollmann and Krüger point out, the experiments only measured the band structure along the $\mathit{\Gamma}-J$ and $\mathit{\Gamma}-J'$, namely the x- and y-directions, showing a very flat band for the higher-lying surface state. This would correspond to the ID band, which in all previous calculations shows stronger dispersion than in the experiment. Accordingly, it was concluded that there is no good agreement between experiment and theory, which could also not be resolved by other structural models than the symmetric dimer, indicating further work to be necessary.[28] Unfortunately, the RKS and UKS band structures of this work, calculated with hybrid functionals for the first time, also do not give any better agreement with the experiment.

Benesch et al. determined several unoccupied surface states experimentally by inverse photoemission (IPE) spectroscopy.[154] The authors also compared their own IPE data and previous ultraviolet photoemission (UPS) results with published theoretical RKS LDA studies, to which the RKS and UKS HSE06 results of this work are added in Table 3.5. Here, the authors tried to match the experimental energy levels of the surface states at J' and $\mathit{\Gamma}$ with the LDA values of the ID^* and σ^* band. Since the LDA band gap strongly underestimates the experimental band gap, the calculated bands were shifted to better fit to the experimental data. Furthermore, because the σ^* band is located within the PBBS at $\mathit{\Gamma}$, they estimated the LDA value at this position by assuming the dispersion of this band to be equal to the σ band in the $\mathit{\Gamma}-J$ section due to the same symmetry. However, they referred to the work of Sabisch

Table 3.5: Experimental and theoretical energetic positions of surface states (SS) and surface resonances (SR) at certain high-symmetry $\vec{k}$-points of the Si-terminated 3C-SiC(001)-p(2×1) reconstructed surface (SD model) with respect to the VBM of the 3C-SiC bulk. The corresponding COs for the results of this work are depicted in Fig. 3.13. Created based on a table from Ref. [154].

		occupied		unoccupied				
Reference	Method	SR at J' [eV]	SS at Γ [eV]	SS at Γ [eV]	SR at Γ [eV]	SR at Γ [eV]	SR at Γ [eV]	SR at Γ [eV]
[38, 153]	UPS	-0.7	0.3	-	-	-	-	-
[152]	UPS	-0.6	0.7	-	-	-	-	-
[151]	UPS	-1.5	0.7	-	-	-	-	-
[154]	IPE	-	-	2.0	3.6	4.3	6.8	9.1
[45]	RKS LDA[a]	-1.1	0.5	2.2	$\approx 3.6^b$	-	-	-
[151]	RKS LDA[a]	-1.3	0.5	1.9	$\approx 3.5^b$	-	-	-
this work	RKS HSE06	-0.9	0.9	1.6	3.4	4.5	-	8.1
this work	UKS HSE06	-1.4	0.6	2.4	3.5	4.4	-	8.5

[a] LDA bands shifted in Ref. [154] to match the experimental band gap

[b] estimated values from Ref. [154] by extrapolating the dispersion of the σ^* band from the ID^* band (erroneously labeled as σ in the respective work[154]) for the $\Gamma-J$ section

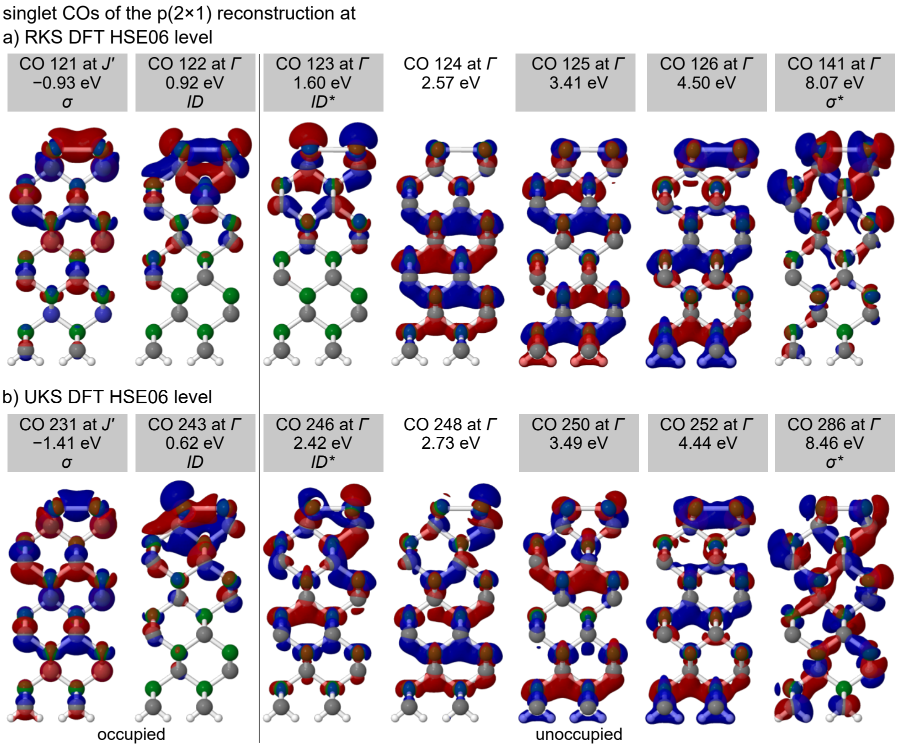

Figure 3.13: Singlet COs near the band gap and their energy levels of the Si-terminated 3C-SiC(001)-p(2×1) reconstructed surface (SD model) at a) RKS and b) UKS DFT HSE06 level with the TZVPP/TZVP basis set for 2×1 supercell 12-layer periodic slab models. The energy levels are given with respect to the VBM of the 3C-SiC bulk. In case of the UKS orbitals, only the COs of the α bands are shown. Only the energy levels highlighted in gray are listed in Table 3.5. The isosurface value of the calculated orbitals amounts to $0.01\,{a_0}^{-3}$.

et al., where the unoccupied surface states were labeled as σ and σ^* and the occupied surface states as π and π^*.[45] This was also done in other theoretical studies,[28,43] which is incorrect when taking the considerations of Section 3.1 into account. Accordingly, the values of the LDA calculations in Table 3.5 have to be treated with caution. The RKS and UKS HSE06 results of this work are more reliable as no artificial band gap enhancement is needed and the energetic values can actually be characterized by the COs of the surface states as depicted in Fig. 3.13.

Since the experimental values of the occupied surface states already differ quite strongly, a quantitative comparison appears to be difficult, which can be attributed to the determination of the VBM not being trivial experimentally and theoretically.[151,154] Still, the RKS and UKS HSE06 energy values for the lowest occupied surface resonance, i.e., the σ band, at J' fit into the range of the previous experimental and theoretical results. In case of the highest occupied surface state, namely the ID band, two of the three experimental studies[151,152] find an energy of 0.7 eV at Γ, which is in between the RKS and UKS HSE06 values of 0.9 eV and 0.6 eV, respectively. The same is true for the IPE results of the lowest unoccupied surface state, i.e., the ID^* band, with a value of 2.0 eV surrounded by the RKS and UKS HSE06 of 1.6 eV and 2.4 eV, respectively. Concerning the highest listed unoccupied surface resonance, the IPE experiments yield an energy of 3.6 eV, which is in good agreement with the RKS and UKS HSE06 values of 3.4 eV and 3.5 eV, respectively. It should be noted that, as apparent from Fig. 3.13, the corresponding COs of this unoccupied surface resonance (CO 125 for RKS and CO 250 for UKS) do not show the intuitively expected σ^* character. Instead, they appear to be a surface resonance mixed from a bulk state formed by Si $d_{x^2-y^2}$ orbitals and a σ bond at the Si dimer atoms constructed from the same orbitals. This d orbital σ bond is more pronounced in the very similar and energetically subsequent surface resonance (CO 126 and CO 252). Actually, in the surface band structure of Benesch et al., there is an energy level at 4.3 eV (2.7 eV in the study before considering the VBM shift of 1.6 eV for the bulk) at Γ,[154] which nicely matches the RKS and UKS values for the latter surface resonance with 4.5 eV and 4.4 eV, respectively. While for an isolated Si dimer the σ^* bond of sp^3 orbitals should be lower in energy than the d orbital σ bond, the former is supposedly destabilized due to the inferior overlap with the d orbital bulk states. The d orbitals contribute significantly to the bulk band structure near the conduction band minimum (CBM) as apparent in the COs and projected DOS (PDOS) plots in Fig. A.8, hence the σ^* bond is found at higher energies of 8.1 eV and 8.5 eV for RKS and UKS (CO 141 and CO 286), respectively. In the data of Benesch et al. there further is an energy level of 9.1 eV at Γ (7.5 eV before bulk VBM shift),[154] which might correspond to this σ^* surface resonance. The σ bond from d orbitals, on the other hand, shows superior overlap with the bulk orbitals of the same kind, explaining why this surface resonance is stabilized and thus located at such low energies. From this discussion, it can be concluded that the extrapolation of the LDA σ^* band done by Benesch et al.[154] giving such a good agreement with the experiment is apparently a coincidence as the d orbital σ surface resonance is energetically just at this position. Besides, the intermediate state (CO 124 and CO 248) not discussed so far is most likely not found experimentally as it is a pure bulk state with low surface amplitudes not detectable by the experimental surface sensitive methods. Regarding the experimental surface band structure of Benesch et al., only one energy level at 6.8 eV (5.2 eV before bulk VBM shift) at Γ[154] is left over and not assigned to a certain CO in this work. However, as there are various states in this energy region, an unambiguous assignment proves to be difficult and will thus not be attempted here.

Overall, as stated before by the cited authors,[28,154] while the qualitative agreement between experiment and theory regarding the electronic structure appears to be good, the quantitative results can neither fully confirm nor rule out the SD model to be the correct structure for the p(2×1) reconstruction of the Si-terminated 3C-SiC(001) surface. As Pollmann and Krüger indicated, other structural models could also not resolve this issue.[28] Since the UKS results of this work could also not give a substantially improved agreement with the experiment, a multiconfigurational treatment of the surface might resolve this issue. Unfortunately, the corresponding cluster model calculations conducted in Section 3.3 will also not be able to answer this particular question because the derivation of a band structure is not possible as will be discussed later. Nevertheless, it can be concluded that the HSE06 method appears to be the best choice with respect to DFT functionals for 3C-SiC since no subsequent shift of the energy levels is needed for a reasonable comparison to the experiment.

Turning the attention to the p(2×1) reconstruction with buckled dimers found for the RKS HSE06 calculations of the Si-terminated 3C-SiC(001) surface, the corresponding electronic structure is depicted in Fig. 3.14. In analogy to the buckled dimers on the Si(001) surface, where the JT splitting results in a doubly occupied sp^3 orbital at the upper and an unoccupied p_z orbital at the lower Si dimer atom,[49–52] the bands determining the band gap are denoted analogously. While the depicted COs do not clearly resemble this electronic structure also given schematically at the bottom of Fig. 3.14, the plotted electron density of the sp^3 band clearly shows the dangling bond lobe at the upper dimer atom. Still, the charge transfer to this atom is very small as the difference in Mulliken charges only amounts to $0.1\,e$. However, in early semiempirical calculations of the buckled dimers on the Si(001)-p(2×1) reconstructed surface, a comparably low value of $0.36\,e$ was found.[49] The lower charge transfer on the 3C-SiC surface might be attributed to the less pronounced buckling due to the smaller lattice constant compared to the Si(001) counterpart. While on the Si(001) surface both dimer atoms move closer to one another with respect to the ideal surface, on the 3C-SiC(001) surface one of the atoms basically stays in the ideal position with only the bond length to the underlying C atoms slightly increasing.

Interestingly, the band gap increase to 0.85 eV of the RKS HSE06 calculation of buckled dimers with respect to the ideal p(1×1) surface with 0.61 eV

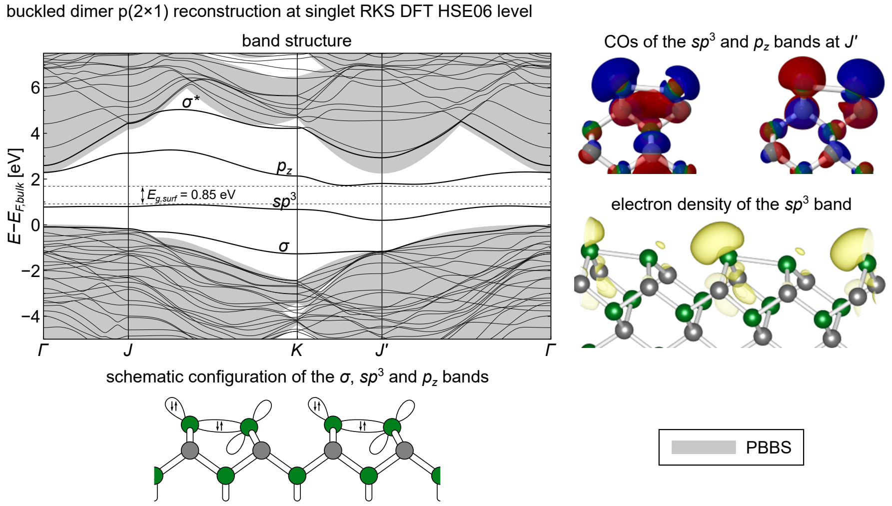

Figure 3.14: Electronic structure of the buckled dimer p(2×1) reconstructed Si-terminated 3C-SiC(001) surface at singlet RKS DFT HSE06 level with the TZVPP/TZVP basis set for a 2×1 supercell 12-layer periodic slab model. The isosurface value of the calculated orbitals and densities amounts to $0.01\,a_0{}^{-3}$.

seems to be in contrast to the calculation of symmetric dimers with the same methodology, which shows a smaller band gap of 0.52 eV. Previous studies even predict the buckled dimer to be metallic,[45] which can, however, supposedly be attributed to the less sophisticated LDA functional and especially the calculations being conducted for an unoptimized buckled structure. A comparison of the frontier COs at J' of the buckled dimer at RKS HSE06 level in Fig. 3.14 and of the symmetric dimer at UKS HSE06 level in Fig. 3.12 shows a very high similarity. This is reasonable as the buckling of the JT effect can be regarded as a spatial-symmetry breaking, while the UKS method induces a spin-symmetry breaking, both with the goal to further decrease the energy compared to the symmetric dimers with restricted and thus also spin-symmetric electronic structure. With this in mind, the band gap increase of the buckled dimers is in agreement with the UKS calculations also giving a larger band gap. However, it also follows from this that buckled dimers might still just be an artifact as a result of the inability of RKS to include static correlation because the UKS calculations, which can consider it to a certain extent, yield stronger reconstruction for symmetric dimers.

Lastly, the electronic structure of the high-spin state of the Si-terminated 3C-SiC(001)-p(2×1) reconstructed surface with symmetric dimers is shown in Fig. 3.15. As apparent in the band structure plot, the α and β bands are no longer degenerate and, as established in Section 2.1.1.2, the α bands are stabilized compared to their β counterparts due to the increased number of α electrons and thus the increased exchange interaction between them. In the electron density plots of the ID and ID^* bands, the shape of the π^* and π orbitals is clearly visible and since both bands are occupied by one electron per unit cell, a true diradicalic character of each dimer is obtained. As already mentioned in the previous section, the parallel spins of the dangling bonds

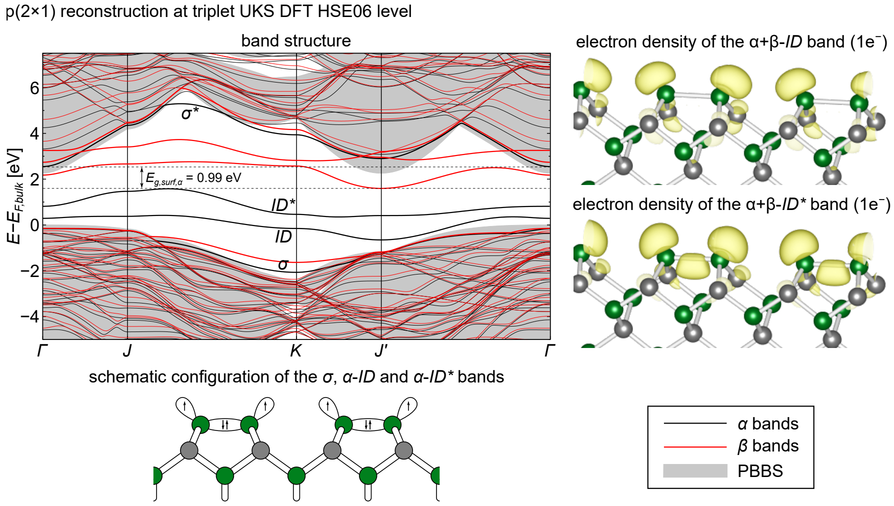

Figure 3.15: Electronic structure of the p(2×1) reconstructed (SD model) Si-terminated 3C-SiC(001) surface at triplet UKS DFT HSE06 level with the TZVPP/TZVP basis set for a 2×1 supercell 12-layer periodic slab model. The isosurface value of the calculated electron densities amounts to $0.005\,{a_0}^{-3}$.

prevent the formation of interdimer bonds, which expresses itself in the missing overlap between the dangling bond lobes of neighboring dimers in the electron density plots. While the electron densities might suggest otherwise, it should be noted that both ID and ID^* bands still exhibit π^* and π character at the same time but to a lesser extent than the corresponding singlet RKS bands as apparent from Fig. A.13. Since the α and β bands are non-degenerate, there are two different surface band gaps, namely $E_{g,surf,\alpha}$ and $E_{g,surf,\beta}$, of which the latter is given in Fig. 3.15 with 0.99 eV. However, because the CBM of the slab model located at Γ is higher in energy than the CBM of the PBBS, the true band gap under consideration of the bulk band structure should amount to about 0.67 eV. From this, it can be concluded that the periodic slab models are not able to properly recover the electronic structure of the bulk, which will be further investigated in Section 3.2.3.5.

3.2.3.4 Reconstructions in Larger Supercells

In the next step, the translational freedom of the Si-terminated 3C-SiC(001) surface was further extended by utilizing larger supercells, namely a rhombic $(\sqrt{5}\times\sqrt{5})R(2\cdot\tan^{-1}(0.5))$ supercell and a 4×2 supercell, with the corresponding 12- and 10-layer periodic slab models being depicted in Fig. 3.16. As the HSE06 functional with the TZVPP/TZVP basis set appeared to be the most reliable choice in the previous sections to investigate the Si-terminated 3C-SiC(001) surface, this methodological combination will mainly be used in the following. Furthermore, only the singlet spin-state will be discussed since the high-spin states yielded, as expected, results identical to the 2×1 supercell calculations presented earlier. At first, it should be checked whether the AUDD or the SD model is favored for the unstrained surface, for which the

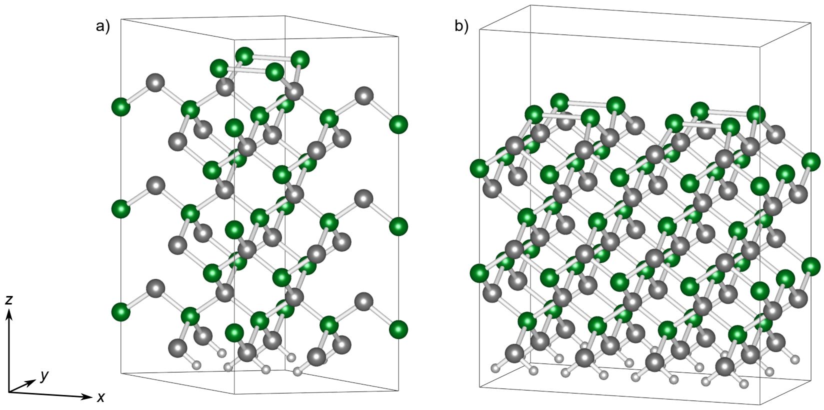

Figure 3.16: H-saturated a) 12- and b) 10-layer periodic slab models for the p(2×1) reconstructed (SD model) Si-terminated 3C-SiC(001) surface in a a) rhombic $(\sqrt{5}\times\sqrt{5})R(2\cdot\tan^{-1}(0.5))$ supercell and a b) 4×2 supercell. Both structures were optimized at singlet UKS DFT HSE06 level with the TZVPP/TZVP basis set and spin arrangement 1 of Table 3.6 for a) and spin arrangement 1 of Table 3.7 for b). The lattice parameter of the unit cells in z is depicted smaller than it is in the actual calculations.

rhombic supercell is sufficient. AUDD model starting structures of different dimer bond lengths and z-height differences between the dimers were created and optimized. In case of the singlet UKS calculations, different spin arrangements are possible since there are four dimer atoms per rhombic unit cell, to which the two α and two β electrons have to be distributed. The total number of different spin arrangements amounts to:

$$\frac{4!}{2!\cdot 2!} = 6 \tag{3.2}$$

Since two arrangements of identical order but inverted spins are energetically degenerate, e.g., $\uparrow\uparrow\downarrow\downarrow$ is equal to $\downarrow\downarrow\uparrow\uparrow$, the number is halved to three and the different possibilities are listed in the first column of Table 3.6, which correspond to the numbering of the dimer atoms depicted in Fig. 3.17a). Regarding the RKS DFT HSE06 calculations, the c(4×2) AUDD starting structure always converged towards a p(2×1) reconstruction either of symmetric or buckled dimers with reconstruction energies ΔE_{dimer} of -0.01 eV and -0.05 eV, respectively, already found in the previous sections. As apparent from Table 3.6, the UKS calculations with the three different spin arrangements all converged exclusively to the SD model but with different dimer bond lengths, reconstruction energies, and surface band gaps. The first spin arrangement is equal to the one chosen before for the singlet UKS calculations of the 2×1 supercells and accordingly gives the same results with ΔE_{dimer} of -0.23 eV. The reconstruction energies of the spin arrangements 2 and 3 amount to -0.10 eV and -0.31 eV, respectively, which corresponds to quite substantial relative deviations of over 50 %. The decreased reconstruction of spin arrangement 2 can be intuitively explained by the parallel spin of the dangling bonds of neighboring dimers in each dimer row preventing the formation of an interdimer bond, which also significantly reduces the dimer bond length to 2.40 Å. Spin arrangement 3 basically consists of α and β high-spin dimers, which occur alternately

Table 3.6: Dimer bond lengths d_{Si-Si}, reconstruction energies ΔE_{dimer}, surface band gaps $E_{g,surf}$, and spin contamination $\Delta\langle\hat{S}^2\rangle$ per dimer for the H-saturated rhombic $(\sqrt{5}\times\sqrt{5})R(2\cdot\tan^{-1}(0.5))$ supercell 12-layer periodic slab model of the Si-terminated 3C-SiC(001)-p(2×1) reconstructed surface (SD model) optimized at singlet UKS DFT HSE06 level with the TZVPP/TZVP basis set for the different possible spin arrangements. The assignment of the spins to the atoms is done according to the numbering in Fig. 3.17a). Spin density values are available in Table A.2.

Start Spins at Si Dimer Atoms 1 to 4 in Fig. 3.17a)	d_{Si-Si} [Å]	ΔE_{dimer} [eV]	$E_{g,surf}$ [eV]	$\Delta\langle\hat{S}^2\rangle$ per Dimer
1:[a] ↑↓ ↑↓	2.46	−0.23	1.36	0.80
2: ↑↓ ↓↑	2.40	−0.10	1.01	0.95
3: ↑↑ ↓↓	2.45	−0.31	1.64	0.81

[a] equal to singlet UKS HSE06 of Table 3.3

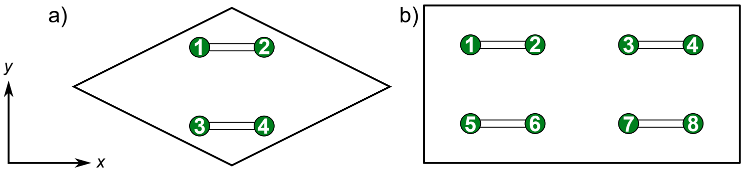

Figure 3.17: Numbering of the dimer atoms of the Si-terminated 3C-SiC(001) surface to define the different spin arrangements used in the singlet UKS DFT calculations for the a) rhombic $(\sqrt{5}\times\sqrt{5})R(2\cdot\tan^{-1}(0.5))$ supercell in Table 3.6 and for the b) 4×2 supercell in Table 3.7.

in each dimer row. In this way, an interdimer bond can supposedly be formed and at the same time, a stabilizing intradimer exchange interaction exists, further reducing the total energy compared to spin arrangement 1. Interestingly, the surface band gaps also increase or decrease with the reconstruction energy as the new spin arrangements yield values of 1.01 eV and 1.64 eV, respectively, surrounding the value of 1.36 eV of spin arrangement 1. However, as further apparent from Table 3.6, these singlet polyradicals are spin-contaminated and can each be interpreted as one determinant needed for a linear combination to give the true singlet radicalic configuration. Furthermore, since the spin contamination is comparable but not equally high for each of the spin arrangements, a comparison of the energies and an energetic ordering proves to be difficult. Nevertheless, from these results one could estimate the correct spatial and electronic structure to be somewhere in the region of these three values. In any case, the hybrid DFT calculations of this work further support the previous theoretical studies finding the SD model to be favored over the AUDD model for unstrained surfaces.[28,42,46–48]

With this in mind, the AUDD model was not considered further for the 4×2 supercell calculations of the Si-terminated 3C-SiC(001) surface presented in the following. Accordingly, the starting structures for the geometry optimizations were restricted to the SD model obtained in the singlet UKS calculations on the 2×1 supercell to investigate the effect of additional spin arrangements, which are possible due to the lower translational symmetry of the 4×2 supercell. Again, the total number of different spin arrangements when assigning four α

and four β electrons to eight dimer atoms calculates as:

$$\frac{8!}{4! \cdot 4!} = 70 \tag{3.3}$$

Besides halving this value to 35 to exclude identical arrangements of inverted spin, additionally, as empirically determined, translational and rotational symmetry have to be considered. To be more precise, this corresponds to translating the spin arrangement by one dimer along x, by one dimer row along y, diagonally by the combination of both of these operations, as well as the combination of the previous three translational operations with the C_2-rotation around the supercell center as well as the sole C_2-rotation, giving overall seven symmetry operations. This reduces the number of unique spin arrangements from 35 to 14 for the 4×2 supercell, which are listed in the first column of Table 3.7 and are associated to the dimer atom numbering depicted in Fig. 3.17b). Among these are, of course, the previous one p(2×1) and two c(4×2) spin arrangements from the 2×1 and rhombic supercells, namely spin arrangements 1, 5, and 14, which stay in their SD model structure with the same spatial and electronic parameters obtained before. All of the remaining spin arrange-

Table 3.7: Reconstruction energies ΔE_{dimer}, surface band gaps $E_{g,surf}$, and spin contamination $\Delta \langle \hat{S}^2 \rangle$ per dimer for the H-saturated 4×2 supercell 10-layer periodic slab model of the Si-terminated 3C-SiC(001) reconstructed surface optimized at singlet UKS DFT HSE06 level with the TZVPP/TZVP basis set for the different possible spin arrangements. The assignment of the spins to the atoms is done according to the numbering in Fig. 3.17b). Spin density values and dimer bond lengths are available in Table A.3.

Start Spins at Si Dimer Atoms 1 to 8 in Fig. 3.17b)	ΔE_{dimer} [eV]	$E_{g,surf}$ [eV]	$\Delta \langle \hat{S}^2 \rangle$ per Dimer
1:[a] ↑↓ ↑↓ ↑↓ ↑↓	−0.23	1.36	0.80
2: ↑↓ ↑↓ ↓↑ ↑↓	−0.24	1.50	0.79
3: ↑↓ ↓↑ ↑↓ ↑↓	−0.17	1.08	0.86
4: ↑↓ ↓↑ ↑↓ ↓↑	−0.09	0.78	0.98
5:[b] ↑↓ ↓↑ ↓↑ ↑↓	−0.10	1.02	0.95
6: ↑↓ ↓↑ ↑↑ ↓↓	−0.20	1.10	0.88
7: ↑↓ ↓↓ ↑↓ ↑↑	−0.21	1.08	0.85
8:[c] ↑↓ ↓↓ ↑↑ ↑↓	−0.29	1.12	0.48
9: ↑↓ ↓↓ ↑↑ ↓↑	−0.21	1.03	0.85
10:[c] ↑↑ ↑↓ ↓↓ ↓↑	−0.29	1.12	0.48
11: ↑↑ ↑↑ ↓↓ ↓↓	−0.17	0.55	0.95
12: ↑↑ ↓↓ ↑↓ ↑↓	−0.27	1.42	0.81
13: ↑↑ ↓↓ ↑↑ ↓↓	−0.29	1.17	0.83
14:[d] ↑↑ ↓↓ ↓↓ ↑↑	−0.31	1.65	0.81

[a] equal to singlet UKS HSE06 of Table 3.3 and spin arrangement 1 of Table 3.6

[b] equal to spin arrangement 2 of Table 3.6

[c] change of sign in atomic spin densities (see Table A.3) during geometry optimization to p(4×1) reconstruction (see Fig. 3.18a)

[d] equal to spin arrangement 3 of Table 3.6

ments, except for 8 and 10, also gave symmetric dimers but the bond length of the four dimers in one supercell could differ in the range of 2.38 Å – 2.48 Å as apparent from Table A.3. The general correlation of equally in- or decreasing ΔE_{dimer} and $E_{g,surf}$ values already observed for the rhombic spin arrangements seems to continue but not as strict as anticipated. The range of reconstruction energies is extended to −0.09 eV – −0.31 eV and of surface band gaps to 0.55 eV – 1.65 eV compared to the rhombic unit cell, though both the strongest reconstruction and largest band gap were already achieved for the spin arrangement 3 of the rhombic case.

The spin arrangements 8 and 10 stand out in Table 3.7 due to their low spin contamination value of 0.48 each, which is about half as low as the remaining spin arrangements. This is reasonable since these calculations did not converge towards a p(2×1) reconstruction with symmetric dimers but instead gave a p(4×1) reconstruction within the 4×2 supercell, which is depicted in Fig. 3.18a). Basically, two dimers themselves dimerize again in this structure by lengthening the intradimer bonds and shortening the interdimer distance compared to the UKS SD model, which also results in each of the original dimers to buckle by $\Delta z_{Si-Si} = 0.19$ Å. The reconstruction energy amounts to −0.29 eV and thus is the second most stable of all possible spin arrangements in the 4×2 supercell. While the outer two Si surface atoms of each p(4×1) unit remain radicalic with spin densities of ±0.66 (see Table A.3), the additional dimerization leads to reduced spin densities at the inner two surface atoms amounting to ±0.13, thus almost representing a closed-shell situation overall reducing the spin contamination. Obviously, in principle, there also exist 14 different spin arrangements for this p(4×1) reconstruction in the 4×2 supercell but since the inner dimer atoms show such low spin densities, only the three possibilities listed in Table 3.8 were explored. Here, spin arrangement 2 is identical to the converged spin arrangements 8 and 10 of Table 3.7. Generally, it appears that the influence of the spin arrangement on the reconstruction energy is negligible, probably due to the large distance of about 4.2 Å – 4.3 Å between the surface Si atoms of neighboring p(4×1) units, which carry the spin

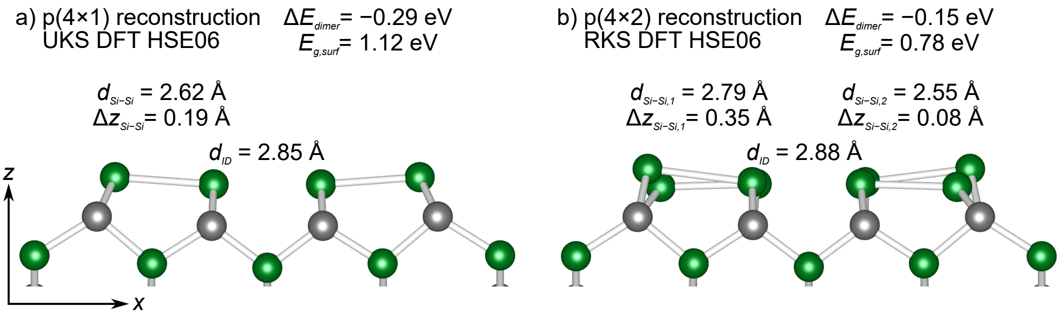

Figure 3.18: a) p(4×1) and b) p(4×2) reconstructions of the Si-terminated 3C-SiC(001) surface found for a H-saturated 4×2 supercell 10-layer periodic slab model at singlet a) UKS and b) RKS DFT HSE06 level with the TZVPP/TZVP basis set. Structure a) corresponds to spin arrangements 8 and 10 in Table 3.7 or spin arrangement 2 in Table 3.8. The structural parameters of b) are given for the dimer row in the front.

Table 3.8: Reconstruction energies ΔE_{dimer}, surface band gaps $E_{g,surf}$, and spin contamination $\Delta \langle \hat{S}^2 \rangle$ per dimer for the H-saturated 4×2 supercell 10-layer periodic slab model of the Si-terminated 3C-SiC(001)-p(4×1) reconstructed surface optimized at singlet UKS DFT HSE06 level with the TZVPP/TZVP basis set for the different possible spin arrangements. The assignment of the spins to the atoms is done according to the numbering in Fig. 3.17b). Spin density values and bond lengths are available in Table A.4.

Start Spins at Si Dimer Atoms 1 to 8 in Fig. 3.17b)	ΔE_{dimer} [eV]	$E_{g,surf}$ [eV]	$\Delta \langle \hat{S}^2 \rangle$ per Dimer
1: $\uparrow 0 \quad 0 \downarrow \quad \uparrow 0 \quad 0 \downarrow$	-0.29	1.12	0.49
2:[a] $\uparrow 0 \quad 0 \uparrow \quad \downarrow 0 \quad 0 \downarrow$	-0.29	1.12	0.48
3: $\uparrow 0 \quad 0 \downarrow \quad \downarrow 0 \quad 0 \uparrow$	-0.30	1.31	0.48

[a] equal to converged spin arrangements 8 and 10 of Table 3.7

density. Still, spin arrangement 3 shows a significantly larger surface band gap of 1.31 eV compared to the 1.12 eV of the other two arrangements.

To check if this p(4×1) reconstruction could also be obtained for the restricted approach, a geometry optimization at RKS HSE06 level of such a starting structure in the 4×2 supercell was additionally conducted. Interestingly, a p(4×2) reconstruction as depicted in Fig. 3.18b) resulted instead, which consists of two dimerized buckled dimers within each of the two 4×1 units. Here, one 4×1 unit buckles in positive and the other in negative x-direction. This reconstruction is remarkably strong for an RKS structure with ΔE_{dimer} of -0.15 eV compared to the symmetric and buckled dimer p(2×1) reconstructions giving values of -0.01 eV and -0.05 eV for the same method, respectively.

Trabada and Ortega[173] were able to find identical p(4×1) and p(4×2) reconstructions for the Si-terminated 3C-SiC(001) surface. However, they obtained the p(4×1) structure in LDA calculations with a plane wave basis set but not the p(4×2) reconstruction at the same level of theory. The latter was only found in semiempirical tight-binding (TB) calculations as the minimum energy structure, with the p(4×1) reconstruction also representing a local minimum. As these authors could obtain the p(4×1) reconstruction using a restricted formalism, it was further attempted to do the same in this work by reducing the supercell size to 4×1 to avoid the formation of the p(4×2) reconstruction, which was successful eventually with a structure very similar to the UKS case (see bond lengths in Table A.5). It was also tried to converge a buckled p(4×1) reconstruction using RKS in the 4×1 supercell, which simply corresponded to one 4×1 unit of the p(4×2) reconstruction, but it converged to the p(2×1) buckled dimer structure. Furthermore, an UKS calculation of the p(4×2) reconstruction was also attempted but it collapsed to the RKS solution immediately. All calculations were additionally carried out with the LDA and PBE functional for a better comparability to the RKS LDA and TB results of Trabada and Ortega[173] as listed in Table 3.9. Regarding the surface band gap, the RKS calculations of the cited authors are in accordance with the results of this work, namely giving a conducting p(4×1) reconstruction and a semiconducting p(4×2) structure. The very small band gap of 0.02 eV

Table 3.9: Comparison of the reconstruction energies ΔE_{dimer} and surface band gaps $E_{g,surf}$ for the p(4×1) and p(4×2) reconstructed Si-terminated 3C-SiC(001) surfaces at singlet RKS and UKS DFT level with the TZVPP/TZVP basis set and different DFT functionals to the theoretical results of Trabada and Ortega.[173] The UKS calculations of this work used spin arrangement 1 of Table 3.8. Spin density values, bond lengths, and spin contamination per dimer of this work's results are available in Table A.5.

Reconstruction	Parameter	RKS					UKS		
		This Work			Ref. [173]		This Work		
		HSE06	PBE	LDA	LDA	TB	HSE06	PBE	LDA
p(4×1)	ΔE_{dimer} [eV]	−0.03	−0.07	−0.04	−0.12	−0.17	−0.29	−0.14	−0.05
	$E_{g,surf}$ [eV]	cond.	0.02	cond.	-	cond.	1.12	0.35	0.14
p(4×2)	ΔE_{dimer} [eV]	−0.15	−0.10	−0.07	-	−0.21	collapse to p(4×2) RKS solution		
	$E_{g,surf}$ [eV]	0.78	0.23	0.22	-	0.33			

in the PBE case supposedly still indicates metallic character and might just be a numerical issue. Furthermore, most of the calculations find the p(4×2) reconstruction to be more stable than the p(4×1) reconstruction with the only exception being the LDA calculations of Trabada and Ortega not obtaining the former as a local minimum at all. This might be a consequence of the quite low energy cutoff of 280 eV and thus a rather small plane wave basis set since the TB calculations of the same authors could also only obtain the p(4×2) structure when using a double-zeta GTO basis set and not for a minimal basis. This insufficient basis could also be a reason for the significantly stronger reconstruction energies compared to this work's results. When employing an unrestricted approach to the p(4×1) structure, the reconstruction is even stronger energetically than the RKS p(4×2) case. Interestingly, at the same time, the surface changes from conducting to semiconducting with respect to the RKS p(4×1) reconstruction. This can be explained as follows: when forming the p(4×1) reconstruction, the interdimer bond inside the 4×1 unit is shortened, while the interdimer bond towards the neighboring 4×1 units is lengthened compared to the p(2×1) reconstruction of symmetric dimers. This results in the ID_{short} and ID^{*}_{short} bands to further split and the ID_{long} and ID^{*}_{long} bands to become more degenerate due to the increased and decreased overlap, respectively, as apparent from the RKS band structure and COs in Fig. 3.19a). Consequently, the Fermi level cuts through both of these bands in the RKS case, causing a partial occupation and thus conducting or metallic behavior of the surface. The UKS formalism in Fig. 3.19b), on the other hand, is able to separate the ID_{long} and ID^{*}_{long} bands again by spin-symmetry breaking and the resulting localization of the α- and β-COs at either of the two Si atoms. Basically, the situation is similar to the p(2×1) reconstruction of symmetric dimers: while RKS tries to maintain a double occupation of the energetically unfavorable ID_{long} bond, UKS is able to break this bond to gain energy. This also explains the substantially stronger reconstruction energies of the p(4×1) UKS results compared to the RKS analogue in Table 3.9. However, despite the different conductivity, the electron densities of the involved bands of both methodologies are almost identical as apparent from Fig. 3.20a) and b). This is reasonable as the situation of half-filled ID_{long} and ID^{*}_{long} bands

a) p(4×1) reconstruction at singlet RKS DFT HSE06 level

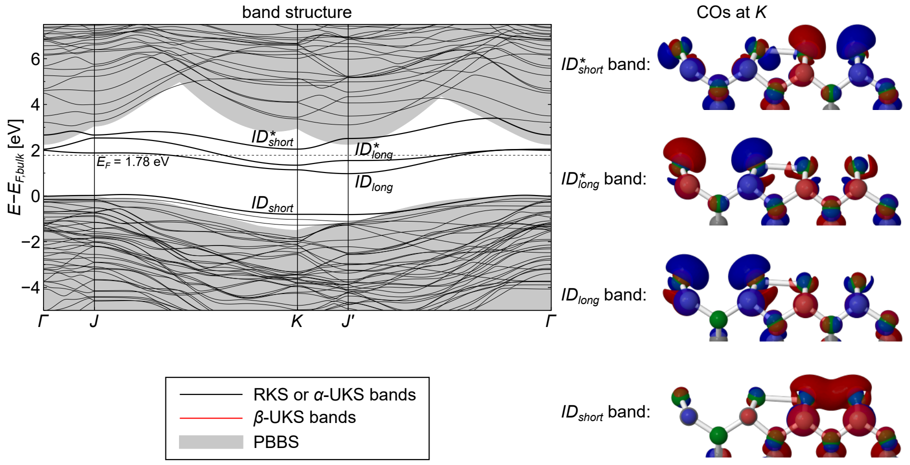

b) p(4×1) reconstruction at singlet UKS DFT HSE06 level

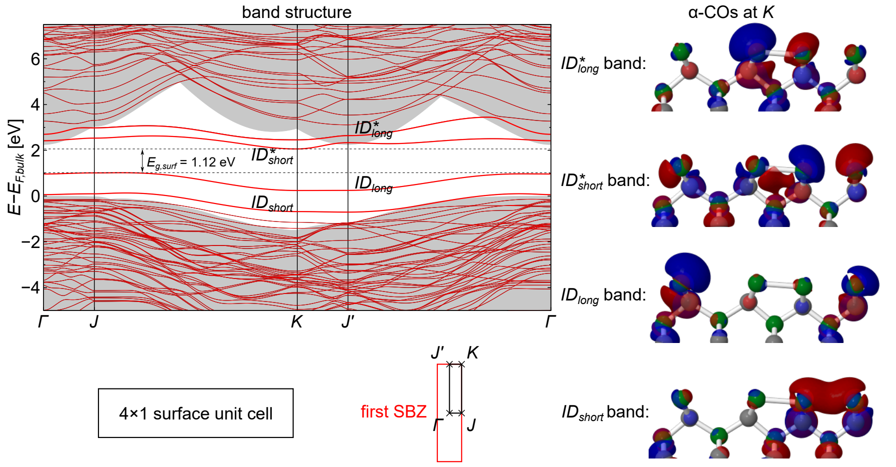

Figure 3.19: Electronic structure of the p(4×1) reconstructed Si-terminated 3C-SiC(001) surface at singlet a) RKS and b) UKS DFT HSE06 level with the TZVPP/TZVP basis set for H-saturated 4×1 supercell 10-layer periodic slab models. The UKS calculation used spin arrangement 1 of Table 3.8. In b), only the β-UKS bands are visible as they coincide with their degenerate α counterparts. The isosurface value of the calculated orbitals amounts to $0.01\,{a_0}^{-3}$. The surface unit cell and the corresponding first SBZ with the employed $\vec{k}$-path is additionally depicted at the bottom.

of RKS is conceptionally very similar to the singly occupied α- and β-ID_{long} bands of UKS. Besides the singlet diradical character itself, this strong change in conductivity with respect to the restricted or unrestricted approach is supposedly also an indicator of the strong multiconfigurational character of this p(4×1) reconstruction.

The RKS p(4×2) reconstruction is the analogue of the buckling of symmetric p(2×1) dimers found before for RKS HSE06: to separate the metallic ID_{long} and ID^*_{long} bands of the p(4×1) RKS geometry, the spatial symmetry with respect to the σ_{yz} mirror plane in the center of the 4×1 unit is broken. Consequently, the ID_{short} and ID_{long} bonds localize as lone pairs at the upper Si atoms of the two buckled dimers of each 4×1 unit as apparent from the

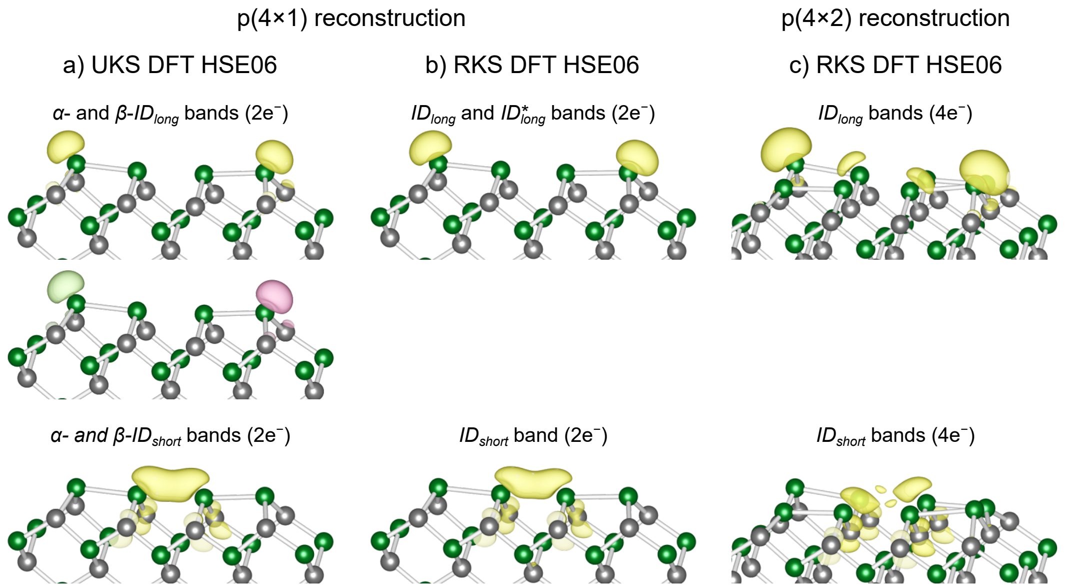

p(4×1) reconstruction

p(4×2) reconstruction

a) UKS DFT HSE06

b) RKS DFT HSE06

c) RKS DFT HSE06

Figure 3.20: Electron and spin densities for the a+b) p(4×1) and c) p(4×2) reconstructions of the Si-terminated 3C-SiC(001) surface found for a H-saturated a+b) 4×1 and c) 4×2 supercell 10-layer periodic slab model at singlet a) UKS and b+c) RKS DFT HSE06 level with the TZVPP/TZVP basis set. Structure a) corresponds to spin arrangement 1 in Table 3.8. The isosurface value amounts to $0.01\,{a_0}^{-3}$.

electron density plots in Fig. 3.20c). While this leads to a regular sp^3 orbital at the outer upwards buckled Si atom of each 4×1 unit similar to the p(2×1) buckled dimers, the sp^3 orbital of the inner upwards buckled Si atom seems to donate electron density to the neighboring p_z orbital of the inner downwards buckled Si atom, which can be interpreted as a dative interdimer bond. Why this buckled structure is favored over the p(2×1) buckled dimers only as p(4×2) and not as p(4×1) reconstruction might be a consequence of the repulsion of neighboring lone pairs at the upmost Si atoms in the p(4×1) case. This effect is reduced in the p(4×2) case due to the alternating buckling of the 4×1 units neighbored in y-direction. Though not stated explicitly in the literature, the same reasoning should explain why the p(2×2) reconstruction of alternately buckled dimers in y-direction is stabilized with respect to the p(2×1) structure of dimers buckled in the same direction on the Si(001) surface.[190] As the lattice constant of 3C-SiC is smaller than that of Si, this effect is supposedly more pronounced for the former material. This smaller lattice constant should also be the reason why further dimerization of the dimers to 4x1 units is possible for Si-terminated 3C-SiC(001) but not for Si(001), where it was not observed yet.

As established before, experimentally a c(4×2) reconstruction is found to be the most stable surface at RT for Si-terminated 3C-SiC(001).[27,28] While the AUDD model fulfills this translational symmetry, theoretically it was generally not observed for unstrained surfaces. Trabada and Ortega[173] already pointed out the close relation of the p(4×2) reconstruction and the AUDD model as the former also shows dimers of alternating height in z. The authors suggest that the p(4×2) reconstruction is only stable at very low temperatures and that the observed c(4×2) reconstruction is only the result of time-averaging of temperature-induced dimer motion in the experiment. While this argumentation is reasonable, the newly obtained UKS p(4×1) reconstruction being more stable than the RKS p(4×2) structure and not showing dimers of alternating height might question this conclusion. On the other hand, since the UKS solution is spin-contaminated, it is hard to judge if this energetic order is correct with respect to the small absolute energy differences.

Nevertheless, using the p(4×1) structure, a novel reconstruction of actual c(4×2) symmetry was additionally created by shifting every second row of 4×1 units by two times the ideal p(1×1) surface basis vector of 3.08 Å in x-direction as depicted in Fig. 3.21. Since this was done in a 4×2 supercell, again three different singlet spin arrangements analogously to Table 3.8 were tested for the UKS formalism and a regular RKS calculation was conducted as well. Furthermore, a UKS and RKS calculation in the rhombic supercell depicted in Fig. 3.21b) was carried out. The rhombic RKS calculation led to buckled dimers of p(2×1) symmetry and the RKS 4×2 supercell calculation was not able to converge at all. The UKS calculation in the rhombic and two of the UKS calculations in the 4×2 supercell gave symmetric dimers, namely spin arrangement 3 in Table 3.6 and spin arrangements 13 and 14 in Table 3.7, respectively. The remaining UKS calculation actually maintained the c(4×2) symmetry with the structure depicted in Fig. 3.22. However, the 4×1 units within this structure are quite different from the p(4×1) reconstruction as the buckling is negligible with Δz_{Si-Si} of 0.01 Å. Furthermore, the bonding interaction between the two dimers in each 4×1 unit seems to be weaker with a distance d_{ID} of 3.10 Å, which is even slightly larger than their distance of 3.08 Å on the ideal p(1×1) surface. This further expresses itself in the relatively weak reconstruction energy of −0.16 eV. Accordingly, this c(4×2) reconstruction energetically ranks among the weaker UKS p(2×1) structures of symmetric dimers in Table 3.7, explaining why the other two c(4×2) calculations converged to symmetric dimers instead. Along these lines, the spin arrangement of the successful c(4×2) optimization can be associated with spin arrangement 11 of Table 3.7 with a reconstruction energy of −0.17 eV, thus weak enough to actually reach the local c(4×2) minimum of similar energy of −0.16 eV. Over-

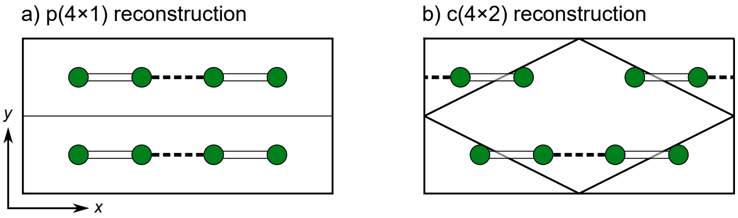

Figure 3.21: b) Novel c(4×2) reconstruction for the Si-terminated 3C-SiC(001) surface derived from the a) p(4×1) structure in a 4×2 supercell by shifting the upper 4x1 unit by two times the ideal p(1×1) surface basis vector of 3.08 Å in x-direction. The interdimer interaction between the two dimers of each 4x1 unit is indicated by the dotted line and the primitive rhombic $(\sqrt{5}\times\sqrt{5})R(2\cdot\tan^{-1}(0.5))$ unit cell is additionally depicted in b).

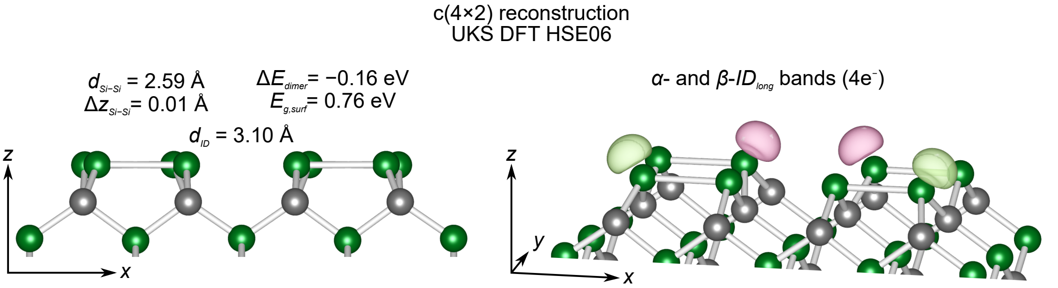

Figure 3.22: Spatial structure and spin density of the novel c(4×2) reconstruction of the Si-terminated 3C-SiC(001) surface found for a H-saturated 4×2 supercell 10-layer periodic slab model at singlet UKS DFT HSE06 level with the TZVPP/TZVP basis set. The isosurface value amounts to 0.01 $a_0{}^{-3}$. The Mulliken atomic spin densities at the outer Si atoms of the 4×1 units amount to ±0.66 and at the inner Si atoms to ±0.12. The spin contamination per dimer amounts to 0.50.

all, this novel c(4×2) reconstruction seems to be less likely than the p(2×1) or p(4×1) reconstructions in the UKS case and than the p(4×2) reconstruction in the RKS case.

3.2.3.5 Slab Model Convergence

As indicated at the end of Section 3.2.3.3, the periodic slab models are not able to recover the electronic structure of the bulk. This was first noticeable in the high-spin p(2×1) reconstruction because there the surface band gap would not occur between two surface state bands in the bulk band gap of the PBBS but between an occupied surface state band and an empty bulk band. But since the bulk-like states of the slab model do not reach the CBM, the surface band gap is overestimated. Sagisaka et al.[127] made a similar observation for their DFT study on the Si(001)-p(2×2) reconstructed surface, in which they showed that a converged bulk band gap within the slab model was only achieved for 78 atomic layers in z-direction. Accordingly, the same was done in this work by optimizing H-saturated slab models of the Si-terminated 3C-SiC(001)-p(2×1) reconstructed surface with symmetric dimers and up to 50 atomic layers at RKS DFT HSE06 level with the TZVPP/TZVP basis set. In analogy to Sagisaka et al., subsequent calculation the PDOS of the two middle layers, i.e., one Si and one C layer, allowed to determine the bulk band gap of each slab model as depicted in Fig. 3.23. It should be noted that this determination was not unambiguous for slab models containing a small number of layers because the middle atomic layers are close enough to the surface to be involved in the surface states, yielding spurious peaks in the energy region of interest. Nevertheless, as further apparent from Table 3.10, the bulk band gaps of the slab models do indeed converge very slowly also for the 3C-SiC(001) surface, only reaching the actual bulk band gap for 50 atomic layers. Furthermore, as anticipated, the surface band gap of the singlet RKS and UKS calculations is already basically converged for eight layers, while the high-spin surface band gap converges at the same rate as the bulk band gap, coming close to the value

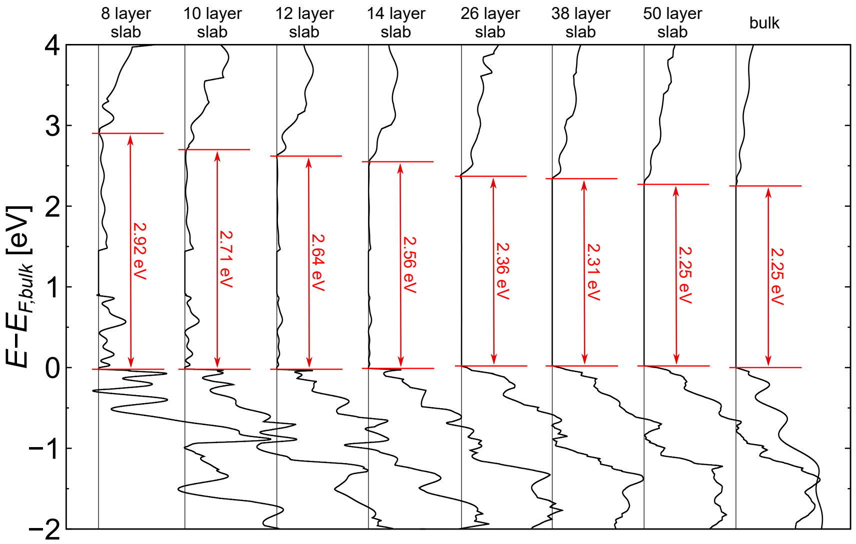

Figure 3.23: PDOS of the two middle atomic layers of H-saturated 2×1 supercell periodic slab models of the Si-terminated 3C-SiC(001)-p(2×1) reconstructed surface (SD model) at RKS DFT HSE06 level with the TZVPP/TZVP basis set to show the convergence of the bulk band gap $E_{g,slab}$ with respect to the number of atomic layers.

Table 3.10: Convergence of the bulk and surface band gaps ($E_{g,slab}$ and $E_{g,surf}$) of H-saturated 2×1 supercell periodic slab models of the Si-terminated 3C-SiC(001)-p(2×1) reconstructed surface (SD model) with respect to the number of atomic layers at RKS and UKS DFT HSE06 level with the TZVPP/TZVP basis set. The values of $E_{g,slab}$ were extracted from PDOS calculations of the two middle atomic layers of the respective RKS slab model (see Fig. 3.23). The UKS calculations used the spin arrangements of Table 3.3. At the bottom, the calculated band gap of bulk 3C-SiC is given. Reprinted with permission from *J. Phys. Chem. C* 2023, 127, 48, 23475–23488. Copyright 2023 American Chemical Society. Added columns with UKS results. Corrected $E_{g,slab}$ for 10 layers with respect to the publication's original value of 2.62 eV.

Number of Atomic Layers	$E_{g,slab}$ [eV]	$E_{g,surf}$ [eV]		
		Singlet RKS	Singlet UKS	High-Spin UKS
8	2.92	0.532	1.372	1.303
10	2.71	0.529	1.362	1.118
12	2.64	0.526	1.347	0.995
14	2.56	0.523	1.345	0.919
26	2.36	0.524	1.340	0.754
38	2.31	0.524	1.340	0.713
50	2.25	0.522	1.340	no convergence
bulk	2.25			

of 0.67 eV predicted before. Unfortunately, the 50-layer high-spin calculation did not converge to fully confirm this. The convergence of the bulk band gap within the slab models is also obvious when comparing the previous band structures of the 12-layer slab models (e.g., Fig. 3.11) with the band structure of the 50-layer slab model depicted in Fig. 3.24, where only in the latter case the bands of the slab model reach the VBM and CBM of the PBBS. The slow convergence can be simply explained by the electronic structure theory of solids: due to the limited number of layers of the slab models in z, only a few

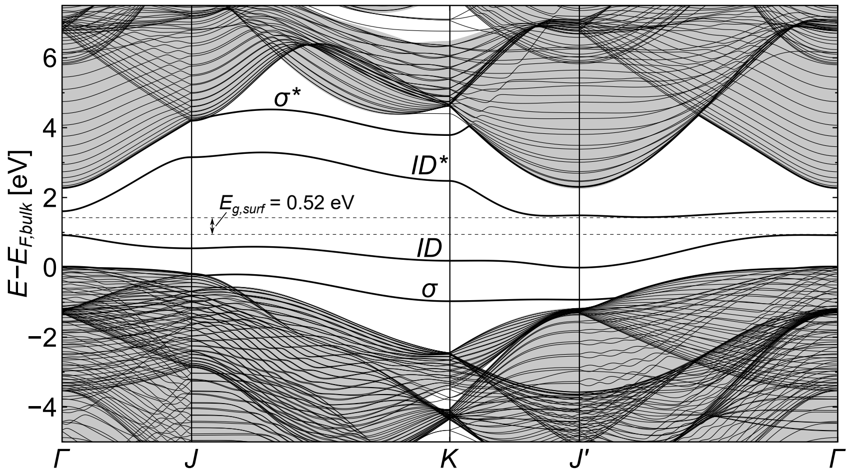

Figure 3.24: Band structure of the Si-terminated 3C-SiC(001)-p(2×1) reconstructed surface (SD model) at RKS DFT HSE06 level with the TZVPP/TZVP basis set for a H-saturated 2×1 supercell periodic slab model with 50 atomic layers. The PBBS is indicated by the gray area. Reprinted with permission from *J. Phys. Chem. C* 2023, 127, 48, 23475–23488. Copyright 2023 American Chemical Society. Slightly modified.

different linear combinations between orbitals of each layer are possible, which corresponds to an insufficient $\vec{k}$-point sampling in this direction. This effect is nicely observable in the charge density plots in the study of Sagisaka et al.,[127] in which they plotted multiple eigenstates of the 78-layer slab models showing different numbers of nodal planes in z-direction, corresponding to the different wave lengths of the Bloch function's wave vector $\vec{k}$. Furthermore, the missing periodicity at the bottom of the smaller slab models leads to an inaccurate embedding potential, also distorting the energy levels of the bulk-like states compared to a true bulk 3C-SiC calculation.

Besides the surface band gap, a closer look at the convergence of the dimer bond length and the reconstruction energy listed in Table 3.11 is taken for the singlet RKS, UKS, and high-spin UKS p(2×1) reconstructions of symmetric dimers. Just like in the work of Sagisaka et al.,[127] the dimer bond length shows a very weak dependence on the number of atomic layers. Despite this, the

Table 3.11: Convergence of the reconstruction energy ΔE_{dimer} and dimer bond length d_{Si-Si} of H-saturated 2×1 supercell periodic slab models of the Si-terminated 3C-SiC(001)-p(2×1) reconstructed surface (SD model) with respect to the number of atomic layers at RKS and UKS DFT HSE06 level with the TZVPP/TZVP basis set. The UKS calculations used the spin arrangements of Table 3.3.

Number of Atomic Layers	Singlet RKS		Singlet UKS		High-Spin UKS	
	ΔE_{dimer} [eV]	d_{Si-Si} [Å]	ΔE_{dimer} [eV]	d_{Si-Si} [Å]	ΔE_{dimer} [eV]	d_{Si-Si} [Å]
8	−0.013	2.811	−0.226	2.465	−0.132	2.390
10	−0.014	2.806	−0.229	2.463	−0.135	2.388
12	−0.015	2.805	−0.230	2.462	−0.136	2.388
14	−0.016	2.797	−0.232	2.463	−0.137	2.388
26	−0.022	2.797	−0.238	2.463	−0.144	2.388
38	−0.030	2.797	−0.246	2.463	−0.153	2.388
50	−0.043	2.794	−0.257	2.463	no convergence	

reconstruction energy still lowers by about 0.03 eV when going from the 10- and 12-layer slab models generally used before to the 50-layer slab models. Such behavior was not found by Sagisaka et al. for the Si(001)-p(2×2) reconstructed surface. While the absolute value of this additional energy gain is very small, in the context of the low reconstruction energies, especially for the RKS case, it still represents a considerable relative amount. Unfortunately, increasing the number of layers to 50 is not feasible for 4×1 and 4×2 supercells as the number of atoms would amount to 208 and 416, respectively, which is why the convergence could not be checked for the p(4×1) and p(4×2) reconstructions. On the other hand, from the results regarding the p(2×1) reconstructions, it is reasonable to expect that no change in the energetic order is occurring as the energy gain per dimer with respect to the number of layers is equal for all investigated cases. Accordingly, the reconstruction energies for the 10- and 12-layer slab models will be kept as a basis for the discussions in the rest of this work with the effect of additional layers in mind when important in the respective context.

It was further checked if the asymmetric H-saturated slab models are sufficient compared to the conceptionally more sophisticated symmetric slab models, as the latter do not need additional H atoms, which could distort the electronic structure. As indicated in Section 2.2.1.5, the helical building blocks of the 3C-SiC(001) surface are not suitable for a simple mirror plane in the middle of symmetric slab models and instead one of the 80 layer groups[191] with a screw axis would be needed. If mirror symmetry would still be applied, this would lead to a change in the layer stacking order, which could also change the bulk band gap when considering the dependence of this quantity with the SiC polytype as established in Chapter 1. Nevertheless, for the sake of simplicity, no symmetry was exploited in this work for the symmetric slab models, of which the 17-layer variant is depicted in Fig. 3.25. Here, a 2×2 supercell is

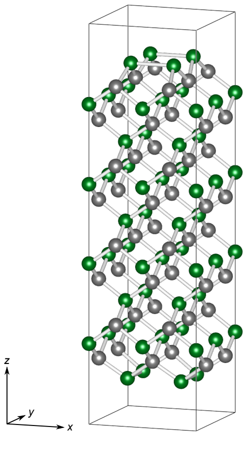

Figure 3.25: Symmetric 2×2 supercell 17-layer periodic slab model for the p(2×1) reconstructed (SD model) Si-terminated 3C-SiC(001) surface. The structure was optimized at singlet UKS DFT HSE06 level with the TZVPP/TZVP basis set and a spin arrangement of p(2×1) symmetry (↑↓ ↑↓, like in Table 3.3) for the dimers of both surfaces. The size of the unit cell in z is depicted smaller than it is in the actual calculations.

Table 3.12: Convergence of the reconstruction energy ΔE_{dimer} and dimer bond length d_{Si-Si} of asymmetric H-saturated 2×1 supercell and symmetric 2×2 supercell periodic slab models of the Si-terminated 3C-SiC(001)-p(2×1) reconstructed surface (SD model) with respect to the number of atomic layers at singlet UKS DFT HSE06 level with the TZVPP/TZVP basis set.

Number of Relaxed Atomic Layers per Surface	Asymmetric Slab Model			Symmetric Slab Model		
	Total Number of Atomic Layers	ΔE_{dimer} [eV]	d_{Si-Si} [Å]	Total Number of Atomic Layers	ΔE_{dimer} [eV]	d_{Si-Si} [Å]
4	8	−0.226	2.465	13	−0.226	2.466
6	10	−0.229	2.463	17	−0.230	2.464
8	12	−0.230	2.462	21	−0.231	2.464

necessary to be able to generate a p(2×1) reconstruction as the Si dimers on each side are twisted by 90°. As apparent from Table 3.12, both the symmetric and asymmetric H-saturated slab models give virtually identical reconstruction energies and dimer bond lengths for the same number of relaxed layers per surface, thus confirming the asymmetric slabs to be sufficient to describe the Si-terminated 3C-SiC(001) surface.

3.2.3.6 Summary

To summarize the single-configurational calculations on periodic slab models of the Si-terminated 3C-SiC(001) surface, Table 3.13 gives an overview of the different reconstructions obtained in this work using this methodology at singlet RKS and UKS DFT level with the TZVPP/TZVP basis set. Here, it is focused solely on the HSE06 functional as it shows the best agreement regarding the electronic structure of the investigated material. Overall, the UKS formalism yields the strongest reconstruction energies, which indicates a radicalic character of the surface and thus static correlation to be important since UKS is able to include it to some degree by spin-symmetry breaking in contrast to RKS. As a consequence, RKS instead breaks the spatial symmetry due to the limited freedom in the electronic structure, resulting in buckled p(2×1) and p(4×2) reconstructions not found for UKS. The UKS p(4×1) reconstruction overall shows the highest energy gain with the UKS p(2×1) SD model also being similarly stable. For the latter, the range of reconstruction

Table 3.13: Overview of the reconstruction energies ΔE_{dimer} of different reconstructions considered in this work for the Si-terminated 3C-SiC(001) surface at singlet RKS and UKS DFT HSE06 level with the TZVPP/TZVP basis set.

Reconstruction	ΔE_{dimer} [eV]	
	Singlet RKS HSE06	Singlet UKS HSE06
p(2×1) symmetric	−0.01	−0.09 – −0.31
p(2×1) buckled	−0.05	-
p(4×1)	−0.03	−0.29 – −0.30
p(4×2)	−0.15	-
c(4×2)	-	−0.16

energies is quite high due to the different possible spin arrangements for the dimer atoms in the 4×2 surface supercell, though in an exact description, there exists only one "ground state" singlet polyradicalic configuration without spin polarization. Along these lines, the novel UKS c(4×2) structure of this work appears to only be an alternative to more unstable p(2×1) spin arrangements and is thus quite unlikely to exist. Generally, it should be kept in mind that the singlet UKS calculations exhibit severe spin contamination, which is why the quantitative values have to be taken with care. Regarding the RKS results, only the p(4×2) reconstruction can compete energetically with the UKS structures and due to its close relation to the AUDD model and thus to the experimentally most commonly observed c(4×2) reconstruction seems to be the best structural model from a theoretical perspective. The AUDD model itself could, in accordance with previous studies, not be observed for the unstrained surface slabs used in this work.

Overall, the strong deviations between the RKS and UKS calculations mainly caused by the close energetic proximity of the ID and ID^* bands and variations thereof for the different reconstructions hint towards the supposedly multiconfigurational character of the Si-terminated 3C-SiC(001) surface. Consequently, it is attempted to give a proper description of this system in the following Section 3.3 through multiconfigurational cluster model calculations.

3.3 Multiconfigurational Cluster Model Calculations

3.3.1 Computational Details

Orca 5.0.0[192] was used to apply the multiconfigurational wave function-based methods CASSCF[89–93] and (strongly contracted) NEVPT2[102–104] to H-saturated cluster models of the ideal p(1×1) and p(2×1) reconstructed Si-terminated 3C-SiC(001) surface. The differently sized cluster models were created from the H-saturated 12-layer periodic slab models obtained before at RKS and UKS DFT[71] HSE06[78–80] level with the TZVPP[155]/TZVP[156] basis set. Before conducting the multiconfigurational calculations, the positions of the saturating H atoms were optimized at RKS DFT HSE06 level with the same TZVPP/TZVP basis used for the periodic slab models, while all other cluster atoms were kept fixed as described in Section 3.3.2.1 in more detail. The HSE06 functional is accessible in Orca via the LibXC[193] library. As further described in Section 3.3.2.1, the size of the active space was dependent on the number of dimers as well as the number of surface state bands included, the latter leading to active spaces being either denoted as reduced ($\mathrm{CAS_{red}}$) or full ($\mathrm{CAS_{full}}$), respectively. For CASSCF and NEVPT2 level geometry optimizations, geometric constraints were imposed as described in Section 3.3.2.2 to approximately mimic the PBCs utilized in the single-configurational calculations.

Generally, an optimization of the first two atomic layers according to Table 3.17 in Section 3.3.2.2 was conducted for all cluster models with the exception of the results of the convergence study regarding the number of relaxed layers presented in Appendix A.2.2. All CASSCF and NEVPT2 wave functions were of state-optimized nature. To significantly reduce the computational cost of the NEVPT2 single-point calculations and geometry optimizations only available with expensive numerical gradients, the resolution-of-identity chain-of-spheres exchange (RIJCOSX) approximation[194] with def2/J[195] and def2/C[196] auxiliary basis sets was utilized. For an improved comparability to the previous single-configurational calculations, the same TZVPP/TZVP basis set was generally employed for the cluster model calculations except for the convergence studies in Appendix A.2.3, in which def2[148] basis sets of different quality were used. A new approach introduced in Section 3.3.2.3 was developed to be able to calculate reconstruction energies between the p(2×1) and p(1×1) cluster models. Images of molecular structures and orbital isosurfaces were created with VESTA.[161]

3.3.2 Si-terminated 3C-SiC(001) Surface

3.3.2.1 Cluster Model and Active Space Construction

Due to the limited size of the cluster models of the Si-terminated 3C-SiC(001) surface in combination with the high-level multiconfigurational methods, the investigations will be restricted to the ideal p(1×1) surface and the p(2×1) reconstruction and not explore larger reconstructions. Still, as stated at the end of the previous section, since all the different reconstructions explored show a similar electronic structure with the ID- and ID^*-like bands responsible for the band gap, the p(2×1) reconstruction can serve as a model system to show the importance of the multiconfigurational treatment for the Si-terminated 3C-SiC(001) surface and its reconstructions as a whole.

As apparent from Table 3.14, the restricted single-configurational HF and DFT calculations show Mulliken atomic charges for the bulk atoms of 3C-SiC in the range of $0.03\,e - 0.36\,e$ with the Si atoms being positively and the C atoms being negatively charged. This is in accordance with the Mulliken charges of $0.14\,e$ obtained in the LDA LCAO periodic slab calculations of Sabisch et al.[45]

Table 3.14: Mulliken atomic charges of bulk 3C-SiC for different restricted methods and basis sets.

Functional	Bulk Atomic Charges [e]	
	pob-TZVP	TZVPP/TZVP
HF	0.08	-
LDA	0.36	0.03
PBE	0.30	0.13
PBE0	0.22	0.12
HSE06	0.21	0.14

Though the known strong basis set and method dependence of the Mulliken population analysis[58,59] is showing in Table 3.14, it can overall be concluded that the ionicity is quite low in 3C-SiC. Consequently, embedding in a point charge field is not necessary for cluster models of this material and simple H-saturated cluster models can be used instead. Furthermore, H atoms are especially suitable since their Pauling[197] electronegativity of 2.1 fits well in between the values of 2.5 for C and of 1.9 for Si, respectively. This should soften the error of introducing these saturating atoms because the C–H and Si–H bonds are qualitatively similarly polarized as the C–Si bonds of the pure material.

An overview of the cluster model creation workflow is given in Fig. 3.26. As apparent, the cluster models exhibiting the ideal p(1×1) and the p(2×1) reconstructed surface were created from the respective H-saturated 12-layer periodic slab models. Here, the ideal p(1×1) slab model was created from the bulk structure optimized at RKS DFT HSE06 level with the TZVPP/TZVP basis set and no further optimization afterwards, while the p(2×1) slab models were optimized at UKS DFT HSE06 level with the TZVPP/TZVP basis set and the p(2×1) spin arrangement of Table 3.3 to yield symmetric dimers with a dimer bond length of 2.46 Å. The UKS p(2×1) structure was chosen over the RKS analogue due to the closer agreement of the former with previous experimental results and especially with the multiconfigurational study of Tamura and Gordon[53] as established before in Section 3.2.3.2. The cluster models varied in size regarding the number of Si dimers in [110]/x- and [$\bar{1}$10]/y-direction and regarding the number of atomic layers in [001]/z-direction to check the convergence for the different parameters of interest. Non-surface atoms were saturated with H atoms and the dangling bonds of the two outermost dimer atoms of each dimer row were saturated as well to ensure a reasonable embedding of the supposedly statically correlated surface states in between. Before conducting the multiconfigurational calculations, the positions of the saturating H atoms were optimized at RKS HSE06 level with the same TZVPP/TZVP basis used for the periodic slab models while all other cluster atoms were kept fixed. In case of the p(2×1) cluster models, also the inner dimer atoms were saturated with H to obtain a closed-shell system more suitable for the RKS optimization. Unfortunately, this additional saturation was not possible for the p(1×1) cluster models due to the limited space when trying to saturate each surface atom with two H atoms as already discussed in Section 3.2.3.1. This inconsistency between the two surfaces was unintentional and a chronological issue because the p(1×1) cluster models were developed after most of the calculations regarding the p(2×1) analogues were finished. Nevertheless, this difference should be negligible because the p(1×1) surface states should mainly influence the geometry of the two adjacent outer H atoms of each dimer row, which are reoptimized during the multiconfigurational calculations anyway.

After the optimization of the saturating H atoms at DFT level, the active space for the multiconfigurational calculations including the surface states could be constructed, for which the H atoms of the p(2×1) cluster models saturating the inner dimer atoms had to be removed first. As discussed before when introducing the MO diagram in Fig. 3.3, each Si dimer of the p(2×1) surface exhibits the four surface states σ, π, π^*, and σ^* with four electrons, of which

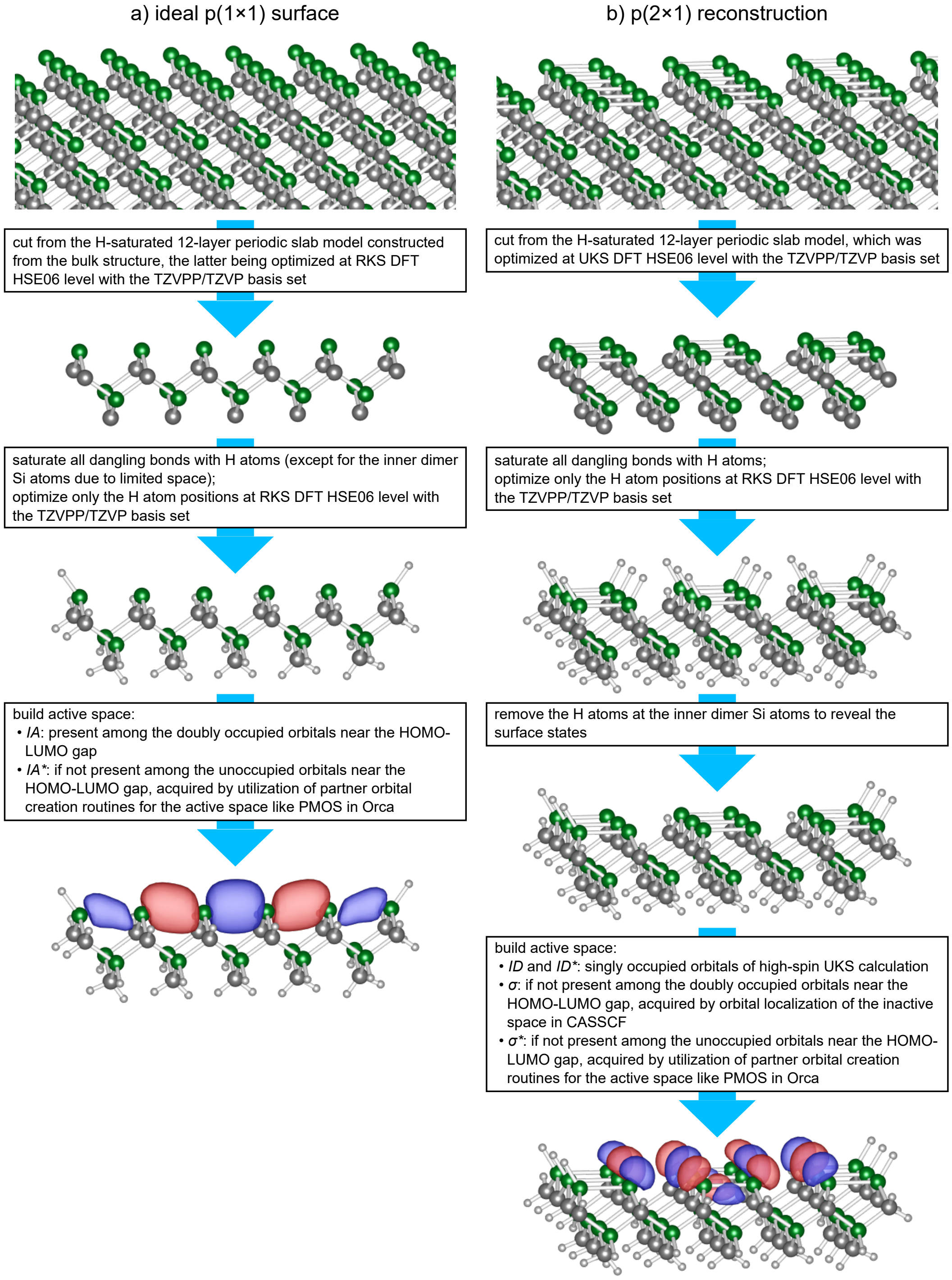

cut from the H-saturated 12-layer periodic slab model constructed from the bulk structure, the latter being optimized at RKS DFT HSE06 level with the TZVPP/TZVP basis set

saturate all dangling bonds with H atoms (except for the inner dimer Si atoms due to limited space);
optimize only the H atom positions at RKS DFT HSE06 level with the TZVPP/TZVP basis set

build active space:

- *IA*: present among the doubly occupied orbitals near the HOMO-LUMO gap
- *IA**: if not present among the unoccupied orbitals near the HOMO-LUMO gap, acquired by utilization of partner orbital creation routines for the active space like PMOS in Orca

cut from the H-saturated 12-layer periodic slab model, which was optimized at UKS DFT HSE06 level with the TZVPP/TZVP basis set

saturate all dangling bonds with H atoms;
optimize only the H atom positions at RKS DFT HSE06 level with the TZVPP/TZVP basis set

remove the H atoms at the inner dimer Si atoms to reveal the surface states

build active space:

- *ID* and *ID**: singly occupied orbitals of high-spin UKS calculation
- *σ*: if not present among the doubly occupied orbitals near the HOMO-LUMO gap, acquired by orbital localization of the inactive space in CASSCF
- *σ**: if not present among the unoccupied orbitals near the HOMO-LUMO gap, acquired by utilization of partner orbital creation routines for the active space like PMOS in Orca

Figure 3.26: Cluster model creation workflow for the a) ideal p(1×1) and b) p(2×1) reconstructed Si-terminated 3C-SiC(001) surface using the examples of the a) 3×1-dimer and b) 3×3-dimer 4-layer cluster models ($Si_{16}C_{17}H_{38}$ and $Si_{38}C_{39}H_{66}$). The isosurface value for the orbitals amounts to $0.03\,a_0{}^{-3}$. Reprinted with permission from *J. Phys. Chem. C* 2023, 127, 48, 23475–23488. Copyright 2023 American Chemical Society. Slightly modified.

the two π states, corresponding to the ID and ID^* bands, are supposedly affected the most by static correlation. Consequently, active spaces of the size CAS(4,4) or CAS(2,2) should be reasonable to describe one dimer faithfully with the former CAS also including the σ and σ^* states as was done before by Tamura and Gordon in their 1-dimer cluster model.[53] In case of the p(1×1) cluster models, each surface atom carries one sp^2 and one p_x orbital with two electrons that are responsible for the IA and IA^* bands, which corresponds to a CAS(4,4) for one pair of Si atoms forming one dimer. Since the surface state bands are located within the bulk band gap of 3C-SiC, the corresponding orbitals of the cluster models are often conveniently located around the HOMO-LUMO gap as described at the bottom of Fig. 3.26. However, finding the desired orbitals can get more challenging as the cluster models increase in size. Thankfully, Orca offers helpful tools like transforming the canonical orbitals of the inactive space to obtain localized orbitals, which is useful to find the σ states for the p(2×1) cluster models. Along these lines, the PMOS routine of Orca (abbreviation not given in manual,[94] presumably means partner molecular orbitals) can subsequently create bonding or antibonding partner orbitals in the external space for the active space orbitals. If the σ states for the p(2×1) or the IA states for the p(1×1) cluster models have already been found and included in the active space, this method accordingly helps to also obtain the corresponding σ^* and IA^* orbitals.

It is obvious that the size of the active space grows linearly with the number of dimers included in the cluster models, but the factorial scaling of the multiconfigurational methods with the size of the CAS drastically limits the extent of the model systems to be investigated. Geometry optimizations with CASSCF or NEVPT2 are only feasible for active spaces up to CAS(14,14) and thus restricted to cluster models of less than 10 dimers. Accordingly, it is questionable if such cluster models are able to recover a sophisticated surface state band structure in comparison to periodic slab models. Nevertheless, as multiconfigurational methods in combination with PBCs are still in an early stage of development, this is presumably among the best approaches available to describe the statically correlated Si-terminated 3C-SiC surface. In case of the p(2×1) reconstruction, it is thus reasonable to create two differently sized active spaces, one including all four surface state bands and one including only the ID and ID^* bands, denoted as full and reduced CASs (CAS_{full} and CAS_{red}), respectively. Excluding the σ and σ^* bands from the CAS_{red} is reasonable since they are most likely not affected by static correlation, which is already indicated by the respective NOONs of 1.98 and 0.02 obtained by Tamura and Gordon.[53] The CAS_{red} thus allows to explore larger cluster models and accordingly increases the scope of convergence studies for the parameters of interest with respect to the cluster model size.

The exact composition of the active spaces is easier to understand using the example of the 3×1 dimer 4-layer cluster model depicted in Fig. 3.27. Here, the label 3×1 corresponds to the cluster exhibiting three dimers in x- and one dimer row in y-direction. Three dimers with a CAS(4,4) would result in a total

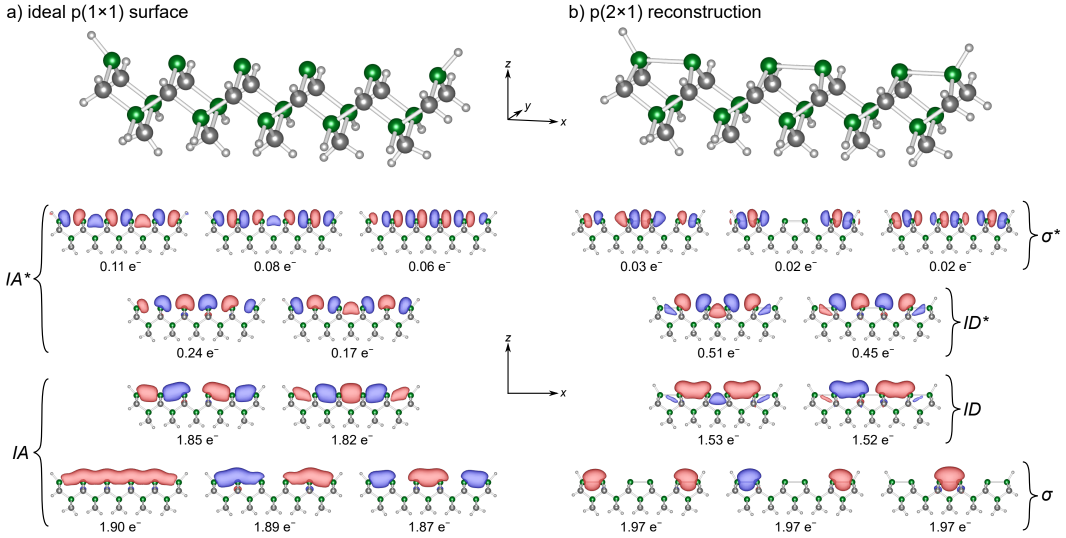

Figure 3.27: H-saturated 3×1-dimer 4-layer cluster models ($Si_{16}C_{17}H_{38}$) of the a) ideal p(1×1) and b) p(2×1) reconstructed (SD model) Si-terminated 3C-SiC(001) surface with the corresponding CAS_{full}(10,10) orbitals and NOONs optimized at CASSCF level with the TZVPP/TZVP basis set and the first two atomic layers relaxed according to Table 3.17. The isosurface value of the orbitals amounts to $0.03\,{a_0}^{-3}$. Reprinted with permission from *J. Phys. Chem. C* 2023, 127, 48, 23475–23488. Copyright 2023 American Chemical Society. Slightly modified.

CAS_{full}(12,12), but since the two outer dimer atoms are saturated with H for the improved embedding, the corresponding singly occupied dangling bonds are removed from the active space. This results in a CAS_{full}(10,10) for this example and generally enables the calculation of slightly larger cluster models due to smaller active spaces. With respect to the electronic structure, this cluster model would thus be more precisely classified as a 2×1-dimer cluster because it consists of one true dimer with the whole CAS(4,4), two half-dimers with a CAS(2,2), each containing a bisected σ bond and one dangling bond, as well as two capping H-saturated half-dimers with a CAS(1,1), representing the other half of the bisected σ bond each. Still, the simple structural naming is kept for the cluster models due to its intuitive derivation. As apparent from Fig. 3.27, the depicted active space orbitals can be assigned to the different bands of the p(1×1) and p(2×1) surfaces by their orbital shape and similar NOONs. Here, the p(2×1) cluster model's CAS_{full}(10,10) includes all surface states, while the CAS_{red}(4,4) accordingly only includes the ID and ID^* orbitals. The sizes K and L of the full and reduced active spaces can be universally calculated for each $M\times N$-dimer cluster model as follows:

$$\text{CAS}_{\text{full}}(K,K): \qquad K = N(4(M-1)+2) \tag{3.4}$$

$$\text{CAS}_{\text{red}}(L,L): \qquad L = N(2(M-1)) \tag{3.5}$$

With the explanation from above in mind, K for the full active space is obtained from N dimer rows, each of which containing $M-1$ dimers with a CAS(4,4) each and two capping H-saturated half-dimers with a CAS(1,1) each. Accordingly, L for the reduced active space results from N dimer rows with

$M-1$ dimers with a CAS(2,2) each and no contribution from the capping H-saturated half-dimers since the σ orbitals are excluded. However, as is further apparent from Fig. 3.27a), a reduction of the active space is not reasonable for the p(1×1) cluster models because this would correspond to not fully including the IA and IA^* bands. This would result in an inconsistent description of the surface states by basically excluding portions of the corresponding bands, distort the total energy, and most likely lead to convergence problems. With Eqs. 3.4 and 3.5 at hand, the number of cluster models feasible for the multi-configurational methods to be applied can be narrowed down to 10 for $\mathrm{CAS}_{\mathrm{red}}$ and to four for $\mathrm{CAS}_{\mathrm{full}}$ as apparent from Table 3.15.

Table 3.15: CAS sizes of the reduced and full active spaces $\mathrm{CAS}_{\mathrm{red}}$ and $\mathrm{CAS}_{\mathrm{full}}$ for different $M \times N$-dimer cluster models of the Si-terminated 3C-SiC(001)-p(2×1) reconstructed surface (SD model) according to Eqs. 3.4 and 3.5. Geometry optimizations for CAS sizes colored in gray are neither feasible at CASSCF nor at NEVPT2 level.

CAS Type	Number of Dimers in y (N)	CAS Size			
		Number of Dimers in x (M)			
		2	3	4	5
$\mathrm{CAS}_{\mathrm{red}}$	1	(2,2)	(4,4)	(6,6)	(8,8)
	2	(4,4)	(8,8)	(12,12)	(16,16)
	3	(6,6)	(12,12)	(18,18)	(24,24)
	4	(8,8)	(16,16)	(24,24)	(32,32)
$\mathrm{CAS}_{\mathrm{full}}$	1	(6,6)	(10,10)	(14,14)	(18,18)
	2	(12,12)	(20,20)	(28,28)	(36,36)
	3	(18,18)	(30,30)	(42,42)	(54,54)
	4	(24,24)	(40,40)	(56,56)	(72,72)

Besides the number of dimers, which corresponds to the extension of the cluster models in the x- and y-directions, the size in z, expressed by the number of atomic layers, is another important convergence parameter to check. However, adding more layers obviously increases the total number of basis functions and thus the computational time for each model, which is already quite high for the 4-layer models due to the active spaces increasing with the number of dimers. Accordingly, the 3×1- and 4×1-dimer cluster models were the only systems

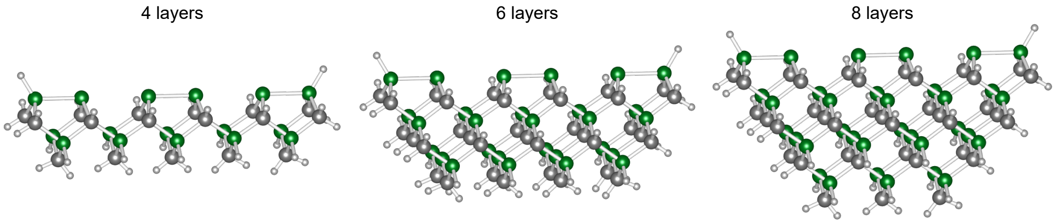

Figure 3.28: H-saturated 3×1-dimer 4-, 6-, and 8-layer cluster models ($Si_{16}C_{17}H_{38}$, $Si_{28}C_{35}H_{58}$, and $Si_{34}C_{38}H_{58}$) of the Si-terminated 3C-SiC(001)-p(2×1) reconstructed surface (SD model) optimized at CASSCF level with the full active space $\mathrm{CAS}_{\mathrm{full}}(10,10)$, the TZVPP/TZVP basis set, and the first two atomic layers relaxed according to Table 3.17.

also explored with six and eight layers besides the default 4-layer size used otherwise in this work. The corresponding p(2×1) reconstructed 3×1-dimer analogues are depicted exemplarily in Fig. 3.28 and all of the cluster models used in this work with their active space orbitals are shown in Appendix A.2.4.

3.3.2.2 Geometry Optimization Constraints

With the cluster models for the Si-terminated 3C-SiC(001) surface being constructed, an approach for the geometry optimization of these had to be developed. Since a cluster model is just a small excerpt of a very large system, the aim was to try to reproduce similar conditions as in the periodic slab model calculations. In the latter, the surface unit cell parameters and the lowest atomic layers were kept fixed with each unit cell being embedded in the periodic potential of the infinite number of identical neighboring unit cells. As mentioned in Section 2.2.2, for covalent systems, the smaller quantum mechanically described cluster model can be embedded into a larger MM cluster to simulate the surrounding material, which was also done for the 1-dimer cluster model of Tamura and Gordon.[53] However, as is apparent from the previous results of Sections 2.1.1 and 3.1, the dimers of each dimer row interact with each other quantum mechanically, which cannot be accounted for by neighboring dimers described at MM level of theory. This boundary problem of the multi-dimer cluster models in this work should be reasonably solved by the saturating outer dimer H atoms encapsulating the surface states, thus, in principle, actually allowing to combine them with MM clusters to provide the steric embedding. However, for the sake of methodological simplicity, it will be refrained from doing so in this work. Still, as Tamura and Gordon[53] point out, generally geometric constraints in cluster models can lead to unphysical structures. Unfortunately, for example, a full CASSCF optimization of the p(2×1) reconstructed 3×1-dimer 4-layer cluster model yields an arch-like or nanotube-like structure with equal distances between all surface Si atoms, which corresponds to a different system than intended. Accordingly, geometry constraints are necessary for the simple H-saturated cluster models to actually obtain physical results in this work. Furthermore, it can be argued that the cluster models are constructed from the periodic slab models and hence already exhibit reasonable relaxation and reconstruction effects for the most part.

To approximate the PBCs of the slab model calculations in Section 2.1.1, the displacements of the different Si and C layers induced by the reconstruction and relaxation of the p(2×1) reconstructed surface at RKS and UKS DFT HSE06 level listed in Table 3.16 are analyzed in detail. As apparent, all layers do virtually not relax in y-direction due to the p(2×1) reconstruction only acting in the x- and z-direction. Accordingly, during the CASSCF and NEVPT2 geometry optimizations, all y-coordinates were fixed for the p(2×1) cluster models. Regarding the x-coordinate, the relaxation apparently occurs alternately in blocks of two layers, namely a rather strong movement of the first two layers,

Table 3.16: Atomic displacements in the H-saturated 12-layer periodic slab models of the Si-terminated 3C-SiC(001)-p(2×1) reconstructed surface (SD model) compared to the ideal p(1×1) surface after optimization at singlet RKS and UKS DFT HSE06 level. The UKS calculations used the spin arrangement of Table 3.3. Reprinted with permission from *J. Phys. Chem. C* 2023, 127, 48, 23475–23488. Copyright 2023 American Chemical Society.

Atomic Layer Number	Element	Atomic Displacements [Å]					
		RKS			UKS		
		Δx	Δy	Δz	Δx	Δy	Δz
1	Si	−0.139	0.000	0.011	−0.311	−0.001	−0.046
	Si	0.138	0.000	0.011	0.312	−0.001	−0.046
2	C	−0.011	0.000	−0.006	−0.027	0.000	−0.010
	C	0.011	0.000	−0.006	0.028	0.000	−0.010
3	Si	0.000	0.000	−0.019	0.001	0.000	−0.058
	Si	0.000	0.000	0.017	−0.002	0.000	0.044
4	C	0.000	0.000	−0.013	0.001	−0.001	−0.032
	C	0.000	0.000	0.011	−0.002	−0.001	0.026
5	Si	0.006	0.000	0.000	0.014	−0.001	−0.002
	Si	−0.006	0.000	0.000	−0.012	−0.001	−0.002
6	C	0.003	0.000	0.000	0.007	0.000	−0.001
	C	−0.003	0.000	0.000	−0.006	0.000	−0.001
7	Si	0.000	0.000	0.002	0.001	0.000	0.005
	Si	0.000	0.000	−0.002	−0.001	0.000	−0.005
8	C	0.000	0.000	0.001	0.001	−0.001	0.004
	C	0.000	0.000	−0.001	−0.001	−0.001	−0.002

layers three and four being static, a relaxation of layers five and six, and so on. Thus, geometric constraints in x mimicking this block-like behavior were also imposed on the p(2×1) cluster models. The very small Δx values for layers three, four, seven, and eight as well as the Δy values in the UKS case are supposedly just numerical noise and not of actual physical importance. Since in the slab models basically all atomic layers show relaxation in z, no constraints in this direction were applied to the p(2×1) cluster models. An overview of the discussed constraints is given in Table 3.17. Obviously, the Si and C atoms of the cluster models representing the ideal p(1×1) surface are fully constrained. Furthermore, for both the p(1×1) and p(2×1) cluster models, almost all saturating H atoms are kept fixed to act as an embedding cage and thus indirectly restrict the movement of the optimized Si and C atoms to simulate neighboring unit cells. The H atoms saturating the outer dimer atoms are an exception to this since the dimers themselves are supposed to have as much spatial freedom as possible. Accordingly, just like the dimer atoms of the first layer they are connected to, these H atoms are only constrained in y-direction. Besides the approximate simulation of the surrounding material, the geometric constraints are also favorable with respect to the NEVPT2 geometry optimizations only available with expensive numerical gradients in Orca, resulting in every fixed coordinate significantly reducing the computational cost.

Regarding the terminology, if an optimization is declared as “two-layer optimization”, the constraints for atomic layers one and two as well as the H atom

Table 3.17: Atomic layer constraints for the H-saturated cluster models of the ideal p(1×1) and p(2×1) reconstructed (SD model) Si-terminated 3C-SiC(001) surface for geometry optimizations with CASSCF and NEVPT2. Reprinted with permission from *J. Phys. Chem. C* 2023, 127, 48, 23475–23488. Copyright 2023 American Chemical Society. Extended by p(1×1) column.

Atomic Layer Number	Element	Constrained?					
		p(1×1)			p(2×1)		
		x	y	z	x	y	z
1	Si	yes	yes	yes	no	yes	no
2	C	yes	yes	yes	no	yes	no
3	Si	yes	yes	yes	yes	yes	no
4	C	yes	yes	yes	yes	yes	no
5	Si	yes	yes	yes	no	yes	no
6	C	yes	yes	yes	no	yes	no
outer dimer H	H	no	yes	no	no	yes	no
all other H	H	yes	yes	yes	yes	yes	yes

constraints given in table Table 3.17 are considered. In case of a four-layer optimization, the constraints for atomic layers three and four are included additionally and so on. Generally, a two-layer optimization was conducted for all cluster models except for results of the convergence study regarding the number of relaxed layers in Appendix A.2.2.

3.3.2.3 Calculation of Reconstruction Energies

Since the active space of the p(1×1) cluster models cannot be reduced as established in Section 3.3.2.1, reconstruction energies ΔE_{dimer} are consequently only obtainable for systems utilizing the full active space $\mathrm{CAS_{full}}$. This stems from the fact that total CASSCF energies are only comparable for the same active space size and, more precisely, only for consistent active orbitals when considering different geometries of the same system,[198] thus making the calculation of reconstruction energies between p(2×1) cluster models with $\mathrm{CAS_{red}}$ and p(1×1) analogues with $\mathrm{CAS_{full}}$ invalid. The calculation of reconstruction energies for cluster models representing surfaces is generally not a standard procedure in computational surface science and thus rarely attempted. Paulus[56] actually determined reconstruction energies for the MCSCF calculations of the 1-dimer cluster model of the Si(001) surface. While not explicitly described in the cited work, this was most likely done by simply calculating the energy difference between the p(2×1) reconstructed and the ideal p(1×1) cluster model. In the context of the $M{\times}N$-dimer cluster models of this work, this would result in the following equation for the reconstruction energy $\Delta E_{dimer,M\times N}$:

$$\Delta E_{dimer,M\times N} = \frac{E_{M\times N,p(2\times1),CAS(K,K)} - E_{M\times N,p(1\times1),CAS(K,K)}}{M \cdot N} \tag{3.6}$$

Here, $E_{M\times N,p(2\times1),CAS(K,K)}$ and $E_{M\times N,p(1\times1),CAS(K,K)}$ are the total energies of the p(2×1) and p(1×1) $M{\times}N$-dimer cluster models calculated with the

$\mathrm{CAS}_{\mathrm{full}}(K,K)$, respectively, and $M{\cdot}N$ is simply the total number of dimers. However, in contrast to the work of Paulus, the outer dimer atoms of each dimer row are additionally saturated in this work. As already indicated in Section 3.3.2.1, it is easily imaginable that the corresponding capping H-saturated half-dimers show a different reconstruction energy than the unsaturated dimers in between that carry the surface states of interest. This would lead to a poor convergence of the actual reconstruction energy, which could be compensated by averaging over very long dimer rows. Obviously, this approach is in contrast to the cluster size restrictions imposed by the multiconfigurational methods and thus adjusted formulas had to be developed:

$$\Delta E_{M\times N} = E_{M\times N,p(2\times1),CAS(K,K)} - E_{M\times N,p(1\times1),CAS(K,K)} \tag{3.7}$$

$$\Delta E_{1\times N} = E_{1\times N,p(2\times1),CAS(2N,2N)} - E_{1\times N,p(1\times1),CAS(2N,2N)} \tag{3.8}$$

$$\Delta E_{dimer,M\times N} = \frac{\Delta E_{M\times N} - \Delta E_{1\times N}}{N(M-1)} \tag{3.9}$$

For the sake of clarity, this approach is additionally depicted in Fig. 3.29 using the example of the 3×1-dimer 4-layer cluster model. Here, $\Delta E_{M\times N}$ is the difference between the total energies of the p(2×1) and p(1×1) $M{\times}N$-dimer cluster models calculated with the $\mathrm{CAS}_{\mathrm{full}}(K,K)$, the latter being a CAS(10,10) in the 3×1-dimer case. $\Delta E_{1\times N}$ is calculated analogously with $E_{1\times N,p(2\times1),CAS(2N,2N)}$ and $E_{1\times N,p(1\times1),CAS(2N,2N)}$ corresponding to the total energies of $1{\times}N$-dimer cluster models of the p(2×1) and p(1×1) surfaces, respectively. In the example of Fig. 3.29, this corresponds to 1×1-dimer cluster models with a CAS(2,2) containing the σ and σ^* orbitals of the dimer bond. The energy difference $\Delta E_{1\times N}$ thus represents the reconstruction energy for the formation of N rows of single fully saturated dimers, or, put differently, the reconstruction energies of two capping H-saturated half-dimers for each of the N dimer rows. In the final Eq. 3.9, this spurious reconstruction energy is now subtracted from the uncorrected reconstruction energy of the whole $M{\times}N$-dimer cluster model, namely $\Delta E_{M\times N}$, which is indicated at the bottom of Fig. 3.29 by the color coding in the 3×1-dimer cluster. At last, this corrected total reconstruction energy now has to be divided by the number of actually unsaturated dimers, which calculates as $N(M-1)$, with the -1 excluding the capping H-saturated half-dimers in each of the N dimer rows. In the 3×1-dimer example, the number of unsaturated dimers is accordingly two. The drastically improved similarity of reconstruction energies of differently sized cluster models for the advanced calculation according to Eqs. 3.7 to 3.9 compared to the simple approach of Eq. 3.6 is apparent in Table 3.18.

It should be noted that the $1{\times}N$-dimer cluster models used for the correction of the reconstruction energies always consisted of only four atomic layers, even though the $M{\times}N$-dimer clusters, for whose reconstruction energy calculation the $1{\times}N$-dimer clusters were needed, sometimes also had six or eight layers. While this seems unreasonable at a first glance, this decision is justified in the discussion connected to the convergence study regarding the number of relaxed atomic layers in Appendix A.2.2. Since the number of dimer rows is limited to a maximum of two for the full active space (see Table 3.15), the 1×1- and 1×2-dimer 4-layer cluster models depicted in Figs. A.15 and A.16 are the only two $1\times N$-dimer clusters considered for the corrected calculation of reconstruction energies.

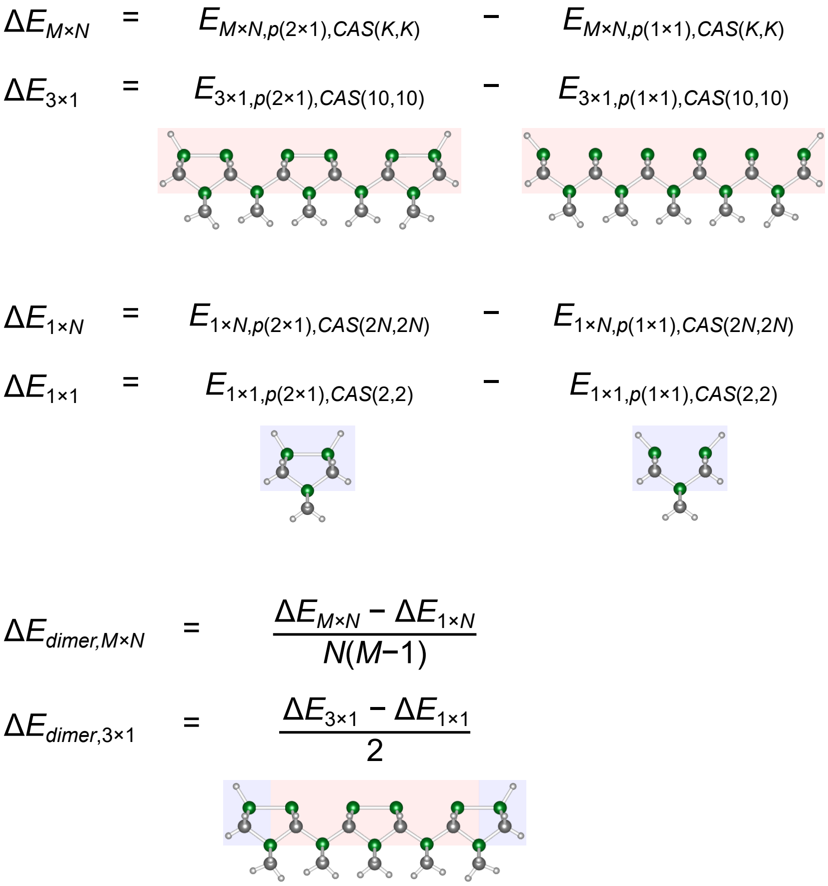

Figure 3.29: Calculation of the CASSCF and NEVPT2 reconstruction energies ΔE_{dimer} for the H-saturated $M\times N$-dimer cluster models of the Si-terminated 3C-SiC(001)-p(2×1) reconstructed surface (SD model) using the example of the 3×1-dimer 4-layer cluster model ($Si_{16}C_{17}H_{38}$). Reprinted with permission from *J. Phys. Chem. C* 2023, 127, 48, 23475–23488. Copyright 2023 American Chemical Society. Slightly modified.

Table 3.18: Comparison of reconstruction energies ΔE_{dimer} calculated according to Eq. 3.6 and according to Eqs. 3.7 to 3.9 for H-saturated $M\times1$-dimer 4-layer cluster models of the Si-terminated 3C-SiC(001)-p(2×1) reconstructed surface (SD model) optimized at CASSCF level for the full active space CAS_{full}, the TZVPP/TZVP basis set, and the first two atomic layers relaxed according to Table 3.17.

Cluster Model	ΔE_{dimer} [eV]	
	Eq. 3.6	Eqs. 3.7 to 3.9
2×1-dimer	−0.564	−0.180
3×1-dimer	−0.435	−0.179
4×1-dimer	−0.371	−0.179

Lastly, it can be rightfully argued that the comparability of the periodic slab model calculations and the cluster model calculations is complicated by changing two methodologies at the same time, namely going from PBCs to the cluster approach and from single- to multiconfigurational electronic structure methods. However, an exploratory study comparing single-configurational reconstruction energies at RKS DFT HSE06 level in Appendix A.2.1 shows only small differences between the periodic slab model and the cluster model approaches as well as indicating an insufficiency of the single-configurational methods for this system. Accordingly, it is reasonable to expect the switch to the cluster model approach to have a negligible impact on the structure and energetics compared to the switch to the multiconfigurational approach, justifying the change of both methodologies at the same time.

3.3.2.4 Spatial and Electronic Structure of the p(2×1) Reconstruction

Since neighboring dimers on the Si-terminated 3C-SiC(001)-p(2×1) reconstructed surface, as already shown before in the single-configurational calculations, interact with each other in x-direction to form the supposedly multiconfigurational ID and ID^* bands, the convergence of the spatial structure of the multi-dimer cluster models with respect to the number of dimers is of high interest. Accordingly, Table 3.19 lists dimer bond lengths d_{Si-Si} and reconstruction energies ΔE_{dimer} for 4-layer cluster models with differing numbers of dimers M in x- and differing numbers of dimer rows N in y-direction optimized at CASSCF and NEVPT2 level for both CAS_red and CAS_full. Even though the number of systems is limited due to the high computational cost of the multiconfigurational methods, if no unexpected convergence changes appear outside of the presented scope, some trends are indicated by the obtained data. Overall, d_{Si-Si} and ΔE_{dimer} are already reasonably converged for a 3×1-dimer cluster for both methods and both active spaces. There generally is a notable increase in the dimer bond length when going from 2×N- to 3×N-dimer clus-

Table 3.19: Dimer bond lengths d_{Si-Si} and reconstruction energies ΔE_{dimer} for H-saturated M×N-dimer 4-layer cluster models of the Si-terminated 3C-SiC(001)-p(2×1) reconstructed surface (SD model) optimized at CASSCF and NEVPT2 level for the two different active space sizes CAS_red and CAS_full, the TZVPP/TZVP basis set, and the first two atomic layers relaxed according to Table 3.17. The dimer bond lengths are taken from the most inner dimers. Reprinted with permission from *J. Phys. Chem. C* 2023, 127, 48, 23475–23488. Copyright 2023 American Chemical Society.

Method	Number of Dimers in y (N)	Number of Dimers in x (M)									
		2	3	4	5	2	3	4	2	3	4
		$d_{Si-Si,CAS_{red}}$ [Å]				$d_{Si-Si,CAS_{full}}$ [Å]			$\Delta E_{dimer,CAS_{full}}$ [eV]		
CASSCF	1	2.448	2.463	2.464	2.466	2.502	2.547	2.550	−0.180	−0.179	−0.179
	2	2.446	2.462	2.463		2.500			−0.182		
	3	2.444	2.460								
	4	2.446									
NEVPT2	1	2.449	2.505			2.472	2.560		−0.120	−0.110	
	2	2.452				2.483			−0.122		

ter models. This is caused by the former clusters only consisting of dimer rows with two capping H-saturated half-dimers and two unsaturated half-dimers, thus no true fully unsaturated dimers are present, which are only available in $M \times N$-dimer cluster models with M larger than two. The shortened dimer bonds of the capping H-saturated half-dimers are in accordance with several previous theoretical studies observing the same behavior upon chemisorption of molecular fragments at one of the dimer atoms.[29,30,32,53,199] Furthermore, the number of dimer rows N seems to play a subordinate role with respect to the reconstruction energy and dimer bond length, indicating weak interaction between the dimer rows and arguably determining the 3×1-dimer to be of sufficient size to explore these two parameters.

Comparing the results for the two active space sizes, a substantial lengthening of the dimer bonds is observable when going from the smaller CAS_{red} to the larger CAS_{full}. This can be attributed to the σ and σ^* orbitals being additionally included in the latter active space, enabling an electron transfer from the bonding to the antibonding orbital indicated by the NOONs of 1.97 and 0.03 in Fig. 3.27. The driving force for the resulting longer dimer bond is supposedly the enhanced interaction of the ID orbitals and thus a stronger interdimer bond. To a certain degree, this contradicts the initial considerations that the σ and σ^* orbitals are not important for the multiconfigurational character of the dimers. While this after all is true as the deviations of the NOONs from the single-configurational occupation numbers of 2 and 0 are minor, this additional small dynamic correlation still significantly influences the energetically very delicate reconstruction connected to the statically correlated ID and ID^* orbitals with NOONs of about 1.5 and 0.5 in Fig. 3.27, respectively. Thus, for a faithful description of the p(2×1) reconstruction, including the σ and σ^* orbitals in the active space is important, which is why the CAS_{full} is the focus of the subsequent calculations.

Along these lines, from Table 3.19, the well-known effect of dynamic correlation being less impactful for larger active spaces[58] is also apparent since the dimer bond lengthening is less significant for CAS_{full} when going from CASSCF to NEVPT2 compared to CAS_{red}. In this particular case, this observation can be explained by the dynamic correlation already partially considered in the CAS_{full} through the inclusion of the σ and σ^* orbitals. These orbitals are not present in the CAS_{red}, resulting in the NEVPT2 method being able to cover a larger extent of dynamic correlation and thus a greater dimer bond lengthening for this smaller active space compared to the CAS_{full} occurs. Nevertheless, the absolute NEVPT2 dimer bond length for the 3×1-dimer cluster is still substantially larger by about 0.05 Å for CAS_{full} than for CAS_{red}. Hence, the dynamic correlation of NEVPT2 cannot fully compensate the insufficient size of the CAS_{red}. Furthermore, when comparing the reconstruction energies, the dynamic correlation of NEVPT2 also significantly reduces the reconstruction strength for CAS_{full} by a significant relative amount to about $-0.11\,\text{eV}$ compared to the value of $-0.18\,\text{eV}$ for CASSCF. This is in accordance with the single-configurational periodic slab model calculations, where the inclusion of approximate dynamic correlation in the hybrid UKS DFT functionals also resulted in less negative reconstruction energies compared to the pure HF method.

Besides the number of dimers, the number of atomic layers is another important convergence parameter to check. Table 3.20 lists the dimer bond lengths and reconstruction energies of 3×1- and 4×1-dimer 4-, 6-, and 8-layer cluster models of the p(2×1) reconstructed surface optimized at CASSCF level for the CAS_{full}. As apparent, d_{Si-Si} is basically converged for six layers, yielding the same value of 2.553 Å for both 3×1- and 4×1-dimer cluster models. ΔE_{dimer}, on the other hand, does not show convergence even for eight atomic layers, which could either be a real physical effect or a limitation of the method for calculating the reconstruction energies because the dimer bond length seemingly does converge. Calculations of even larger cluster models would be necessary to answer this question, which is unfortunately not possible due to the computational cost. For the same reason, NEVPT2 optimizations were also not possible for the 4×1-dimer clusters and the 3×1-dimer 6- and 8-layer clusters. However, with the NEVPT2 results of the 3×1-dimer 4-layer cluster of Table 3.19, one could estimate d_{Si-Si} to be longer by about 0.01 Å – 0.02 Å and the reconstruction energies to be more positive by about 0.06 eV – 0.07 eV than the CASSCF 8-layer cluster results, yielding values of about 2.56 Å – 2.57 Å and −0.05 eV – −0.07 eV as given at the bottom of Table 3.20.

The convergence of the p(2×1) cluster models is further influenced by the choice of the basis set and the number of relaxed atomic layers. In case of the former, the TZVPP/TZVP basis set used so far seems to describe the spatial structure of the p(2×1) surface appropriately as discussed in Appendix A.2.3 in more detail. Concerning the number of relaxed layers, the situation is less clear and it is referred to the detailed discussion in Appendix A.2.2. To quickly summarize, the decision to optimize only the first two atomic layers of the clus-

Table 3.20: Dimer bond lengths d_{Si-Si} and reconstruction energies ΔE_{dimer} for H-saturated 3×1- and 4×1-dimer 4-, 6-, and 8-layer cluster models ($Si_{16}C_{17}H_{38}$, $Si_{28}C_{35}H_{58}$, $Si_{34}C_{38}H_{58}$, $Si_{22}C_{23}H_{50}$, $Si_{40}C_{49}H_{78}$, and $Si_{50}C_{54}H_{78}$) of the Si-terminated 3C-SiC(001)-p(2×1) reconstructed surface (SD model) optimized at CASSCF level with the full active space CAS_{full}, the TZVPP/TZVP basis set, and the first two atomic layers relaxed according to Table 3.17. The dimer bond lengths are taken from the most inner dimers. Additionally, estimated NEVPT2 values extrapolated from the 3×1-dimer 4-layer cluster of Table 3.19 are given at the bottom. Reprinted with permission from *J. Phys. Chem. C* 2023, 127, 48, 23475–23488. Copyright 2023 American Chemical Society. Extended by the estimated NEVPT2 values.

Number of Atomic Layers in z	Cluster Model			
	3×1-dimer		4×1-dimer	
	$d_{Si-Si,CAS_{full}}$ [Å]	$\Delta E_{dimer,CAS_{full}}$ [eV]	$d_{Si-Si,CAS_{full}}$ [Å]	$\Delta E_{dimer,CAS_{full}}$ [eV]
4	2.547	−0.179	2.550	−0.179
6	2.553	−0.132	2.553	−0.141
8	2.553	−0.120	2.553	−0.132
8 (estimated NEVPT2)	$d_{Si-Si,CAS_{full}}$: 2.56 Å – 2.57 Å		$\Delta E_{dimer,CAS_{full}}$: −0.05 eV – −0.07 eV	

ter models is a compromise between the multi-configurational reoptimization of the surface states located mainly in the first two layers and keeping the relaxation of all the lower atomic layers already present in the single-configurational UKS DFT HSE06 reference structure used for the construction of the cluster models.

Now, a comparison of the estimated high-level multiconfigurational dimer bond lengths and reconstruction energies of 2.56 Å – 2.57 Å and −0.05 eV – −0.07 eV given at the bottom of Table 3.20 with the DFT calculations of Section 3.2 is made. Regarding d_{Si-Si}, the RKS results with values of 2.7 Å – 2.8 Å are in lesser accordance with the multiconfigurational calculations than the UKS results with 2.45 Å – 2.55 Å. The UKS reconstruction energies of −0.06 eV – −0.28 eV also show better agreement than the RKS values of about −0.02 eV, though it is apparent from the different convergence studies that the method of calculating ΔE_{dimer} for cluster models is presumably not fully sophisticated and thus these numbers have to be treated with care. Furthermore, as discussed in the atomic layer convergence study of the periodic slab models in Section 3.2.3.5, the single-configurational reconstruction energies are supposedly also more negative by about 0.03 eV, which would then favor the RKS results. Nevertheless, overall there is no definitive agreement with either the RKS or the UKS formalism, which can be explained by a closer analysis of the electronic structure of the multiconfigurational calculations. As apparent from Table 3.21, the NOONs of the ID and ID^* orbitals of the p(2×1) reconstructed 3×1- and 4×1-dimer 4-layer cluster models at CASSCF and NEVPT2 level with the CAS_full amount to about 1.5 and 0.5, respectively, which indicates an approximately equal mixture of the fully closed-shell and the fully radicalic configurations. This is further supported when examining the composition of the corresponding CASSCF wave function of the 3×1-dimer 4-layer cluster model given in Table 3.22. Here, about 56 % are contributed by the pure closed-shell configuration [...2200...] (only considering the two ID and the two ID^* orbitals) and about 17 % by the fully radicalic configuration [...1111...]. Furthermore, there is a sum of about 23 % of the five configurations with the remaining possible permutations of two doubly occupied and two unoccupied ID and ID^* orbitals, of which two linearly combined also result in radicalic character, e.g, [...2002...] and [...0220...]. This interpretation is done analo-

Table 3.21: NOONs of the ID and ID^* orbitals for H-saturated 3×1- and 4×1-dimer 4-layer cluster models ($Si_{16}C_{17}H_{38}$ and $Si_{22}C_{23}H_{50}$) of the Si-terminated 3C-SiC(001)-p(2×1) reconstructed surface (SD model) optimized at CASSCF and NEVPT2 level for the full active space CAS_full, the TZVPP/TZVP basis set, and the first two atomic layers relaxed according to Table 3.17. The corresponding NOs are depicted in Figs. A.23, A.24, A.31 and A.32.

Cluster Model	NOONs of CAS_full			
	CASSCF		NEVPT2	
	ID Orbitals	ID^* Orbitals	ID Orbitals	ID^* Orbitals
3×1-dimer	1.53, 1.52	0.51, 0.45	1.54, 1.53	0.50, 0.44
4×1-dimer	1.53, 1.52, 1.52	0.52, 0.48, 0.44		

gously to the assignment of diradicalic character to methylene by Schmidt and Gordon,[55] who described the molecule by a two-configurational wave function including the configurations [20] and [02]. With this knowledge about the wave function at hand, it is reasonable for the dimer bond length and reconstruction energies of the multiconfigurational calculations to lie in between the single-configurational RKS and UKS results. The wave function composition also confirms the suspected strong multiconfigurational character of the Si-terminated 3C-SiC(001)-p(2×1) reconstructed surface. From the NOONs of 1.5 and 0.5 for the ID and ID^* orbitals, it can further be concluded that the closed-shell RKS solution with occupation numbers of 2 and 0 overestimates the interdimer bond strength, while the UKS formalism underestimates this interaction with occupation numbers of 1 and 1. However, it has to be kept in mind that a true diradicalic solution, in which both ID and ID^* bands would be singly occupied, is not present in the UKS solution but instead the broken spin-symmetry α- and β-ID bands are singly occupied.

Comparing the multiconfigurational multi-dimer results of this work to the 1-dimer cluster model of Tamura and Gordon,[53] the effect of the interaction of neighboring dimers in the x-direction becomes apparent. In the CAS(4,4) calculation of the cited authors, the isolated π and π^* orbitals are almost degenerate with NOONs of 1.08 and 0.92. Optimizing an identical cluster model without MM embedding depicted in Fig. A.17 at CASSCF level with the TZVPP/TZVP basis set and the topmost two atomic layers allowed to relax, the dimer is slightly less diradicalic with NOONs of 1.17 and 0.83. Nevertheless, through the linear combination of neighboring dimers, these π and π^* orbitals energetically split up further into the resulting ID and ID^* states showing significantly different NOONs of about 1.5 and 0.5. This increased interdimer interaction also expresses itself in longer dimer bonds of about 2.55 Å

Table 3.22: Configuration composition of the CASSCF singlet ground state wave function for the H-saturated 3×1-dimer 4-layer cluster model ($Si_{16}C_{17}H_{38}$) of the ideal p(1×1) and p(2×1) reconstructed (SD model) Si-terminated 3C-SiC(001) surface optimized at CASSCF level with the full active space $\mathrm{CAS_{full}}$, the TZVPP/TZVP basis set, and the first two atomic layers relaxed according to Table 3.17. The occupation numbers in the configurations belong to the orbitals depicted in Figure 3.27 in the order of going from bottom up and from left to right. Only configurations with a percentage greater than 1 % are listed. Reprinted with permission from *J. Phys. Chem. C* 2023, 127, 48, 23475–23488. Copyright 2023 American Chemical Society.

Ideal p(1×1) Surface		p(2×1) Reconstruction	
Configuration	Percentage [%]	Configuration	Percentage [%]
[2222200000]	70.6	[2222200000]	55.6
[2221111000]	2.1	[2221111000]	17.2
[2222020000]	1.7	[2222020000]	6.0
[2212110100]	1.3	[2220022000]	5.3
		[2220202000]	4.6
		[2220220000]	4.0
		[2222002000]	2.9

for the $\mathrm{CAS}_{\mathrm{full}}$ $M\times N$-dimer clusters with M greater than two compared to the value of 2.46 Å in case of the 1-dimer cluster of Tamura and Gordon[53] or of 2.49 Å for the identical 1-dimer cluster model optimized as mentioned above.

The composition of the wave function of the ideal p(1×1) 3×1-dimer 4-layer cluster model is also listed in Table 3.22 with 70 % being contributed by the closed-shell configuration. The second most relevant configuration makes up only about 2 % and only two further configurations are contributing more than 1 %. On one hand, this confirms the highly multiconfigurational character anticipated before due to a very large number of different configurations representing the wave function. This is also apparent from the NOONs of the IA and IA^* orbitals given in Figs. A.23, A.24, A.31 and A.32 being in the range of about 1.90 − 1.80 and 0.25 − 0.05, respectively, thus all deviating significantly from the single-configurational occupation numbers of 2 and 0. On the other hand, it can be argued that an RKS description of the ideal p(1×1) surface is more reasonable than an RKS or UKS calculation of the p(2×1) surface because of the comparatively high contribution of the single closed-shell configuration to the wave function in the former case, which for the RKS formalism is also free of spin contamination.

With the multiconfigurational multi-dimer cluster model calculations at hand, it is interesting to ask if any insights regarding the band structure can be obtained. Paulus[56] already addressed this issue in their multiconfigurational cluster calculations of the supposedly metallic Si(001)-p(2×1) reconstructed surface with symmetric dimers. There, it was concluded that cluster model approaches cannot answer this question, which, even though not explicitly stated, is supposedly owed to the small system size compared to the real surface or periodic slab model calculations. However, using the example of the 3×3-dimer 4-layer cluster model of the p(2×1) reconstruction, the corresponding ID and ID^* orbitals of the $\mathrm{CAS}_{\mathrm{red}}(12{,}12)$ depicted in Fig. 3.30 already show a band-like behavior by forming different linear combinations between the π and π^* orbitals of neighboring unit cells. As apparent, these orbitals can be assigned to different $\vec{k}$-points on the $\vec{k}$-path of the corresponding first SBZ. For example, the different lobes of the ID orbitals all show the same phase factor at $\mathit{\Gamma}$, a fully alternating phase factor in the y-direction at J', and the phase factor alternating for every second unit cell in y-direction while being zero for the unit cell in between at the midpoint of the $\mathit{\Gamma}-J'$-path, which is in accordance with the electronic structure theory of solids established in Section 2.2.1. However, the size of this cluster model limits the number of $\vec{k}$-points to six compared to the slab model calculations, in which the PBCs basically give free choice over the $\vec{k}$-point sampling and thus the number of different linear combinations/Bloch functions considered. Furthermore, besides the limited number of atomic layers in the cluster models, the missing PBCs also result in an inferior embedding of the clusters and thus distorts their electronic structure. Nevertheless, even if these systematic problems were not present and one would conduct multiconfigurational periodic slab model calculations, the band structure is generally interpreted with a single-configurational picture in mind.

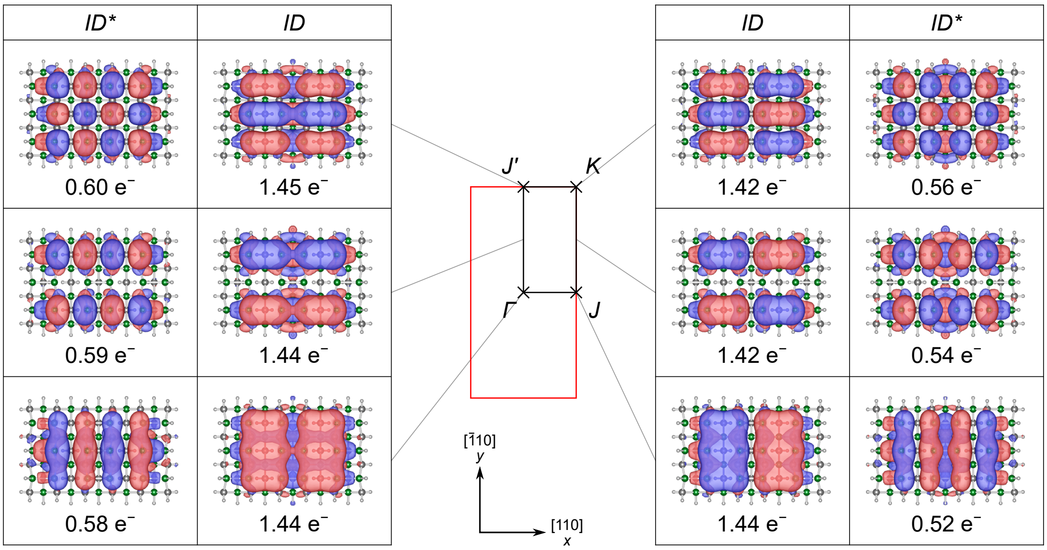

Figure 3.30: H-saturated 3×3-dimer 4-layer cluster model ($Si_{38}C_{39}H_{66}$) with the corresponding $CAS_{red}(12,12)$ orbitals assigned to different points on the $\vec{k}$-path of the first SBZ of the Si-terminated 3C-SiC(001)-p(2×1) reconstructed surface (SD model) optimized at CASSCF level with the TZVPP/TZVP basis set, and the first two atomic layers relaxed according to Table 3.17. The isosurface value of the orbitals amounts to $0.01\,a_0{}^{-3}$. Reprinted with permission from *J. Phys. Chem. C* 2023, 127, 48, 23475–23488. Copyright 2023 American Chemical Society. Slightly modified.

Accordingly, for semiconductors and insulators, bands can either be fully occupied or completely empty and for metals, there additionally exist partly filled bands at the intersection with the Fermi level. Multiconfigurational methods break with this convention as the wave function can consist of configurations that would be regarded as excited states in a single-configurational picture, which results in NOONs being able to take any real value between 0 and 2.

As described in Section 2.1.2.3, NOONs and NOs are used in multiconfigurational calculations because canonical orbitals with canonical orbital energies are not available in the first place. Accordingly, it is not possible to determine HOMO and LUMO and thus no energy gap between them to estimate the band gap of the material using multiconfigurational approaches. Thankfully, these methods offer the calculation of excited states and thus of excitation energies, which, as discussed before in Section 3.2.2, are the correct way to calculate the optical band gap in contrast to orbital energy differences, anyway. Table 3.23 lists such vertical state-optimized CASSCF and NEVPT2 excitation energies E_{exc} for the excitation from the singlet ground state to the first excited singlet state for the 3×1- and 4×1-dimer 4-layer cluster models of the ideal p(1×1) and p(2×1) reconstructed surface and the full active space CAS_{full}. The given values indicate both surfaces to be semiconducting and are thus in agreement with previous DFT calculations of the p(2×1) reconstructed[39,40,42–45,151] and the ideal p(1×1) surface,[42,44,45] the DFT results of this work as well as experimental work done on the p(2×1) reconstruction.[38,151–154] Interestingly, the excitation energies for the p(1×1) surface with about 2.1 eV − 2.2 eV are larger

Table 3.23: Vertical state-optimized CASSCF and NEVPT2 excitation energies E_{exc} for H-saturated 3×1- and 4×1-dimer 4-layer cluster models ($Si_{16}C_{17}H_{38}$ and $Si_{22}C_{23}H_{50}$) of the ideal p(1×1) and p(2×1) reconstructed (SD model) Si-terminated 3C-SiC(001) surface optimized at CASSCF and NEVPT2 level for the full active space CAS_{full}, the TZVPP/TZVP basis set, and the first two atomic layers relaxed according to Table 3.17. The values correspond to the energy difference between the singlet ground state and the first excited singlet state. Reprinted with permission from *J. Phys. Chem. C* 2023, 127, 48, 23475–23488. Copyright 2023 American Chemical Society.

Cluster Model	Ideal p(1×1) Surface		p(2×1) Reconstruction	
	$E_{exc,CASSCF}$ [eV]	$E_{exc,NEVPT2}$ [eV]	$E_{exc,CASSCF}$ [eV]	$E_{exc,NEVPT2}$ [eV]
3×1-dimer	2.22	2.10	0.69	0.87
4×1-dimer	2.09		0.65	

than for the p(2×1) reconstruction with about 0.6 eV − 0.9 eV. This relative trend is apparently in accordance with the RKS DFT HSE06 calculations of the respective surfaces giving surface band gaps $E_{g,surf}$ of 0.61 eV and 0.53 eV, while contradicting the UKS p(2×1) value of 1.34 eV. On the other hand, from a quantitative perspective, the RKS value of the p(1×1) surface seems to drastically underestimate the multiconfigurational surface band gaps. Overall, a comparison appears to be quite complicated since the multiconfigurational approach is necessary for a faithful description of the investigated system but the cluster models are apparently too small to give quantitative results. The insufficient size regarding the number of dimers is indicated by the slight but significant decrease and increase of the p(1×1) and p(2×1) CASSCF excitation energies, respectively, when going from a 3×1- to a 4×1-dimer cluster model. The inclusion of dynamic correlation using the NEVPT2 method for the 3×1-dimer cluster slightly amplifies this decrease for the p(1×1) excitation energy, while it counteracts this decrease for the p(2×1) reconstruction. However, due to the low number of investigated systems, reliable generalized trends for the excitation energies cannot be derived. Regarding the number of atomic layers, the excitation energies seem to be virtually unaffected as apparent from Table 3.24, which is presumably owed to the high localization of the surface states in the first two atomic layers as exemplary depicted in Fig. 3.27. Concerning the basis set, it is well-known that diffuse basis functions are needed for highly

Table 3.24: Vertical state-optimized CASSCF excitation energies E_{exc} for H-saturated 3×1- and 4×1-dimer 4-, 6-, and 8-layer cluster models ($Si_{16}C_{17}H_{38}$, $Si_{28}C_{35}H_{58}$, $Si_{34}C_{38}H_{58}$, $Si_{22}C_{23}H_{50}$, $Si_{40}C_{49}H_{78}$, and $Si_{50}C_{54}H_{78}$) of the ideal p(1×1) and p(2×1) reconstructed (SD model) Si-terminated 3C-SiC(001) surface optimized at CASSCF level with the full active space CAS_{full}, the TZVPP/TZVP basis set, and the first two atomic layers relaxed according to Table 3.17. The values correspond to the energy difference between the singlet ground state and the first excited singlet state. Reprinted with permission from *J. Phys. Chem. C* 2023, 127, 48, 23475–23488. Copyright 2023 American Chemical Society.

Number of Atomic Layers in z	Cluster Model			
	3×1-dimer		4×1-dimer	
	$E_{exc,p(1\times1)}$ [eV]	$E_{exc,p(2\times1)}$ [eV]	$E_{exc,p(1\times1)}$ [eV]	$E_{exc,p(2\times1)}$ [eV]
4	2.22	0.69	2.09	0.65
6	2.24	0.71	2.11	0.67
8	2.24	0.71	2.12	0.67

excited electronic states.[58] However, as apparent from Table A.12 in the basis set convergence study of Appendix A.2.3, the TZVPP/TZVP basis set used for the cluster calculations is already sufficient in comparison to def2 basis sets of different quality[148] including diffuse basis functions.

To summarize, the cluster models show promising results regarding the dimer bond length and the local description of the statically correlated ID and ID^* orbitals of the Si-terminated 3C-SiC(001)-p(2×1) reconstructed surface but proper multiconfigurational methods for periodic slab models, which are unfortunately still in development, are needed for reasonable reconstruction energies and a faithful band structure.

4 Conclusion and Outlook

In this work, a detailed theoretical description of the Si-terminated 3C-SiC(001) surface was carried out utilizing periodic slab model calculations with single-configurational HF and KS DFT and multiconfigurational cluster model calculations using CASSCF and NEVPT2. As illustrated in Fig. 4.1, the single-configurational calculations gave rise to a variety of reconstructions highly sensitive to the usage of a restricted or unrestricted approach. Starting from the ideal p(1×1) surface, two weak reconstructions can be obtained when applying the restricted flavor, namely the p(2×1) structure with symmetric dimers and a p(4×1) structure with an additional dimerization of two such dimers. Speaking in the depicted localized orbital picture, the degenerate doubly occupied interatomic (IA) bonds of the ideal p(1×1) surface split up into the intradimer σ and interdimer (ID) bonds of the p(2×1) surface. In case of the p(4×1) reconstruction, the ID bonds further split up into one bond for the short and the long interdimer distances each, namely ID_{short} and ID_{long}. The corresponding antibonding interdimer (ID^*) bonds are energetically close to their bonding counterpart, which results in a statically correlated situation and thus questions the usage of single-configurational methods. For the p(4×1) surface, this even induces metallic behavior as the bands correspond-

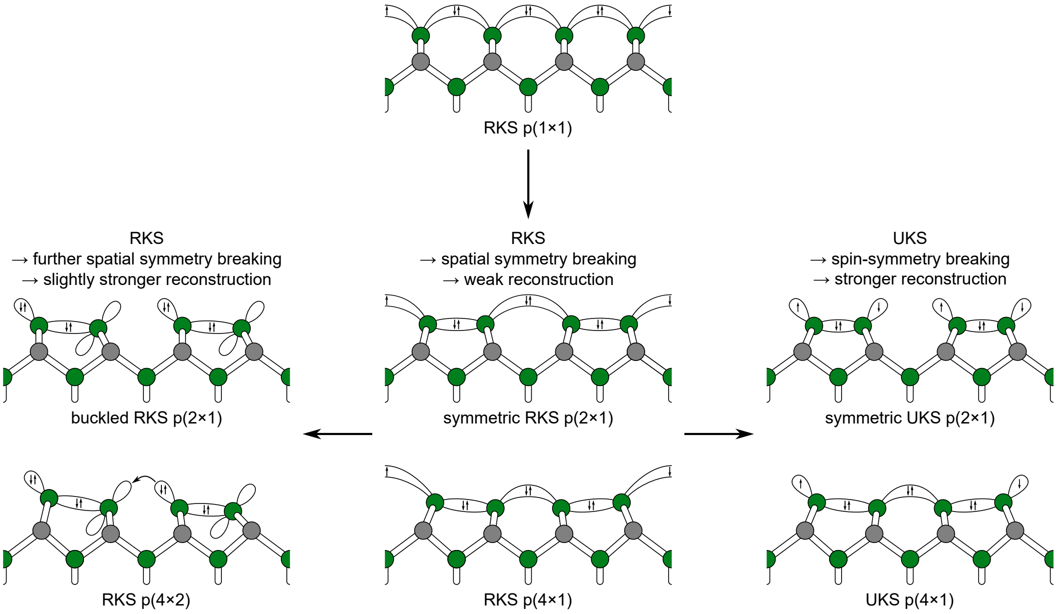

Figure 4.1: Summary of the restricted and unrestricted single-configurational calculations for the different reconstructions of the Si-terminated 3C-SiC(001) surface.

ing to the severely stretched ID_{long} and ID^*_{long} bonds cross at the Fermi level, even though the experimentally observed p(2×1) and c(4×2) reconstructions as well as all other theoretical results of this work observed semiconducting properties.

Now, two processes have emerged to further energetically lower these weakly stabilized structures with poor restricted description. On one hand, additional spatial symmetry breaking within this restricted approach is possible (left side of Fig. 4.1). This results in the p(2×1) structure to give bucked dimers with a slightly stronger reconstruction energy. Here, the former ID bonds localize as sp^3-like lone pairs at the upper dimer atom and empty p_z-like orbitals emerge at the lower dimer atom like on the closely related Si(001) surface. Similarly, the p(4×1) structure transforms into a p(4×2) reconstruction, consisting of two buckled dimers in each structural 4×1 unit, which are again additionally dimerized. The alternative process to breaking spatial symmetry corresponds to spin-symmetry breaking when applying the unrestricted approach (right side of Fig. 4.1). Here, the p(2×1) structure still consists of symmetric dimers but with shorter dimer bonds and stronger stabilization than the buckled dimers. This is achieved by the spin-localization basically bisecting the ID bonds into singly occupied sp^3-like dangling bonds. The same effect is observable for the p(4×1) reconstruction, whose electronic structure changes from metallic to semiconducting over the course of this process. Since the spin-symmetry breaking gives structures favored over the ones with broken spatial symmetry and since it is able to partially include static correlation, the buckled structures are most likely artifacts as a result of the overall very flat potential energy surface of this system. However, the unrestricted single-configurational solutions are also merely mimicking a singlet polyradicalic electronic structure because only the α- and β-ID orbitals are singly occupied instead of both the ID and ID^* orbitals. This causes severely spin-contaminated results and questions the quantitative reliability also of the unrestricted single-configurational methods.

The multiconfigurational cluster model calculations of the p(2×1) reconstructed surface with symmetric dimers are able to resolve the problems of the single-configurational approaches. Here, the NOONs of the ID and ID^* orbitals amount to about 1.5 and 0.5, respectively. This indicates a highly multiconfigurational character of this system and an approximately equal mixture of the closed-shell and radicalic configurations, which could be further confirmed by the composition of the corresponding wave function. The reconstruction strength is also in accordance with this observation as the multiconfigurational dimer bond lengths and the reconstruction energies are located in between the restricted and unrestricted single-configurational values for the p(2×1) reconstruction with symmetric dimers obtained before as indicated in Fig. 4.2, though there is slightly better agreement with the unrestricted approach. Accordingly, it can be concluded that the restricted single-configurational method overestimates the strength of the ID bond by its enforced double occupation and the unrestricted counterpart underestimates it by its complete bisection. It should be emphasized that the inclusion of multiple dimers in each dimer

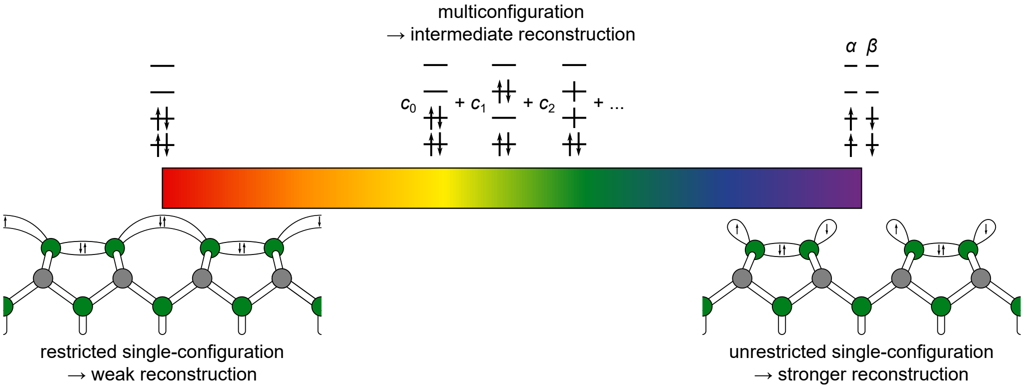

Figure 4.2: Summary of the single- and multiconfigurational calculations for the Si-terminated 3C-SiC(001)-p(2×1) reconstructed surface (SD model). Reprinted with permission from *J. Phys. Chem. C* 2023, 127, 48, 23475–23488. Copyright 2023 American Chemical Society. Modified.

row of the cluster models is essential to obtain these results since otherwise a mainly radicalic solution is obtained like in the study of Tamura and Gordon[53] because no formation of the ID and ID^* orbitals is possible. Furthermore, the cluster models of the ideal p(1×1) surface confirmed the anticipated strong multiconfigurational character of this system through the NOONs of the IA and IA^* orbitals and the composition of the wave function. While no band structure can be obtained for these cluster models due to their insufficient size, vertical excitation energies from the singlet ground state to the first excited singlet state indicate both the p(1×1) and p(2×1) surfaces to be semiconducting.

Overall, the Si-terminated 3C-SiC(001) surface proved to be highly challenging from a theoretical perspective due to its strongly correlated surface state bands. Even though this work was already able to improve the understanding of the spatial and electronic structure of this system, the cluster model approach is far from optimal to represent the actual surface as became apparent in the various convergence studies. While the strong multiconfigurational character could be shown, as of today, single-configurational periodic slab model calculations might still be the only viable option for extensive subsequent theoretical investigations like, e.g., surface reactions due to the limited computational power and multiconfigurational methods for solid state systems still being at an early stage of development. Here, the unrestricted approach is supposedly preferred over the restricted calculations as it gave slightly better agreement with the multiconfigurational methods and experimental data. It can be argued that the error introduced by the spin contamination for this methodology is most likely in the same order of magnitude as the error of KS DFT itself and should thus not be overemphasized from a pragmatic point of view. Along these lines, the application of the AP scheme recently developed for DFT calculations employing PBCs[184] might improve the UKS results by obtaining the non-spin-contaminated configuration representing true singlet diradicalic Si dimers. On the other hand, it should be kept in mind that the multiconfigurational cluster model calculations showed this exact configuration to only contribute about 17 % to the exact ground state wave function, questioning the relevance of such corrections for this particular system. Still, it is interesting from a scientific perspective how this would influence the spatial structure of the reconstruction. Concerning the ideal p(1×1) surface, presumably no further improvement is possible with single-configurational methods because unrestricted calculations will always collapse to the restricted solutions. Since this system is also of multiconfigurational character, using it as reference structure to calculate reconstruction energies will at all times introduce an error that could only be quantified by multiconfigurational slab model calculations. Still, it might be possible that both the ideal and the reconstructed surfaces exhibit errors of similar size, leading to reasonable single-configurational results due to error cancellation.

Turning the attention to the multiconfigurational description of the Si-terminated 3C-SiC(001) surface, the cluster model approach is generally inferior to periodic slab models due to the missing periodic boundary conditions. In this work in particular, the limited number of dimers and atomic layers due to the computational cost of the high-level methods further reduces the accuracy of the obtained results. Nevertheless, in recent years, some groups have developed approximate solvers for CASSCF to enable calculations for large active spaces with up to about 50 electrons and 50 orbitals,[200–202] which would enable to extend the cluster model size beyond what was achieved here and gain more reliable results. However, geometry optimizations seem not to be implemented for these methods, thus limiting their value when trying to find the actual multiconfigurational spatial structure. Furthermore, it might be possible that the number of basis functions becomes the limiting factor for the cluster model size because the cited studies restricted their benchmarks to comparably small molecules.

Instead of simply increasing the cluster model size, an alternative approach would be to use advanced embedding methods going beyond the simple H-saturation applied in this work. Here, several approaches are possible, for example, an embedding of the quantum cluster in a larger MM cluster like done by Tamura and Gordon[53] or into a periodic embedding potential obtained from periodic slab model DFT calculations, which can either be static during the high-level calculation as done by Klüner et al.[133] or updated in a self-consistent manner with the wave-function-in-DFT method of Chulhai and Goodpaster.[134] However, it is questionable whether such MM or single-configurational DFT embedding potentials can improve the results compared to the plain H-saturated cluster models because the multiconfigurational treatment would still be limited to the orbitals in the small quantum cluster instead of the actual periodic Bloch functions. This concern is supported by the excitation energies not converging with the number of dimers in this work. Recently, density matrix embedding theory (DMET) for solid state systems employing PBCs and $\vec{k}$-point sampling has been developed, where in each unit cell a so-called impurity can be treated with high-level methods.[135,136] However, the interaction between these impurities of different unit cells are only considered at a lower mean-field level of theory, which also does not correspond to true periodic bands calculated at a multiconfigurational level. Nevertheless, these methods have shown to perform quite well in benchmark calculations against periodic full CI or periodic CCSD for small systems and even a band structure can be obtained.[135] For a true description of the Si-terminated 3C-SiC(001) surface, a combination of multiconfigurational methods like CASSCF with periodic slab models would be necessary. The PySCF program package[130,203] actually allows to carry out such calculations but it is restricted to only contain the $\mathit{\Gamma}$-point in the $\vec{k}$-point grid. Hence, the size of the supercell would need to be increased to counteract the poor $\vec{k}$-point sampling to arrive at the thermodynamic limit. Accordingly, just like in case of the cluster models, the supercell size is then quickly limited by the active space size.[130,203] Nevertheless, this approach should still give an improved embedding and thus description of the surface compared to the cluster model calculations of this work.

With this, it can be concluded that a faithful description of the statically correlated Si-terminated 3C-SiC(001) surface goes beyond the limitations of current state-of-the-art electronic structure methods and can thus be regarded as an excellent benchmark system for future developments in this field. Nevertheless, in this work, it was still possible to shed light on this dark frontier of multiconfigurational solid state surface calculations to a degree not being achieved before for this material and the corresponding results are eagerly waiting to be measured against future investigations.

A Appendix

A.1 Single-Configurational Calculations with PBCs

A.1.1 Calculation of Reciprocal Space Surface Basis Vectors

In this section, it is shown how the reciprocal space surface basis vectors $\vec{b}_1$ and $\vec{b}_2$ are derived from the real space surface basis vectors $\vec{a}_1$ and $\vec{a}_2$ using the example of the ideal p(1×1) surface, the p(2×1) reconstruction, and the c(4×2) reconstruction of 3C-SiC(001). In analogy to the bulk case presented in Section 2.2.1.1, the reciprocal space surface basis vectors are calculated as follows:[204]

$$\vec{b}_1 = 2\pi \frac{\vec{a}_2 \times \vec{n}}{|\vec{a}_1 \times \vec{a}_2|} \qquad \vec{b}_2 = 2\pi \frac{\vec{n} \times \vec{a}_1}{|\vec{a}_1 \times \vec{a}_2|} \tag{A.1}$$

Here, $\vec{n}$ is the surface normal of the respective surface and × indicates the cross product of two vectors, giving a new vector orthogonal to the plane spanned by the two initial vectors, which in the 3D case is calculated according to the formula below:

$$\vec{a} \times \vec{b} = \begin{pmatrix} a_1 \\ a_2 \\ a_3 \end{pmatrix} \times \begin{pmatrix} b_1 \\ b_2 \\ b_3 \end{pmatrix} = \begin{pmatrix} a_2 b_3 - a_3 b_2 \\ a_3 b_1 - a_1 b_3 \\ a_1 b_2 - a_2 b_1 \end{pmatrix} \tag{A.2}$$

The length of the resulting vector is proportional to the area of the parallelogram spanned by the two initial vectors. Accordingly, the size of this area is dependent on the angle between both vectors, resulting in a maximum value for orthogonal and a minimum value of zero for parallel or antiparallel vectors. The size of the area of the two real space surface basis vectors $\vec{a}_1$ and $\vec{a}_2$ is calculated in the denominator of Eq. A.1, which can alternatively be written as:

$$|\vec{a}_1 \times \vec{a}_2| = |\vec{a}_1|\,|\vec{a}_2| \sin(\angle(\vec{a}_1, \vec{a}_2)) \tag{A.3}$$

In case of a (001) surface for a cubic system (basis vectors coinciding with the Cartesian axes), the surface normal $\vec{n}$ is:

$$\vec{n} = \begin{pmatrix} 0 \\ 0 \\ 1 \end{pmatrix} \tag{A.4}$$

The length or magnitude of a vector is calculated as follows:

$$|\vec{a}| = \sqrt{a_1^2 + a_2^2 + a_3^2} \tag{A.5}$$

With this information at hand, the reciprocal space surface basis vectors for the different surfaces in this work can be calculated.

Ideal p(1×1) Surface

For the ideal p(1×1) surface, the real space surface basis vectors $\vec{a}_1$ and $\vec{a}_2$ are:

$$\vec{a}_1 = \begin{pmatrix} 1 \\ 0 \\ 0 \end{pmatrix} \qquad \vec{a}_2 = \begin{pmatrix} 0 \\ 1 \\ 0 \end{pmatrix} \tag{A.6}$$

Insertion into the numerators of the fractions in Eq. A.1 yields:

$$\vec{b}_1\text{:}\ \ \vec{a}_2 \times \vec{n} = \begin{pmatrix} 0 \\ 1 \\ 0 \end{pmatrix} \times \begin{pmatrix} 0 \\ 0 \\ 1 \end{pmatrix} = \begin{pmatrix} 1\cdot 1 - 0\cdot 0 \\ 0\cdot 0 - 0\cdot 1 \\ 0\cdot 0 - 1\cdot 0 \end{pmatrix} = \begin{pmatrix} 1 \\ 0 \\ 0 \end{pmatrix} \tag{A.7}$$

$$\vec{b}_2\text{:}\ \ \vec{n} \times \vec{a}_1 = \begin{pmatrix} 0 \\ 0 \\ 1 \end{pmatrix} \times \begin{pmatrix} 1 \\ 0 \\ 0 \end{pmatrix} = \begin{pmatrix} 0\cdot 0 - 1\cdot 0 \\ 1\cdot 1 - 0\cdot 0 \\ 0\cdot 0 - 0\cdot 1 \end{pmatrix} = \begin{pmatrix} 0 \\ 1 \\ 0 \end{pmatrix} \tag{A.8}$$

Since in case of the ideal p(1×1) surface the real space basis vectors are orthogonal, the denominators of the fractions in Eq. A.1 simply amount to:

$$|\vec{a}_1| = \sqrt{1^2 + 0^2 + 0^2} = 1 \tag{A.9}$$

$$|\vec{a}_2| = \sqrt{0^2 + 1^2 + 0^2} = 1 \tag{A.10}$$

$$|\vec{a}_1 \times \vec{a}_2| = |\vec{a}_1|\,|\vec{a}_2| \sin(90^\circ) = 1 \cdot 1 \cdot 1 = 1 \tag{A.11}$$

Thus, the reciprocal space surface basis vectors are:

$$\vec{b}_1 = 2\pi \frac{\begin{pmatrix} 1 \\ 0 \\ 0 \end{pmatrix}}{1} = \begin{pmatrix} 2\pi \\ 0 \\ 0 \end{pmatrix} \tag{A.12}$$

$$\vec{b}_2 = 2\pi \frac{\begin{pmatrix} 0 \\ 1 \\ 0 \end{pmatrix}}{1} = \begin{pmatrix} 0 \\ 2\pi \\ 0 \end{pmatrix} \tag{A.13}$$

p(2×1) Reconstruction

For the p(2×1) reconstructed surface, the real space surface basis vectors $\vec{a}_1$ and $\vec{a}_2$ are:

$$\vec{a}_1 = \begin{pmatrix} 2 \\ 0 \\ 0 \end{pmatrix} \qquad \vec{a}_2 = \begin{pmatrix} 0 \\ 1 \\ 0 \end{pmatrix} \tag{A.14}$$

Insertion into the numerators of the fractions in Eq. A.1 yields:

$$\vec{b}_1\text{:}\ \ \vec{a}_2 \times \vec{n} = \begin{pmatrix} 0 \\ 1 \\ 0 \end{pmatrix} \times \begin{pmatrix} 0 \\ 0 \\ 1 \end{pmatrix} = \begin{pmatrix} 1\cdot 1 - 0\cdot 0 \\ 0\cdot 0 - 0\cdot 1 \\ 0\cdot 0 - 1\cdot 0 \end{pmatrix} = \begin{pmatrix} 1 \\ 0 \\ 0 \end{pmatrix} \tag{A.15}$$

$$\vec{b}_2\text{:}\ \ \vec{n} \times \vec{a}_1 = \begin{pmatrix} 0 \\ 0 \\ 1 \end{pmatrix} \times \begin{pmatrix} 2 \\ 0 \\ 0 \end{pmatrix} = \begin{pmatrix} 0\cdot 0 - 1\cdot 0 \\ 1\cdot 2 - 0\cdot 0 \\ 0\cdot 0 - 0\cdot 2 \end{pmatrix} = \begin{pmatrix} 0 \\ 2 \\ 0 \end{pmatrix} \tag{A.16}$$

Since in case of the p(2×1) reconstructed surface the real space basis vectors are orthogonal, the denominators of the fractions in Eq. A.1 simply amount to:

$$|\vec{a}_1| = \sqrt{2^2 + 0^2 + 0^2} = 2 \tag{A.17}$$

$$|\vec{a}_2| = \sqrt{0^2 + 1^2 + 0^2} = 1 \tag{A.18}$$

$$|\vec{a}_1 \times \vec{a}_2| = |\vec{a}_1|\,|\vec{a}_2| \sin(90^\circ) = 2\cdot 1\cdot 1 = 2 \tag{A.19}$$

Accordingly, the reciprocal space surface basis vectors are:

$$\vec{b}_1 = 2\pi \frac{\begin{pmatrix} 1 \\ 0 \\ 0 \end{pmatrix}}{2} = \begin{pmatrix} \pi \\ 0 \\ 0 \end{pmatrix} \tag{A.20}$$

$$\vec{b}_2 = 2\pi \frac{\begin{pmatrix} 0 \\ 2 \\ 0 \end{pmatrix}}{2} = \begin{pmatrix} 0 \\ 2\pi \\ 0 \end{pmatrix} \tag{A.21}$$

c(4×2) Reconstruction

For the c(4×2) reconstructed surface, the real space surface basis vectors of the rhombic unit cell $\vec{a}_1$ and $\vec{a}_2$ are:

$$\vec{a}_1 = \begin{pmatrix} 2 \\ -1 \\ 0 \end{pmatrix} \qquad \vec{a}_2 = \begin{pmatrix} 2 \\ 1 \\ 0 \end{pmatrix} \tag{A.22}$$

Insertion into the numerators of the fractions in Eq. A.1 yields:

$$\vec{b}_1\colon\ \vec{a}_2 \times \vec{n} = \begin{pmatrix} 2 \\ 1 \\ 0 \end{pmatrix} \times \begin{pmatrix} 0 \\ 0 \\ 1 \end{pmatrix} = \begin{pmatrix} 1 \cdot 1 - 0 \cdot 0 \\ 0 \cdot 0 - 2 \cdot 1 \\ 2 \cdot 0 - 1 \cdot 0 \end{pmatrix} = \begin{pmatrix} 1 \\ -2 \\ 0 \end{pmatrix} \tag{A.23}$$

$$\vec{b}_2\colon\ \vec{n} \times \vec{a}_1 = \begin{pmatrix} 0 \\ 0 \\ 1 \end{pmatrix} \times \begin{pmatrix} 2 \\ -1 \\ 0 \end{pmatrix} = \begin{pmatrix} 0 \cdot 0 - 1 \cdot (-1) \\ 1 \cdot 2 \quad - \quad 0 \cdot 0 \\ 0 \cdot (-1) - 0 \cdot 2 \end{pmatrix} = \begin{pmatrix} 1 \\ 2 \\ 0 \end{pmatrix} \tag{A.24}$$

The angle between the real space surface basis vectors of the rhombic unit cell of the c(4×2) reconstructed surface can be calculated using the arctangent (see Fig. A.1):

$$\angle(\vec{a}_1, \vec{a}_2) = 2 \cdot \tan^{-1}\left(\frac{1}{2}\right) \approx 53.13^\circ \tag{A.25}$$

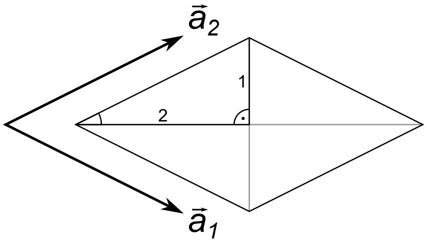

Figure A.1: Calculation of the angle between the real space surface basis vectors in the primitive rhombic $(\sqrt{5}\times\sqrt{5})R(2 \cdot \tan^{-1}(0.5))$ unit cell of the Si-terminated 3C-SiC(001)-c(4×2) reconstructed surface.

Hence, the denominators of the fractions in Eq. A.1 amount to:

$$|\vec{a}_1| = \sqrt{2^2 + (-1)^2 + 0^2} = \sqrt{5} \tag{A.26}$$

$$|\vec{a}_2| = \sqrt{2^2 + 1^2 + 0^2} = \sqrt{5} \tag{A.27}$$

$$|\vec{a}_1 \times \vec{a}_2| = |\vec{a}_1|\,|\vec{a}_2| \sin\left(2 \cdot \tan^{-1}\left(\frac{1}{2}\right)\right) = \sqrt{5} \cdot \sqrt{5} \cdot 0.8 = 4 \tag{A.28}$$

Accordingly, the reciprocal space surface basis vectors are:

$$\vec{b}_1 = 2\pi \frac{\begin{pmatrix} 1 \\ -2 \\ 0 \end{pmatrix}}{4} = \begin{pmatrix} 0.5\pi \\ -\pi \\ 0 \end{pmatrix} \tag{A.29}$$

$$\vec{b}_2 = 2\pi \frac{\begin{pmatrix} 1 \\ 2 \\ 0 \end{pmatrix}}{4} = \begin{pmatrix} 0.5\pi \\ \pi \\ 0 \end{pmatrix} \tag{A.30}$$

Comparison of the p(1×1), p(2×1), and c(4×2) lattices

As apparent from Table A.1, in case of the ideal p(1×1) surface and the p(2×1) reconstruction, the intuitive rule applies that doubling a vector in real space results in the corresponding reciprocal space vector to be halved. However, it is also apparent that this proportionality seems to not be fulfilled in case of the c(4×2) reconstruction, which might be confusing at first but is explained in the following. When, for example, going from the real space vector

$$\begin{pmatrix} 1 \\ 0 \\ 0 \end{pmatrix} \quad \text{to} \quad \begin{pmatrix} 2 \\ 0 \\ 0 \end{pmatrix}$$

with lengths of 1 and 2, respectively, the corresponding lengths in reciprocal space amount to 2π and π. The latter values can be obtained by the simple ratios $\frac{2\pi}{1}$ and $\frac{2\pi}{2}$ with the real space lengths in the denominator, respectively. These ratios are often the first intuitive approach when being confronted with the inversely proportional relation of the real and reciprocal space basis vectors for the first time. But this would also imply that in case of the real space vector

$$\begin{pmatrix} 2 \\ -1 \\ 0 \end{pmatrix}$$

of the c(4×2) reconstruction with a length of about 2.24, the length of the corresponding reciprocal space vector should be $\frac{2\pi}{2.24} \approx 0.89\pi$. This at first glance would also make sense intuitively since one would expect a vector with a real space length of 2.24 to be shorter in reciprocal space than a vector with a real space length of 2. However, as the calculations conducted above show, the actual length of the former vector in reciprocal space amounts to 1.12π. This difference is caused by the calculation of reciprocal space basis vectors not only considering the length of the real space vector in the denominator of Eq. A.1 but instead the length of the cross product of both real space vectors.

Table A.1: Comparison of the real and reciprocal space surface basis vectors for the ideal p(1×1), p(2×1) reconstructed, and c(4×2) reconstructed surfaces and their relative lengths in Fig. 2.6.

Recon- struction	Real Space			Reciprocal Space		
	Basis Vectors $\vec{a}_i$	Length $\lvert\vec{a}_i\rvert$	Relative Length in Fig. 2.6	Corresponding Basis Vectors $\vec{b}_i$	Length $\lvert\vec{b}_i\rvert$	Relative Length in Fig. 2.6
p(1×1), p(2×1)	$\begin{pmatrix} 1 \\ 0 \\ 0 \end{pmatrix}, \begin{pmatrix} 0 \\ 1 \\ 0 \end{pmatrix}$	1	1	$\begin{pmatrix} 2\pi \\ 0 \\ 0 \end{pmatrix}, \begin{pmatrix} 0 \\ 2\pi \\ 0 \end{pmatrix}$	2π	2
p(2×1)	$\begin{pmatrix} 2 \\ 0 \\ 0 \end{pmatrix}$	2	2	$\begin{pmatrix} \pi \\ 0 \\ 0 \end{pmatrix}$	π	1
c(4×2)	$\begin{pmatrix} 2 \\ -1 \\ 0 \end{pmatrix}, \begin{pmatrix} 2 \\ 1 \\ 0 \end{pmatrix}$	$\sqrt{5} \approx 2.24$	≈ 2.24	$\begin{pmatrix} 0.5\pi \\ -\pi \\ 0 \end{pmatrix}, \begin{pmatrix} 0.5\pi \\ \pi \\ 0 \end{pmatrix}$	$\frac{\sqrt{5}}{2}\pi \approx 1.12\pi$	≈ 1.12

As already explained above, this cross product corresponds to the area of the parallelogram spanned by the two real space vectors, which is dependent on the angle between both vectors. Since this angle in the c(4×2) case is not orthogonal, the area spanned by the two vectors is not at its maximum value but only at 80 % with a value of 4 as indicated in Eq. A.28. When using the maximum area of 5, one would in fact obtain the intuitively expected reciprocal space basis vector length of about 0.89π. Accordingly, one has to be careful when comparing the lengths of reciprocal space basis vectors of two different reciprocal lattices with different angles between the respective real space basis vectors.

A.1.2 Details on $\vec{k}$-Point Grids in CRYSTAL17

Since the CRYSTAL17 manual[124] is quite sparse at times, here some additional information regarding the $\vec{k}$-point grids are given, which were acquired over the course of this (and previous) work. Hopefully, this comes to good use for future users of the mentioned program package or users conducting calculations with PBCs in general.

A detailed understanding of the $\vec{k}$-point grids employed in CRYSTAL17 is important to correctly interpret and conduct the respective calculations. While not explicitly mentioned in the manual, from the analysis of the output files, it is apparent that $\varGamma$-centered grids are used by default in CRYSTAL17 without any possibility of changing the sampling scheme like in, e.g., VASP.[122,123] The first SBZ of the Si-terminated 3C-SiC(001)-p(2×1) reconstructed surface investigated in this work with the $\varGamma$-centered 6×12×1 Monkhorst-Pack $\vec{k}$-point grid is depicted in Fig. A.2 and used as first example. Since in the calculations

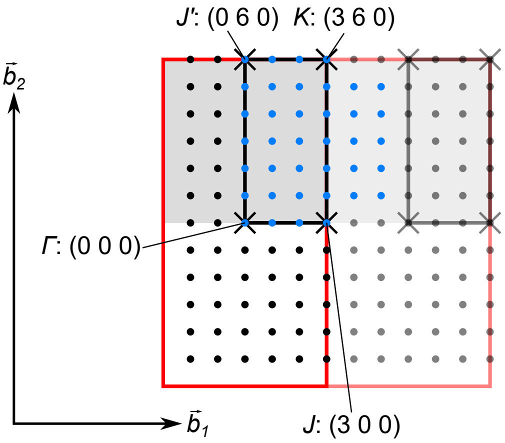

Figure A.2: $\varGamma$-centered 6×12×1 Monkhorst-Pack $\vec{k}$-point grid (black dots) used in the calculations of the Si-terminated 3C-SiC(001)-p(2×1) reconstructed surface (SD model). The first SBZ is indicated by red lines, the IBZ when imposing $P1$-symmetry is shaded in gray, and the $\vec{k}$-path for band structure calculations is indicated by black lines. The neighboring first SBZ is additionally shown in a faded manner. The blue dots represent the irreducible $\vec{k}$-points of the IBZ that are actually calculated.

only $P1$-symmetry was applied to enable a maximum of variational freedom for the geometry optimizations, the IBZ corresponds to half the BZ as established in Section 2.2.1.1. It has to be kept in mind that the actual surface in real space is of higher symmetry, which is why the actual IBZ corresponds to only one fourth of the BZ where the $\vec{k}$-path for band structure calculations is located. Under $P1$-symmetry, 38 irreducible $\vec{k}$-points are present as highlighted by the blue dots in Fig. A.2. The four apparently missing irreducible $\vec{k}$-points at the top and bottom right hand side of this blue grid are actually not needed since they are obtainable by applying the translation and inversion symmetry of the reciprocal space on other irreducible $\vec{k}$-points. As apparent in the output of CRYSTAL17 in Fig. A.3, further information regarding the coordinates of the $\vec{k}$-points are available. These coordinates are obtained by simply counting the position of the respective $\vec{k}$-point along the three reciprocal basis vectors $\vec{b}_1$, $\vec{b}_2$, and $\vec{b}_3$. Since the output corresponds to a surface slab model, one $\vec{k}$-point along $\vec{b}_3$ is sufficient as already discussed in Section 2.2.1.5. Consequently, in combination with Fig. A.2, the high-symmetry $\vec{k}$-points of the $\vec{k}$-path Γ, J, K, and J' are assignable to the coordinates (0 0 0), (3 0 0), (3 6 0), and (0 6 0), respectively. This is further indicated by the descriptors C and R, corresponding to complex and purely real $\vec{k}$-points, respectively, with only the high-symmetry $\vec{k}$-points being classified as R. This is consistent with the discussion in the context of the 1D example in Fig. 2.7, where only the Bloch functions at the center of the first BZ at $k = 0$ and at the edges at $k = \frac{\pi}{a}$ have purely real phase factors, which is transferable to higher dimensions. Knowledge of the reciprocal space coordinates of the high-symmetry $\vec{k}$-points was important in this work to correctly plot the band structure and find the corresponding orbitals. Especially in the latter case, this was relevant because one CRYSTAL17 orbital calculation creates one orbital file for each $\vec{k}$-point of the $\vec{k}$-point grid employed, with the names of the orbital files only differing in the three coordinate numbers listed in the output.

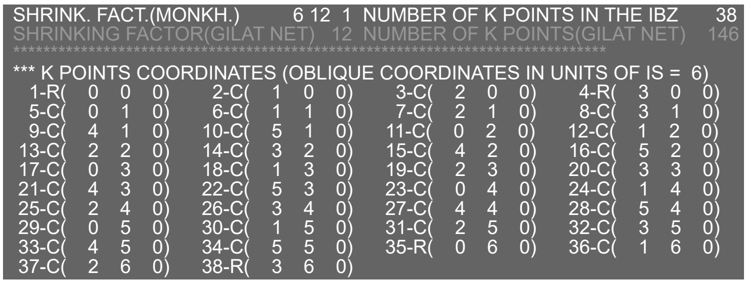

```
SHRINK. FACT.(MONKH.)        6 12  1  NUMBER OF K POINTS IN THE IBZ      38
SHRINKING FACTOR(GILAT NET)   12  NUMBER OF K POINTS(GILAT NET)    146
*******************************************************************************

*** K POINTS COORDINATES (OBLIQUE COORDINATES IN UNITS OF IS =  6)
   1-R(   0   0   0)      2-C(   1   0   0)      3-C(   2   0   0)      4-R(   3   0   0)
   5-C(   0   1   0)      6-C(   1   1   0)      7-C(   2   1   0)      8-C(   3   1   0)
   9-C(   4   1   0)     10-C(   5   1   0)     11-C(   0   2   0)     12-C(   1   2   0)
  13-C(   2   2   0)     14-C(   3   2   0)     15-C(   4   2   0)     16-C(   5   2   0)
  17-C(   0   3   0)     18-C(   1   3   0)     19-C(   2   3   0)     20-C(   3   3   0)
  21-C(   4   3   0)     22-C(   5   3   0)     23-C(   0   4   0)     24-C(   1   4   0)
  25-C(   2   4   0)     26-C(   3   4   0)     27-C(   4   4   0)     28-C(   5   4   0)
  29-C(   0   5   0)     30-C(   1   5   0)     31-C(   2   5   0)     32-C(   3   5   0)
  33-C(   4   5   0)     34-C(   5   5   0)     35-R(   0   6   0)     36-C(   1   6   0)
  37-C(   2   6   0)     38-R(   3   6   0)
```

Figure A.3: Excerpt of the CRYSTAL17 output regarding the $\vec{k}$-point grid for the calculation of the Si-terminated 3C-SiC(001)-p(2×1) reconstructed surface (SD model) using the Γ-centered 6×12×1 Monkhorst-Pack $\vec{k}$-point grid depicted in Fig. A.2.

With the information presented, for the calculation of orbitals, it can further be concluded that one has to pay attention to the CRYSTAL17 output if the $\vec{k}$-point grid applied does actually contain the $\vec{k}$-points of interest. For example, when using the odd $\vec{k}$-point grid of Fig. 2.16b), none of the high-

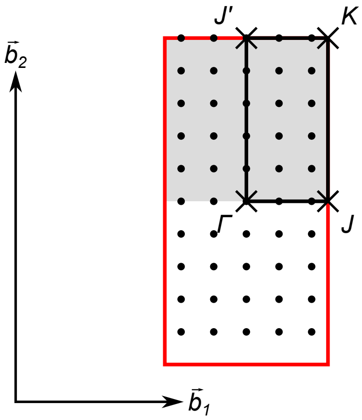

Figure A.4: Γ-centered 5×10×1 Monkhorst-Pack $\vec{k}$-point grid (black dots) for the Si-terminated 3C-SiC(001)-p(2×1) reconstructed surface (SD model). The first SBZ is indicated by red lines, the IBZ when imposing $P1$-symmetry is shaded in gray, and the $\vec{k}$-path for band structure calculations is indicated by black lines. This $\vec{k}$-point grid was not used in the calculations conducted in this work.

symmetry $\vec{k}$-points on the BZ edges would be included. Or if one would apply a Γ-centered 5×10×1 $\vec{k}$-point grid to the BZ of the p(2×1) reconstruction as shown in Fig. A.4, J and K would be excluded from the $\vec{k}$-point grid due to an odd number of $\vec{k}$-points along $\vec{b}_1$. Thankfully, CRYSTAL17 offers to specify a new $\vec{k}$-point grid for the non-self-consistent calculation of orbitals or the band structure (as discussed in Section 2.2.1.6), so one does not need to repeat the, e.g., geometry optimization conducted in advance.

Going a step further, one has to be even more careful when the first BZ does not coincide with the reciprocal unit cell like it was conveniently the case for the p(2×1) reconstruction. In case of the c(4×2) reconstruction, the real and reciprocal surface unit cells are rhombuses, while the first SBZ is an irregular hexagon (see Fig. A.5). However, CRYSTAL17 is still using the reciprocal space surface unit cells and not the SBZ during the actual calculations, which is why the $\vec{k}$-point grid has to be chosen carefully to also include the high-symmetry $\vec{k}$-points of the SBZ. This issue is apparent in Fig. A.5a), showing the Γ-centered 6×6×1 $\vec{k}$-point grid used in the calculations. Here, the high-symmetry $\vec{k}$-points U and M are not included in the $\vec{k}$-point grid since they would correspond to non-integer coordinates when using the nomenclature defined in the CRYSTAL17 calculations. Now, one should not get misled by the corresponding output in Fig. A.6 because the descriptor R is not necessarily connected to the high-symmetry $\vec{k}$-points but only to the center, corners, and edge centers of the reciprocal surface unit cell. Instead, a Γ-centered 16×16×1 $\vec{k}$-point grid as shown in Fig. A.5b) would be needed to consider all high-symmetry $\vec{k}$-points. Again, in CRYSTAL17 the $\vec{k}$-point grid can be adjusted after, e.g., a geometry optimization. For the sake of completeness, the corresponding inputs for the calculation of orbitals and the band structure using this $\vec{k}$-point grid for the Si-terminated 3C-SiC(001)-c(4×2) reconstruction are given in Fig. A.7. Further information regarding the input parameters are available in the CRYSTAL17 manual.[124]

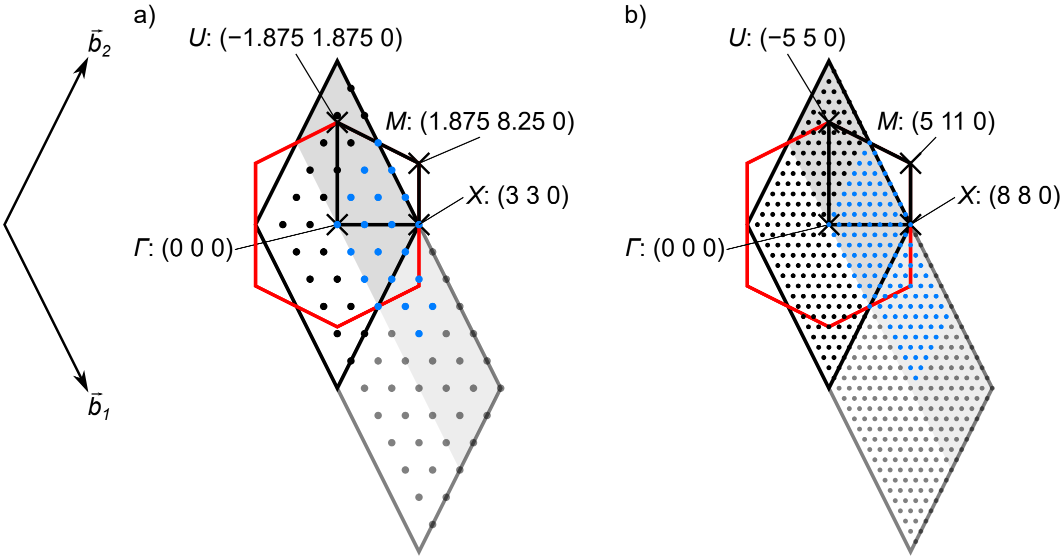

Figure A.5: Γ-centered a) 6×6×1 and b) 16×16×1 Monkhorst-Pack $\vec{k}$-point grids (black dots) for the Si-terminated 3C-SiC(001)-c(4×2) reconstructed surface (AUDD model). The reciprocal surface unit cell is depicted by black lines, the irreducible part of the reciprocal surface unit cell when imposing $P1$-symmetry is shaded in gray, the first SBZ is indicated by red lines, and the $\vec{k}$-path for band structure calculations is indicated by the black lines on top. Only $\vec{k}$-point grid a) was used for the c(4×2) calculations conducted in this work.

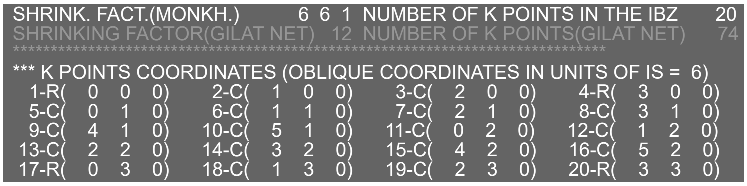

```
SHRINK. FACT.(MONKH.)          6  6  1  NUMBER OF K POINTS IN THE IBZ      20
SHRINKING FACTOR(GILAT NET)   12  NUMBER OF K POINTS(GILAT NET)            74
*******************************************************************************

*** K POINTS COORDINATES (OBLIQUE COORDINATES IN UNITS OF IS =  6)
  1-R(   0   0   0)     2-C(   1   0   0)     3-C(   2   0   0)     4-R(   3   0   0)
  5-C(   0   1   0)     6-C(   1   1   0)     7-C(   2   1   0)     8-C(   3   1   0)
  9-C(   4   1   0)    10-C(   5   1   0)    11-C(   0   2   0)    12-C(   1   2   0)
 13-C(   2   2   0)    14-C(   3   2   0)    15-C(   4   2   0)    16-C(   5   2   0)
 17-R(   0   3   0)    18-C(   1   3   0)    19-C(   2   3   0)    20-R(   3   3   0)
```

Figure A.6: Excerpt of the CRYSTAL17 output regarding the $\vec{k}$-point grid for the calculation of the Si-terminated 3C-SiC(001)-c(4×2) reconstructed surface (AUDD model) using the Γ-centered 6×6×1 Monkhorst-Pack $\vec{k}$-point grid depicted in Fig. A.5a).

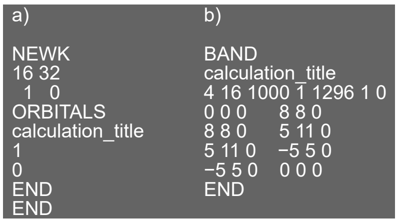

```
a)                    b)

NEWK                  BAND
16 32                 calculation_title
  1   0               4 16 1000 1 1296 1 0
ORBITALS              0 0 0     8 8 0
calculation_title     8 8 0     5 11 0
1                     5 11 0    −5 5 0
0                     −5 5 0    0 0 0
END                   END
END
```

Figure A.7: Exemplary CRYSTAL17 inputs for the calculation of a) orbitals and b) the band structure of the Si-terminated 3C-SiC(001)-c(4×2) reconstructed surface (AUDD model) using the Γ-centered 16×16×1 Monkhorst-Pack $\vec{k}$-point grid depicted in Fig. A.5b) to include all high-symmetry $\vec{k}$-points of the first SBZ.

A.1.3 Projected Bulk Band Structure of 3C-SiC(001)

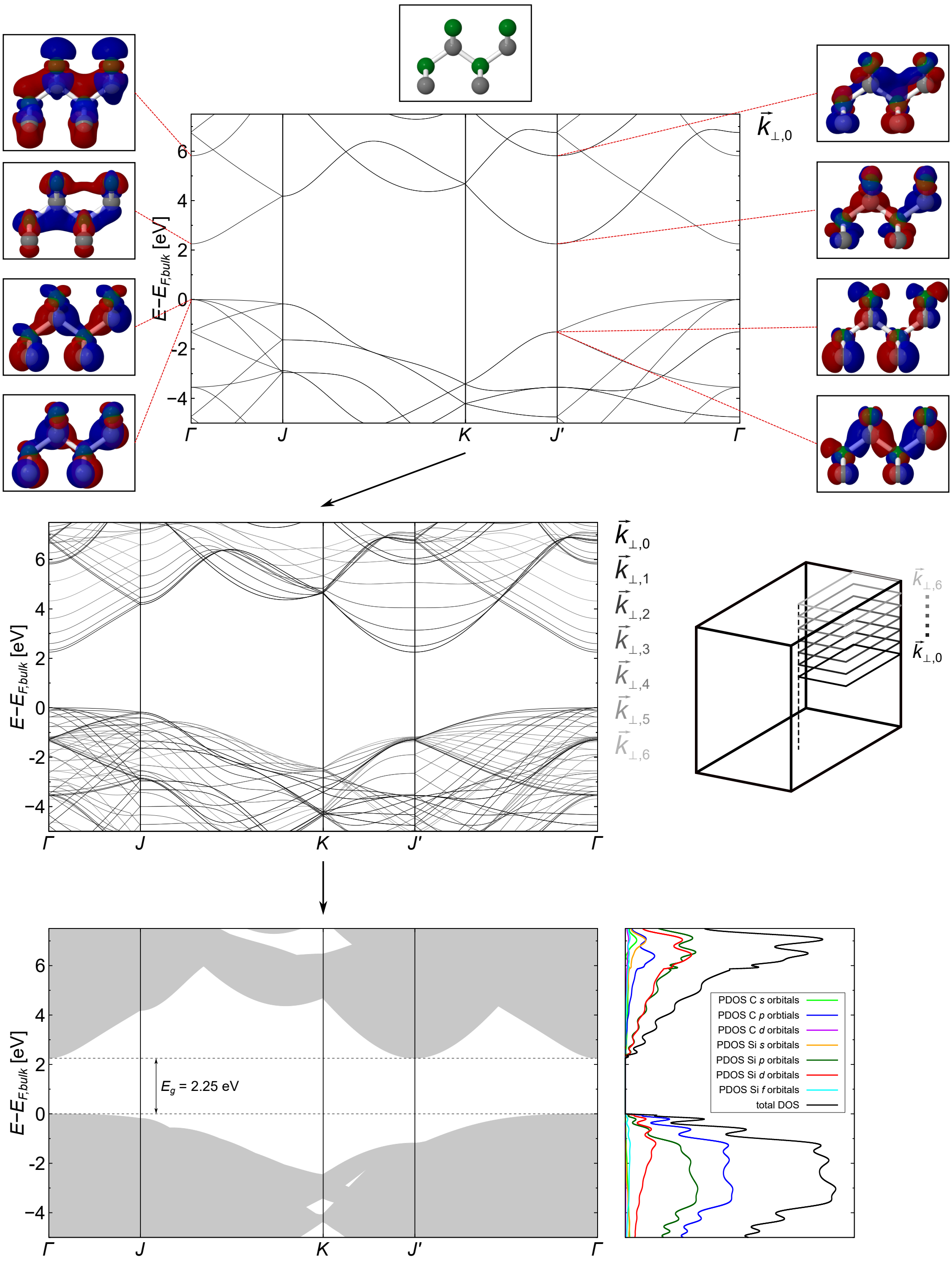

Figure A.8: Creation of the PBBS for a reciprocal unit cell (center right) corresponding to a bulk 3C-SiC unit cell fitting underneath the 2×1 supercell slab models of the (001) surface at RKS DFT HSE06 level with the TZVPP/TZVP basis set. For more information on the process, see Section 2.2.1.5. Additionally, the COs near the band gap at Γ and J' for a slice of the PBBS at $\vec{k}_{\perp,0}$ and the PDOS of the bulk band structure are given. The isosurface value for the orbitals amounts to $0.015\,{a_0}^{-3}$.

A.1.4 2×1 Supercell Band Structures with Crystalline Orbitals

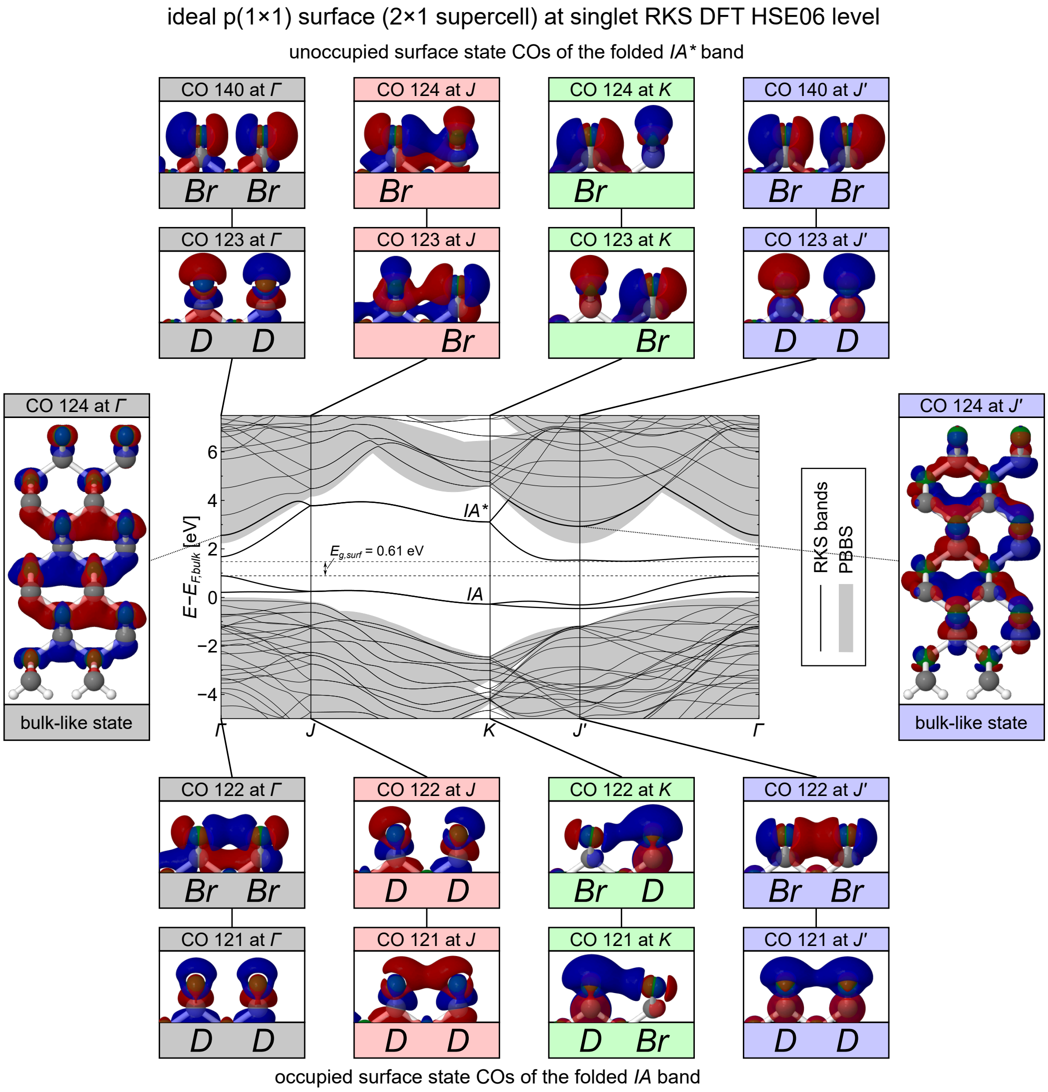

Figure A.9: COs of the surface states of the ideal Si-terminated 3C-SiC(001)-p(1×1) surface (2×1 supercell) at RKS DFT HSE06 level with the TZVPP/TZVP basis set for a 2×1 supercell 12-layer periodic slab model to show the swapping of the sp^2 dangling bond (D) and the bridging (Br) p_x orbitals of the folded IA and IA^* bands around the HOCO-LUCO gap with respect to the high-symmetry $\vec{k}$-points. Additionally, two exemplary bulk-like states of the slab model located in the PBBS are also shown. CO 122 is the HOCO and CO 123 is the LUCO. The isosurface value for the orbitals amounts to $0.01\,{a_0}^{-3}$. Reprinted with permission from *J. Phys. Chem. C* 2023, 127, 48, 23475–23488. Copyright 2023 American Chemical Society. Slightly modified and extended by bulk-like state COs.

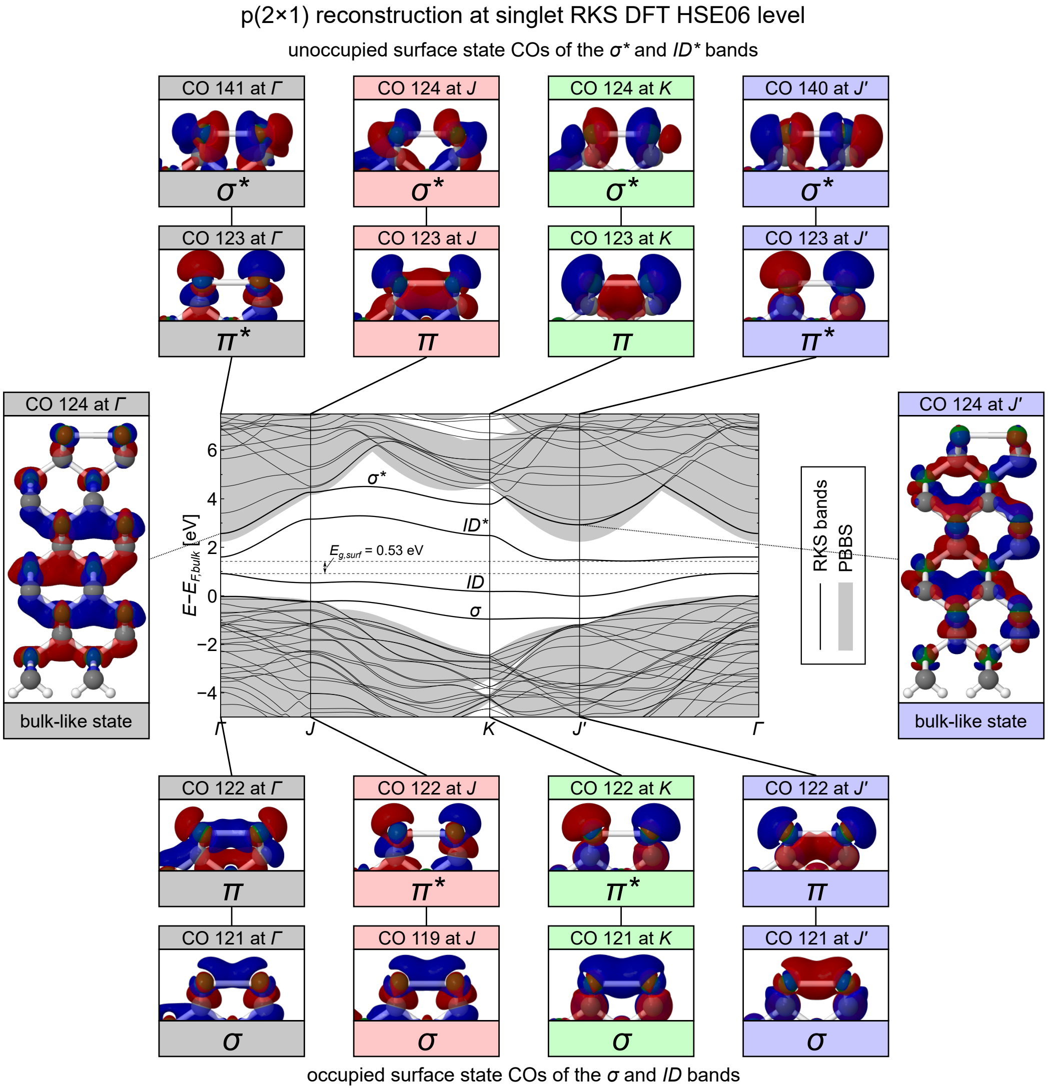

Figure A.10: COs of the surface states of the Si-terminated 3C-SiC(001)-p(2×1) reconstructed surface (SD model) at singlet RKS DFT HSE06 level with the TZVPP/TZVP basis set for a 2×1 supercell 12-layer periodic slab model to show the swapping of the π and π^* orbitals of the ID and ID^* bands around the HOCO-LUCO gap with respect to the high-symmetry $\vec{k}$-points. Additionally, the σ and σ^* COs and two exemplary bulk-like states of the slab model located in the PBBS are also shown. CO 122 is the HOCO and CO 123 is the LUCO. The isosurface value for the calculated orbitals amounts to $0.01\,{a_0}^{-3}$. Reprinted with permission from *J. Phys. Chem. C* 2023, 127, 48, 23475–23488. Copyright 2023 American Chemical Society. Slightly modified and extended by σ, σ^*, and bulk-like state COs.

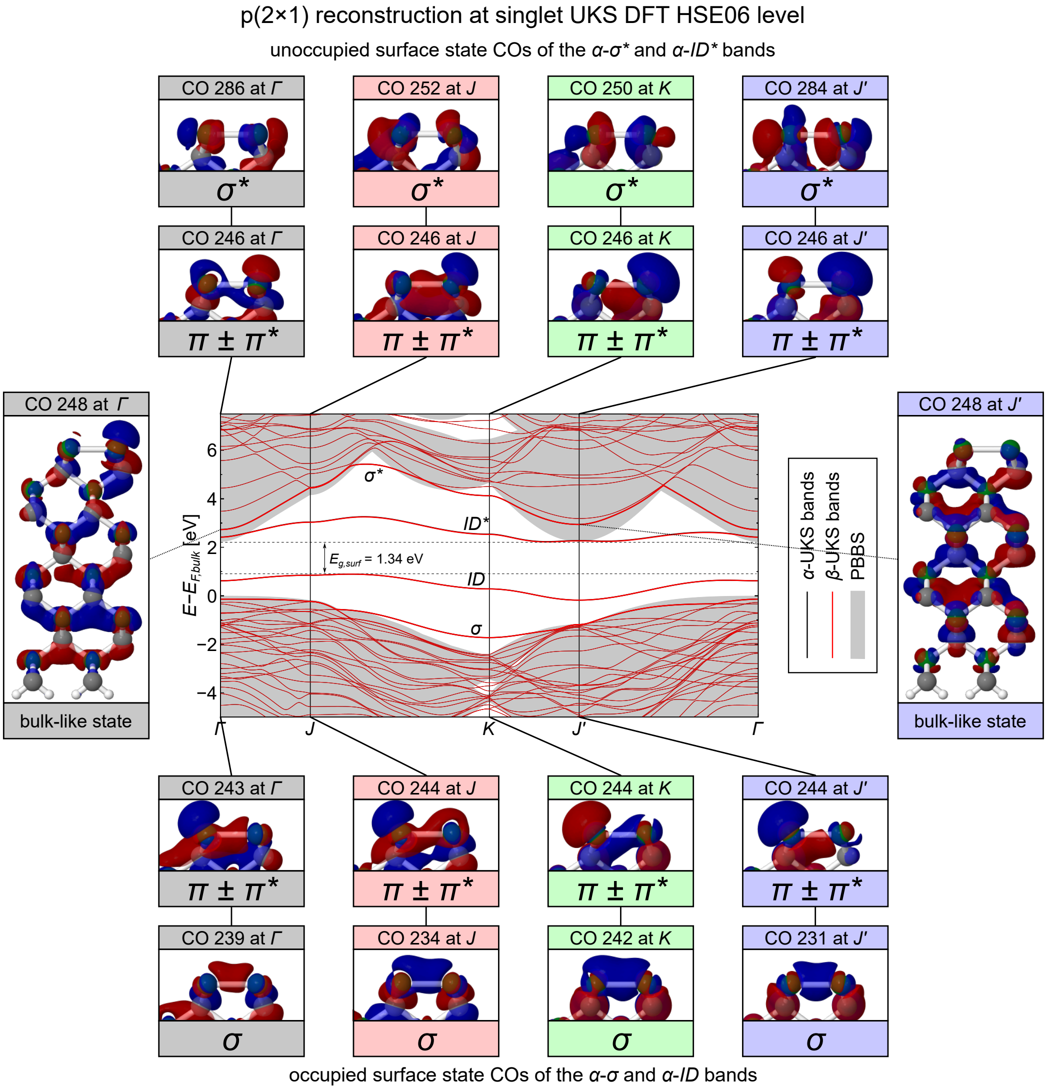

Figure A.11: COs of the surface states with respect to the high-symmetry $\vec{k}$-points of the Si-terminated 3C-SiC(001)-p(2×1) reconstructed surface (SD model) at singlet UKS DFT HSE06 level with the TZVPP/TZVP basis set for a 2×1 supercell 12-layer periodic slab model. The label $\pi \pm \pi^*$ indicates that the respective ID and ID^* band COs are supposedly broken-symmetry linear combinations of the pure π and π^* orbitals. Additionally, two exemplary bulk-like states of the slab model located in the PBBS are also shown. COs 243/244 are the α/β-HOCOs and COs 245/246 are the α/β-LUCOs. Only the COs of the α bands are shown. The isosurface value for the calculated orbitals amounts to $0.01\,{a_0}^{-3}$. Only the β-UKS bands are visible as they coincide with their degenerate α counterparts.

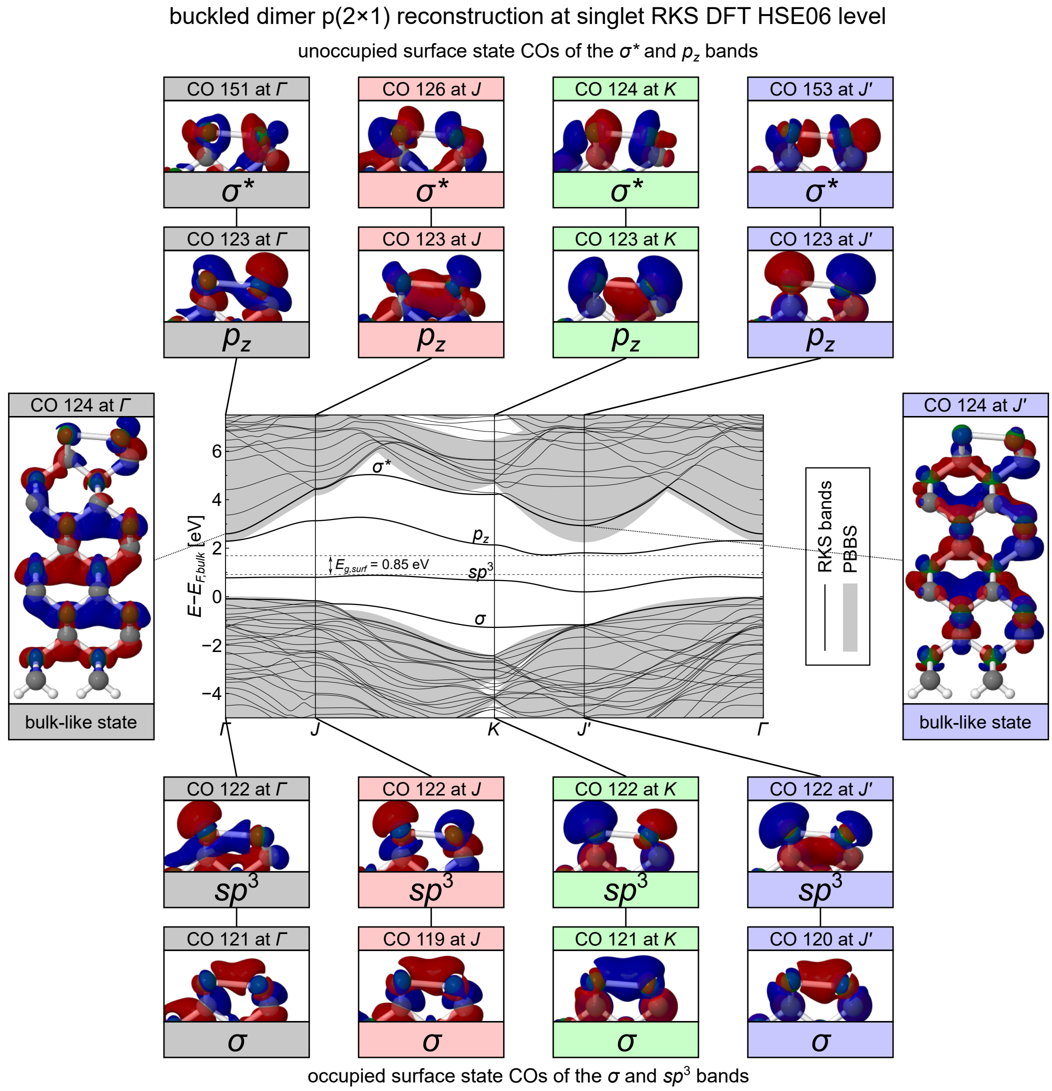

Figure A.12: COs of the surface states with respect to the high-symmetry $\vec{k}$-points of the buckled dimer Si-terminated 3C-SiC(001)-p(2×1) reconstructed surface at RKS DFT HSE06 level with the TZVPP/TZVP basis set for a 2×1 supercell 12-layer periodic slab model. Additionally, two exemplary bulk-like states of the slab model located in the PBBS are also shown. CO 122 is the HOCO and CO 123 is the LUCO. The isosurface value for the calculated orbitals amounts to $0.01\,a_0{}^{-3}$.

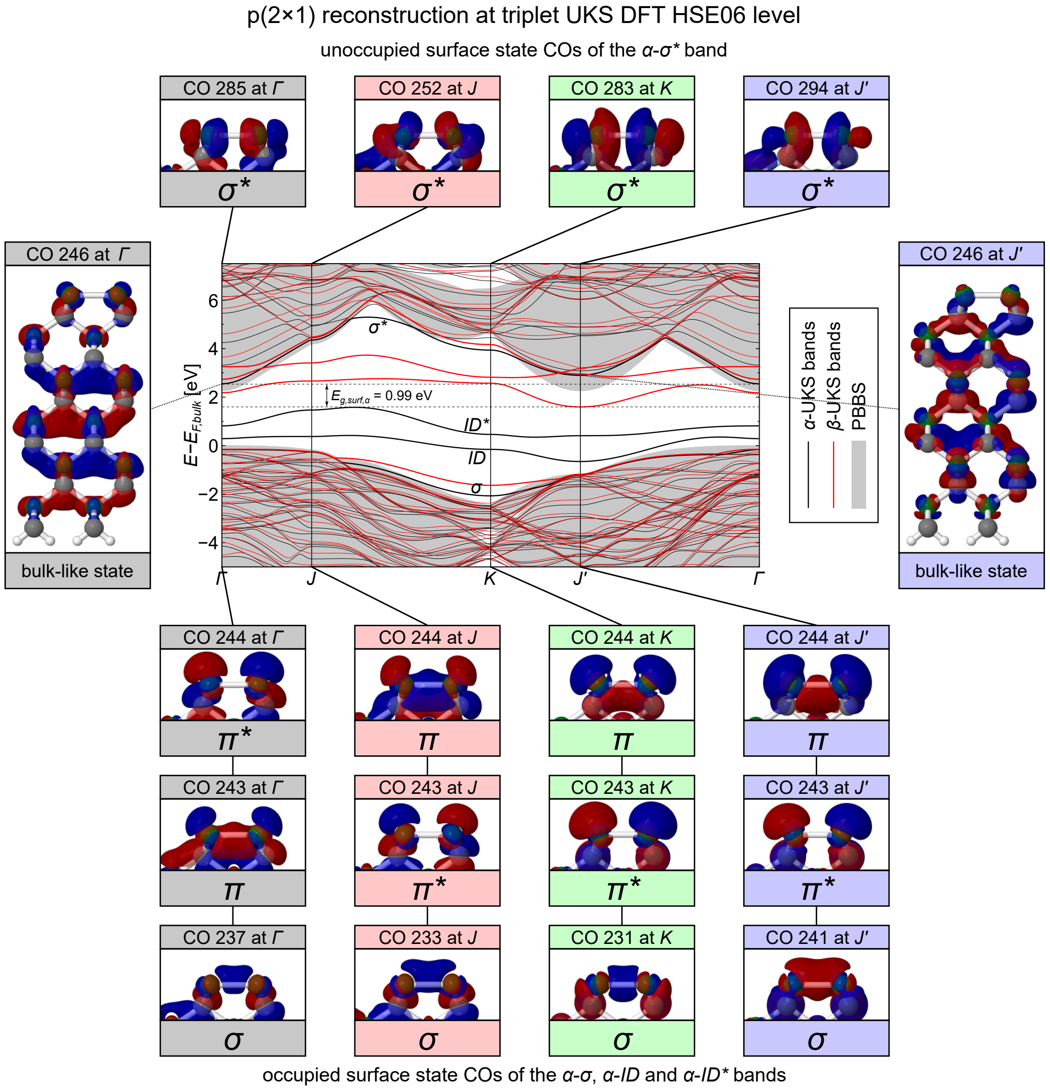

Figure A.13: COs of the surface states with respect to the high-symmetry $\vec{k}$-points of the Si-terminated 3C-SiC(001)-p(2×1) reconstructed surface (SD model) at triplet UKS DFT HSE06 level with the TZVPP/TZVP basis set for a 2×1 supercell 12-layer periodic slab model. Additionally, two exemplary bulk-like states of the slab model located in the PBBS are also shown. COs 244/242 are the α/β-HOCOs and COs 246/245 are the α/β-LUCOs. Only the COs of the α bands are shown. The isosurface value for the calculated orbitals amounts to $0.01\,{a_0}^{-3}$.

A.1.5 Additional Supercell Calculation Data

Table A.2: Mulliken atomic spin densities for the H-saturated rhombic $(\sqrt{5}\times\sqrt{5})R(2\cdot\tan^{-1}(0.5))$ supercell 12-layer periodic slab model of the Si-terminated 3C-SiC(001)-p(2×1) reconstructed surface (SD model) optimized at singlet UKS DFT HSE06 level with the TZVPP/TZVP basis set for the different possible spin arrangements. The assignment of the spins to the atoms is done according to the numbering in Fig. 3.17a).

Start Spins at Si Dimer Atoms 1 to 4 in Fig. 3.17a)	Spin Density at Si Dimer Atoms			
	Si1	Si2	Si3	Si4
1:[a] ↑↓ ↑↓	+0.64	−0.64	+0.64	−0.64
2: ↑↓ ↓↑	+0.69	−0.69	−0.69	+0.69
3: ↑↑ ↓↓	+0.72	+0.72	−0.72	−0.72

[a] equal to singlet UKS HSE06 of Table 3.3

Table A.3: Mulliken atomic spin densities and dimer bond lengths d_{Si-Si} for the H-saturated 4×2 supercell 10-layer periodic slab model of the Si-terminated 3C-SiC(001) reconstructed surface optimized at singlet UKS DFT HSE06 level with the TZVPP/TZVP basis set for the different possible spin arrangements. The assignment of the spins to the atoms is done according to the numbering in Fig. 3.17b).

Start Spins at Si Dimer Atoms 1 to 8 in Fig. 3.17b)	Spin Density at Si Dimer Atoms							
	Si1	Si2	Si3	Si4	Si5	Si6	Si7	Si8
1:[a] ↑↓ ↑↓ ↑↓ ↑↓	+0.64	−0.64	+0.64	−0.64	+0.64	−0.64	+0.64	−0.64
2: ↑↓ ↑↓ ↓↑ ↑↓	+0.63	−0.63	+0.63	−0.63	−0.63	+0.63	−0.63	+0.63
3: ↑↓ ↓↑ ↑↓ ↑↓	+0.71	−0.70	−0.69	+0.70	+0.63	−0.62	+0.60	−0.60
4: ↑↓ ↓↑ ↑↓ ↓↑	+0.70	−0.70	−0.70	+0.70	+0.70	−0.70	−0.70	+0.70
5:[b] ↑↓ ↓↑ ↓↑ ↑↓	+0.69	−0.69	−0.69	+0.69	−0.69	+0.69	+0.69	−0.69
6: ↑↓ ↓↑ ↑↑ ↓↓	+0.71	−0.69	−0.71	+0.69	+0.72	+0.70	−0.72	−0.70
7: ↑↓ ↓↓ ↑↓ ↑↑	+0.60	−0.71	−0.76	−0.69	+0.71	−0.60	+0.69	+0.76
8:[c] ↑↓ ↓↓ ↑↑ ↑↓	−0.13[c]	−0.66	−0.66	−0.13	+0.13	+0.66	+0.66	+0.13[c]
9: ↑↓ ↓↓ ↑↑ ↓↑	+0.61	−0.70	−0.77	−0.70	+0.78	+0.70	−0.61	+0.70
10:[c] ↑↑ ↑↓ ↓↓ ↓↑	+0.13	+0.66	+0.66	+0.13[c]	−0.13	−0.66	−0.66	−0.13[c]
11: ↑↑ ↑↑ ↓↓ ↓↓	+0.78	+0.78	+0.78	+0.78	−0.78	−0.78	−0.78	−0.78
12: ↑↑ ↓↓ ↑↓ ↑↓	+0.73	+0.72	−0.72	−0.73	+0.64	−0.63	+0.63	−0.64
13: ↑↑ ↓↓ ↑↑ ↓↓	+0.73	+0.73	−0.73	−0.73	+0.73	+0.73	−0.73	−0.73
14:[d] ↑↑ ↓↓ ↓↓ ↑↑	+0.72	+0.72	−0.72	−0.72	−0.72	−0.72	+0.72	+0.72

Start Spins at Si Dimer Atoms 1 to 8 in Fig. 3.17b)	Dimer Bond Lengths [Å]			
	$d_{Si1-Si2}$	$d_{Si3-Si4}$	$d_{Si5-Si6}$	$d_{Si7-Si8}$
1:[a] ↑↓ ↑↓ ↑↓ ↑↓	2.46	2.46	2.46	2.46
2: ↑↓ ↑↓ ↓↑ ↑↓	2.46	2.46	2.46	2.46
3: ↑↓ ↓↑ ↑↓ ↑↓	2.39	2.38	2.47	2.48
4: ↑↓ ↓↑ ↑↓ ↓↑	2.40	2.40	2.40	2.40
5:[b] ↑↓ ↓↑ ↓↑ ↑↓	2.40	2.40	2.40	2.40
6: ↑↓ ↓↑ ↑↑ ↓↓	2.39	2.39	2.45	2.45
7: ↑↓ ↓↓ ↑↓ ↑↑	2.44	2.43	2.44	2.43
8:[c] ↑↓ ↓↓ ↑↑ ↑↓	2.62	2.62	2.62	2.62
9: ↑↓ ↓↓ ↑↑ ↓↑	2.44	2.43	2.43	2.44
10:[c] ↑↑ ↑↓ ↓↓ ↓↑	2.62	2.62	2.62	2.62
11: ↑↑ ↑↑ ↓↓ ↓↓	2.39	2.39	2.39	2.39
12: ↑↑ ↓↓ ↑↓ ↑↓	2.45	2.45	2.46	2.46
13: ↑↑ ↓↓ ↑↑ ↓↓	2.45	2.45	2.45	2.45
14:[d] ↑↑ ↓↓ ↓↓ ↑↑	2.45	2.45	2.45	2.45

[a] equal to singlet UKS HSE06 of Table 3.3 and spin arrangement 1 of Tables 3.6 and A.2

[b] equal to spin arrangement 2 of Tables 3.6 and A.2

[c] change of sign in atomic spin densities during geometry optimization to p(4×1) reconstruction

[d] equal to spin arrangement 3 of Tables 3.6 and A.2

Table A.4: Mulliken atomic spin densities and bond lengths d for the H-saturated 4×2 supercell 10-layer periodic slab model of the Si-terminated 3C-SiC(001)-p(4×1) reconstructed surface optimized at singlet UKS DFT HSE06 level with the TZVPP/TZVP basis set for the different possible spin arrangements. The assignment of the spins to the atoms is done according to the numbering in Fig. 3.17b). The bond lengths d_{Si-Si} and d_{ID} are depicted in Fig. 3.18a).

Start Spins at Si Dimer Atoms 1 to 8 in Fig. 3.17b)	Spin Density at Si Dimer Atoms								Bond Lengths [Å]	
	Si1	Si2	Si3	Si4	Si5	Si6	Si7	Si8	d_{Si-Si}	d_{ID}
1: ↑0 0↓ ↑0 0↓	+0.68	+0.14	−0.14	−0.68	+0.68	+0.14	−0.14	−0.68	2.61	2.88
2:[a] ↑0 0↑ ↓0 0↓	+0.66	+0.13	+0.13	+0.66	−0.66	−0.13	−0.13	−0.66	2.62	2.85
3: ↑0 0↓ ↓0 0↑	+0.67	+0.15	−0.15	−0.67	−0.67	−0.15	+0.15	−0.67	2.62	2.88

[a] equal to converged spin arrangements 8 and 10 of Tables 3.7 and A.3

Table A.5: Mulliken atomic spin densities, bond lengths d, and spin contamination $\Delta \langle \hat{S}^2 \rangle$ per dimer for the p(4×1) and p(4×2) reconstructed Si-terminated 3C-SiC(001) surfaces for different DFT functionals at singlet RKS and UKS level with the TZVPP/TZVP basis set. The UKS calculations used spin arrangement 1 of Tables 3.8 and A.4. The bond lengths d_{Si-Si} and d_{ID} are depicted in Fig. 3.18a) and bond lengths $d_{Si-Si,1}$, d_{ID}, and $d_{Si-Si,2}$ in Fig. 3.18b).

Reconstruction	Method		Spin Density at Si Dimer Atoms				Bond Lengths [Å]			$\Delta \langle \hat{S}^2 \rangle$ per Dimer
			Si1/Si5	Si2/Si6	Si3/Si7	Si4/Si8	$d_{Si-Si(,1)}$	d_{ID}	$d_{Si-Si,2}$	
p(4×1)	RKS	HSE06	-	-	-	-	2.68	2.81	-	0.00
		PBE	-	-	-	-	2.68	2.87	-	0.00
		LDA	-	-	-	-	2.67	2.88	-	0.00
	UKS	HSE06	+0.68	+0.14	−0.14	−0.68	2.61	2.88	-	0.49
		PBE	+0.63	+0.12	−0.12	−0.63	2.63	2.95	-	0.47
		LDA	+0.53	+0.09	−0.09	−0.53	2.64	2.94	-	0.36
p(4×2)	RKS	HSE06	-	-	-	-	2.79	2.88	2.55	0.00
		PBE	-	-	-	-	2.79	2.92	2.57	0.00
		LDA	-	-	-	-	2.76	2.90	2.56	0.00
	UKS	HSE06	collapse to p(4×2) RKS solution							
		PBE								
		LDA								

A.2 Multiconfigurational Cluster Model Calculations

A.2.1 Justification of the Cluster Model Approach

Table A.6 gives the reconstruction energies of single-configurational $M \times N$-dimer 4-layer cluster models of the Si-terminated 3C-SiC(001)-p(2×1) reconstructed surface. The cluster models were created according to the workflow depicted in Fig. 3.26 but using the RKS DFT HSE06 structure from the periodic slab model calculations with a dimer bond length of 2.80 Å for the p(2×1) clusters. Furthermore, no additional optimization of the atomic layers or the saturating H atoms was carried out. It is apparent that the reconstruction energies of both structural models are in the same order of magnitude of about −0.01 eV and thus justify the usage of the cluster model approach. Unfortunately, UKS cluster model calculations proved to be difficult since the spin

Table A.6: Single-configurational reconstruction energies ΔE_{dimer} for H-saturated $M \times N$-dimer 4-layer cluster models of the Si-terminated 3C-SiC(001)-p(2×1) reconstructed surface (SD model) at RKS DFT HSE06 level using the TZVPP/TZVP basis set. The cluster models were created according to Fig. 3.26 but using the RKS DFT HSE06 periodic slab model structure for the p(2×1) clusters ($d_{Si-Si} = 2.80\,\text{Å}$). No further optimization of the atomic layers and saturating H atoms was conducted. The reconstruction energies are calculated according to the same formalism used for the multiconfigurational cluster model calculations (Eqs. 3.7 to 3.9 in Section 3.3.2.3).

Number of Dimers in y (N)	Number of Dimers in x (M)			
	2	3	4	5
	ΔE_{dimer} [eV]			
1	+0.005	−0.004	−0.008	−0.010
2		−0.011		
3		−0.012		
PBCs	−0.015			

arrangements for the surface atoms could not be controlled as reliable as in the periodic slab model calculations, possibly due to the missing translational symmetry. Accordingly, no comparison to the presumably more sophisticated UKS results with PBCs is possible.

As Table A.7 shows, the agreement between the cluster and periodic slab models decreases when the optimization of the first two atomic layers is also included like in the multiconfigurational cluster model calculations. This is expected as the geometry constraints for the cluster models are not able to exactly mirror the PBCs. Furthermore, the convergence of the dimer bond lengths appears to be worse and requires larger cluster models than for the multiconfigurational calculations (compare Table 3.19). At least in the restricted case, this could further indicate the insufficiency of the single-configurational approaches to describe this surface and supports the usage of multiconfigurational methods especially for cluster model calculations.

Table A.7: Single-configurational reconstruction energies ΔE_{dimer} and dimer bond lengths d_{Si-Si} for H-saturated $M \times N$-dimer 4-layer cluster models of the Si-terminated 3C-SiC(001)-p(2×1) reconstructed surface (SD model) at RKS DFT HSE06 level using the TZVPP/TZVP basis set. The cluster models were created according to Fig. 3.26 but using the RKS DFT HSE06 periodic slab model structure for the p(2×1) clusters ($d_{Si-Si} = 2.80\,\text{Å}$). The first two atomic layers are relaxed according to Table 3.17. The reconstruction energies are calculated according to the same formalism used for the multiconfigurational cluster model calculations (Eqs. 3.7 to 3.9 in Section 3.3.2.3).

Number of Dimers in y (N)	Number of Dimers in x (M)							
	2	3	4	5	2	3	4	5
	ΔE_{dimer} [eV]				d_{Si-Si} [Å]			
1	+0.066	+0.024	+0.005	−0.004	2.54	2.85	2.89	2.94
2		+0.001				2.81		
3		−0.007				2.79		
PBCs	−0.015				2.80			

A.2.2 Relaxed Layer Convergence

In Table A.8, the dimer bond lengths d_{Si-Si} and reconstruction energies ΔE_{dimer} for 3×1-dimer 4-, 6-, and 8-layer cluster models optimized at CASSCF and NEVPT2 level with the CAS_{full}, the TZVPP/TZVP basis set, and differing numbers of relaxed atomic layers according to Table 3.17 are given. Even though d_{Si-Si} does not converge when increasing the number of relaxed layers as is normally the case when doing so in periodic slab calculations, the changes are of small magnitude in the range of a few 0.001 Å. Interestingly, for the CASSCF calculations of the 6- and 8-layer cluster models, the dimer bond length seems to decrease at first to a minimum value at three relaxed layers and then increases again when going to six relaxed layers, almost cycling back to the 1-layer relaxation value. ΔE_{dimer} also does not converge the more atomic layers are relaxed and instead continuously becomes more negative, especially for the 6-layer cluster model. It can be argued that this comes to no surprise because the cluster models built from the UKS DFT HSE06 structure are allowed to further relax towards the multiconfigurational minimum with each additional layer included in the optimization, which obviously results in lower total energies with respect to the corresponding unoptimized p(1×1) cluster model and thus more negative ΔE_{dimer} values. Accordingly, it could be argued that a geometry optimization without constraints might be the best way to calculate the reconstruction energy but, as already mentioned in Section 3.3.2.2, this can lead to unphysical cluster model geometries not representing the surface of interest anymore.

Another possible approach to resolve the convergence problem was to adjust the 1×N-dimer cluster models, which are used to correct the reconstruction energies of the $M \times N$-dimer clusters by the spurious reconstruction energies of the capping H-saturated half-dimers in each of the N dimer rows as described in detail in Section 3.3.2.3. As further mentioned, only the 1×1- and 1×2-

Table A.8: Dimer bond lengths d_{Si-Si} and reconstruction energies ΔE_{dimer} for H-saturated 3×1-dimer 4-, 6-, and 8-layer cluster models ($Si_{16}C_{17}H_{38}$, $Si_{28}C_{35}H_{58}$, and $Si_{34}C_{38}H_{58}$) of the Si-terminated 3C-SiC(001)-p(2×1) reconstructed surface (SD model) optimized at CASSCF and NEVPT2 level with the full active space CAS_{full}, the TZVPP/TZVP basis set, and differing numbers of relaxed atomic layers according to Table 3.17. The dimer bond lengths are taken from the most inner dimer. Reprinted with permission from *J. Phys. Chem. C* 2023, 127, 48, 23475–23488. Copyright 2023 American Chemical Society.

Method	Number of Relaxed Atomic Layers in z	Cluster Model					
		3×1-dimer 4-layer		3×1-dimer 6-layer		3×1-dimer 8-layer	
		d_{Si-Si} [Å]	ΔE_{dimer} [eV]	d_{Si-Si} [Å]	ΔE_{dimer} [eV]	d_{Si-Si} [Å]	ΔE_{dimer} [eV]
CASSCF	1	2.550	−0.174	2.557	−0.125	2.557	−0.113
	2	2.547	−0.179	2.553	−0.132	2.553	−0.120
	3	2.548	−0.179	2.551	−0.144	2.551	−0.133
	4	2.548	−0.181	2.552	−0.152	2.553	−0.143
	5			2.556	−0.181	2.557	−0.162
	6			2.558	−0.253	2.556	−0.163
NEVPT2	1	2.554	−0.100				
	2	2.560	−0.110				
	3	2.567	−0.115				
	4	2.562	−0.119				

dimer 4-layer cluster models depicted in Figs. A.15 and A.16 were used for this purpose even though some of the $M \times N$-dimer cluster models contained more than four layers. This is also the case in Table A.8, for which the 1×1-dimer 4-layer cluster model was used and only its number of relaxed atomic layers was adjusted to match the geometry constraints of the corresponding 3×1-dimer cluster models. But because the 1×1-dimer cluster only contains four layers, no 5- and 6-layer optimization could be conducted for that system. Accordingly, for the 5- and 6-layer optimizations of the 3×1-dimer clusters, only the 1×1-dimer correction value $\Delta E_{1\times1}$ for four optimized layers could be used. This discrepancy was assumed to be the cause of the poor convergence of reconstruction energies as there actually is a significant jump in the corresponding values in Table A.8 when going from four to five relaxed layers. Accordingly, additional 1×1-dimer cluster models with six atomic layers as depicted in the second column of Table A.9 were created to also be able to optimize up to six layers within these. But as apparent from the ΔE_{dimer} values in the same table, no substantial improvement with respect to the convergence was achieved. On the contrary, the absolute reconstruction strength decreases to values as low as $-0.015\,\text{eV}$ for the larger 1×1-dimer cluster models. This can presumably be attributed to them containing more atomic layers, which results in more negative total energies when relaxing many of these layers and thus more negative values for the correcting reconstruction energy $\Delta E_{1\times1}$. If these get subtracted from the unchanged total reconstruction energies $\Delta E_{3\times1}$ of the 3×1-dimer cluster models, the values for ΔE_{dimer} become more positive. However, the intended purpose of the correcting energy $\Delta E_{1\times1}$ is to only account for the spurious formation of the σ bond between the capping H-saturated half-dimer and the unsaturated half-dimers that actually represent the surface states. But by adding more layers to relax, the relaxation energy of the atomic layers further below is also included in $\Delta E_{1\times1}$. This effect was intended to be accounted for by constructing the cluster models from the already relaxed UKS DFT HSE06 periodic slab models of the p(2×1) surface, so actually no further relaxation of the lower atomic layers should be necessary in the cluster model approach. Accordingly, using 1×1-dimer cluster models with many relaxed atomic layers can be interpreted as an overcorrection of the reconstruction energy of the 3×1-dimer cluster models and thus the 1×1-dimer 4-layer clusters should be sufficient.

In conclusion, when calculating cluster model reconstruction energies in this work, it is aimed for a compromise between accounting for the multiconfigurational reconstruction energy only by relaxing the topmost two atomic layers in all p(2×1) cluster models and at the same time considering the relaxation of atomic layers further below the surface by keeping the single-configurational structure of the periodic slab models. Obviously, this approach is by no means optimal but supposedly the only way of approximately determining multiconfigurational cluster model reconstruction energies for the statically correlated 3C-SiC(001)-p(2×1) reconstructed surface.

Table A.9: Reconstruction energies ΔE_{dimer} for H-saturated 3×1-dimer 4-, 6-, and 8-layer cluster models ($Si_{16}C_{17}H_{38}$, $Si_{28}C_{35}H_{58}$, and $Si_{34}C_{38}H_{58}$) of the Si-terminated 3C-SiC(001)-p(2×1) reconstructed surface (SD model) optimized at CASSCF level for the full active space CAS_{full}, the TZVPP/TZVP basis set, differing numbers of relaxed atomic layers according to Table 3.17, and differing 1×1-dimer cluster models for the correction of the reconstruction energies according to Eqs. 3.7 to 3.9. Additionally, the two contributions $\Delta E_{1\times1}$ and $\Delta E_{3\times1}$ for the calculation of the reconstruction energy for all cluster models are given as grayed out values. Reprinted with permission from *J. Phys. Chem. C* 2023, 127, 48, 23475–23488. Copyright 2023 American Chemical Society.

Number of Relaxed Atomic Layers in z	1×1-dimer Cluster for Correcting ΔE_{dimer}		Cluster Model					
			3×1-dimer 4-layer 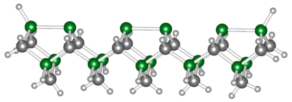		3×1-dimer 6-layer 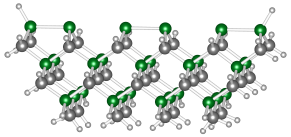		3×1-dimer 8-layer 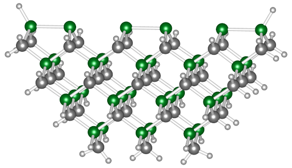	
	Figure	$\Delta E_{1\times1}$ [eV]	$\Delta E_{3\times1}$ [eV]	ΔE_{dimer} [eV]	$\Delta E_{3\times1}$ [eV]	ΔE_{dimer} [eV]	$\Delta E_{3\times1}$ [eV]	ΔE_{dimer} [eV]
1	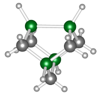	−0.945	−1.293	−0.174	−1.194	−0.125	−1.170	−0.113
2		−0.948	−1.306	−0.179	−1.212	−0.132	−1.188	−0.120
3		−0.963	−1.321	−0.179	−1.251	−0.144	−1.229	−0.133
4		−0.964	−1.327	−0.181	−1.268	−0.152	−1.251	−0.143
5					−1.325	−0.181	−1.288	−0.162
6					−1.470	−0.253	−1.291	−0.163
1	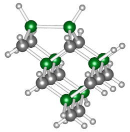	−1.014	−1.293	−0.140	−1.194	−0.090	−1.170	−0.078
2		−1.019	−1.306	−0.143	−1.212	−0.096	−1.188	−0.084
3		−1.021	−1.321	−0.150	−1.251	−0.115	−1.229	−0.104
4		−1.029	−1.327	−0.149	−1.268	−0.120	−1.251	−0.111
5		−1.055			−1.325	−0.135	−1.288	−0.117
6		−1.057			−1.470	−0.207	−1.291	−0.117
1	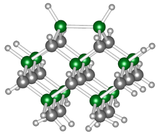	−1.117	−1.293	−0.088	−1.194	−0.039	−1.170	−0.027
2		−1.119	−1.306	−0.094	−1.212	−0.047	−1.188	−0.034
3		−1.131	−1.321	−0.095	−1.251	−0.060	−1.229	−0.049
4		−1.147	−1.327	−0.090	−1.268	−0.060	−1.251	−0.052
5		−1.173			−1.325	−0.076	−1.288	−0.058
6		−1.260			−1.470	−0.105	−1.291	−0.015

A.2.3 Basis Set Convergence

As mentioned in Section 3.3.2.4, the calculation of excited states often requires diffuse basis functions to describe the electron density located further away from the system compared to the ground state. Accordingly, different basis set combinations were created using def2 basis sets of different quality[148], namely def2-SVP/def2-SVPD to def2-QZVPD, for comparison with the TZVPP/TZVP basis set generally used otherwise. For this, the investigated 3×1- and 4×1-dimer 4-layer cluster models were divided into four different regions according to Fig. A.14. Here, the Si dimer atoms and the outer saturating H atoms represent region 1, which most likely needs the highest basis set quality since it contains the major part of the surface states as apparent from Fig. 3.27. Region 2 corresponds to the underlying C layer and region 3 to the third and fourth layer. All remaining H atoms are included in region 4, which arguably requires the lowest basis set quality as it only serves for saturating purposes. According to this hierarchy, the basis set combinations 1 – 6 listed in Table A.10 are constructed with combination 6 exhibiting the highest quality. Before tackling the excited state calculations, the influence

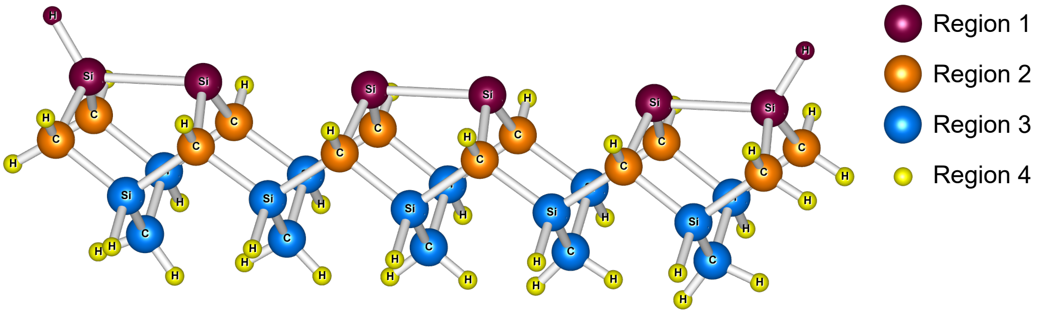

Figure A.14: Basis set regions for the convergence studies regarding the basis set size using the example of the H-saturated 3×1-dimer 4-layer cluster model ($Si_{16}C_{17}H_{38}$) of the Si-terminated 3C-SiC(001)-p(2×1) reconstructed surface (SD model). Reprinted with permission from *J. Phys. Chem. C* 2023, 127, 48, 23475–23488. Copyright 2023 American Chemical Society.

Table A.10: Basis set combinations for the convergence studies regarding the basis set size for the H-saturated M×1-dimer 4-layer cluster models of the Si-terminated 3C-SiC(001)-p(2×1) reconstructed surface (SD model). The regions 1 to 4 are depicted in Fig. A.14. Reprinted with permission from *J. Phys. Chem. C* 2023, 127, 48, 23475–23488. Copyright 2023 American Chemical Society.

Basis Set Combination	Employed Basis Set			
	Region 1	Region 2	Region 3	Region 4
1	def2-SVPD	def2-SVP	def2-SVP	def2-SVP
2	def2-TZVPD	def2-SVP	def2-SVP	def2-SVP
3	def2-TZVPD	def2-TZVP	def2-SVP	def2-SVP
4	def2-TZVPD	def2-TZVP	def2-TZVP	def2-SVP
5	def2-TZVPD	def2-TZVP	def2-TZVP	def2-TZVP
6	def2-QZVPD	def2-TZVP	def2-TZVP	def2-TZVP

of the basis set quality on the ground state geometry given in Table A.11 is discussed. As apparent, there is a significant jump for both the dimer bond length and the reconstruction energy when going from basis set combination 1, which consists only of def2-SVP basis set with additional diffuse functions for region 1, to basis set combination 2, which is identical to combination 1 but has a def2-TZVPD basis for region 1. All basis set combinations of higher quality generally only show small changes, confirming the importance of a high basis set quality for the dimer atoms. Basis set combination 3 seems to be an outlier in case of the CASSCF reconstruction energies, which could not be resolved. The TZVPP/TZVP basis set shows reasonable performance within this convergence series, generally ranking between basis set combinations 1 and 2 and showing deviations of about 0.01 Å – 0.02 Å for d_{Si-Si} and about 0.01 eV – 0.02 eV for ΔE_{dimer} compared to the basis set combination 6 for CASSCF and basis set combination 4 for NEVPT2. This justifies the general usage of the TZVPP/TZVP basis set for the rest of this work, especially for the sake of the improved comparability with the single-configurational calculations. However, it should be noted that the difference in dimer bond lengths between CASSCF and NEVPT2 are only 0.02 Å for the TZVPP/TZVP basis set, while it amounts to almost 0.05 Å for basis set combination 6. This discrepancy can be attributed to the rather low NEVPT2 value of the TZVPP/TZVP basis set, falling out of the convergence series of the other basis sets, which is also true for the corresponding reconstruction energy. This can be explained by correlation methods like NEVPT2 generally showing a greater dependence on the basis set quality,[58] resulting in the missing diffuse functions of the TZVPP/TZVP

Table A.11: Dimer bond lengths d_{Si-Si} and reconstruction energies ΔE_{dimer} for the H-saturated 3×1- and 4×1-dimer 4-layer cluster models ($Si_{16}C_{17}H_{38}$ and $Si_{22}C_{23}H_{50}$) of the Si-terminated 3C-SiC(001)-p(2×1) reconstructed surface (SD model) optimized at CASSCF and NEVPT2 level with the full active space CAS_{full}, the respective basis set combination, and the first two atomic layers relaxed according to Table 3.17. The detailed basis set combinations are listed in Table A.10. The dimer bond lengths are taken from the most inner dimer.

Method	Basis Set Combination	Cluster Model			
		3×1-dimer 4-layer		4×1-dimer 4-layer	
		d_{Si-Si} [Å]	ΔE_{dimer} [eV]	d_{Si-Si} [Å]	ΔE_{dimer} [eV]
CASSCF	1	2.551	−0.197	2.553	−0.196
	2	2.539	−0.182	2.541	−0.182
	3	2.537	−0.178	2.540	−0.177
	4	2.537	−0.189	2.538	−0.188
	5	2.536	−0.189	2.537	−0.188
	6	2.535	−0.190	2.536	−0.189
	TZVPP/TZVP	2.547	−0.179	2.550	−0.179
NEVPT2	1	2.609	−0.097		
	2	2.580	−0.088		
	3	2.583	−0.084		
	4	2.581	−0.096		
	TZVPP/TZVP	2.560	−0.110		

basis set to show a bigger impact for this method than for CASSCF.

The convergence study for the vertical CASSCF and NEVPT2 excitation energies E_{exc} for the 3×1-dimer 4-layer cluster models of the p(1×1) and p(2×1) surfaces is given in Table A.12. Basically, the convergence behavior is similar to that of the dimer bond length and reconstruction energy shown before, namely reaching reasonable convergence for basis set combination 2 and basis set combination 3 giving an outlier value for the p(2×1) surface. Without going into the details, the TZVPP/TZVP basis set again yields reasonable values with respect to this convergence series, showing deviations of only a few 0.01 eV compared to the basis set combination 6 for CASSCF and basis set combination 4 for NEVPT2. Accordingly, using this basis set for the excitation energies is also justified, especially when considering the significant uncertainty of this metric with respect to the number of dimers discussed at the end of Section 3.3.2.4.

Table A.12: Vertical state-optimized CASSCF and NEVPT2 excitation energies E_{exc} for the H-saturated 3×1-dimer 4-layer cluster model ($Si_{16}C_{17}H_{38}$) of the ideal p(1×1) and p(2×1) reconstructed (SD model) Si-terminated 3C-SiC(001) surface optimized at CASSCF and NEVPT2 level with the full active space CAS_{full}, the respective basis set, and the first two atomic layers relaxed according to Table 3.17. The detailed basis set combinations are listed in Table A.10. The excitation energy values correspond to the energy difference between the singlet ground state and the first excited singlet state. Reprinted with permission from *J. Phys. Chem. C* 2023, 127, 48, 23475–23488. Copyright 2023 American Chemical Society.

Basis Set Combination	Ideal p(1×1) Surface		p(2×1) Reconstruction	
	$E_{exc,CASSCF}$ [eV]	$E_{exc,NEVPT2}$ [eV]	$E_{exc,CASSCF}$ [eV]	$E_{exc,NEVPT2}$ [eV]
1	2.39	2.40	0.75	0.89
2	2.28	2.30	0.72	0.81
3	2.26	2.13	0.70	0.96
4	2.25	2.12	0.71	0.80
5	2.25		0.71	
6	2.25		0.70	
TZVPP/TZVP	2.22	2.10	0.69	0.87

A.2.4 Cluster Models

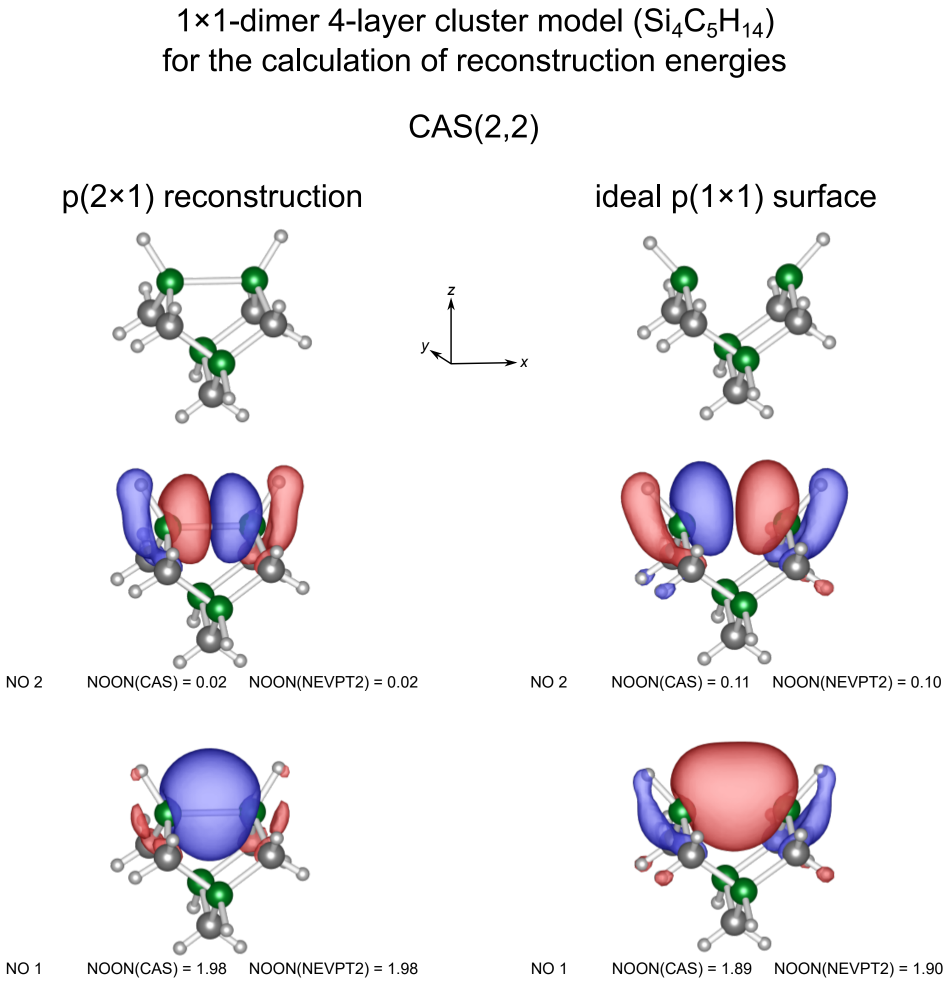

Figure A.15: 1×1-dimer 4-layer cluster model ($Si_4C_5H_{14}$) of the Si-terminated 3C-SiC(001)-p(2×1) reconstructed surface (SD model) and the ideal p(1×1) surface with the corresponding active space orbitals and NOONs at different levels of theory using the TZVPP/TZVP basis set and the first two atomic layers being relaxed according to Table 3.17. This cluster model was used to calculate the reconstruction energies for $M\times1$-dimer X-layer cluster models. The isosurface value of the orbitals amounts to $0.03\,a_0{}^{-3}$. Reprinted with permission from *J. Phys. Chem. C* 2023, 127, 48, 23475–23488. Copyright 2023 American Chemical Society. Slightly modified.

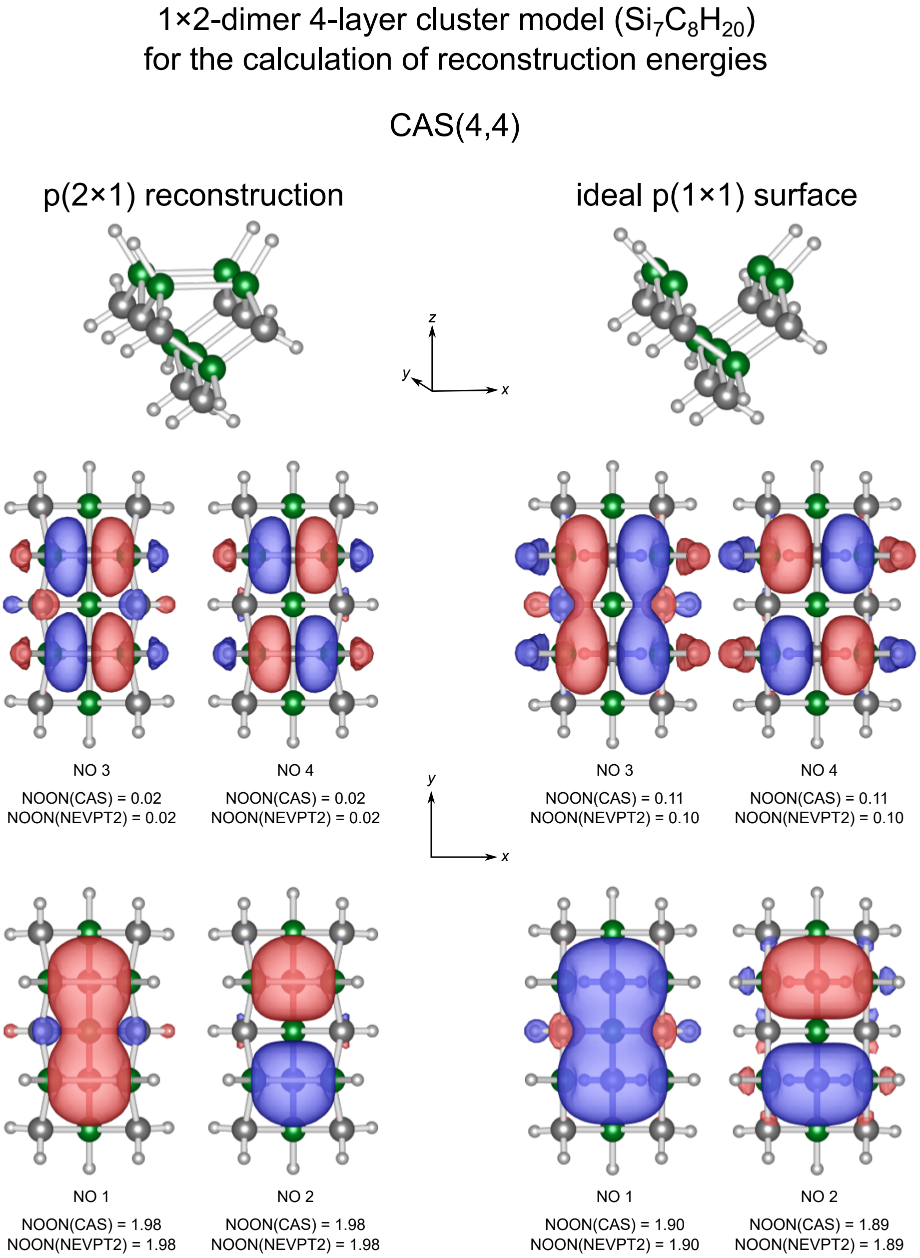

Figure A.16: 1×2-dimer 4-layer cluster model ($Si_7C_8H_{20}$) of the Si-terminated 3C-SiC(001)-p(2×1) reconstructed surface (SD model) and the ideal p(1×1) surface with the corresponding active space orbitals and NOONs at different levels of theory using the TZVPP/TZVP basis set and the first two atomic layers being relaxed according to Table 3.17. This cluster model was used to calculate the reconstruction energies for $M\times2$-dimer X-layer cluster models. The isosurface value of the orbitals amounts to $0.03\,{a_0}^{-3}$. Reprinted with permission from *J. Phys. Chem. C* 2023, 127, 48, 23475–23488. Copyright 2023 American Chemical Society. Slightly modified.

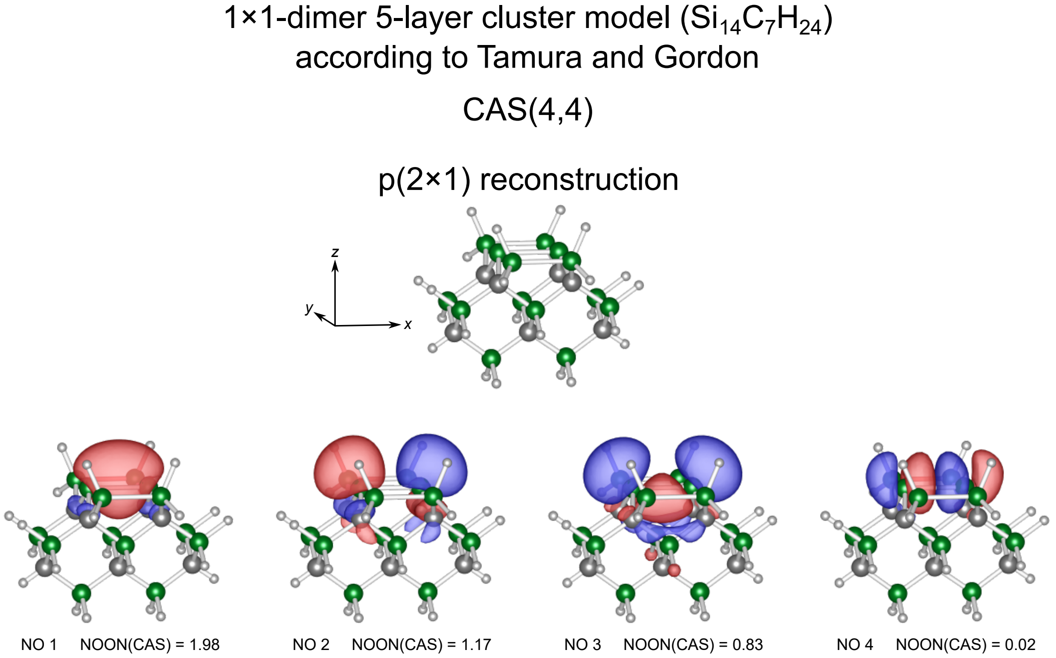

Figure A.17: 1×1-dimer 5-layer cluster model ($Si_{14}C_7H_{24}$) of the Si-terminated 3C-SiC(001)-p(2×1) reconstructed surface (SD model) according to Tamura and Gordon[53] with the corresponding active space orbitals and NOONs using the TZVPP/TZVP basis set and the first two atomic layers being relaxed according to Table 3.17. The isosurface value of the orbitals amounts to $0.015\,{a_0}^{-3}$. Reprinted with permission from *J. Phys. Chem. C* 2023, 127, 48, 23475–23488. Copyright 2023 American Chemical Society. Slightly modified.

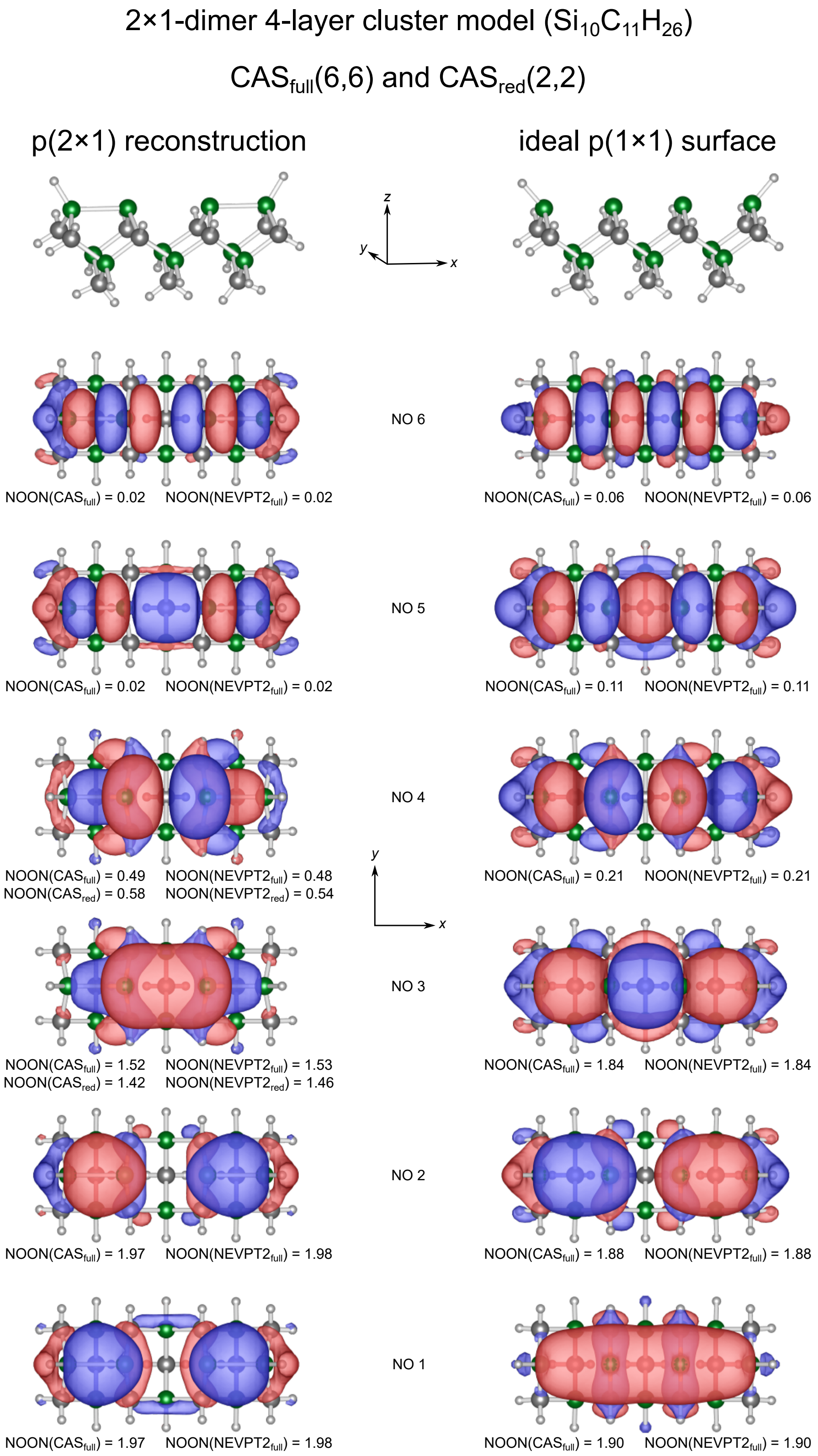

Figure A.18: 2×1-dimer 4-layer cluster model ($Si_{10}C_{11}H_{26}$) of the Si-terminated 3C-SiC(001)-p(2×1) reconstructed surface (SD model) and the ideal p(1×1) surface with the corresponding active space orbitals and NOONs at different levels of theory using the TZVPP/TZVP basis set and the first two atomic layers being relaxed according to Table 3.17. The isosurface value of the orbitals amounts to $0.015\,{a_0}^{-3}$. Reprinted with permission from *J. Phys. Chem. C* 2023, 127, 48, 23475–23488. Copyright 2023 American Chemical Society. Slightly modified.

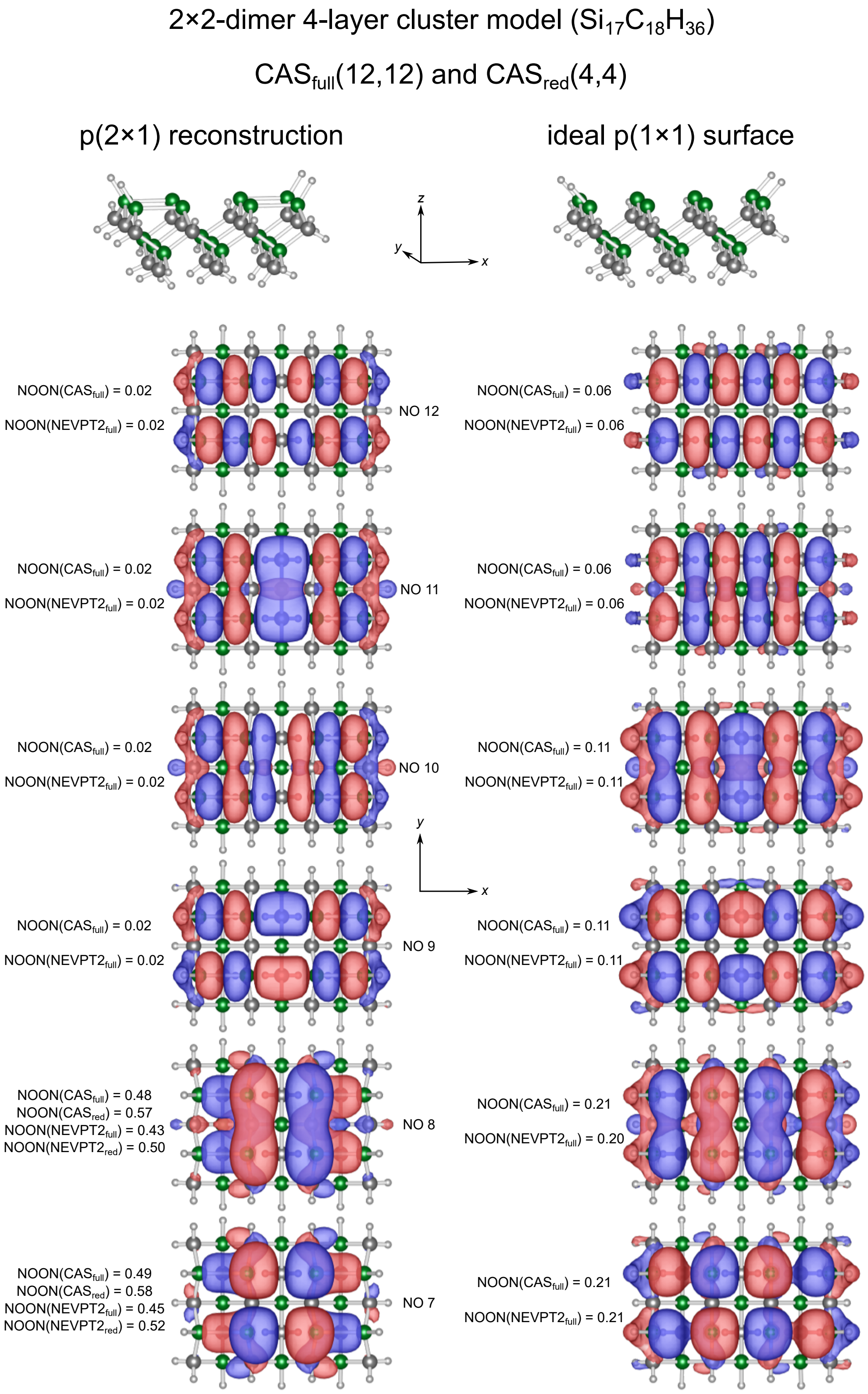

Figure A.19: 2×2-dimer 4-layer cluster model ($Si_{17}C_{18}H_{36}$) of the Si-terminated 3C-SiC(001)-p(2×1) reconstructed surface (SD model) and the ideal p(1×1) surface with the corresponding active space orbitals and NOONs at different levels of theory using the TZVPP/TZVP basis set and the first two atomic layers being relaxed according to Table 3.17. The isosurface value of the orbitals amounts to $0.015\,{a_0}^{-3}$. Reprinted with permission from *J. Phys. Chem. C* 2023, 127, 48, 23475–23488. Copyright 2023 American Chemical Society. Slightly modified.

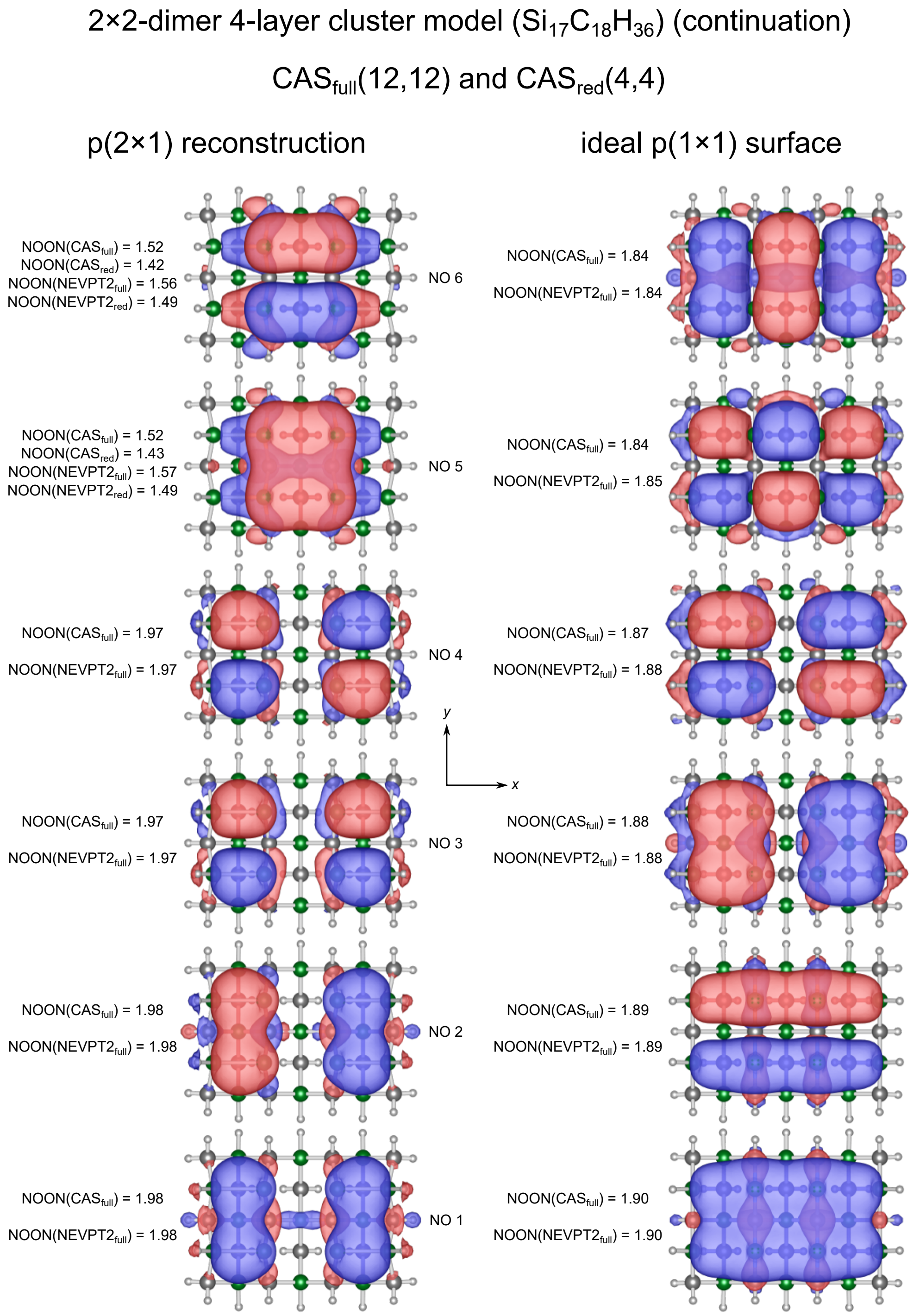

Figure A.20: Continuation of the 2×2-dimer 4-layer cluster model ($Si_{17}C_{18}H_{36}$) of the Si-terminated 3C-SiC(001)-p(2×1) reconstructed surface (SD model) and the ideal p(1×1) surface with the corresponding active space orbitals and NOONs at different levels of theory using the TZVPP/TZVP basis set and the first two atomic layers being relaxed according to Table 3.17. The isosurface value of the orbitals amounts to $0.015\,a_0{}^{-3}$. Reprinted with permission from *J. Phys. Chem. C* 2023, 127, 48, 23475–23488. Copyright 2023 American Chemical Society. Slightly modified.

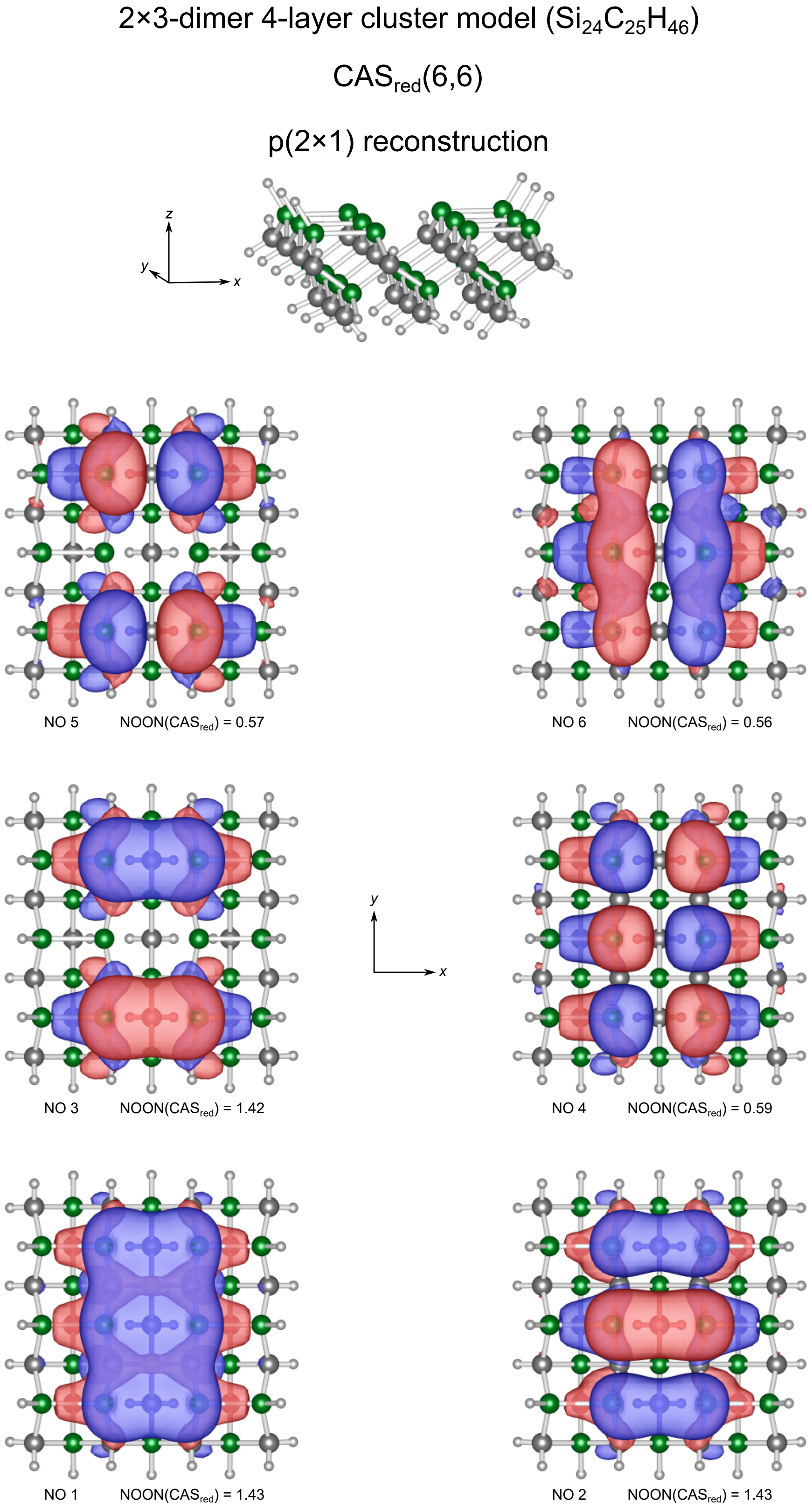

Figure A.21: 2×3-dimer 4-layer cluster model ($Si_{24}C_{25}H_{46}$) of the Si-terminated 3C-SiC(001)-p(2×1) reconstructed surface (SD model) with the corresponding active space orbitals and NOONs using the TZVPP/TZVP basis set and the first two atomic layers being relaxed according to Table 3.17. The isosurface value of the orbitals amounts to $0.015\,{a_0}^{-3}$. Reprinted with permission from *J. Phys. Chem. C* 2023, 127, 48, 23475–23488. Copyright 2023 American Chemical Society. Slightly modified.

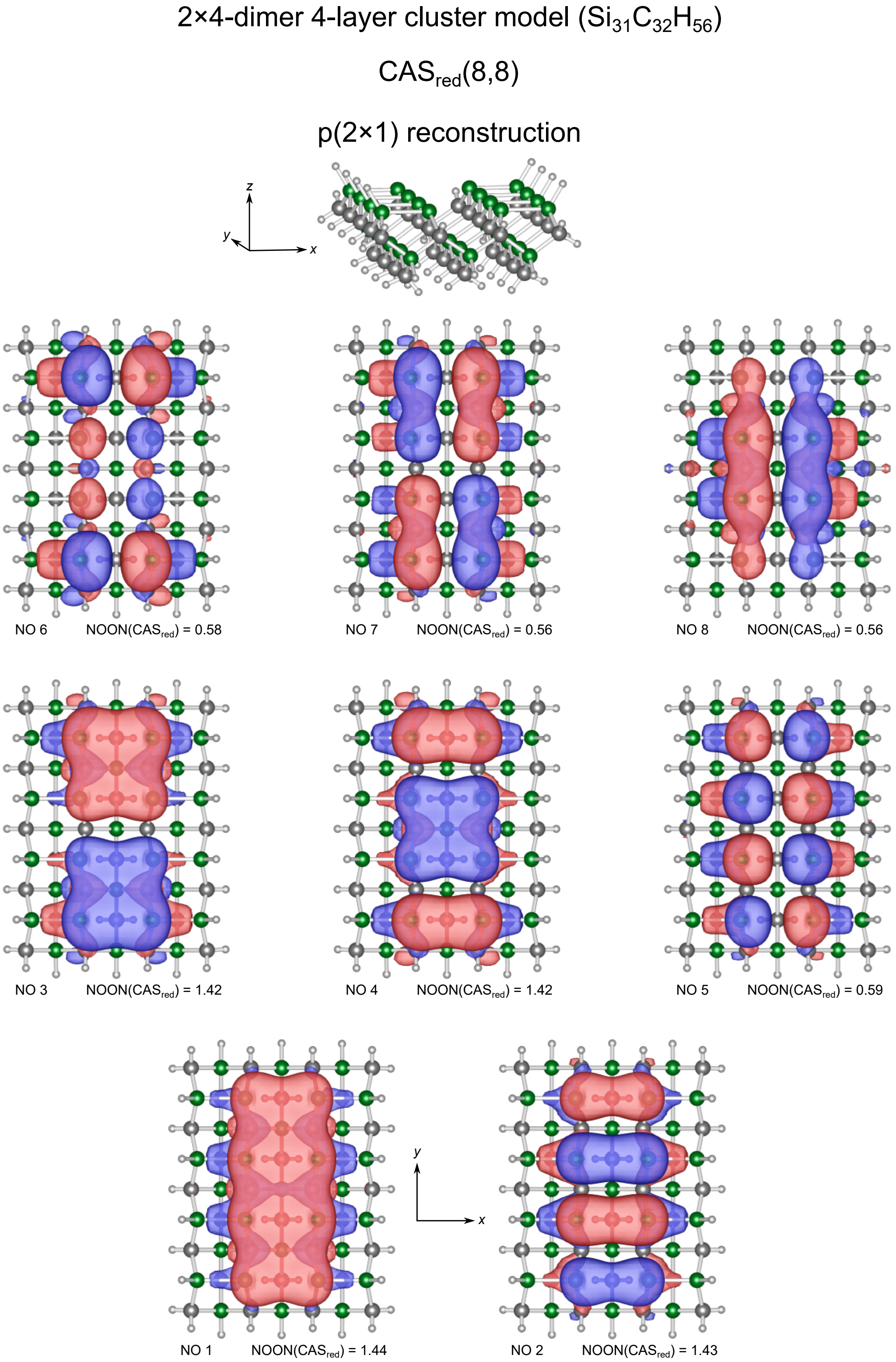

Figure A.22: 2×4-dimer 4-layer cluster model ($Si_{31}C_{32}H_{56}$) of the Si-terminated 3C-SiC(001)-p(2×1) reconstructed surface (SD model) with the corresponding active space orbitals and NOONs using the TZVPP/TZVP basis set and the first two atomic layers being relaxed according to Table 3.17. The isosurface value of the orbitals amounts to $0.015\,{a_0}^{-3}$. Reprinted with permission from *J. Phys. Chem. C* 2023, 127, 48, 23475–23488. Copyright 2023 American Chemical Society. Slightly modified.

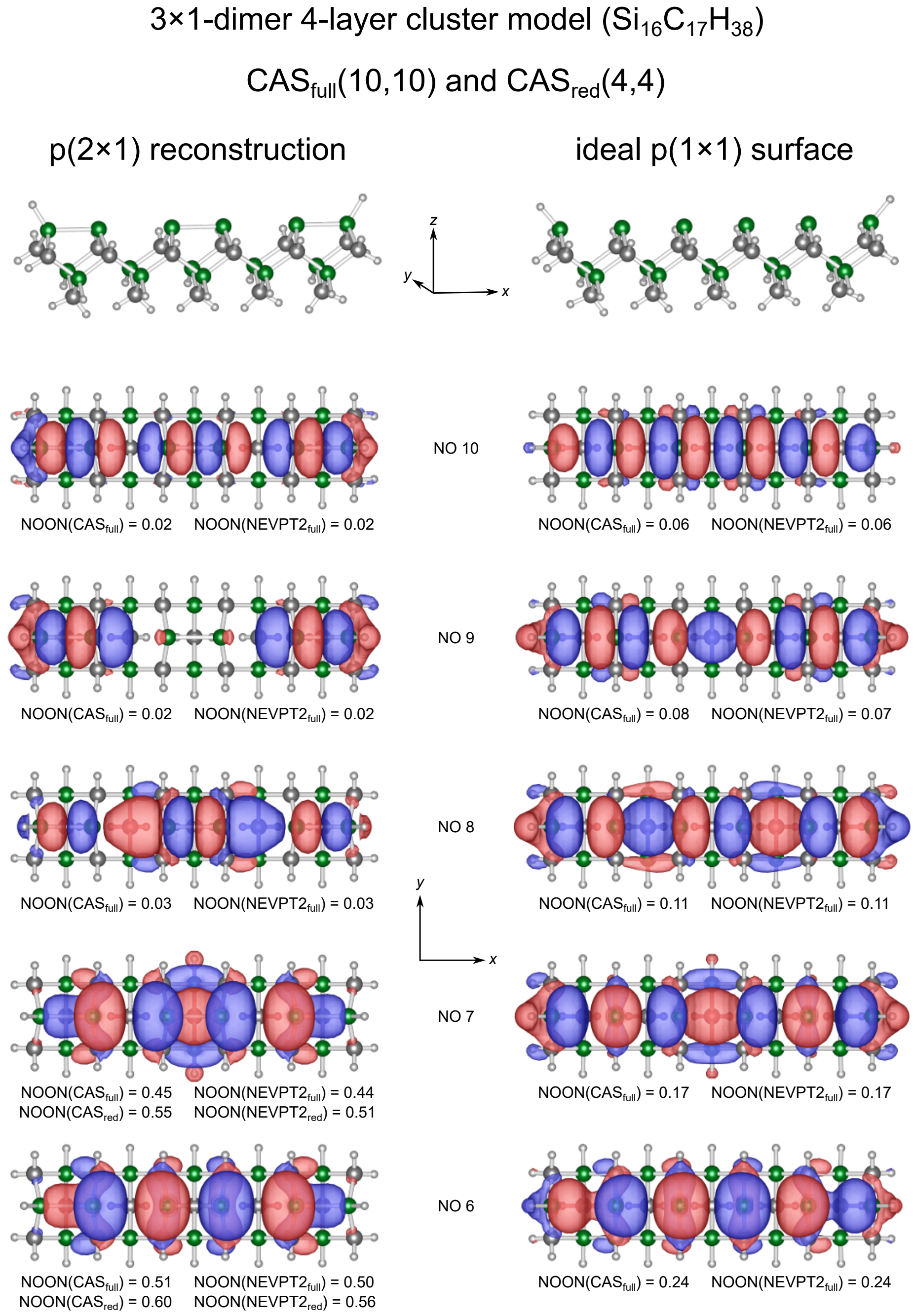

Figure A.23: 3×1-dimer 4-layer cluster model ($Si_{16}C_{17}H_{38}$) of the Si-terminated 3C-SiC(001)-p(2×1) reconstructed surface (SD model) and the ideal p(1×1) surface with the corresponding active space orbitals and NOONs at different levels of theory using the TZVPP/TZVP basis set and the first two atomic layers being relaxed according to Table 3.17. The isosurface value of the orbitals amounts to $0.015\,{a_0}^{-3}$. Reprinted with permission from *J. Phys. Chem. C* 2023, 127, 48, 23475–23488. Copyright 2023 American Chemical Society. Slightly modified.

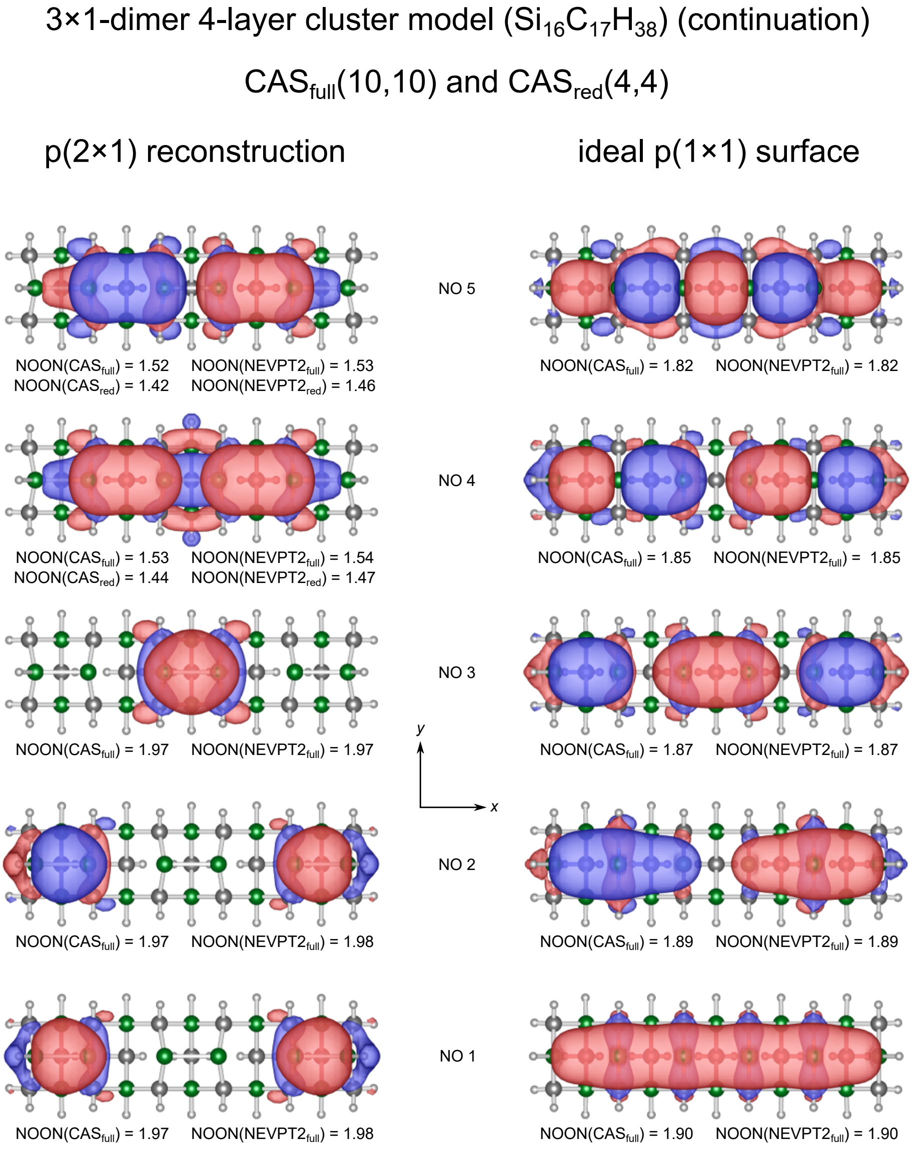

Figure A.24: Continuation of the 3×1-dimer 4-layer cluster model ($Si_{16}C_{17}H_{38}$) of the Si-terminated 3C-SiC(001)-p(2×1) reconstructed surface (SD model) and the ideal p(1×1) surface with the corresponding active space orbitals and NOONs at different levels of theory using the TZVPP/TZVP basis set and the first two atomic layers being relaxed according to Table 3.17. The isosurface value of the orbitals amounts to $0.015\,a_0{}^{-3}$. Reprinted with permission from *J. Phys. Chem. C* 2023, 127, 48, 23475–23488. Copyright 2023 American Chemical Society. Slightly modified.

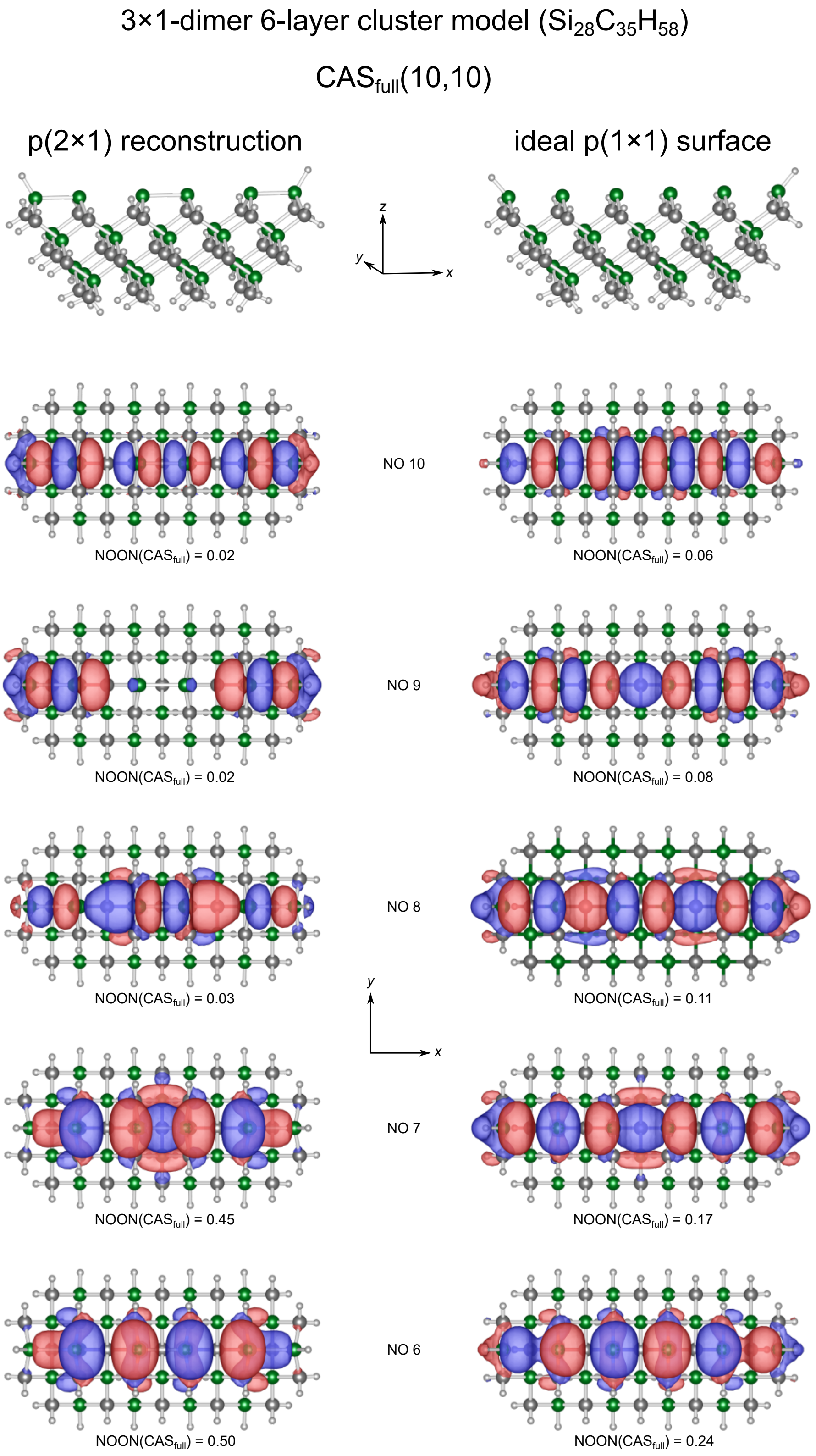

Figure A.25: 3×1-dimer 6-layer cluster model ($Si_{28}C_{35}H_{58}$) of the Si-terminated 3C-SiC(001)-p(2×1) reconstructed surface (SD model) and the ideal p(1×1) surface with the corresponding active space orbitals and NOONs using the TZVPP/TZVP basis set and the first two atomic layers being relaxed according to Table 3.17. The isosurface value of the orbitals amounts to $0.015\,a_0{}^{-3}$. Reprinted with permission from *J. Phys. Chem. C* 2023, 127, 48, 23475–23488. Copyright 2023 American Chemical Society. Slightly modified.

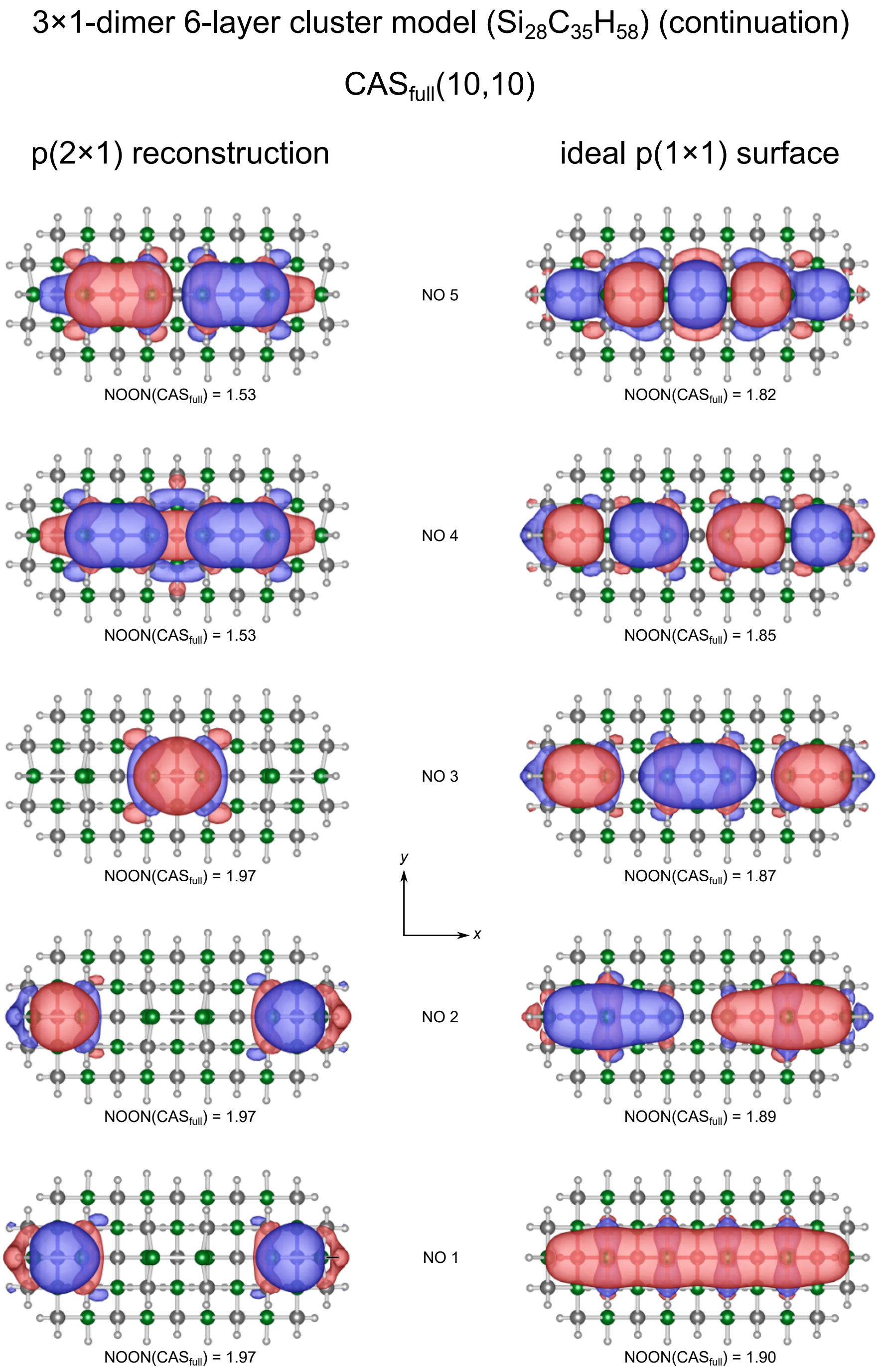

Figure A.26: Continuation of the 3×1-dimer 6-layer cluster model ($Si_{28}C_{35}H_{58}$) of the Si-terminated 3C-SiC(001)-p(2×1) reconstructed surface (SD model) and the ideal p(1×1) surface with the corresponding active space orbitals and NOONs using the TZVPP/TZVP basis set and the first two atomic layers being relaxed according to Table 3.17. The isosurface value of the orbitals amounts to $0.015\,{a_0}^{-3}$. Reprinted with permission from *J. Phys. Chem. C* 2023, 127, 48, 23475–23488. Copyright 2023 American Chemical Society. Slightly modified.

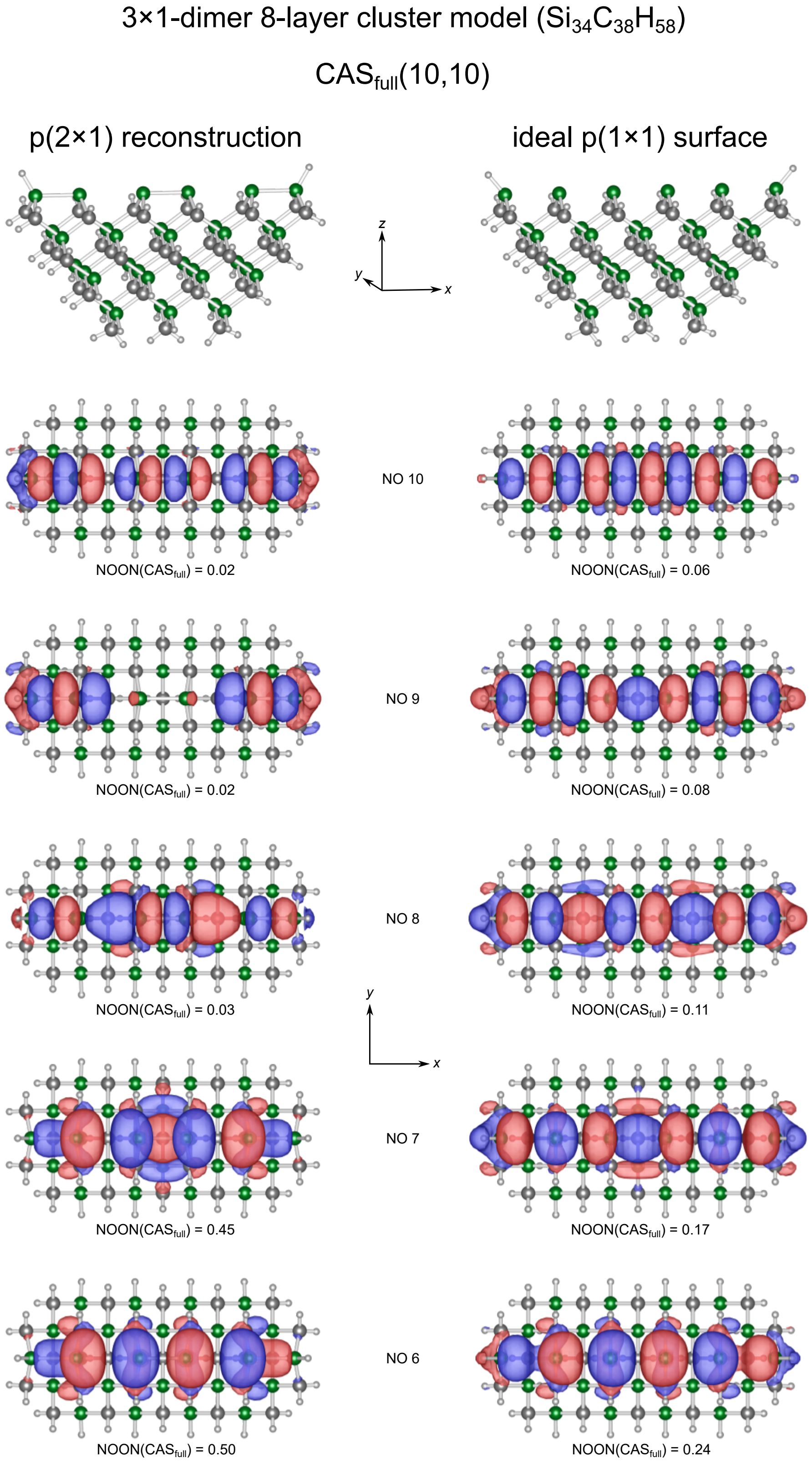

Figure A.27: 3×1-dimer 8-layer cluster model ($Si_{34}C_{38}H_{58}$) of the Si-terminated 3C-SiC(001)-p(2×1) reconstructed surface (SD model) and the ideal p(1×1) surface with the corresponding active space orbitals and NOONs using the TZVPP/TZVP basis set and the first two atomic layers being relaxed according to Table 3.17. The isosurface value of the orbitals amounts to $0.015\,{a_0}^{-3}$. Reprinted with permission from *J. Phys. Chem. C* 2023, 127, 48, 23475–23488. Copyright 2023 American Chemical Society. Slightly modified.

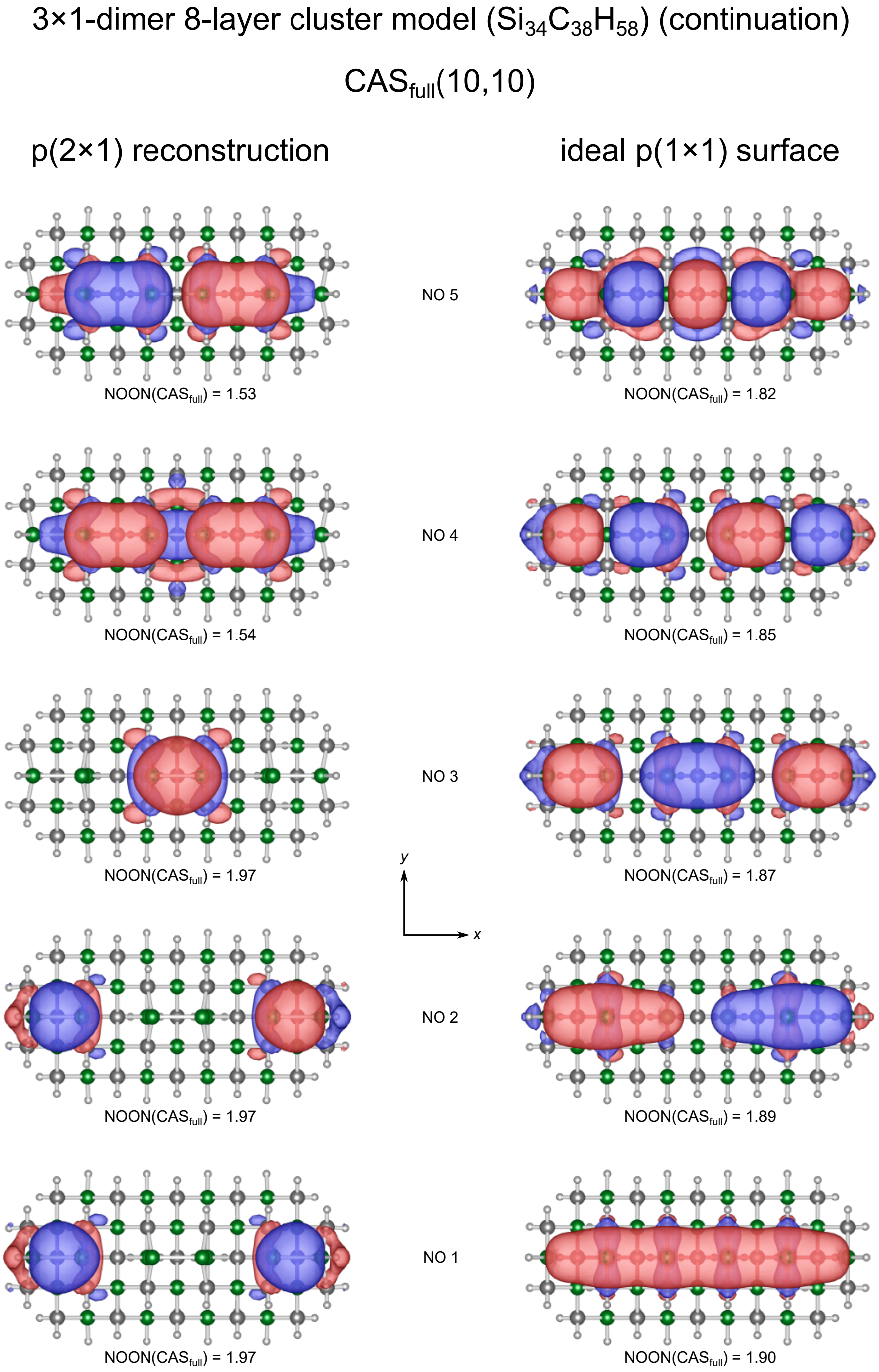

Figure A.28: Continuation of the 3×1-dimer 8-layer cluster model ($Si_{34}C_{38}H_{58}$) of the Si-terminated 3C-SiC(001)-p(2×1) reconstructed surface (SD model) and the ideal p(1×1) surface with the corresponding active space orbitals and NOONs using the TZVPP/TZVP basis set and the first two atomic layers being relaxed according to Table 3.17. The isosurface value of the orbitals amounts to $0.015\,a_0{}^{-3}$. Reprinted with permission from *J. Phys. Chem. C* 2023, 127, 48, 23475–23488. Copyright 2023 American Chemical Society. Slightly modified.

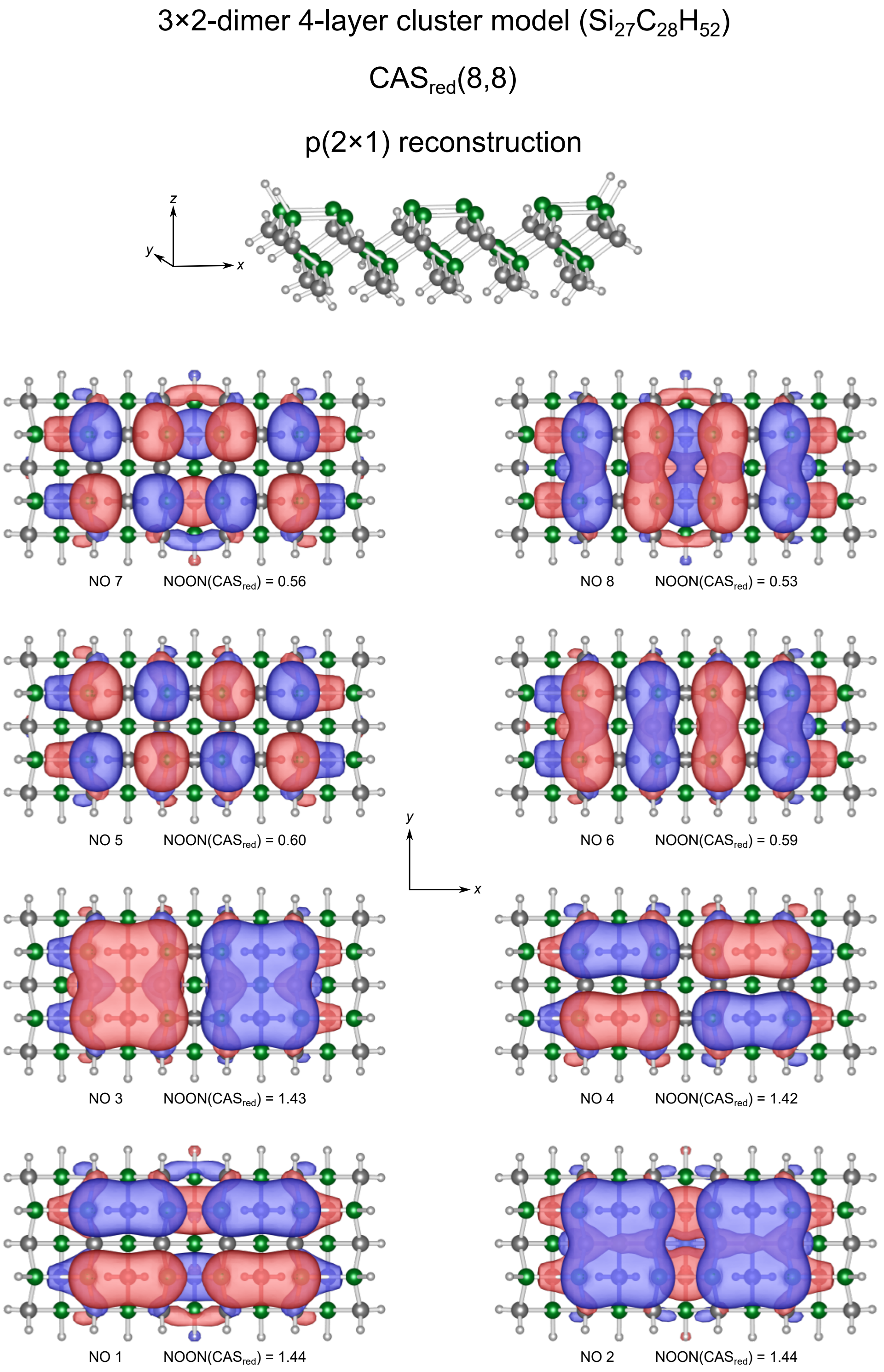

Figure A.29: 3×2-dimer 4-layer cluster model ($Si_{27}C_{28}H_{52}$) of the Si-terminated 3C-SiC(001)-p(2×1) reconstructed surface (SD model) with the corresponding active space orbitals and NOONs using the TZVPP/TZVP basis set and the first two atomic layers being relaxed according to Table 3.17. The isosurface value of the orbitals amounts to $0.015\,{a_0}^{-3}$. Reprinted with permission from *J. Phys. Chem. C* 2023, 127, 48, 23475–23488. Copyright 2023 American Chemical Society. Slightly modified.

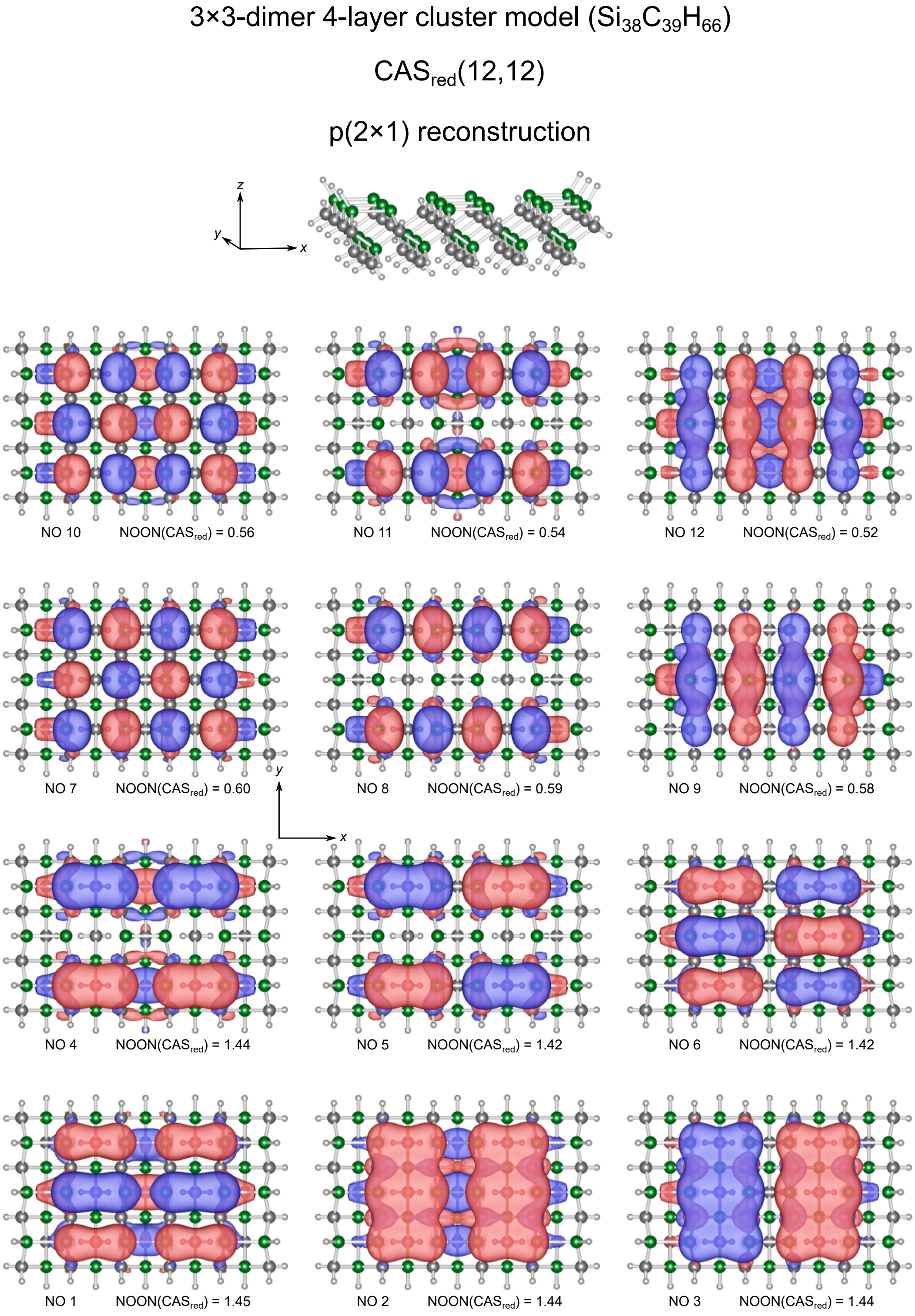

Figure A.30: 3×3-dimer 4-layer cluster model ($Si_{38}C_{39}H_{66}$) of the Si-terminated 3C-SiC(001)-p(2×1) reconstructed surface (SD model) with the corresponding active space orbitals and NOONs using the TZVPP/TZVP basis set and the first two atomic layers being relaxed according to Table 3.17. The isosurface value of the orbitals amounts to $0.015\,{a_0}^{-3}$. Reprinted with permission from *J. Phys. Chem. C* 2023, 127, 48, 23475–23488. Copyright 2023 American Chemical Society. Slightly modified.

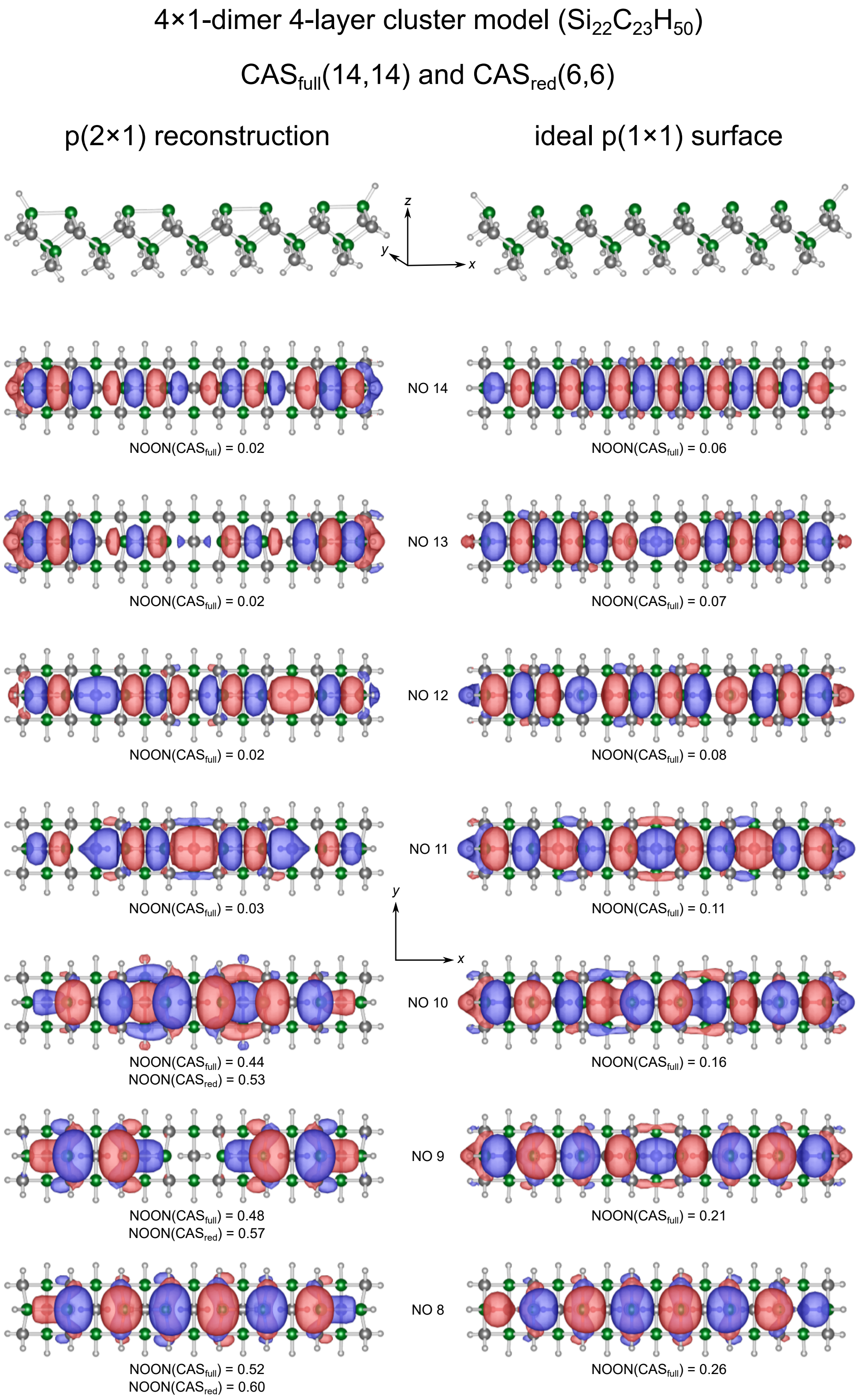

Figure A.31: 4×1-dimer 4-layer cluster model ($Si_{22}C_{23}H_{50}$) of the Si-terminated 3C-SiC(001)-p(2×1) reconstructed surface (SD model) and the ideal p(1×1) surface with the corresponding active space orbitals and NOONs at different levels of theory using the TZVPP/TZVP basis set and the first two atomic layers being relaxed according to Table 3.17. The isosurface value of the orbitals amounts to $0.015\,{a_0}^{-3}$. Reprinted with permission from *J. Phys. Chem. C* 2023, 127, 48, 23475–23488. Copyright 2023 American Chemical Society. Slightly modified.

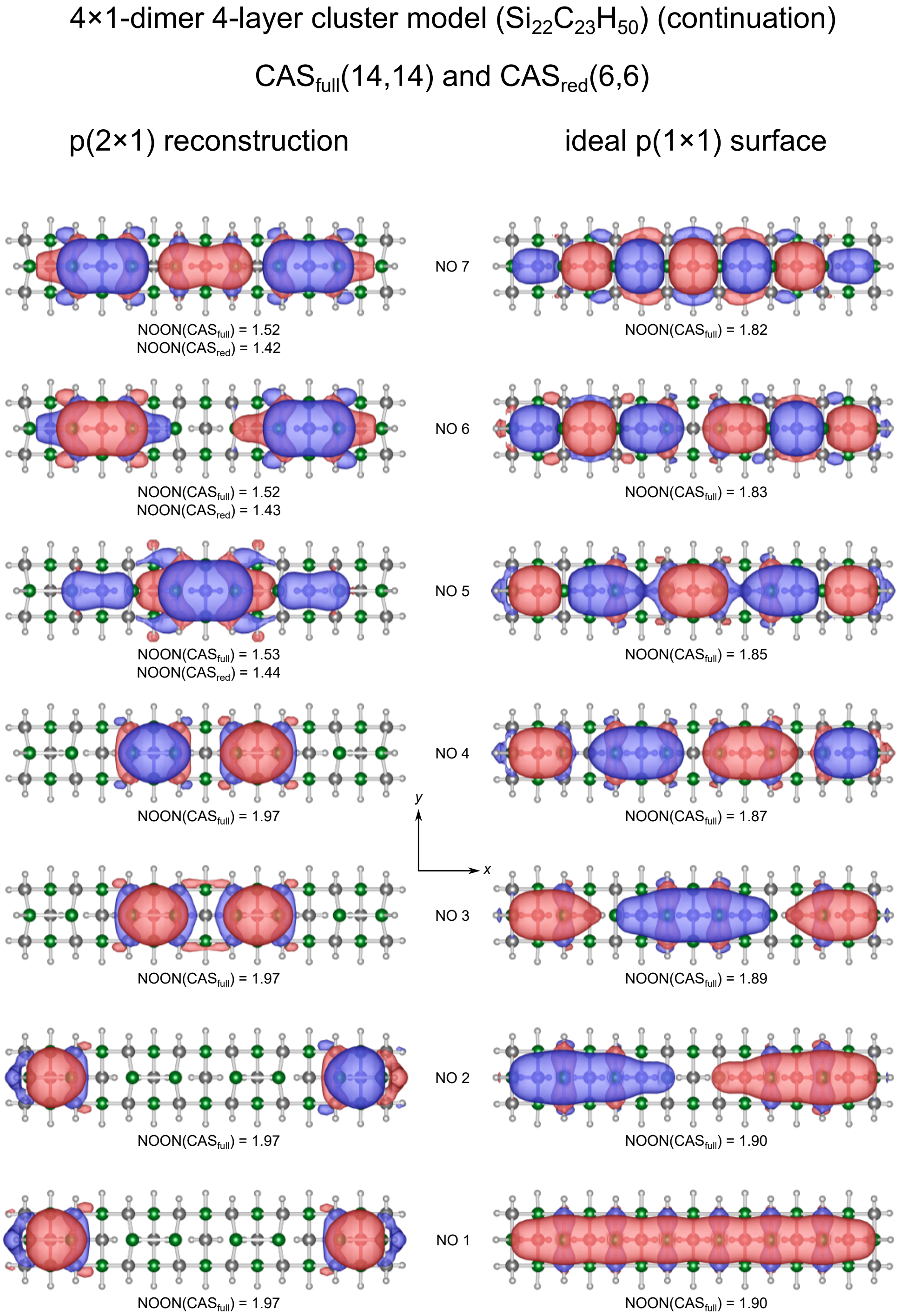

Figure A.32: Continuation of the 4×1-dimer 4-layer cluster model ($Si_{22}C_{23}H_{50}$) of the Si-terminated 3C-SiC(001)-p(2×1) reconstructed surface (SD model) and the ideal p(1×1) surface with the corresponding active space orbitals and NOONs at different levels of theory using the TZVPP/TZVP basis set and the first two atomic layers being relaxed according to Table 3.17. The isosurface value of the orbitals amounts to $0.015\,a_0{}^{-3}$. Reprinted with permission from *J. Phys. Chem. C* 2023, 127, 48, 23475–23488. Copyright 2023 American Chemical Society. Slightly modified.

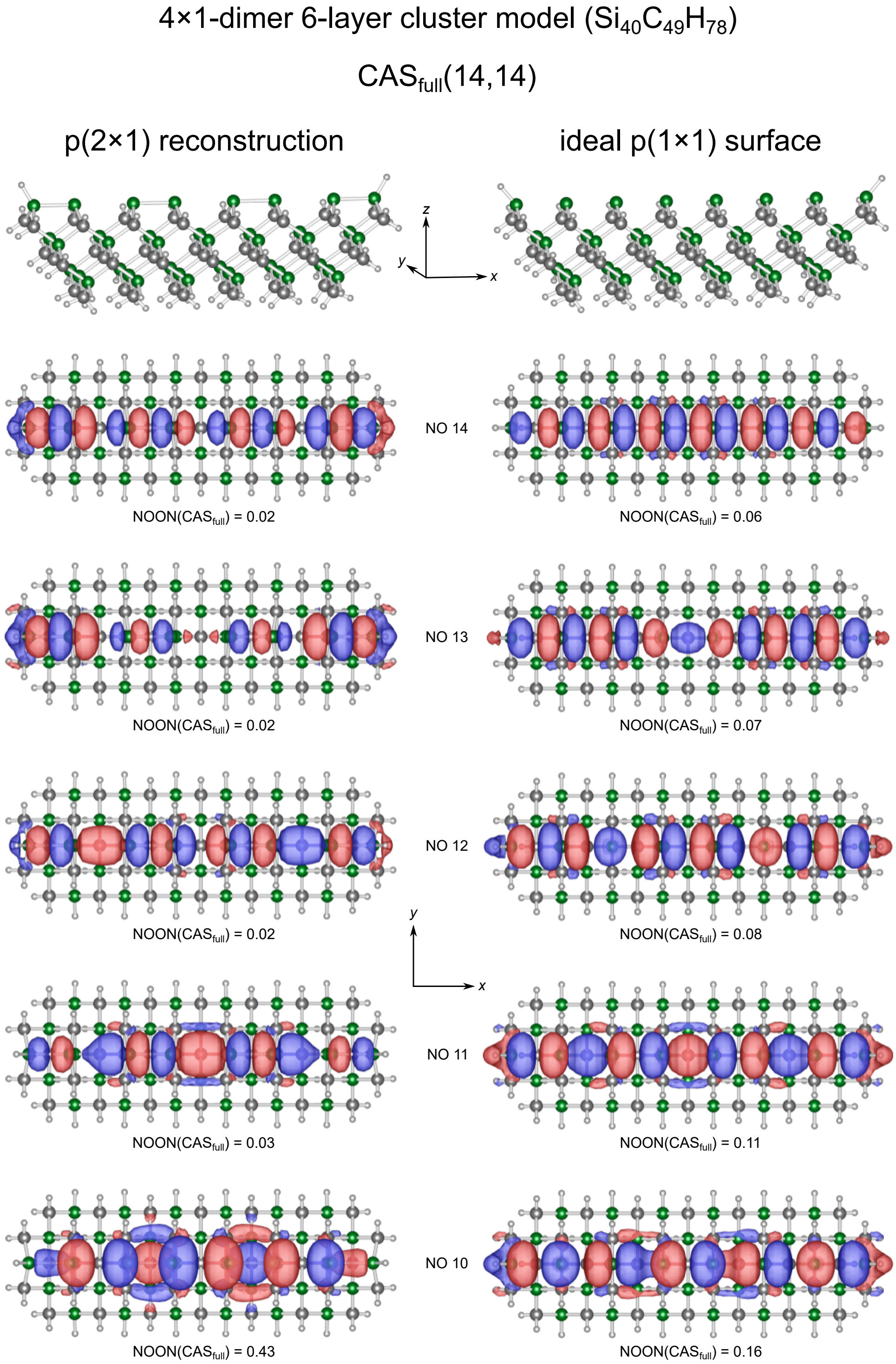

Figure A.33: 4×1-dimer 6-layer cluster model ($Si_{40}C_{49}H_{78}$) of the Si-terminated 3C-SiC(001)-p(2×1) reconstructed surface (SD model) and the ideal p(1×1) surface with the corresponding active space orbitals and NOONs using the TZVPP/TZVP basis set and the first two atomic layers being relaxed according to Table 3.17. The isosurface value of the orbitals amounts to $0.015\,{a_0}^{-3}$. Reprinted with permission from *J. Phys. Chem. C* 2023, 127, 48, 23475–23488. Copyright 2023 American Chemical Society. Slightly modified.

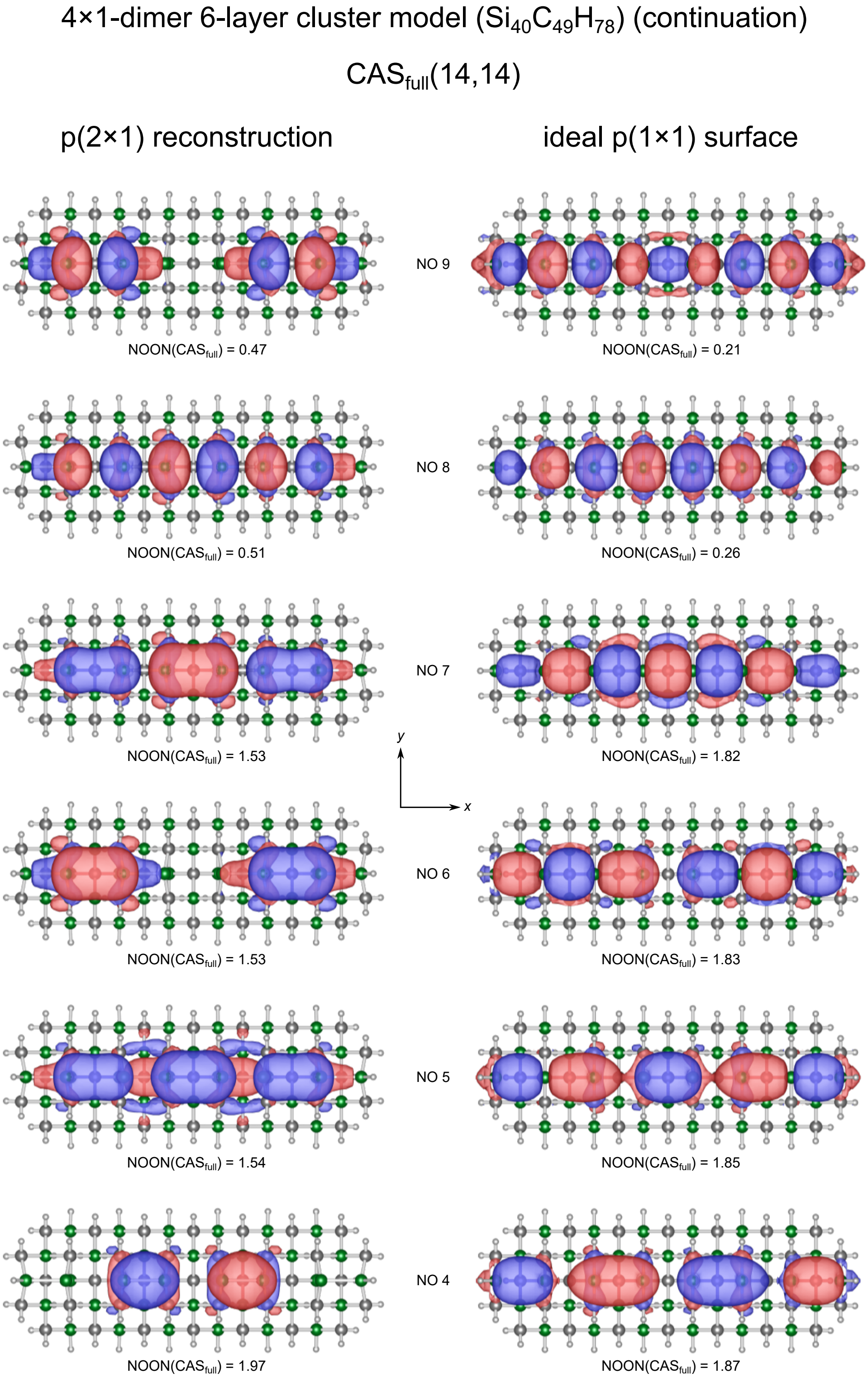

Figure A.34: Continuation of the 4×1-dimer 6-layer cluster model ($Si_{40}C_{49}H_{78}$) of the Si-terminated 3C-SiC(001)-p(2×1) reconstructed surface (SD model) and the ideal p(1×1) surface with the corresponding active space orbitals and NOONs using the TZVPP/TZVP basis set and the first two atomic layers being relaxed according to Table 3.17. The isosurface value of the orbitals amounts to $0.015\,{a_0}^{-3}$. Reprinted with permission from *J. Phys. Chem. C* 2023, 127, 48, 23475–23488. Copyright 2023 American Chemical Society. Slightly modified.

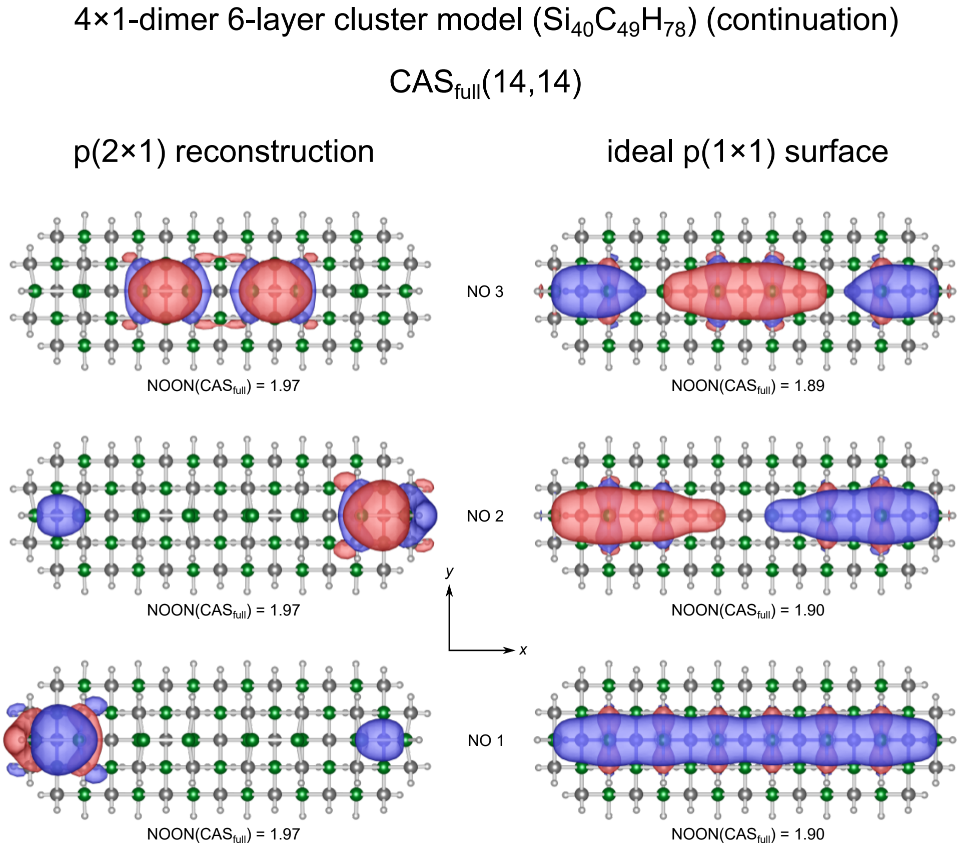

Figure A.35: Continuation of the 4×1-dimer 6-layer cluster model ($Si_{40}C_{49}H_{78}$) of the Si-terminated 3C-SiC(001)-p(2×1) reconstructed surface (SD model) and the ideal p(1×1) surface with the corresponding active space orbitals and NOONs using the TZVPP/TZVP basis set and the first two atomic layers being relaxed according to Table 3.17. The isosurface value of the orbitals amounts to $0.015\,{a_0}^{-3}$. Reprinted with permission from *J. Phys. Chem. C* 2023, 127, 48, 23475–23488. Copyright 2023 American Chemical Society. Slightly modified.

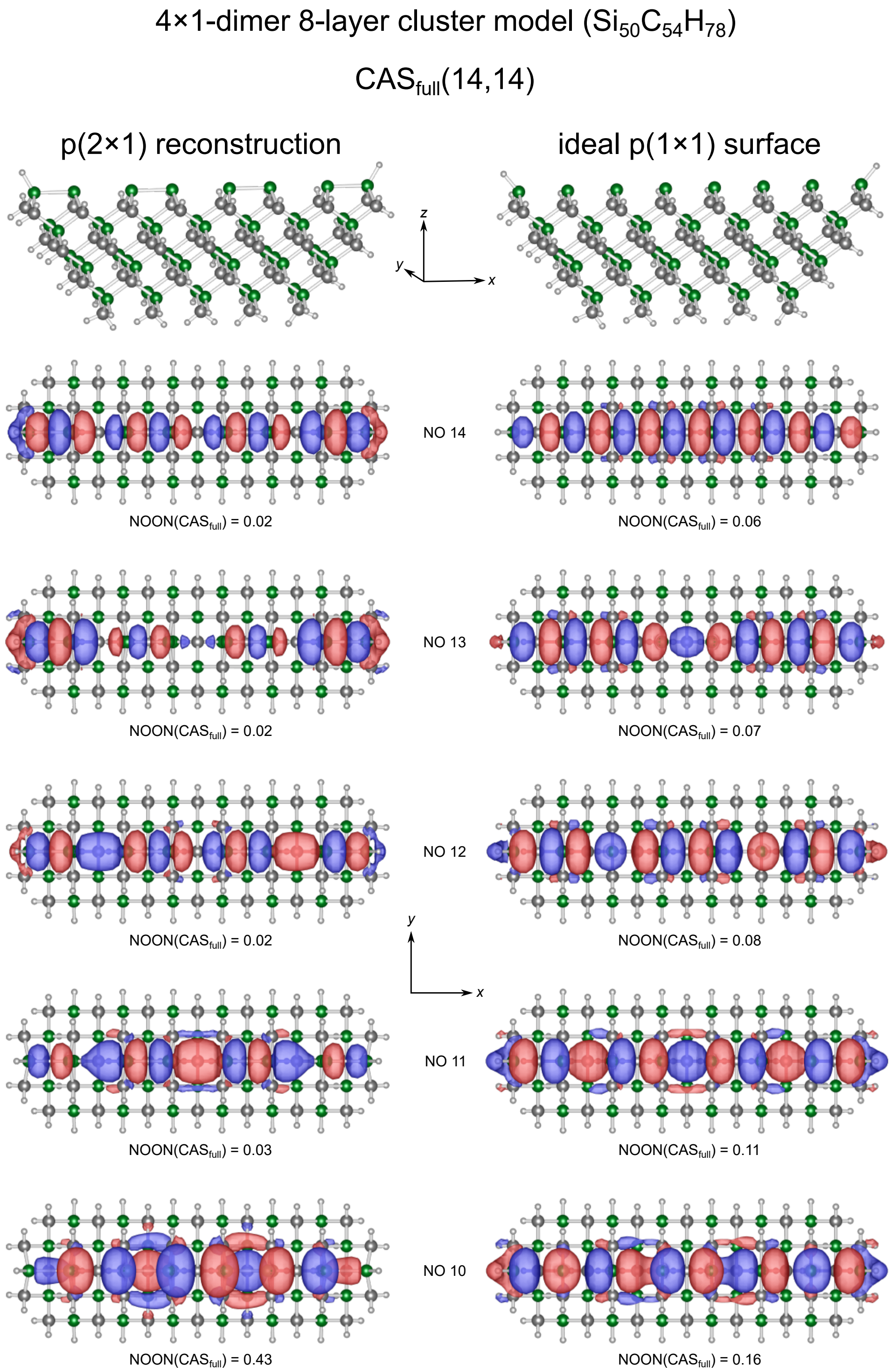

Figure A.36: 4×1-dimer 8-layer cluster model ($Si_{50}C_{54}H_{78}$) of the Si-terminated 3C-SiC(001)-p(2×1) reconstructed surface (SD model) and the ideal p(1×1) surface with the corresponding active space orbitals and NOONs using the TZVPP/TZVP basis set and the first two atomic layers being relaxed according to Table 3.17. The isosurface value of the orbitals amounts to $0.015\,{a_0}^{-3}$. Reprinted with permission from *J. Phys. Chem. C* 2023, 127, 48, 23475–23488. Copyright 2023 American Chemical Society. Slightly modified.

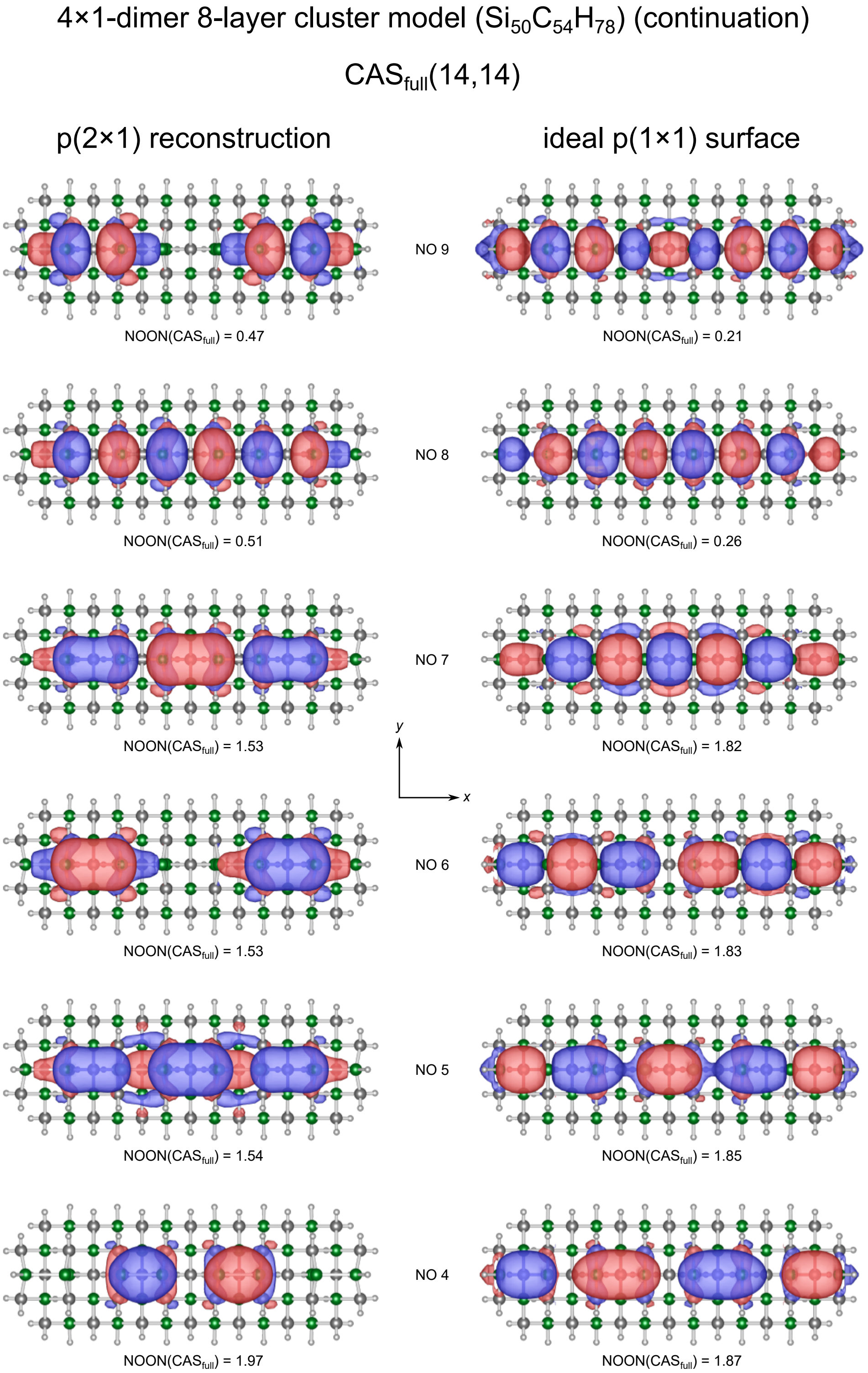

Figure A.37: Continuation of the 4×1-dimer 8-layer cluster model ($Si_{50}C_{54}H_{78}$) of the Si-terminated 3C-SiC(001)-p(2×1) reconstructed surface (SD model) and the ideal p(1×1) surface with the corresponding active space orbitals and NOONs using the TZVPP/TZVP basis set and the first two atomic layers being relaxed according to Table 3.17. The isosurface value of the orbitals amounts to $0.015\,{a_0}^{-3}$. Reprinted with permission from *J. Phys. Chem. C* 2023, 127, 48, 23475–23488. Copyright 2023 American Chemical Society. Slightly modified.

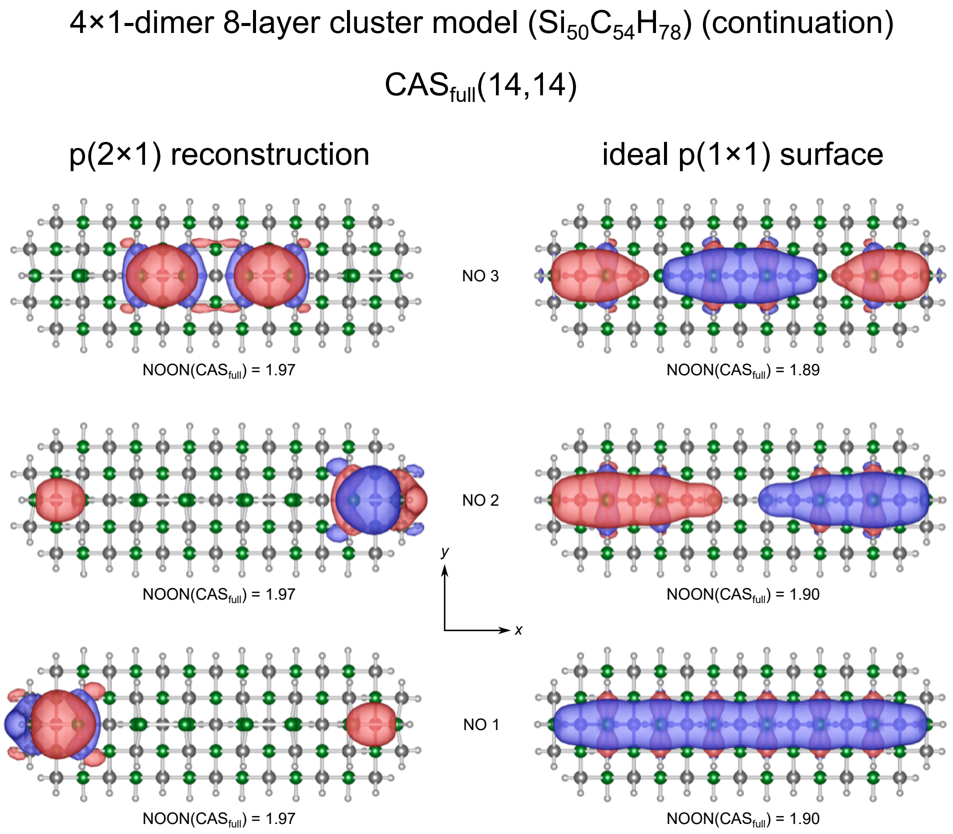

Figure A.38: Continuation of the 4×1-dimer 8-layer cluster model ($Si_{50}C_{54}H_{78}$) of the Si-terminated 3C-SiC(001)-p(2×1) reconstructed surface (SD model) and the ideal p(1×1) surface with the corresponding active space orbitals and NOONs using the TZVPP/TZVP basis set and the first two atomic layers being relaxed according to Table 3.17. The isosurface value of the orbitals amounts to $0.015\,{a_0}^{-3}$. Reprinted with permission from *J. Phys. Chem. C* 2023, 127, 48, 23475–23488. Copyright 2023 American Chemical Society. Slightly modified.

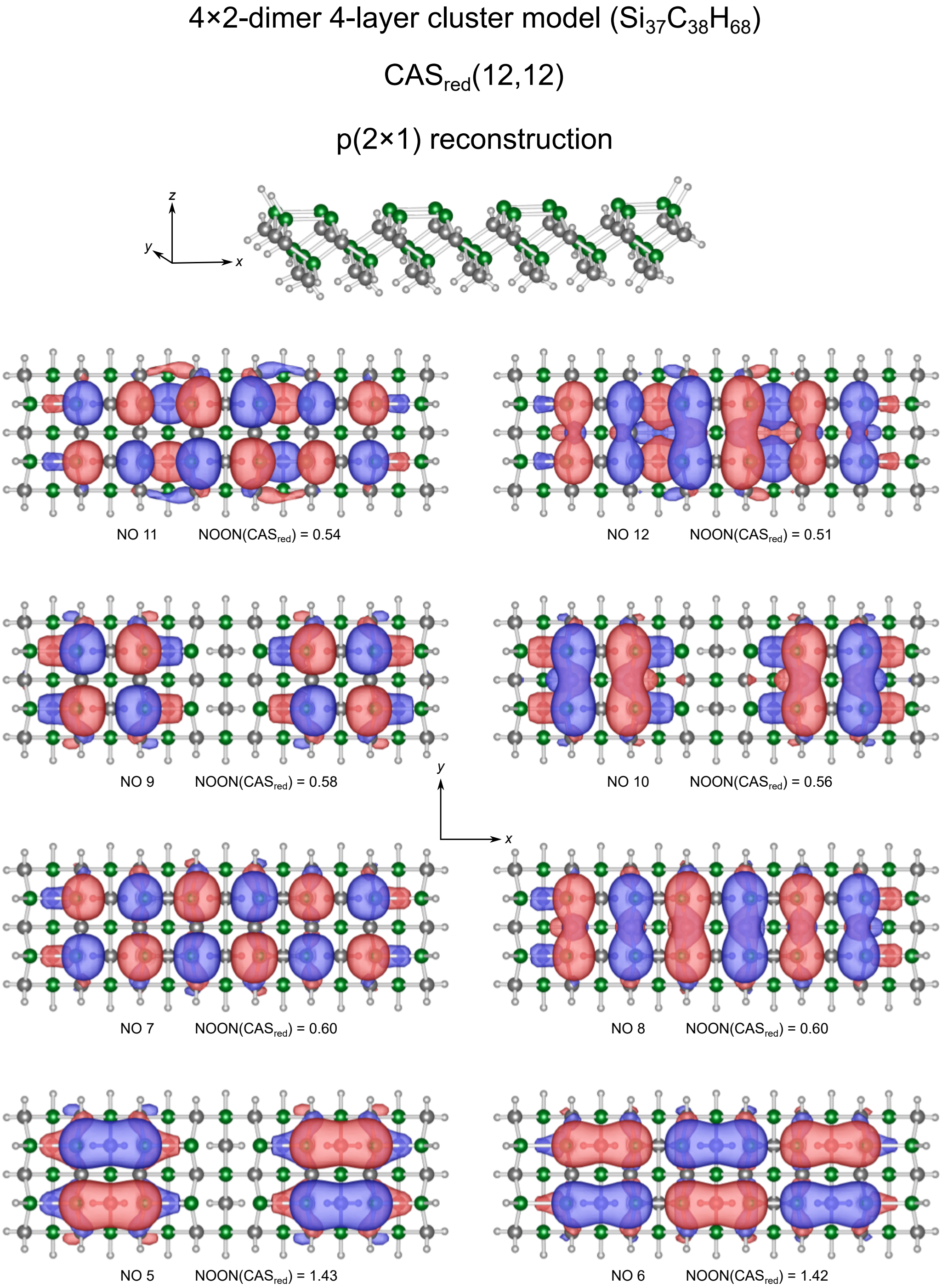

Figure A.39: 4×2-dimer 4-layer cluster model ($Si_{37}C_{38}H_{68}$) of the Si-terminated 3C-SiC(001)-p(2×1) reconstructed surface (SD model) with the corresponding active space orbitals and NOONs using the TZVPP/TZVP basis set and the first two atomic layers being relaxed according to Table 3.17. The isosurface value of the orbitals amounts to $0.015\,a_0{}^{-3}$. Reprinted with permission from *J. Phys. Chem. C* 2023, 127, 48, 23475–23488. Copyright 2023 American Chemical Society. Slightly modified.

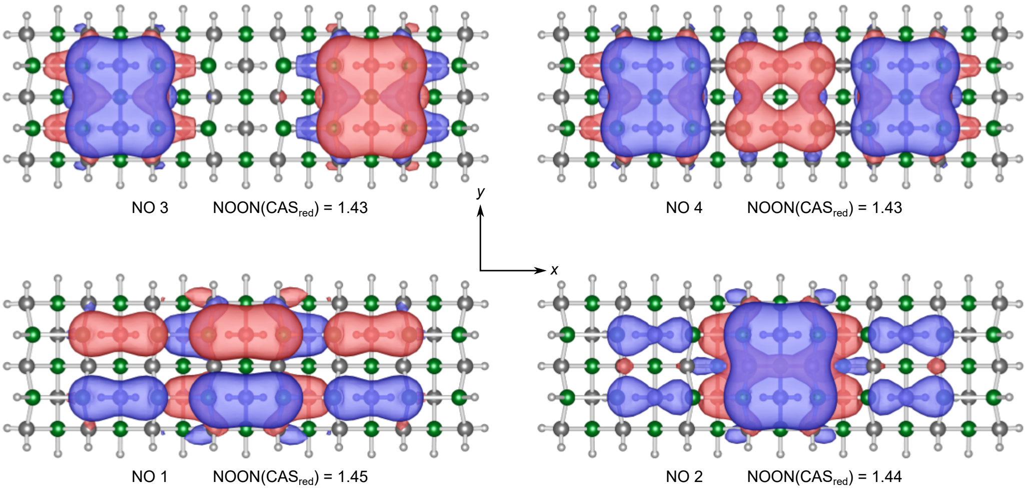

4×2-dimer 4-layer cluster model ($Si_{37}C_{38}H_{68}$) (continuation)

$CAS_{red}(12,12)$

p(2×1) reconstruction

Figure A.40: Continuation of the 4×2-dimer 4-layer cluster model ($Si_{37}C_{38}H_{68}$) of the Si-terminated 3C-SiC(001)-p(2×1) reconstructed surface (SD model) with the corresponding active space orbitals and NOONs using the TZVPP/TZVP basis set and the first two atomic layers being relaxed according to Table 3.17. The isosurface value of the orbitals amounts to $0.015\,{a_0}^{-3}$. Reprinted with permission from *J. Phys. Chem. C* 2023, 127, 48, 23475–23488. Copyright 2023 American Chemical Society. Slightly modified.

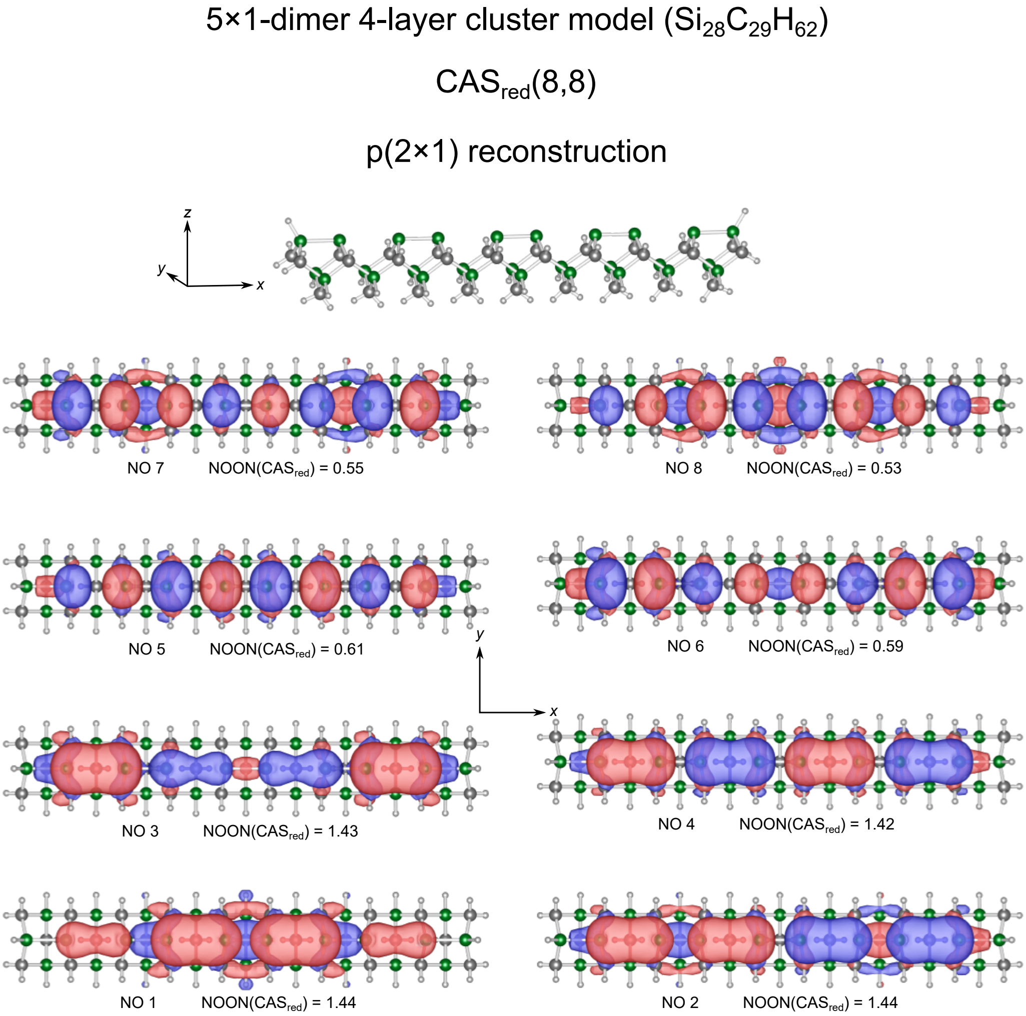

Figure A.41: 5×1-dimer 4-layer cluster model ($Si_{28}C_{29}H_{62}$) of the Si-terminated 3C-SiC(001)-p(2×1) reconstructed surface (SD model) with the corresponding active space orbitals and NOONs using the TZVPP/TZVP basis set and the first two atomic layers being relaxed according to Table 3.17. The isosurface value of the orbitals amounts to $0.015\,{a_0}^{-3}$. Reprinted with permission from *J. Phys. Chem. C* 2023, 127, 48, 23475–23488. Copyright 2023 American Chemical Society. Slightly modified.

List of Abbreviations

1D	one-dimensional
2D	two-dimensional
3D	three-dimensional
AO	atomic orbital
AP	approximate projection
AUDD	alternating up-and-down dimer
bc	body-centered
BOA	Born-Oppenheimer approximation
BZ	Brillouin zone
CASPT2	complete active space perturbation theory of second order
CASSCF	complete active space self-consistent field
CAS(m,n)	complete active space with m electrons and n orbitals
c	centered
CBM	conduction band minimum
CC	coupled cluster
CI	configuration interaction
CIS	configuration interaction singles
CISD	configuration interaction singles doubles
CO	crystalline orbital
CSF	configuration state function
CVD	chemical vapor deposition
DFT	density functional theory
DMET	density matrix embedding theory
DOS	density of states
ESR	electron spin resonance
fc	face-centered
fcc	face-centered cubic
GGA	generalized gradient approximation
GTO	Gaussian type orbital
HF	Hartree-Fock
HOCO	highest occupied crystalline orbital
HOMO	highest occupied molecular orbital
HSE06	Heyd–Scuseria–Ernzerhof range-separated hybrid density functional
IA	interatomic
IBZ	irreducible Brillouin zone
ID	interdimer
IPCC	Intergovernmental Panel on Climate Change
IPE	inverse photoemission

JT	Jahn-Teller
KS DFT	Kohn-Sham DFT
LCAO	linear combination of atomic orbitals
LDA	local density approximation
LED	light-emitting diode
LEED	low energy electron diffraction
LUCO	lowest unoccupied crystalline orbital
LUMO	lowest unoccupied molecular orbital
MCSCF	multiconfigurational self-consistent field
MM	molecular mechanics
MO	molecular orbital
MP2	Møller-Plesset perturbation theory of second order
MR	multireference
MRAD	missing-row asymmetric-dimer
MRCI	multireference configuration interaction
NEVPT2	N-electron valence state perturbation theory of second order
NO	natural orbital
NOON	natural orbital occupation number
p	primitive
PBBS	projected bulk band structure
PBCs	periodic boundary conditions
PBE	Perdew-Burke-Ernzerhof density functional
PBE0	Perdew-Burke-Ernzerhof hybrid density functional
PDOS	projected density of states
PED	photoelectron diffraction
RHF	restricted HF
RIJCOSX	resolution-of-identity chain-of-spheres exchange
RKS	restricted KS DFT
ROHF	restricted open-shell HF
ROKS	restricted open-shell KS DFT
RT	room temperature
SBZ	surface Brillouin zone
SCF	self-consistent field
SD	symmetric dimer (and Slater determinant in Chapter 2)
STS	scanning tunneling spectroscopy
TB	tight-binding
TISE	time-independent Schrödinger equation
TZVP	triple-zeta-valence + polarization
TZVPP	triple-zeta-valence + double polarization
UHF	unrestricted HF
UKS	unrestricted KS DFT
UPS	ultraviolet photoemission
VBM	valence band maximum

List of References

[1] K. Takahashi, A. Yoshikawa, A. Sandhu, *Wide Bandgap Semiconductors*, Springer, **2007**.

[2] J. Jian, J. Sun, *Sol. RRL* **2020**, *4*, 2000111.

[3] F. Bechstedt, P. Käckell, A. Zywietz, K. Karch, B. Adolph, K. Tenelsen, J. Furthmüller, *Phys. Status Solidi B* **1997**, *202*, 35–62.

[4] R. Cheung, *Silicon Carbide Microelectromechanical Systems for Harsh Environments*, Imperial College Press, **2006**.

[5] Y. Goldberg, M. Levinshtein, S. Rumyantsev in *Properties of Advanced Semiconductor Materials: GaN, AlN, InN, BN, SiC, SiGe*, (Eds.: M. E. Levinshtein, S. L. Rumyantsev, M. S. Shur), John Wiley & Sons, **2001**, Chapter 5.

[6] T. Kimoto, J. A. Cooper, *Fundamentals of Silicon Carbide Technology*, John Wiley & Sons, **2014**.

[7] L. Patrick, D. R. Hamilton, W. J. Choyke, *Phys. Rev.* **1966**, *143*, 526–536.

[8] A. F. Holleman, E. Wiberg, *Lehrbuch der anorganischen Chemie*, De Gruyter, **1976**.

[9] P. Friedrichs, T. Kimoto, L. Ley, G. Pensl, *Silicon Carbide: Volume 2: Power Devices and Sensors*, Wiley-VCH, **2009**.

[10] B. Shi, A. I. Ramones, Y. Liu, H. Wang, Y. Li, S. Pischinger, J. Andert, *IET Power Electron.* **2023**, *16*, 2103–2120.

[11] Robert Bosch GmbH, “Silicon carbide chips: Teaming up to produce a key technology of the future”, can be found under https://www.bosch.com/stories/semiconductor-manufacturing/, accessed 14.05.2024, **2023**.

[12] IPCC, *Climate Change 2022: Mitigation of Climate Change*, Cambridge University Press, **2022**.

[13] Yole Développement, “Silicon carbide: from gold rush to commodity?”, can be found under https://www.yolegroup.com/strategy-insights/silicon-carbide-from-gold-rush-to-commodity, accessed 14.05.2024, **2023**.

[14] K. Khazen, H. J. von Bardeleben, *Front. Quantum Sci. Technol.* **2023**, *2*, 1115039.

[15] M. H. Ullah, R. Eskandarpour, H. Zheng, A. Khodaei, *IET Gener. Transm. Distrib.* **2022**, *16*, 4239–4257.

[16] F. La Via, A. Severino, R. Anzalone, C. Bongiorno, G. Litrico, M. Mauceri, M. Schoeler, P. Schuh, P. Wellmann, *Mat. Sci. Semicon. Proc.* **2018**, *78*, 57–68.

[17] L. Cheng, Q. Xiang, Y. Liao, H. Zhang, *Energy Environ. Sci.* **2018**, *11*, 1362–1391.

[18] I. Lauermann, R. Memming, D. Meissner, *J. Electrochem. Soc.* **1997**, *144*, 73–80.

[19] Q.-B. Ma, B. Kaiser, J. Ziegler, D. Fertig, W. Jaegermann, *J. Phys. D: Appl. Phys.* **2012**, *45*, 325101.

[20] N. Ichikawa, M. Kato, M. Ichimura, *Appl. Phys. Lett.* **2016**, *109*, 153904.

[21] J. W. Sun, V. Jokubavicius, L. Gao, I. Booker, M. Jansson, X. Y. Liu, J. P. Hofmann, E. J. M. Hensen, M. K. Linnarsson, P. J. Wellmann, et al., *Mater. Sci. Forum* **2016**, *858*, 1028–1031.

[22] S. Tengeler, PhD thesis, Technical University of Darmstadt, **2017**.

[23] J. Jian, Y. Shi, M. Syväjärvi, R. Yakimova, J. Sun, *Sol. RRL* **2019**, *4*, 1900364.

[24] X. Han, S. Heuser, X. Tong, N. Yang, X.-Y. Guo, X. Jiang, *Chem. Eur. J.* **2020**, *26*, 3586–3590.

[25] J.-X. Jian, V. Jokubavicius, M. Syväjärvi, R. Yakimova, J. Sun, *ACS Nano* **2021**, *15*, 5502–5512.

[26] V. M. Bermudez, *Phys. Status Solidi B* **1997**, *202*, 447–473.

[27] P. G. Soukiassian, H. B. Enriquez, *J. Phys.: Condens. Matter* **2004**, *16*, S1611–S1658.

[28] J. Pollmann, P. Krüger, *J. Phys.: Condens. Matter* **2004**, *16*, S1659–S1703.

[29] G. Cicero, A. Catellani, G. Galli, *Phys. Rev. Lett.* **2004**, *93*, 016102.

[30] G. Cicero, G. Galli, A. Catellani, *J. Phys. Chem. B* **2004**, *108*, 16518–16524.

[31] G. Cicero, J. C. Grossman, A. Catellani, G. Galli, *J. Am. Chem. Soc.* **2005**, *127*, 6830–6835.

[32] A. Catellani, G. Cicero, G. Galli, *J. Chem. Phys.* **2006**, *124*, 024707.

[33] C. U. Gonzalez-Valle, S. Kumar, B. Ramos-Alvarado, *J. Phys. Chem. C* **2018**, *122*, 7179–7186.

[34] L. Douillard, O. Fauchoux, V. Aristov, P. Soukiassian, *Appl. Surf. Sci.* **2000**, *166*, 220–223.

[35] V. Y. Aristov, L. Douillard, O. Fauchoux, P. Soukiassian, *Phys. Rev. Lett.* **1997**, *79*, 3700–3703.

[36] P. Soukiassian, F. Semond, L. Douillard, A. Mayne, G. Dujardin, L. Pizzagalli, C. Joachim, *Phys. Rev. Lett.* **1997**, *78*, 907–910.

[37] J. Pollmann, X. Peng, J. Wieferink, P. Krüger, *Surf. Sci. Rep.* **2014**, *69*, 55–104.

[38] L. Duda, L. S. O. Johansson, B. Reihl, H. W. Yeom, S. Hara, S. Yoshida, *Surf. Sci.* **1999**, *439*, 199–210.

[39] P. Käckell, J. Furthmüller, F. Bechstedt, *Appl. Surf. Sci.* **1996**, *104-105*, 45–48.

[40] P. Käckell, J. Furthmüller, F. Bechstedt, *Surf. Sci.* **1996**, *352-354*, 55–59.

[41] A. Catellani, G. Galli, F. Gygi, *Phys. Rev. Lett.* **1996**, *77*, 5090–5093.

[42] A. Catellani, G. Galli, F. Gygi, F. Pellacini, *Phys. Rev. B* **1998**, *57*, 12255–12261.

[43] B. Pieczyrak, L. Jurczyszyn, B. Stankiewicz, *Czech. J. Phys.* **2006**, *56*, 85–92.

[44] J. Pollmann, P. Krüger, M. Rohlfing, M. Sabisch, D. Vogel, *Appl. Surf. Sci.* **1996**, *104-105*, 1–16.

[45] M. Sabisch, P. Krüger, A. Mazur, M. Rohlfing, J. Pollmann, *Phys. Rev. B* **1996**, *53*, 13121–13132.

[46] A. Tejeda, E. Wimmer, P. Soukiassian, D. Dunham, E. Rotenberg, J. D. Denlinger, E. G. Michel, *Phys. Rev. B* **2007**, *75*, 195315.

[47] W. Lu, P. Krüger, J. Pollmann, *Phys. Rev. Lett.* **1998**, *81*, 2292–2295.

[48] S. A. Shevlin, A. J. Fisher, *Phys. Rev. B* **2000**, *62*, 6904–6907.

[49] D. J. Chadi, *Phys. Rev. Lett.* **1979**, *43*, 43–47.

[50] C. Yang, H. Chuan Kang, *J. Chem. Phys.* **1999**, *110*, 11029–11037.

[51] D. R. Alfonso, *Appl. Phys. Lett.* **1999**, *75*, 2404–2406.

[52] S. B. Healy, C. Filippi, P. Kratzer, E. Penev, M. Scheffler, *Phys. Rev. Lett.* **2001**, *87*, 016105.

[53] H. Tamura, M. S. Gordon, *J. Chem. Phys.* **2003**, *119*, 10318–10324.

[54] J. Xi, H. Jiang, C. Liu, D. Morgan, I. Szlufarska, *Corros. Sci.* **2019**, *146*, 1–9.

[55] M. W. Schmidt, M. S. Gordon, *Annu. Rev. Phys. Chem.* **1998**, *49*, 233–266.

[56] B. Paulus, *Surf. Sci.* **1998**, *408*, 195–202.

[57] A. Szabo, N. S. Ostlund, *Modern Quantum Chemistry*, Dover Publications, **1996**.

[58] C. J. Cramer, *Essentials of Computational Chemistry*, 2nd ed., John Wiley & Sons, **2004**.

[59] F. Jensen, *Introduction to Computational Chemistry*, 2nd ed., John Wiley & Sons, **2009**.

[60] D. R. Hartree, *Math. Proc. Cambridge Philos. Soc.* **1928**, *24*, 89–110.

[61] V. Fock, *Z. Phys.* **1930**, *61*, 126–148.

[62] C. Møller, M. S. Plesset, *Phys. Rev.* **1934**, *46*, 618–622.

[63] J. Čížek, *J. Chem. Phys.* **1966**, *45*, 4256–4266.

[64] P. Hohenberg, W. Kohn, *Phys. Rev.* **1964**, *136*, B864–B871.

[65] C. R. Jacob, M. Reiher, *Int. J. Quantum Chem.* **2012**, *112*, 3661–3684.

[66] L. H. Thomas, *Math. Proc. Cambridge Philos. Soc.* **1927**, *23*, 542–548.

[67] E. Fermi, *Rend. Accad. Naz. Lincei.* **1927**, *6*, 602–607.

[68] F. Bloch, *Z. Phys.* **1929**, *57*, 545–555.

[69] P. A. M. Dirac, *Math. Proc. Cambridge Philos. Soc.* **1930**, *26*, 376–385.

[70] J. C. Slater, *Phys. Rev.* **1951**, *81*, 385–390.

[71] W. Kohn, L. J. Sham, *Phys. Rev.* **1965**, *140*, A1133–A1138.

[72] W. Koch, M. C. Holthausen, *A Chemist's Guide to Density Functional Theory*, 2nd ed., Wiley-VCH, **2001**.

[73] T. Tsuneda, *Density Functional Theory in Quantum Chemistry*, Springer, **2014**.

[74] J. P. Perdew, A. Zunger, *Phys. Rev. B* **1981**, *23*, 5048–5079.

[75] J. P. Perdew, K. Burke, M. Ernzerhof, *Phys. Rev. Lett.* **1996**, *77*, 3865–3868.

[76] M. Ernzerhof, G. E. Scuseria, *J. Chem. Phys.* **1999**, *110*, 5029–5036.

[77] C. Adamo, V. Barone, *J. Chem. Phys.* **1999**, *110*, 6158–6170.

[78] J. Heyd, G. E. Scuseria, M. Ernzerhof, *J. Chem. Phys.* **2003**, *118*, 8207–8215.

[79] J. Heyd, G. E. Scuseria, M. Ernzerhof, *J. Chem. Phys.* **2006**, *124*, 219906.

[80] A. V. Krukau, O. A. Vydrov, A. F. Izmaylov, G. E. Scuseria, *J. Chem. Phys.* **2006**, *125*, 224106.

[81] F. Neese, *Coordin. Chem. Rev.* **2009**, *253*, 526–563.

[82] V. G. Chilkuri, T. Applencourt, K. Gasperich, P.-F. Loos, A. Scemama in *New Electron Correlation Methods and their Applications, and Use of Atomic Orbitals with Exponential Asymptotes*, (Eds.: M. Musial, P. E. Hoggan), Academic Press, **2021**, Chapter 3.

[83] J. M. Brom, *J. Chem. Educ.* **2018**, *95*, 1592–1600.

[84] R. Dovesi, A. Erba, R. Orlando, C. M. Zicovich-Wilson, B. Civalleri, L. Maschio, M. Rérat, S. Casassa, J. Baima, S. Salustro, et al., *WIREs Comput. Mol. Sci.* **2018**, *8*, e1360.

[85] K. Yamaguchi, Y. Takahara, T. Fueno, K. N. Houk, *Theor. Chim. Acta* **1988**, *73*, 337–364.

[86] J. Gräfenstein, A. M. Hjerpe, E. Kraka, D. Cremer, *J. Phys. Chem. A* **2000**, *104*, 1748–1761.

[87] J. A. Pople, P. M. W. Gill, N. C. Handy, *Int. J. Quantum Chem.* **1995**, *56*, 303–305.

[88] J. Gräfenstein, E. Kraka, D. Cremer, *Chem. Phys. Lett.* **1998**, *288*, 593–602.

[89] B. O. Roos, P. R. Taylor, P. E. M. Siegbahn, *Chem. Phys.* **1980**, *48*, 157–173.

[90] B. O. Roos, *Int. J. Quantum Chem.* **1980**, *18*, 175–189.

[91] P. Siegbahn, A. Heiberg, B. Roos, B. Levy, *Phys. Scr.* **1980**, *21*, 323–327.

[92] P. E. M. Siegbahn, J. Almlöf, A. Heiberg, B. O. Roos, *J. Chem. Phys.* **1981**, *74*, 2384–2396.

[93] B. O. Roos in *Advances in Chemical Physics: Ab Initio Methods in Quantum Chemistry Part 2*, (Ed.: K. P. Lawley), John Wiley & Sons, **1987**, Chapter 7.

[94] F. Neese, F. Wennmohs, Orca 5.0.4 User's Manual, Max-Planck-Institut für Kohlenforschung, Mühlheim a. d. Ruhr, **2023**.

[95] L. González, D. Escudero, L. Serrano-Andrés, *ChemPhysChem* **2011**, *13*, 28–51.

[96] N. Ben Amor, C. Noûs, G. Trinquier, J.-P. Malrieu, *J. Chem. Phys.* **2020**, *153*, 044118.

[97] E. Schrödinger, *Ann. Phys.* **1926**, *385*, 437–490.

[98] C. Angeli, M. Pastore, R. Cimiraglia, *Theor. Chem. Acc.* **2006**, *117*, 743–754.

[99] K. Andersson, P.-Å. Malmqvist, B. O. Roos, A. J. Sadlej, K. Wolinski, *J. Phys. Chem.* **1990**, *94*, 5483–5488.

[100] K. Andersson, P.-Å. Malmqvist, B. O. Roos, *J. Chem. Phys.* **1992**, *96*, 1218–1226.

[101] K. G. Dyall, *J. Chem. Phys.* **1995**, *102*, 4909–4918.

[102] C. Angeli, R. Cimiraglia, S. Evangelisti, T. Leininger, J.-P. Malrieu, *J. Chem. Phys.* **2001**, *114*, 10252–10264.

[103] C. Angeli, R. Cimiraglia, J.-P. Malrieu, *Chem. Phys. Lett.* **2001**, *350*, 297–305.

[104] C. Angeli, R. Cimiraglia, J.-P. Malrieu, *J. Chem. Phys.* **2002**, *117*, 9138–9153.

[105] R. Dronskowski, *Computational Chemistry of Solid State Materials*, Wiley-VCH, **2005**.

[106] R. Dovesi, B. Civalleri, C. Roetti, V. R. Saunders, R. Orlando in *Reviews in Computational Chemistry*, John Wiley & Sons, **2005**, Chapter 1.

[107] C. Kittel, *Introduction to Solid State Physics*, 8th ed., John Wiley & Sons, **2005**.

[108] D. S. Sholl, J. A. Steckel, *Density Functional Theory: A Practical Introduction*, John Wiley & Sons, **2009**.

[109] F. Bloch, *Z. Phys.* **1929**, *52*, 555–600.

[110] D. J. Tannor, *Introduction to Quantum Mechanics*, University Science Books, **2007**.

[111] R. Hoffmann, *Angew. Chem. Int. Edit.* **1987**, *26*, 846–878.

[112] W. Setyawan, S. Curtarolo, *Comp. Mater. Sci.* **2010**, *49*, 299–312.

[113] P. Kratzer, J. Neugebauer, *Front. Chem.* **2019**, *7*, 106.

[114] W. Massa, *Kristallstrukturbestimmung*, 8th ed., Springer Spektrum, **2015**.

[115] J. K. Burdett, *Prog. Solid State Chem.* **1984**, *15*, 173–255.

[116] J. A. Appelbaum, G. A. Baraff, D. R. Hamann, *Phys. Rev. B* **1975**, *11*, 3822–3831.

[117] L. Duda, L. S. O. Johansson, B. Reihl, H. W. Yeom, S. Hara, S. Yoshida, *Phys. Rev. B* **2000**, *61*, R2460–R2463.

[118] P. W. Atkins, R. Friedman, *Molecular Quantum Mechanics*, 4th ed., Oxford University Press, **2005**.

[119] R. Hoffmann, C. Janiak, C. Kollmar, *Macromolecules* **1991**, *24*, 3725–3746.

[120] A. Groß, *Theoretical Surface Science*, 2nd ed., Springer, **2009**.

[121] L. Gerhards, T. Klüner, *J. Phys. Chem. C* **2021**, *125*, 13313–13323.

[122] G. Kresse, J. Furthmüller, *Comp. Mater. Sci.* **1996**, *6*, 15–50.

[123] G. Kresse, J. Furthmüller, *Phys. Rev. B* **1996**, *54*, 11169–11186.

[124] R. Dovesi, V. R. Saunders, C. Roetti, R. Orlando, C. M. Zicovich-Wilson, F. Pascale, B. Civalleri, K. Doll, N. M. Harrison, I. J. Bush, et al., CRYSTAL17 User's Manual, University of Torino, Turin, **2018**.

[125] A. Zangwill, *Physics at Surfaces*, Cambridge University Press, **1988**.

[126] F. Bechstedt, J. Furthmüller, *J. Phys.: Condens. Matter* **2004**, *16*, S1721–S1732.

[127] K. Sagisaka, J. Nara, D. Bowler, *J. Phys.: Condens. Matter* **2017**, *29*, 145502.

[128] H. J. Monkhorst, J. D. Pack, *Phys. Rev. B* **1976**, *13*, 5188–5192.

[129] F. Hummel, T. Tsatsoulis, A. Grüneis, *J. Chem. Phys.* **2017**, *146*, 124105.

[130] Q. Sun, X. Zhang, S. Banerjee, P. Bao, M. Barbry, N. S. Blunt, N. A. Bogdanov, G. H. Booth, J. Chen, Z.-H. Cui, et al., *J. Chem. Phys.* **2020**, *153*, 024109.

[131] V. Staemmler in *Theoretical Aspects of Transition Metal Catalysis*, Springer, **2005**, Chapter 7.

[132] P. Deák, *Phys. Status Solidi B* **2000**, *217*, 9–21.

[133] T. Klüner, N. Govind, Y. A. Wang, E. A. Carter, *J. Chem. Phys.* **2002**, *116*, 42–54.

[134] D. V. Chulhai, J. D. Goodpaster, *J. Chem. Theory. Comput.* **2018**, *14*, 1928–1942.

[135] H. Q. Pham, M. R. Hermes, L. Gagliardi, *J. Chem. Theory Comput.* **2019**, *16*, 130–140.

[136] Z.-H. Cui, T. Zhu, G. K.-L. Chan, *J. Chem. Theory Comput.* **2019**, *16*, 119–129.

[137] L. Gerhards, T. Klüner, *Phys. Chem. Chem. Phys.* **2022**, *24*, 2051–2069.

[138] J. Dabrowski in *Silicon Surfaces and Formation of Interfaces*, (Eds.: J. Dabrowski, H.-J. Müller), World Scientific, **2000**, Chapter 3.

[139] C. Elschenbroich, *Organometallchemie*, 6th ed., Teubner, **2008**.

[140] Y. Apeloig, R. Pauncz, M. Karni, R. West, W. Steiner, D. Chapman, *Organometallics* **2003**, *22*, 3250–3256.

[141] R. Konecny, R. Hoffmann, *J. Am. Chem. Soc.* **1999**, *121*, 7918–7924.

[142] J. P. Malrieu, G. Trinquier, *J. Am. Chem. Soc.* **1989**, *111*, 5916–5921.

[143] H. B. Wedler, P. Wendelboe, P. P. Power, *Organometallics* **2018**, *37*, 2929–2936.

[144] R. C. Fischer, P. P. Power, *Chem. Rev.* **2010**, *110*, 3877–3923.

[145] Z. Glasovac, I. Antol, M. Vazdar, D. Margetić, *Theor. Chem. Acc.* **2009**, *124*, 421–430.

[146] M. Kira, *Organometallics* **2011**, *30*, 4459–4465.

[147] E. A. Carter, W. A. Goddard, *J. Chem. Phys.* **1988**, *88*, 1752–1763.

[148] F. Weigend, R. Ahlrichs, *Phys. Chem. Chem. Phys.* **2005**, *7*, 3297.

[149] T. L. Windus, M. S. Gordon, *J. Am. Chem. Soc.* **1992**, *114*, 9559–9568.

[150] H. Kobayashi, T. Iwamoto, M. Kira, *J. Am. Chem. Soc.* **2005**, *127*, 15376–15377.

[151] P. Käckell, F. Bechstedt, H. Hüsken, B. Schröter, W. Richter, *Surf. Sci.* **1997**, *391*, L1183–L1187.

[152] H. Hüsken, B. Schröter, W. Richter, *Surf. Sci.* **1998**, *407*, 114–120.

[153] L. Duda, L. S. O. Johansson, B. Reihl, H. W. Yeom, S. Hara, S. Yoshida, *Surf. Rev. Lett.* **1999**, *06*, 1151–1157.

[154] C. Benesch, H. Merz, H. Zacharias, *Surf. Sci.* **2001**, *492*, 225–234.

[155] A. J. Karttunen, D. Usvyat, M. Schütz, L. Maschio, *Phys. Chem. Chem. Phys.* **2017**, *19*, 7699–7707.

[156] A. J. Karttunen, T. Tynell, M. Karppinen, *J. Phys. Chem. C* **2015**, *119*, 13105–13114.

[157] A. Schäfer, C. Huber, R. Ahlrichs, *J. Chem. Phys.* **1994**, *100*, 5829–5835.

[158] M. F. Peintinger, D. V. Oliveira, T. Bredow, *J. Comput. Chem.* **2012**, *34*, 451–459.

[159] R. S. Mulliken, *J. Chem. Phys.* **1955**, *23*, 1833–1840.

[160] Jmol: an open-source Java viewer for chemical structures in 3D. http://www.jmol.org/, accessed 20.06.2023.

[161] K. Momma, F. Izumi, *J. Appl. Cryst.* **2011**, *44*, 1272–1276.

[162] A. Taylor, R. M. Jones in *Silicon Carbide - A High Temperature Semiconductor*, (Eds.: J. R. O'Connor, J. Smiltens), Pergamon Press, **1960**.

[163] I. C. Gerber, J. G. Ángyán, M. Marsman, G. Kresse, *J. Chem. Phys.* **2007**, *127*, 054101.

[164] E. J. Baerends, O. V. Gritsenko, R. van Meer, *Phys. Chem. Chem. Phys.* **2013**, *15*, 16408.

[165] W. Chen, A. Pasquarello, *Phys. Rev. B* **2012**, *86*, 035134.

[166] T. Oda, Y. Zhang, W. J. Weber, *Chem. Phys. Lett.* **2013**, *579*, 58–63.

[167] B. Wenzien, P. Käckell, F. Bechstedt, *Surf. Sci.* **1994**, *307–309*, 989–994.

[168] A. Gali, B. Aradi, P. Deák, W. J. Choyke, N. T. Son, *Phys. Rev. Lett.* **2000**, *84*, 4926–4929.

[169] B. Aradi, A. Gali, P. Deák, J. E. Lowther, N. T. Son, E. Janzén, W. J. Choyke, *Phys. Rev. B* **2001**, *63*, 245202.

[170] T. Müller, *Angew. Chem. Int. Ed.* **2001**, *40*, 3033–3036.

[171] T. V. Pavlova, *Phys. Chem. Chem. Phys.* **2020**, *22*, 21851–21857.

[172] L. Douillard, F. Semond, V. Y. Aristov, P. Soukiassian, B. Delley, A. Mayne, G. Dujardin, E. Wimmer, *Mater. Sci. Forum* **1998**, *264–268*, 379–382.

[173] D. G. Trabada, J. Ortega, *J. Phys. Condens. Matter* **2009**, *21*, 182003.

[174] B. I. Craig, P. V. Smith, *Surf. Sci.* **1990**, *233*, 255–260.

[175] H. Yan, A. P. Smith, H. Jónsson, *Surf. Sci.* **1995**, *330*, 265–275.

[176] A. S. Menon, L. Radom, *J. Phys. Chem. A* **2008**, *112*, 13225–13230.

[177] T. Suzuki, V. Venkataramanan, M. Aono, *Jpn. J. Appl. Phys.* **2001**, *40*, L1119.

[178] C. Madhu, A. Sundaresan, C. N. R. Rao, *Phys. Rev. B* **2008**, *77*, 201306.

[179] S. C. Erwin, F. J. Himpsel, *Nat. Commun.* **2010**, *1*, 58.

[180] A. Konopka, B. Aşik, U. Gerstmann, E. Rauls, N. J. Vollmers, M. Rohrmüller, W. G. Schmidt, B. Friedel, S. Greulich-Weber, *IOP Conf. Ser.: Mater. Sci. Eng.* **2010**, *15*, 012013.

[181] M. Kurahashi, A. Pratt, Y. Yamauchi, *Surf. Sci.* **2011**, *605*, 612–615.

[182] U. Gerstmann, M. Rohrmüller, N. J. Vollmers, A. Konopka, S. Greulich-Weber, E. Rauls, M. Landmann, S. Sanna, A. Riefer, W. G. Schmidt in *High Performance Computing in Science and Engineering '12*, Springer, **2012**, 129–143.

[183] T. J. Frankcombe, *J. Phys. Chem. C* **2014**, *118*, 26926–26930.

[184] K. Tada, S. Yamanaka, T. Kawakami, Y. Kitagawa, M. Okumura, K. Yamaguchi, S. Tanaka, *Chem. Phys. Lett.* **2021**, *765*, 138291.

[185] Y. Kitagawa, T. Saito, Y. Nakanishi, Y. Kataoka, T. Matsui, T. Kawakami, M. Okumura, K. Yamaguchi, *J. Phys. Chem. A* **2009**, *113*, 15041–15046.

[186] J. M. Powers, A. Wander, M. A. Van Hove, G. A. Somorjai, *Surf. Sci.* **1992**, *260*, L7–L10.

[187] M. Shoji, Y. Yoshioka, K. Yamaguchi, *Chem. Phys. Lett.* **2014**, *608*, 50–54.

[188] M. L. Shek, *Surf. Sci.* **1996**, *349*, 317–332.

[189] R. Kaplan, *Surf. Sci.* **1989**, *215*, 111–134.

[190] A. Ramstad, G. Brocks, P. J. Kelly, *Phys. Rev. B* **1995**, *51*, 14504–14523.

[191] G. de la Flor, B. Souvignier, G. Madariaga, M. I. Aroyo, *Acta Crystallogr. A* **2021**, *77*, 559–571.

[192] F. Neese, *WIREs Comput. Mol. Sci.* **2022**, *12*, e1606.

[193] S. Lehtola, C. Steigemann, M. J. T. Oliveira, M. A. L. Marques, *SoftwareX* **2018**, *7*, 1–5.

[194] F. Neese, F. Wennmohs, A. Hansen, U. Becker, *Chem. Phys.* **2009**, *356*, 98–109.

[195] F. Weigend, *Phys. Chem. Chem. Phys.* **2006**, *8*, 1057–1065.

[196] A. Hellweg, C. Hättig, S. Höfener, W. Klopper, *Theor. Chem. Acc.* **2007**, *117*, 587–597.

[197] L. Pauling, *J. Am. Chem. Soc.* **1932**, *54*, 3570–3582.

[198] M. Bensberg, M. Reiher, *J. Phys. Chem. Lett.* **2023**, *14*, 2112–2118.

[199] A. Catellani, G. Cicero, *J. Phys. D: Appl. Phys.* **2007**, *40*, 6215–6224.

[200] J. E. T. Smith, B. Mussard, A. A. Holmes, S. Sharma, *J. Chem. Theory Comput.* **2017**, *13*, 5468–5478.

[201] D. S. Levine, D. Hait, N. M. Tubman, S. Lehtola, K. B. Whaley, M. Head-Gordon, *J. Chem. Theory Comput.* **2020**, *16*, 2340–2354.

[202] J. Greiner, I. Gianni, T. Nottoli, F. Lipparini, J. J. Eriksen, J. Gauss, *J. Chem. Theory Comput.* **2024**, *20*, 4663–4675.

[203] Q. Sun, T. C. Berkelbach, N. S. Blunt, G. H. Booth, S. Guo, Z. Li, J. Liu, J. D. McClain, E. R. Sayfutyarova, S. Sharma, et al., *WIREs Comput. Mol. Sci.* **2017**, *8*, e1340.

[204] F. Bechstedt in *Principles of Surface Physics*, (Ed.: F. Bechstedt), Springer, **2003**, Chapter 1.

Curriculum Vitae

Personal Data

Name	Niklas Thoben
Date of Birth	08.03.1995
Place of Birth	Löningen, Germany
Nationality	German

Education

10.2019 – present	PhD Student (Theoretical Chemistry) Carl von Ossietzky Universität Oldenburg Thesis: *Describing the Statically Correlated Si-terminated 3C-SiC(001) Surface with Single- and Multiconfigurational Methods* Working Group Klüner
10.2016 – 09.2019	Master of Science (Chemistry) Carl von Ossietzky Universität Oldenburg Grade: 1.05 Thesis: *Theoretische Untersuchungen zur Photodesorption von CO auf Si(100)* Working Group Klüner
10.2013 – 09.2016	Bachelor of Science (Chemistry) Carl von Ossietzky Universität Oldenburg Grade: 1.41 Thesis: *Hydroxy-Spezies auf Rutil(110): Einfluss auf Adsorptionsenergien* Working Group Klüner
08.2005 – 06.2013	A level Copernicus Gymnasium Löningen Grade: 1.3

Conferences and Presentations

26. – 31.03.2023	DPG Spring Meeting, Dresden Talk: *Revisiting the Strongly Correlated Si-terminated 3C-SiC(001)-p(2×1) Surface with Density- and Wave Function-Based Methods*
16. – 21.02.2020	Sanibel Symposium, St. Simons Island, USA Poster: *Theoretical Investigations on the Photodesorption of CO on Si(100)*
9.12.2019	Physical-Chemical Colloquium, University of Duisburg-Essen Talk: *Theoretical Investigations on the Photodesorption of CO on Si(100)*
14.11.2019	Day of Chemistry, Carl von Ossietzky Universität Oldenburg Award for Best Master's Degree of the Institute of Chemistry in 2019 Talk: *Theoretische Untersuchungen zur Photodesorption von CO auf Si(100)*
11. – 12.03.2019	Oldenburg Symposium on Chemical Bond Activation, Oldenburg Poster: *Ab initio Adsorption Study of CO on Si(100)*
11. – 16.03.2018	DPG Spring Meeting, Berlin Talk: *Hydroxy-Species on TiO_2-Rutile(110): ab initio Adsorption Studies*

Publications

N. Thoben, T. Klüner, Revisiting the Strongly Correlated Si-terminated 3C-SiC(001)-p(2×1) Reconstructed Surface with Single- and Multiconfigurational Methods, *J. Phys. Chem. C* **2023**, *127*, 23475–23488. DOI: 10.1021/acs.jpcc.3c06305

N. Thoben, T. Kaper, S. de Graaff, L. Gerhards, M. Schmidtmann, T. Klüner, R. Beckhaus, S. Doye, Density Functional Theory Calculations for Multiple Conformers Explaining the Regio- and Stereoselectivity of Ti-Catalyzed Hydroaminoalkylation Reactions, *ChemPhysChem* **2023**, *24*, e202300370. DOI: 10.1002/cphc.202300370

Teaching Record

che115 – Theoretical and Mathematical Foundations of Chemistry

- (co-)supervision of the tutorials (WiSe 22/23, 21/22, 20/21, 19/20)
- (co-)supervision of the additional tutorials of the program "Studienstart – alles klar?" (WiSe 23/24, 22/23, 19/20, 18/19, 17/18)
- digitalization and revision of the exercises and solutions for online teaching during the COVID-19 pandemic

che261 – Quantum Mechanics

- (co-)supervision of the practical computational chemistry course (WiSe 22/23, 21/22, 20/21)
- comprehensive revision of the practical computational chemistry course script (WiSe 22/23)

che471 – Theoretical Chemistry

- supervision of the quantum chemistry tutorials (WiSe 21/22)
- supervision of the quantum dynamics tutorials (SuSe 21)
- comprehensive revision of the exercises and solutions of the quantum dynamics tutorials (SuSe 21)

che472 – Research Internship Theoretical Chemistry

- (co-)supervision of the Hartree-Fock programming course
  - WiSe 22/23: A. Büker, S. Emken
  - SuSe 22: D. Benedens, F. Eilers, D. Hirsch, T. Wittemann
  - SuSe 21: S. Erdmann, T. Reetz
  - SuSe 20: K. Schwitalla
  - SuSe 19: M. Coners, M. Lang, J. Rada, T. Zimmermann
  - WiSe 18/19: J. Brauer, O. Ostendorf
  - WiSe 17/18: L. Bührmann, T. Kaper, L. Stelter
- (co-)supervision of the quantum dynamics programming course
  - SuSe 23: S. Emken
  - SuSe 22: D. Benedens, A. Büker, F. Eilers, D. Hirsch
  - SuSe 21: S. Erdmann
  - SuSe 20: M. Coners, M. Lang, T. Reetz, K. Schwitalla, T. Zimmermann
- supervision of the research projects of D. Benedens and A. Büker (SuSe 23)
- comprehensive revision of the Hartree-Fock programming course script (WiSe 17/18, SuSe 22)
- creation of a 70-page script from scratch for the quantum dynamics programming course (SuSe 20)

bam – Bachelor Thesis

- supervision of the Bachelor thesis of F. Römisch (SuSe 23)

Further Obligations

- management of exams (registration, room reservation, creation of exercises, supervision, correction, post-exam review)
- management of the employment of tutors
- administration of the working group website

Acknowledgement

With the end of this work, also being part of this working group for more than eight years comes to an end. Because of this, I would like to thank several people, even though I can't mention everyone, so bear with me if you can't find yourself here.

First of all, I greatly thank Prof. Dr. Thorsten Klüner for giving me the opportunity to investigate such a challenging topic as well as always being available for fruitful discussions and the pleasant working atmosphere. Furthermore, I am thankful for introducing me to the mathematical foundations of chemistry in the first semester of my studies, which was the starting point to further dive into the blurry but exciting world of quantum mechanics for the rest of my academic career.

Moreover, I kindly thank Prof. Dr. Thomas Müller for taking on the task of the second assessor for this thesis. Along these lines, I also appreciate Prof. Dr. Katharina Al-Shamery for accepting to be the third assessor for the disputation connected to this thesis.

Over the years, several great co-workers came and went during my time with the working group, whom I'd like to thank: Dr. Jan Mitschker for being a role model PhD and a great supervisor during my bachelor thesis. Dr. Wilke Dononelli for further including me into the working group by recruiting me as tutor and letting me discover my passion for teaching my knowledge to freshman students. Dr. Thomas Teusch for being a great office colleague and challenging me to try to understand the mysterious concept of the reciprocal space during my research internship he supervised, which actually culminated in being a major subject of this thesis. Dr. Thorben Petersen for always helping out with any occurring scientific problem and the occasional coffee breaks. A special shout-out is devoted to Dr. Luca Gerhards, who was a fellow student before my PhD studies, a great office colleague for the first two years of my PhD studies and still a good friend of mine until today after he left the group. I fondly remember the fun times in the office mainly consisting of getting on Thomas' nerves, laughing about absurd memes and trying to understand complex theoretical concepts. Along these lines, I also thank Dr. Tobias Kaper for being a great companion during the second half of my PhD studies and further beyond. I further thank Tobias for including me in the refreshing research project in the field of organic chemistry together with, among others, Prof. Dr. Sven Doye, whom I also thank for the pleasant cooperation when writing the corresponding publication. I am further grateful for our postdoc Dr. Halil Sözen, my fellow PhD students Luisa Stelter, Stephan Erdmann, and

Thies Reetz, as well as several other students that were associated with our working group, with special mention Tobias Wittemann, for the good times, the pleasant working atmosphere, and without all of whom it would have been impossible to tackle all the teaching connected to our working group. Last but not least, I thank our admin Robert Röhse for always maintaining the IT infrastructure of the working group and for the sarcastic and often excessive but always very entertaining discussions about everything and anything.

Obviously, there also exist people outside of the university bubble. With this, I further thank my friends, with whom I could always have a blast independent of the progress of my research project, and along these lines I especially thank Korfi and Erik, with whom I share (arguably too often) a love-hate relationship with League of Legends. I am also grateful for my family and especially my parents for always supporting me in every way possible no matter what happens. At the end, my utmost gratitude is devoted to my lovely fiancée Julia, who unconditionally is there for me at all times and just in general fills my life with joy.

No one knows what the future holds. That's why its potential is infinite, as this encounter makes clear. This is the choice of Steins Gate.

— Okabe Rintarou

Declaration

This declaration is given exclusively in German:

Hiermit versichere ich, dass ich diese Arbeit selbstständig verfasst und die benutzten Hilfsmittel vollständig angegeben habe.

Teile dieser Arbeit sind bereits in der folgenden Publikation veröffentlicht worden:

N. Thoben, T. Klüner, *J. Phys. Chem. C* **2023**, *127*, 23475–23488.
DOI: 10.1021/acs.jpcc.3c06305

Diese Dissertation liegt oder lag weder in ihrer Gesamtheit noch in Teilen einer anderen wissenschaftlichen Hochschule zur Begutachtung in einem Promotionsverfahren vor.

Angestrebt wird der Grad des Doktors der Naturwissenschaften (Dr. rer. nat.).

Ich versichere, dass ich die Regelungen zu guter wissenschaftlicher Praxis der Carl von Ossietzky Universität Oldenburg befolgt habe.

Im Zusammenhang mit diesem Promotionsvorhaben sind von mir keine kommerziellen Vermittlungs- oder Beratungsdienste (Promotionsberatung) in Anspruch genommen worden.

Oldenburg, 16.10.2024

Niklas Thoben